UNIVERSITÉ LAVAL

Magnetic Field Stimulation of Magnetic Nanoparticles for the Intensification of Scalar Transport

Thèse

Shahab Boroun

Doctorat en génie chimique
Philosophiæ doctor (Ph. D.)

Québec, Canada

Magnetic Field Stimulation of Magnetic Nanoparticles for the Intensification of Scalar Transport

Thèse

Shahab Boroun

Sous la direction de :

Faïçal Larachi, directeur de recherche

Résumé

Dans cette thèse, le transport de scalaires dans des ferrofluides / ferrogels est étudié théoriquement et expérimentalement. L'intérêt principal est de quantifier expérimentalement le processus de transport de masse dans des ferrofluides / ferrogels exposés à un champ magnétique externe et de comprendre les mécanismes sous-jacents à ces processus à la lumière de simulations ferrohydrodynamiques (FHD). Nous visons également à utiliser les phénomènes de transport améliorés, identifiés dans les ferrofluides pour des applications de génie de la réaction chimique, par le biais d'études expérimentales sur le mélange / micromélange en micro-canal.

L'introduction présente les principes de base de la dynamique des ferrofluides et des nanoparticules magnétiques (NPM) du point de vue de la mécanique des fluides et de la physique des colloïdes. Le cadre de ferrohydrodynamique, englobant les équations du mouvement des ferrofluides en relation avec la relaxation magnétique, y est expliqué. La littérature récente pertinente au transport de scalaires et au mélange dans les ferrofluides est examinée et les mécanismes d'intensification de transport de masse dans le ferrofluides excités par divers types de champs magnétiques sont discutés.

Le première chapitre présente des observations expérimentales et des simulations numériques sur le transport de scalaires dans un ferrofluide de type Brownien au repos mais soumis à un champ magnétique rotatif (CMR). Les expériences de transport de masse ont été conduites dans un mélangeur capillaire en T excité transversalement par un champ magnétique uniforme. Une augmentation significative du transport de masse a été observée en présence de CMR dans une direction normale à l'axe de rotation du champ magnétique. Un tel contrôle directionnel par CMR a permis de mettre en évidence le caractère anisotrope du flux de masse puisque la diffusion moléculaire était le seul mécanisme de transport agissant dans une direction parallèle à l'axe du capillaire. Le rôle de l'advection du ferrofluide induite par CMR (écoulement *spin-up*) quant à l'amélioration du transport de masse a été examiné à la lumière de la solution de l'équation d'advection-diffusion et de la comparaison des prédictions numériques de FHD avec les résultats expérimentaux. Une analyse comparative systématique des simulations numériques par rapport aux observations expérimentales a révélé que la diffusivité effective dans le ferrofluide peut être représentée par un tenseur diagonal dont les composantes sont fonction de la fréquence du CMR et de la concentration des NPM.

Dans le deuxième chapitre, nous avons exploité le concept de diffusion effective anormale anisotrope dans les ferrofluides pour expliquer les variations de la dispersion axiale observées

expérimentalement pour un écoulement de Poiseuille en présence de CMR. Les résultats expérimentaux ont montré que la distribution des temps de séjour (DTS) en présence de CMR est moins asymétrique avec un temps de percée de plus en plus retardé lorsque la fréquence de CMR et/ou la concentration en nanoparticules magnétiques augmente(nt). La solution de l'équation d'advection-diffusion couplée aux équations de transport de quantité de mouvement sous champ magnétique rotatif signale une faible contribution de l'advection dans le phénomène observé. Les simulations numériques ont également montré que la réduction de la dispersion axiale était le résultat d'une diffusivité effective anisotrope anormale dans le ferrofluide suggérant une échelle de mélange de l'ordre de quelques nanomètres dictée par l'effet de la rotation du champ magnétique sur la matrice liquide porteuse non-magnétique des NPM..

Dans le troisième chapitre, les propriétés de transport de masse du ferrofluide identifiées ont ensuite été examinées pour des applications de mélange et de micromélange via des techniques réactionnelles. Une étude comparative a été menée pour évaluer l'efficacité du mélange entre des fluides magnétiques et non magnétiques dans un mélangeur de type T capillaire, cylindrique et soumis à des champs magnétiques statique (CMS), oscillant (CMO) et rotatif. En utilisant la réaction modèle de Villermaux-Dushman, nous avons mis en évidence la sensibilité de la sélectivité de cette réaction au micromélange et au transfert de masse au niveau moléculaire. Les résultats ont montré une réduction substantielle de la résistance au transport à l'échelle nanométrique avec des effets mesurables sur la distribution des produits lorsque le mélange est stimulé par un cham magnétique rotatif.

Dans le chapitre quatre, nous étendons le concept de mélange NPM/CMR aux ferrogels, préparés en ensemençant des (dipôles durs) nanoparticules de cobalt-ferrite dans un hydrogel de polyacrylamide. L'analyse quantitative des données d'aimantation a révélé l'existence de NPM hydrodynamiquement libres, donc sensibles à la relaxation brownienne, ainsi que des NPM mécaniquement bloquées dans la structure du ferrogel. Un ferrogel contenant des MNP hydrodynamiquement libres engendre des diffusivités effectives d'un soluté passif largement supérieures à la diffusion moléculaire intrinsèque mesurée pour le même soluté au sein de la structure de ferrogel en absence de champ magnétique rotatif.

Les résultats expérimentaux et théoriques de cette thèse pourraient ouvrir la voie à l'utilisation de MNP/ferrofluide stimulés par champ magnétique pour la conception et le développement de systèmes micro-fluidiques et de matériaux magnétiques multifonctionnels dotés de propriétés de transport contrôlables à distance.

Abstract

In this PhD thesis, the transport of scalars in ferrofluids/ferrogels is theoretically and experimentally studied. The major interest is to experimentally quantify mass transport process in ferrofluids/ferrogels exposed to external magnetic fields and also to understand the mechanisms underlying the observed enhanced mass transport processes through ferrohydrodynamic (FHD) simulations. We also aim at utilizing the identified enhanced transport phenomena in ferrofluids for reaction engineering applications through experimental studies on mixing/micromixing in microchannels.

The introduction presents the basic principles and fundamentals of ferrofluid and magnetic nanoparticles (MNP) dynamics from fluid mechanics and colloidal physics perspectives. The framework of ferrohydrodynamics (FHD), encompassing the ferrofluid equations of motion in connection with magnetic relaxation is explained. The recent literature relevant to the subject of scalar transport and mixing in ferrofluids is reviewed and the mechanisms of rate intensification of mass transport in ferrofluid subjected to various types of magnetic fields are discussed.

The first chapter reports experimental observations and numerical simulations on the transport of scalars in quiescent Brownian ferrofluids under rotating magnetic field (RMF). The mass transport experiments were conducted in a cylindrical capillary T-mixer in presence/absence of transverse uniform RMF. Significant enhancement in mass transport was observed in presence of RMF in a direction normal to rotation axis of magnetic field. RMF directional control of mass flux enhancement was anisotropic since the molecular diffusion was the only detected transport mechanism in a direction parallel to the capillary axis. The significance of RMF driven ferrofluid advection (spin-up flow) in mass transport enhancement was examined in the light of the solution of advection-diffusion equation and subsequent comparison of numerical predictions with experimental results. Systematic analysis of numerical simulations compared to experimental observations unveiled that the effective diffusivity in ferrofluid consists of a diagonal tensor whose components are a function of RMF frequency and MNP concentration.

In the second chapter, we exploited the concept of anisotropic anomalous effective diffusion in ferrofluids to explain the experimentally observed variations of axial dispersion in ferrofluid capillary Poiseuille flow in presence of external RMF. The experimental results showed that residence time distribution (RTD) in presence of RMF is more symmetric with retarded breakthrough time when frequency of RMF and magnetic nanoparticles (MNP) concentration are

increased. The solution of advection-diffusion equation coupled to FHD equations of motion predicted weak contribution of advection in the observed phenomenon. The numerical simulations showed that the reduced axial dispersion is the outcome of anomalous anisotropic effective diffusivity in ferrofluid exposed to external uniform RMF.

In chapter three, the identified mass transport properties of ferrofluid were further examined for (micro)-mixing applications in reaction engineering. A comparative study was conducted to evaluate the mixing efficiency between magnetic and non-magnetic fluids in a cylindrical capillary T-type mixer subjected to static (SMF), oscillating (OMF) and rotating magnetic fields. By using a probe reaction set (the Villermaux-Dushman reaction) with sensitive selectivity to mass transfer rate, mixing at molecular level was also investigated. The results showed substantial elimination of mass transfer rate influence on product distribution of chemical reactions when the mixing process is intensified with RMF.

In chapter four, we extend the concept of mixing by MNP/RMF to ferrogels, prepared by seeding hard-dipole cobalt-ferrite MNP in polyacrylamide hydrogels. Quantitative analysis of magnetization data indicated the existence of hydrodynamically free MNPs, susceptible to Brownian relaxation along with mechanically blocked ones. A ferrogel consisting of hydrodynamically free MNP exhibits effective diffusivities higher than the intrinsic molecular diffusion of passive solute within the ferrogel structure.

The experimental and theoretical findings in this thesis may open the way for application of magnetic field-stimulated MNP/ferrofluid for design and development of microfluidic systems and multifunctional magnetic materials with remote-controllable transport properties.

Table of content

Résumé iii
Abstract v
List of Figures xi
List of Tables xv
Acknowledgements xvii
Foreword xviii
Introduction 1
- Mixing, magnetic nanoparticles and magnetism 2
- Mixing based on ferrohydrodynamics (FHD) 3
- FHD transport equations 4
- Mixing with static magnetic fields (SMF) 6
- Mixing with oscillating magnetic fields (OMF) 11
- Mixing with rotating magnetic fields (RMF) 15
- Comparison of RMF with OMF and SMF in lateral nanomixing of ferrofluid capillary flows 19
- Scope of thesis 21
- Nomenclature 22
- References 24
Chapter 1: Anomalous anisotropic transport of scalars in dilute ferrofluids under uniform rotating magnetic fields – Mixing time measurements and ferrohydrodynamic simulations 26
Résumé 27
1.1. Abstract 29
1.2. Introduction 30
1.3. Experimental 33
1.3.1. Preparation of cobalt ferrite nanoparticles, and acidic and basic ferrofluids 33
1.3.2. Magnet device 33
1.3.3. Transverse mixing via stop-flow technique 34
1.3.4. Quantification of transverse mixing 35
1.3.5. Quantification of axial diffusive transport 36

1.4. Numerical Simulations 37
1.4.1. FHD governing equations 37
1.4.2. Scaling FHD equations for rotating magnetic fields 39
1.4.3. Boundary conditions 40
1.4.4. Scalar transport 41
1.4.5. Numerical method 41
1.5. Results and Discussion 42
1.5.1. Properties of cobalt ferrite nanoparticles and ferrofluids 42
1.5.2. Transverse mixing via stop-flow RMF excitation 44
1.5.3. Assessment of spin-up flow via FHD simulations 47
1.5.3.1. Role of ferrofluid azimuthal velocity on convective mixing 47
1.5.3.2. Role of MNP angular velocity on diffusive mixing 50
1.5.3.3. Kelvin body force 51
1.5.3.4. Magnetization 52
1.5.3.5. RMF frequency and MNP concentration 54
1.5.3.6. Scale effect and spin-up flow 55
1.5.4. FHD model confrontation to mixing index experiments 57
1.5.4.1. Failure of isotropic diffusion tensor 57
1.5.4.2. Determination of effective diffusivity tensor 59
1.6. Conclusion 62
1.7. Nomenclature 63
1.8. References 65
Chapter 2: Residence time distribution of passive scalars in magnetic nanofluid Poiseuille flow under rotating magnetic fields 67
Résumé 68
2.1. Abstract 69
2.2. Introduction 70
2.3. Experimental 72
2.3.1. Magnet device 72
2.3.2. Synthesis and characterization of Cobalt ferrite nanoparticles and ferrofluid 72
2.3.3. Residence time distribution tests 73

2.4. Ferrohydrodynamic model 74
2.4.1. Scalar transport 75
2.4.2. Boundary and initial conditions 76
2.4.3. Numerical solution 77
2.5. Results and discussion 77
2.5.1. Magnetic properties of MNP and ferrofluid 77
2.5.2. Tracer dispersion in ferrofluid Poiseuille flow - RMF disabled 78
2.5.3. Tracer dispersion in ferrofluid Poiseuille flow - RMF enabled 82
2.5.4. Magnetization and magnetic body couple density 84
2.5.5. Linear and angular velocities in ferrofluid Poiseuille flow - RMF enabled 87
2.5.6. Simulated versus experimental RTDs - RMF enabled 89
2.6. Conclusion 91
2.7. Nomenclature 92
2.8. References 94
Chapter 3: Enhancing liquid micromixing using low-frequency rotating nanoparticles 96
Résumé 97
3.1. Abstract 98
3.2. Introduction 99
3.3. Experimental 101
3.3.1. Nanofluid preparation 101
3.3.2. Magnet device 101
3.3.3. Mixing device 102
3.3.4. Model reaction systems 103
3.3.4.1. Acid-base neutralization for probing mixing index 103
3.3.4.2. Villermaux-Dushman reaction for probing micromixing 105
3.4. Results and Discussion 106
3.4.1. Acid-base neutralization for probing mixing index without magnetic field 106
3.4.2. Acid-base neutralization for probing mixing index with magnetic field enabled 107
3.4.2.1. Observations under SMF 107
3.4.2.2. Observations under OMF 109
3.4.2.3. Observations under RMF 109

3.4.3. Villermaux-Dushman reaction for probing micromixing with magnetic field enabled 112
3.4.3.1. IEM model for interpretation of micromixing phenomena 112
3.4.3.2. Low-Re micromixing 114
3.4.3.3. Moderate-Re micromixing 116
3.5. Conclusion 117
3.6. Nomenclature 118
3.7. References 118
Chapter 4: Tuning Mass Transport in Magnetic Nanoparticle-filled Viscoelastic Hydrogels using Low-Frequency Rotating Magnetic Fields 120
Résumé 121
4.1. Abstract 122
4.2. Introduction 123
4.3. Materials and Methods 125
4.4. Results and Discussion 127
4.4.1. Characteristics of Cobalt-Ferrite Nanoparticles 127
4.4.2. Characteristics of Hydro/Ferrogels 128
4.4.3. Intrinsic Diffusional Mass Transport in Hydro/Ferrogels 136
4.4.4. Mass Transport in Hydro/Ferrogels under RMF 137
4.5. Conclusion 140
4.6. Nomenclature 141
4.7. References 142
Conclusion and suggestions for future works 144
Appendix.1 148
Appendix.2 149
Appendix.3 153
Appendix.4 155

List of Figures

Fig 1 Schematics of the flow of ferrofluid and water in (A) ferrofluid-core and (B) ferrofluid-cladding configurations (reproduced with permission from ref. 14).....8
Fig 2 Simulated velocity profiles (A) with no magnetic field, and with applied uniform magnetic field in (B) ferrofluid-cladding and (C) ferrofluid-core configurations (Reproduced with permission from ref. 14). 9
Fig 3 (A) Microfluidic chip with electromagnet (B) simulated magnetic field lines with corresponding peak strength of H = 60 Oe. The three rectangles in (B) represent observation windows for mixing quality evaluation based on grayscale analysis (reproduced with permission from ref. 15). 10
Fig 4 Experimental observation and numerical prediction of finger-shaped instabilities development in the observation windows at t = (A) 0 s (B) 0.5 s (C) 2 s for magnetic field peak strength H = 60 Oe (Reproduced with permission from ref. 15). 10
Fig 5 Impact of AC-field magnetoviscosity phenomena with respect to the relative order of Brownian, hydrodynamic and AC time scales: a)$\tau AC > \tau h > \tau B$, $\Delta\eta > 0$; b) $\tau h > \tau AC > \tau B$, $\Delta\eta > 0$; c) $\tau B > \tau h > \tau AC$, $\Delta\eta < 0$.....13
Fig 6 Schematic representation of confined space for numerical analysis of RTD (reproduced with permission from ref. 23).....14
Fig 7 Optical images of magnetic suspension of 16 nm magnetite nanoparticles submitted to a uniform RMF of 31.4 kA/m with a frequency of (a) 10 Hz (b) 50 Hz (c) 100 Hz (d) 200Hz. Suspension consists of 0.005 volume fraction of MNPs (reproduced with permission from ref. 29). 16
Fig 8 Schematic of 2-pole 3-phase magnetic field generator top view and the inserted capillary cell (reproduced with permission from ref. 19). 18
Fig 9 Effect of Reynolds number and RMF frequency on axial dispersion coefficient shown as a dimensionless number. Experiments performed with φ = 0.001, H = 31.4 kA/m (reproduced with permission from ref. 24).....19
Fig 10 Ratio of axial dispersion coefficient under the effect of magnetic field (D_{eff}) to reference axial dispersion coefficient at H = 0 and φ = 0 (D) as a function of RMF and OMF frequency (reproduced with permission from ref. 31). 20
Fig 11 Relative axial dispersion evolution under RMF and SMF versus magnetic field strength. Magnetic volume fraction in RMF and SMF are 0.001 and 0.005, respectively (reproduced with permission from ref. 31).....20
Fig 1.1 T-mixer/capillary (a) and capillary (b) magnet assemblies for quantification of transverse and axial scalar transport in rotating magnetic fields. Schematic of RMF generator, three-pair two-pole stator coils, and capillary centrally-aligner with cylindrical magnet bore in both assemblies for a perpendicular rotating magnetic field.....34
Fig 1.2 Ambient-temperature (a) equilibrium magnetization curve of powdery cobalt ferrite nanoparticles (a) and scaled equilibrium magnetization curve of cobalt-ferrite ferrofluid (φ = [0.001 – 0.004] and M_d = 295 kA/m). 43
Fig 1.3 Evolution of transient magnetic-field-free response of scaled mixing index after flow interruption measured 3 cm downstream of the T junction (φ = 0.001). Solid line shows fit from a first-order dynamic model, $1 - e - tDR2\theta$, with dimensionless time constant θ = 0.43. 45
Fig 1.4 Evolution of transient response of scaled mixing index after flow interruption and RMF activation measured 3 cm downstream of the T junction: f = 50 Hz/ φ = 0.001 (a); f = 200 Hz/ φ = 0.001 (b); f = 100 Hz/ φ = 0.002 (c); f = 100 Hz/ φ = 0.004 (d). Solid lines show fit from a first-order dynamic model, $1 - e - tDR2\theta$, with dimensionless time constants θ = 0.095 (a); θ = 0.015 (b) θ = 0.034 (c) θ = 0.010 (d).....46

Fig 1.5 Sensitivity to spin viscosity of ferrofluid radial profiles of (a) scaled linear azimuthal velocity, (b) azimuthal Péclet number, (c) MNP axial angular velocity, (d) asymmetric-stress z-projection, (e) ratio of ferrofluid z-component vorticity to MNP axial angular velocity in the presence of RMF (f = 200 Hz, φ = 0.002). 49
Fig 1.6 Radial distribution of magnetic body force (a) and ratio of magnetic body force to total force from symmetric and asymmetric stresses (b) in presence of RMF (f = 200 Hz, φ = 0.002).52
Fig 1.7 Radial distributions of lag angle between magnetic field and magnetization vectors (a) and scaled magnetic body couple (b) in presence of RMF (f = 200 Hz, φ = 0.002). 53
Fig 1.8 Variation of azimuthal velocity maxima in presence of RMF (a) as a function of RMF frequency (φ = 0.002) and (b) MNPs volume fraction (f = 200 Hz). 54
Fig 1.9 Radial distribution of scaled axial internal angular velocity in presence of RMF (f = 200 Hz) for different MNP volume fractions. 55
Fig 1.10 Sensitivity to channel size and spin viscosity of ferrofluid radial profiles of (a,c) MNP axial angular velocity, (b,d) azimuthal Péclet number in the presence of RMF (f = 200 Hz, φ = 0.002). 56
Fig 1.11 Experimental and simulated transient response of scaled mixing index with and without RMF excitation (f = 200 Hz, φ = 0.004). 58
Fig 1.12 Experimental and calculated transient response of passive tracer concertation in (a) absence of RMF and (b) presence of RMF (f = 200 Hz, φ = 0.004). 59
Fig 1.13 Transverse component effective diffusivity tensor as function of RMF frequency and MNP volume fraction. 60
Fig 1.14 Measured transient response of scaled mixing index after flow interruption and RMF activation: f = 50 Hz/ φ = 0.001 (a); f = 200 Hz/ φ = 0.001 (b); f = 100 Hz/ φ = 0.002 (c); f = 100 Hz/ φ = 0.004 (d). Solid lines show model predictions with fitted values of effective diffusivities. 61
Fig 2.1 Capillary tube/magnet assembly for quantification of RTD in rotating magnetic fields: Schematics of RMF generator, three-pair two-pole stator coils, and capillary centrally-aligned with cylindrical magnet. 72
Fig 2.2 Ambient-temperature (a) equilibrium magnetization curve of powdery cobalt ferrite nanoparticles (a) and dimensionless equilibrium magnetization curve of cobalt-ferrite ferrofluid (φ = [0.001 – 0.004] and M_d = 295 kA/m). 78
Fig 2.3 Effect of spin viscosity on (a) the radial profile of MNP angular velocity component normalized by ½ azimuthal vorticity component of the ferrofluid (φ = 0.004) and (b) on the ferrofluid rotational viscosity as a function of MNP volume fraction for a ferrofluid Poiseuille flow ($Re = 1$, RMF disabled). 79
Fig 2.4 (a) Transient tracer concentration signals measured at two downstream points along capillary and (b) corresponding experimental (solid line) and simulated (dashed line) RTD for magnetic-field-free ferrofluid Poiseuille flow ($\varphi = 0.004$, $Re = 1$). Light blue shade shows 95% confidence level for repeat tests. 81
Fig 2.5 Influence of rotating magnetic field frequency on the transient tracer concentration signals measured at two downstream points along capillary for a ferrofluid Poiseuille flow ($H_0 = 10^3$ kA/m, φ = 0.004, Re = 1). 82
Fig 2.6 Transverse effective diffusivity as function of RMF frequency and MNP volume fraction for water-based cobalt ferrite ferrofluid (range $H_0 = 10^3$ kA/m, φ = [0.001-0.004], f = [0-200] Hz). 84
Fig 2.7 Transient response of angle between magnetization and magnetic field intensity vectors ($H_0 = 10^3$ kA/m, φ = 0.004, Re = 1). 85
Fig 2.8 Plots of dimensionless magnetization spatial distribution in capillary cross-section and angular distribution of dimensionless magnetization and dimensionless magnetic body couple components in (a,b) radial, (c,d) azimuthal, and (e,f) axial directions (Simulation results at $H_0 = 10^3$ kA/m, f = 200 Hz, φ = 0.004, Re = 1). 85

Fig 2.9 Schematic representation of relative orientation of magnetization, magnetic field, vorticity and magnetic body couple vector components when radial component of magnetization is (a) normal or (b) parallel to ferrofluid vorticity.....87
Fig 2.10 Dimensionless internal angular velocities and dimensionless linear velocities in (a,c) azimuthal and (b,d) axial directions (Simulation results at $H_0 = 10^3$ kA/m, f = 200 Hz, $\varphi = 0.004$, Re = 1).....88
Fig 2.11 Experimental and numerical RTDs obtained for ferrofluid Poiseuille flow (Re = 1) in presence of external RMF ($H_0 = 10^3$ kA/m): (a) f = 50 Hz/ $\varphi = 0.001$; (b) f = 200 Hz/ $\varphi = 0.001$; (c) f = 50 Hz/ $\varphi = 0.004$; (d) f = 200 Hz/ $\varphi = 0.004$. 90
Fig 3.1 Schematic representation of magnet, mixing device and conductivity electrodes. The magnet can generate a) SMF when energized by DC power supply, b) OMF when energized by AC power source and c) RMF when energized by a three-phase power supply. d) Possible configurations of mixing device relative to three types of magnetic fields. Conductivity electrodes are in contact with the fluid passing through a bed of glass beads while anions and cation periodically migrate between electrodes excited with AC current.....102
Fig 3.2 Mixing index as a function of Re number and magnetic field disabled. Experiments carried out with MNP mass fraction $\varphi = 0.05$. Vertical bars show repeat-test standard-deviations.....107
Fig 3.3 a) Mixing index as a function of φ in SMF (H = 49.3 kA/m), OMF (H = 53 kA/m) and RMF (H = 31.4 kA/m, f = 25 Hz): α with OFF magnetic field is shown as dashed line. b) Mixing index as a function of H in SMF, OMF and 25 Hz RMF ($\varphi = 0.05$). Vertical bars show repeat-test standard-deviations. 108
Fig 3.4 Mixing index as a function of frequency at H = 31.4 kA/m and $\varphi = 0.05$: with OFF magnetic field is shown as dashed line. Vertical bars show repeat-test standard-deviations. 110
Fig 3.5 Mixing index without magnetic field (reference condition) compared with that of RMF (31.4 kA/m, 50 Hz), SMF (30.5 kA/m) and OMF (31.4 kA/m). Vertical bars show repeat-test standard-deviations. 110
Fig 3.6 Inferred micromixing as a function of UV absorbance for the tested utilized concentration sets 1 to 4 (identified, respectively, with blue, red, green and yellow markers). 114
Fig 3.7 Illustration of t_m as a function of SMF, OMF and RMF intensities. While in the absence of magnetic field, large micromixing times are obtained, application of SMF, OMF or RMF leads to a reduction of t_m by approximately 3 orders of magnitude. The corresponding colors (see figure 6) represent the concentration sets of Table 3.1. 115
Fig 3.8 Illustration of t_m as a function of RMF frequency ($\varphi = 0.05$ and H = 31.2 kA/m) and MNP mass fraction (H = 31.2 kA/m and f = 25 Hz). Micromixing time in absence of magnetic field is shown as dashed line. The corresponding colors (see figure 6) represent the concentration sets of Table 3.1.....116
Fig 4.1 Schematic illustration of the magnet device used for the generation of RMF: the alternative currents fed to each pair of coils have shifted phases so that the magnetic field inside the bore rotates in synchrony with the currents frequency.....126
Fig 4.2 XRD pattern of cobalt-ferrite MNPs (a). Magnetization of powdery (dry) MNPs measured at ambient temperature (b). Hydrodynamic size distribution of MNPs measured by dynamic light scattering method (c). Zeta potential of MNPs in colloidal state as a function of pH at φ = 0.05 (d). 128
Fig 4.3 Magnetization of G2 (top) and G6 (bottom) ferrogels measured at ambient temperature. All the M-H curves show hysteresis loops identified by the remanent magnetization and coercivity noticeable at every mass fraction of MNPs. The M_r values calculated for the ferrogels, as demonstrated in figure 4, are less than 0.73 ruling out plausibility of MNPs relaxation. 129
Fig 4.4 Reduced remanent magnetization of G2 and G6 ferrogels: M_r of powdery MNPs is shown as a dashed line.....129
Fig 4.5 Mass fraction of blocked MNPs in ferrogels calculated from Eq.5.....131

Fig 4.6 Storage modulus of hydrogels measured at constant strain amplitude (a) and corresponding ξ calculated from Eq.6 using G´ values measured at 1 Hz (b). 132
Fig 4.7 Storage modulus enhancement factors of G2 and G6 samples: mass fractions of MNPs in ferrogels are converted to volume-based fractions to compare experimental results with theoretical values shown as dashed line. 133
Fig 4.8 Swelling ratios of hydrogels and ferrogels as a function of φ values. 135
Fig 4.9 Estimated effective diffusion coefficients of rhodamine B in hydrogel and ferrogel samples. 136
Fig 4.10 Effective diffusion coefficient enhancement factors in presence of 31.4 kA/m RMF with 10 Hz rotation frequency (a). Scaled mass of mechanically free MNPs (b). 137
Fig 4.11 Enhancement factors of effective diffusion coefficient in G2 (a), G3 (b) and G4 (c) ferrogels as a function of RMF frequency: RMF intensity = 31.4 kA/m in all experiments. 139

List of Tables

Table 3.1 Concentration sets for micromixing studies by Villermaux-Dushman reaction.....113

To my wife and my son

“Acquire new knowledge whilst thinking over the old, and you may become a teacher of others”

Confucius

“I think it's much more interesting to live not knowing than to have answers which might be wrong”

Richard Feynman

Acknowledgements

I would like to express my sincere thanks and appreciation to all those who have made this thesis possible. My deepest gratitude goes first and foremost to my supervisor, Professor Faïçal Larachi, for being a true mentor during my studies.

I acknowledge all the people at Laval University, especially Jerome Nöel for his outstanding help in the fabrication and modification of different experimental setups. I also gratefully acknowledge Rodica Neagu Plesu for her help in conducting light scattering experiments.

My sincere gratefulness to all my friends in the group, Ali Entezari-Zarandi, Dariush Azizi, Amir Motamed and Olivier Gravel.

I would like to acknowledge the support of my parents, Fatemeh and Hasan and siblings, Elham and Shahram, for their support during the time of my study.

Finally, I would like to express my gratitude and love to my wife, Banin, a real soulmate, for understanding the bleak journey I was in.

Foreword

This thesis is composed of introduction, 4 chapters and conclusion in the form of integrated peer-reviewed articles. The objectives and general methodology are presented in the Introduction. The introduction includes the key references closely relevant to the subject studied in the thesis. The introduction is reproduced in this thesis with slight modifications from a book chapter published by Royal Society of Chemistry. Chapters 1 to 4 present the scientific findings and relevant discussions, conclusions and references. Chapters 1 and 2 are recently submitted for publication in peer-reviewed journals. Chapters 3 and 4 are published in peer-reviewed journals.

Introduction: Prospects of Magnetic Nanoparticles for Magnetic Field-Assisted Mixing of Fluids with Relevance to Chemical Engineering
Authors: Shahab Boroun[a], Faïçal Larachi[a*]
[a]Department of Chemical Engineering, Université Laval, 1065 Avenue de la Médecine, Québec, Québec G1V 0A6, Canada.
Book: Alternative Energy Sources for Green Chemistry 2016, Royal Society of Chemistry.
DOI: 10.1039/9781782623632
The chapter has been written by Shahab Boroun. The scientific revision was done by Prof. Faïçal Larachi.

Chapter 1: Anomalous anisotropic transport of scalars in dilute ferrofluids under uniform rotating magnetic fields – Mixing time measurements and ferrohydrodynamic simulations
Authors: Shahab Boroun[a], Faïçal Larachi[a*]
[a]Department of Chemical Engineering, Université Laval, 1065 Avenue de la Médecine, Québec, Québec G1V 0A6, Canada.
Submitted: Chemical Engineering Journal, Elsevier.
The experiments and simulations in addition to manuscript writing have been accomplished by Shahab Boroun. The scientific revision was done by Prof. Faïçal Larachi.

Chapter 2: Residence time distribution of passive scalars in magnetic nanofluid Poiseuille flow under rotating magnetic fields
Authors: Shahab Boroun[a], Faïçal Larachi[a*]
[a]Department of Chemical Engineering, Université Laval, 1065 Avenue de la Médecine, Québec, Québec G1V 0A6, Canada.
Submitted: AIChE Journal, John Wiley & Sons.
The experiments and simulations in addition to manuscript writing have been accomplished by Shahab Boroun. The scientific revision was done by Prof. Faïçal Larachi.

Chapter 3: Enhancing liquid micromixing using low-frequency rotating nanoparticles
Authors: Shahab Boroun[a], Faïçal Larachi[a*]
[a]Department of Chemical Engineering, Université Laval, 1065 Avenue de la Médecine, Québec, Québec G1V 0A6, Canada.
Journal: AIChE Journal, 2016, 63, 337-346, John Wiley & Sons.
DOI: 10.1002/aic.15456
The experiments and simulations in addition to manuscript writing have been accomplished by Shahab Boroun. The scientific revision was done by Prof. Faïçal Larachi.

Chapter 4: Tuning Mass Transport in Magnetic Nanoparticle-filled Viscoelastic Hydrogels using Low-Frequency Rotating Magnetic Fields
Authors: Shahab Boroun[a], Faïçal Larachi[a*]
[a]Department of Chemical Engineering, Université Laval, 1065 Avenue de la Médecine, Québec, Québec G1V 0A6, Canada.
Journal: Soft Matter, 2017, 13, 6259-6269, Royal Society of Chemistry.
DOI: 10.1039/C7SM01228D
The experiments and manuscript writing have been accomplished by Shahab Boroun.
The scientific revision was done by Prof. Faïçal Larachi.

Another review article is published on the subject of transport phenomenon in magnetic materials. Details of this publication are as follow:

Appendix.4: Role of magnetic nanoparticles in mixing, transport phenomena and reaction engineering — challenges and opportunities
Authors: Shahab Boroun[a], Faïçal Larachi[a*]
[a]Department of Chemical Engineering, Université Laval, 1065 Avenue de la Médecine, Québec, Québec G1V 0A6, Canada.
Journal: Current opinion in chemical engineering, 2016, 13, 91-99, Elsevier.
DOI: 10.1016/j.coche.2016.08.011
The manuscript has been written by Shahab Boroun. The scientific revision was done by Prof. Faïçal Larachi.

Some of the research findings were also presented in the following conferences:

S. Boroun, F. Larachi, **"Micromixing Studies in Low-Frequency Rotating Magnetic Field Probed Via Villermaux-Dushman Reaction**, 24th International Symposium on Chemical Reaction Engineering, Minneapolis Minnesota, U.S.A., 2016.

S. Boroun, F. Larachi, **Smart magneto-responsive hydrogels triggered by low frequency rotating magnetic fields for controlled release applications,** 66th Canadian Chemical Engineering Conference, Quebec City, Canada, 2016.

S. Boroun, F. Larachi, **Mass Transport Intensification Driven by Magnetic Field Rotation of Nanoparticles – From Viscous to Viscoelastic Soft Matter**, 10th International Symposium on Catalysis in Multiphase Reactors, Qingdao, China, 2017.

F. Larachi, **S. Boroun**, O. Gravel, P. Hajiani, **Magnetic nanofluid excitation in magnetic fields - Chemical reaction engineering perspective**, Banf international research station for mathematical innovation and discovery, Oaxaca, Mexico, 2018.

Introduction

Prospects of magnetic nanoparticles for magnetic field-assisted mixing of fluids with relevance to chemical engineering

I. Mixing, magnetic nanoparticles and magnetism

Development of efficient unit operations in chemical processing has been always one of the main goals in process intensification (PI). An efficient operation encompasses several subcategories from safety, economy, environment and sustainability points of view. It results in diverse research fields and remarkable efforts to develop intensified technologies with beneficial consequences. Among the various aspects in the field of process intensification, maximizing the effectiveness of transport phenomena has tremendous impact on intermolecular interactions, and interfacial and bulk materials processing.[1] In every transport process, mixing has a crucial role in homogenization of a specific property such as temperature or concentration and its effectiveness determines the unit energy consumption and size. This significant designation has a deterministic influence in chemical reactions that mixing and reaction rates are in the same order of magnitude in terms of characteristic time constants. In this case, mixing effectiveness affects product distribution as well.[2]

In recent years, various external energy fields such as centrifugal, electric and ultrasonic were the subject of multiple studies to offer an alternative energy source for PI purposes. In this chapter, magnetic field is introduced as a potential energy source to enhance homogenization in fluid phases. Basically, magnetic field energy transfer to a medium requires an interaction with a magnetic material. The nonmagnetic nature of conventional fluids makes the magnetic assisted mixing supposedly impractical. Nevertheless, magnetic suspensions obtained from dispersing magnetic particles in organic or aqueous liquid media make the general idea feasible. In addition, the considerable and also tunable magnetization of magnetic suspensions and also well-established theories in description of magnetic hydrodynamics enables modelling and design of magnetic assisted mixing systems. In particular, the benign nature of most magnetic particles to biological samples beside their multi-functionality and targetability, make them attractive tools for lab-on-chip or micro-total-analysis systems[3]. However, utilization of magnetic manipulation is not limited to this classification and can be spanned to the broad concept of micromixing in chemical synthesis and processing with its advantageous features in PI.[4]

In this chapter, the main properties of magnetic nanoparticles (MNP) are introduced and subsequently the properties of their colloidal dispersions are discussed. After a brief presentation of the governing

equations of motion of polar fluids, how magnetic fluids can be actuated, driven and exploited in a mixing application is presented. Finally, the latest theoretical and experimental findings regarding the application of magnetic fields in the actuation of magnetic fluids for mixing purposes are thoroughly presented.

II. Mixing based on ferrohydrodynamics (FHD)

Application of magnetic nanoparticles in mixing processes has been studied for more than a decade; however, the physical and mathematical principles of magnetic assisted mixing phenomena have a substantial precedent in the context of FHD and magnetism. Accordingly, introducing an overview in both of these topics can be instructive prior to the presentation of any practical application. Understanding the basic physical properties of magnetic nanoparticles (MNPs) is essential because they bestow the hosting fluid medium with a polar nature that is the main consideration in the derivation of the governing equations of motion for such nanofluids. The medium of interest in this current subject of mixing is basically in fluid phase, hence the properties MNPs when dispersed in a liquid carrier should also be studied form both magnetic and hydrodynamics aspects. It should be noted that such colloidal dispersions of MNPs are also known as ferrofluids. While Brownian agitation prevents nanoparticle sedimentation and, to some extent, magnetic dipole-dipole induced agglomeration, it is insufficient to undo agglomeration by the short-range van der Waals attraction, thus requiring surfactant agents and/or the nanoparticles to be electrically charged to achieve stability of the colloidal system by providing sufficient steric or electrostatic repulsion forces on each particle surface in the carrier aqueous or organic liquid.[5]

Magnetization of magnetic nanoparticles is a size-dependent property. In the length scales ranging from several to tens of nanometers, MNPs are single domains and before approaching a critical diameter they exhibit superparamagnetism[5]. This category of particles shows considerable saturation magnetization in magnetic fields while their magnetization drastically declines when magnetic field drops to zero and consequently results in zero coercivity. Hence, superparamagnetic nanoparticles (SMNPs) are known as soft magnets since they intrinsically have no permanent magnetism.

Aligned magnetic moments of SMNPs in the absence of magnetic fields are randomized due to thermal fluctuations. Accordingly, an important parameter for characterization of soft magnets is defined as Neelian relaxation characteristic time, which determines the time scales of randomization of magnetic moments inside the crystalline structure as a result of thermal agitation. This time scale is described by an expression in the form of Eq.1.

$$\tau_n = \tau e^{\frac{KV_p}{k_B T}} \quad (1)$$

Where k_B is Boltzmann's constant, V_p is the magnetic particle core volume, K is an anisotropy constant, τ is the reciprocal of the Larmor frequency of the magnetization vector in the anisotropic nanoparticle field, and T is the temperature. As the size of nanoparticles increases, the magnetic energy barrier (KV_p) of domains become stronger and Neelian relaxation time increases exponentially. In this state, MNPs turn into hard magnets showing coercivity in their magnetization curve.[6] As the particle size further increases, the single domain of magnetic moments splits into subdomains. This energetically favoured transition from single domain to multi-domain structure occurs at a critical diameter which is unique for each magnetic material. As an example, magnetite critical transition diameter is estimated to be 128 nm[5]. Multi-domain magnets still show coercivity in their magnetization curves but it decreases drastically when the size of the nanoparticles increase.

Although hard magnets have quite large and negligible Neelian relaxation times, their corresponding ferrofluids can exhibit another form of relaxation mechanism known as Brownian relaxation. This mechanism stems from the fact that the dispersed particles are uninterruptedly exposed to the Brownian movement of molecules in the carrier fluid and the resultant of which is the perturbation of the magnetic moments *via* bodily movements of the nanoparticle. This relaxation time is given by Eq 1.2.[7]

$$\tau_b = \frac{3V_H \eta}{k_B T} \quad (2)$$

Where V_H denotes the hydrodynamic volume of the particle including the surfactant layer and η is the dynamic viscosity of the liquid. It is important to note that as particle size increases τ_n increases exponentially while τ_b grows linearly. Thus, for larger particles, Neelian relaxation can be neglected when compared to Brownian relaxation.[8]

II.I. FHD transport equations

Description of the governing equations of motion for an incompressible and polar fluid makes the inference of possible mixing mechanisms theoretically possible. Derivation of FHD transport equation as accomplished by Shliomis[9] requires analysis of both linear and angular momentum transport phenomena. We can here provide a brief description of the physical basics of the mathematical derivation. In the absence of magnetic field, each nanoparticle follows the fluid velocity field ($\underline{\mathbf{V}}$) and can spin if the velocity field has a nonzero vorticity $\left(\underline{\boldsymbol{\nabla}} \times \underline{\mathbf{V}} \neq 0\right)$. In the presence of magnetic field, the exerted magnetic torque can impede or augment the intrinsic spin of

nanoparticles.[10] The particles as a result of external torque gain an internal angular momentum which is in continuous exchange with linear momentum of ferrofluid. Assuming magnetic colloids as a polar continuum, each fluid sub-continuum element is in both angular and linear momentum exchange with its surrounding and classical linear momentum transport is no longer valid in such systems. The asymmetric nature of the stress tensor in the equation of motion modifies the linear momentum transport formulation in the form given by Eq.3.

$$\rho \frac{\boldsymbol{D}\underline{\mathbf{V}}}{\boldsymbol{D}t} = -\underline{\boldsymbol{\nabla}}p + \rho\underline{\mathbf{F}} + 2\zeta\underline{\boldsymbol{\nabla}} \times \underline{\boldsymbol{\omega}} + (\zeta + \eta)\underline{\boldsymbol{\nabla}}^2\underline{\mathbf{V}} \tag{3}$$

Where ρ is the fluid density, $\boldsymbol{\omega}$ is the spin density vector, p is the hydrodynamic pressure, ζ is the vortex viscosity and $\underline{\mathbf{F}}$ is sum of gravitational and magnetic body forces.

For the angular momentum transport, one has:

$$\rho I \frac{\boldsymbol{D}\underline{\boldsymbol{\omega}}}{\boldsymbol{D}t} = \rho\underline{\mathbf{G}} + \underline{\mathbf{A}} + (\lambda' + \eta')\underline{\boldsymbol{\nabla}}\,\underline{\underline{\boldsymbol{\nabla}}}.\underline{\boldsymbol{\omega}} + \eta'\underline{\boldsymbol{\nabla}}^2\underline{\boldsymbol{\omega}} \tag{4}$$

Where λ' is the bulk spin viscosity, η' is the shear spin viscosity and ρ$\underline{\mathbf{G}}$ is the magnetic angular momentum received from the external magnetic field ($\mu_0\underline{\mathbf{M}} \times \underline{\mathbf{H}}$) to the magnetic body and its value is reduced or augmented by $\underline{\mathbf{A}}$. Physically, $\underline{\mathbf{A}}$ is an outcome of the asynchrony between rotation of fluid sub-continuum originated from inherent vorticity and magnetic driven spin. Thus, this parameter should be a function of their difference correlated with a coefficient referred to vortex viscosity:

$$\underline{\mathbf{A}} = 2\zeta\left(\underline{\boldsymbol{\nabla}} \times \underline{\mathbf{V}} - 2\underline{\boldsymbol{\omega}}\right) \tag{5}$$

For a magnetic material, the magnetic body force density ($\mathbf{F_m}$), also known as Kelvin force, is cast as follows:[7]

$$\underline{\mathbf{F_m}} = \mu_0(\underline{\mathbf{M}}.\underline{\boldsymbol{\nabla}})\underline{\mathbf{H}} \tag{6}$$

Where μ_0 is the vacuum permeability, $\underline{\mathbf{M}}$ is the magnetization vector and $\underline{\mathbf{H}}$ is the magnetic field vector. Kelvin force manifests itself when there is a spatial heterogeneity in the applied magnetic field or magnetic susceptibility of the colloidal suspension.

The magnetization vector in Eq.3 and 4 is not necessarily aligned with the applied magnetic field lines and may be shifted and perturbed from the saturation magnetization ($\underline{\mathbf{M}}^{\mathbf{e}}$) in a fluid experiencing a magnetic field. By introducing a mathematical description of each phenomenon playing role in magnetization, a phenomenological equation for magnetization can be derived in the following form:[9]

$$\frac{\mathbf{D}\underline{\mathbf{M}}}{\mathbf{D}t} = \underline{\boldsymbol{\omega}} \times \underline{\mathbf{M}} + \tau^{-1}\left(\underline{\mathbf{M}} - \underline{\mathbf{M}^{\mathbf{e}}}\right) \tag{7}$$

The first term in the right hand side of this equation represents the shift of the magnetization vector while rotating in an average angular velocity $\underline{\boldsymbol{\omega}}$ whereas the second term defines perturbation of the magnetization as a result of relaxation. MNPs exhibit dissimilar behaviors in response to various magnetic fields. Consequently, in the following sections the interplay between magnetic fields and MNPs, possible realizable mixing mechanisms and the practical approaches will be explained.

II.II. Mixing with static magnetic fields (SMF)

SMF are invariant in time and can be spatially uniform or non-uniform. While a moderate intensity magnetic field applied to a stagnant and homogeneous ferrofluid cannot trigger any directional manipulation and movement of naoparticles[8], a magnetic field applied to a sheared ferrofluid, may affect the linear momentum or the angular movement of suspended particles. Any individual particle in a velocity field such that $\underline{\boldsymbol{\nabla}} \times \underline{\mathbf{V}} \neq 0$, freely rotates with fluid vorticity as result of hydrodynamic torque. A normal to vorticity magnetic field impedes free rotation of particles whereas the stationary magnetic torque resists the hydrodynamic torque. This resistance to rotation induces an additional dissipation of fluid kinetic energy and is known as positive magnetoviscosity[11].

If the magnetic field direction is in the same direction of vorticity vector, the magnetization vector is superposed on the axis of rotation without any interference with the exerted hydrodynamic torque and accordingly particles have no angular momentum exchange with their carrier fluid. In this condition, a linear momentum transport balance with an additional term accounting for magnetic body force (Kelvin force) will suffice to describe fluid flow[12]. We will show how this situation can be exploited in a mixing application but primarily, to better unveil the potential of Kelvin force on mixing, a vector operation on Eq.6 can be instructive. By using the vector identity:

$$\left(\underline{\mathbf{H}}.\underline{\boldsymbol{\nabla}}\right)\underline{\mathbf{H}} = \frac{\mathbf{1}}{\mathbf{2}}\underline{\boldsymbol{\nabla}}(\underline{\mathbf{H}}.\underline{\mathbf{H}}) - \underline{\mathbf{H}} \times (\underline{\boldsymbol{\nabla}} \times \underline{\mathbf{H}}) \tag{8}$$

Assuming the magnetic susceptibility (χ_i) being equal to the ratio of magnetization vector to magnetic field, then the Kelvin force can be rewritten as:

$$\underline{\boldsymbol{F_m}} = \frac{\mathbf{1}}{\mathbf{2}}\mu_0\underline{\boldsymbol{\nabla}}(\chi_i\underline{\mathbf{H}}.\underline{\mathbf{H}}) - \underline{\mathbf{H}} \times (\underline{\boldsymbol{\nabla}} \times \underline{\mathbf{H}}) \tag{9}$$

By applying Ampere's law for magnetic fields ($\underline{\boldsymbol{\nabla}} \times \underline{\mathbf{H}} = \mathbf{0}$):

$$\underline{\boldsymbol{F_m}} = \frac{\mathbf{1}}{\mathbf{2}}\mu_0\left|\underline{\mathbf{H}}\right|^2\underline{\boldsymbol{\nabla}}(\chi_i) + \frac{\mathbf{1}}{\mathbf{2}}\mu_0\chi_i\underline{\boldsymbol{\nabla}}\left(\underline{\mathbf{H}}.\underline{\mathbf{H}}\right) \quad (10)$$

Eq.10 suggests two conceivable mechanisms for driving a magnetic fluid. The first mechanism is based on the spatial heterogeneity of magnetic field intensity as expressed in the second term of Eq.10 RHS. The second mechanism is based on the fact that magnetic susceptibility is a concentration dependent parameter. This means that even in a uniform magnetic field and gradient magnetic concentration, a driving force for the movement of MNPs also possibly exists.

Tsai et al.[13] presented the first application of SMF in mixing by placing a permanent magnet with moderate magnetization (2.2 kG) underneath the channel of a Y-mixer with the magnetic field perpendicular to the flow direction. Mixing performance characterized based on visualization in an observation window downstream of the channel, shows near complete mixing between magnetic and nonmagnetic fluids flowing alongside each other in Reynolds numbers about unity. Mixing between (nonmagnetic) water and a ferrofluid on the basis of pure diffusion shows no prominent evolution downstream of the channel; however, the indistinct and blurred interface confirms that MNPs have protruded into the contiguous stream when the magnet is placed under the channel.

Characterization of mixedness based on visualization can reveal how MNPs are dispersed into a sample for specific applications when MNPs are the targeted materials and their uniform dispersion in another sample is crucial. However, one may expect a thorough homogenization between fluids wherein MNPs act exclusively as mixers. The unique property of ferrofluids makes the latter objective possible. Every magnetic particle dispersed in a carrier liquid is in intermolecular interactions with chemisorbed surfactant and solvent molecules. Particles moving in a specific direction will drag the accompanying solvent molecules inducing bulk movement of the whole nanofluid, a phenomenon analogous to electroosmotic flow. Zhu et al.[14] experimentally verified such behavior in a microfluidic device designed for water/ferrofluid mixing studies and confirmed simultaneous homogenization of both MNPs and solvents. The geometry of the studied system is a circular chamber, 1 mm in diameter with three inlets. With such configuration of inlet channels, two flow patterns can be established. In one pattern, ferrofluid is the core stream and in the other one is the cladding one. A uniform magnetic field with adjustable intensities up to 10 mT is applied perpendicular to main flow direction as depicted in Figure 1.

Prior to experimental investigations, the mixing efficiency between ferrofluid and water was predicted by solving the coupled linear momentum transport and advection-diffusion equation of concentration in the conditions that Reynolds number is close to 1. By assuming a linear relationship

between magnetic susceptibility and MNP concentration, velocity of the suspension and concentration distribution of MNPs can be calculated. Despite the magnetic field direction is apparently normal to fluid vorticity the effect of angular momentum exchange on velocity profiles is neglected in the adopted formulation. Nonetheless, the simulation results depicted in Figure 2 show that in the absence of magnetic force all the velocity vectors include axially directed components while magnetic actuation can produce vertical components as well. This deviation from parabolic profile is even more severe in the cladding pattern in which the flow field in some regions exhibits remarkably irregular and vortical patterns. Thus, it is expected that the magnetic force perpendicular to flow direction can drag magnetic fluid toward nonmagnetic regions and reduces the diffusion path.

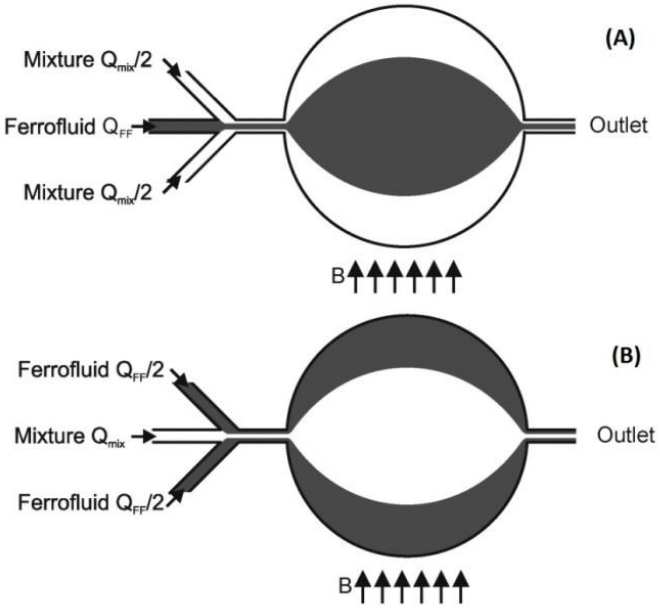

Fig 1 Schematics of the flow of ferrofluid and water in (A) ferrofluid-core and (B) ferrofluid-cladding configurations (reproduced with permission from ref. 14).

Calculated and measured mixing efficiencies in the ferrofluid cladding configuration are higher for specified flow rates. However, for both configurations a magnetic flux *ca*. 10 mT is required to reach to maximum mixing efficiency and also a minimum magnetic intensity is required to trigger magnetic force and evince its effect.

Since the simulated and experimental mixing efficiencies are based on concentration distribution of MNPs, an uncertainty in concentration uniformity of carriers in both flow patterns exist. To resolve this ambiguity, the authors devised an experiment in which a mixture of water and fluorescent dye flows on one side and ferrofluid flows next to it in the same fluidic cell. Analysis of fluorescent dye

intensity in the entire cell under the action of SMF reveals a relatively uniform pattern and validates homogeneous distribution of the carrier fluid as well as the magnetic nanoparticles in the entire volume of mixing chamber.

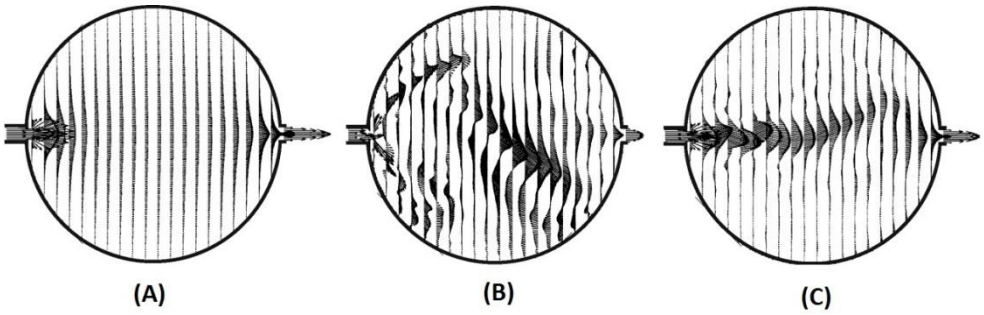

Fig 2 Simulated velocity profiles (A) with no magnetic field, and with applied uniform magnetic field in (B) ferrofluid-cladding and (C) ferrofluid-core configurations (Reproduced with permission from ref. 14).

Wen et al.[15] further scrutinized the mixing mechanism under SMF and demonstrated the effect of magnetic fields on stretching magnetic fluids and on the inception of instabilities in micro-devices. The observed and simulated transient concentration patterns provide a more vivid understanding of the dominant mechanism for the enhanced mixing. As depicted in Figure 3, the studied mixer consists of an electromagnet placed alongside the exit channel of a Y-mixer with a 1000×150 μm cross-section.

The fluids in contact are water and a ferrofluid consisting of 10 nm magnetite nanoparticles. The degree of mixing is quantified by grayscale analysis of three observation windows nearby up, mid and downstream of the channel. The adopted formulation to model the fluid motion is similar to Zhu et al.'s approach; however, in the magnetic body force term, the gradient of magnetic susceptibility is neglected without justification and instead, a magnetic force field as a result of gradient magnetic field is considered as a body force. Spatial non-uniformity in the magnetic field imposes some difficulties in the calculation of the magnetic force field. It requires numerically solving Maxwell–Ampere's law and Gauss's law for magnetic flux density provided that the coil geometry and current in the electromagnet are known.

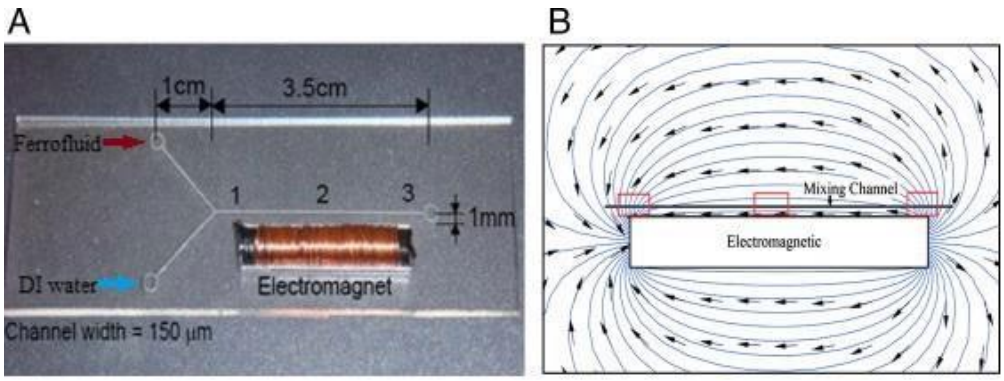

Fig 3 (A) Microfluidic chip with electromagnet (B) simulated magnetic field lines with corresponding peak strength of H = 60 Oe. The three rectangles in (B) represent observation windows for mixing quality evaluation based on grayscale analysis (reproduced with permission from ref. 15).

A mixing process without application of magnetic field would result in less than 20% homogeneity while a magnetic field having 90 Oe peak strength improves mixing up to near 95%. The simulated and observed concentrations profiles confirm development of instabilities in the shape of narrow finger structures in up and downstream channel regions as illustrated in Figure 4.

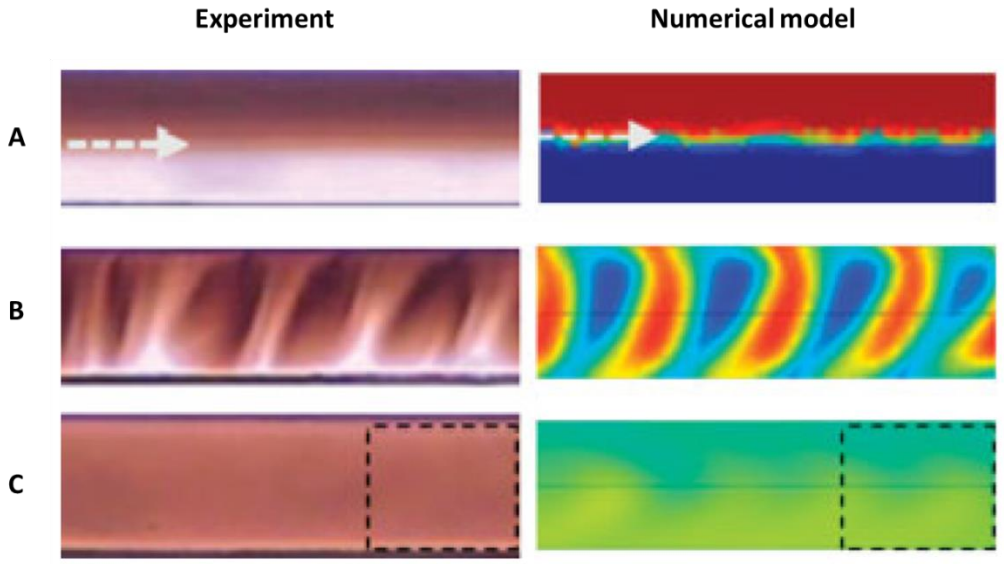

Fig 4 Experimental observation and numerical prediction of finger-shaped instabilities development in the observation windows at t = (A) 0 s (B) 0.5 s (C) 2 s for magnetic field peak strength H = 60 Oe (Reproduced with permission from ref. 15).

These structures reduce the diffusion path from the length scale of the device to the fingers. By virtue of a scaling analysis of diffusional transport, the role of instabilities in promoting mixing can be interpreted with order of magnitude estimations:[16]

$$t_m = \frac{l^2}{D_i} \tag{11}$$

where t_m, l and D_i are, respectively, the diffusion time, length and coefficient. The mixing time between two parallel streams in the length scale of 1 mm with an approximate diffusion coefficient in the order of 10^{-9} m^2/s can be estimated to amount to *ca*. 1 ks. The length of observation window in Figure 4 tests is 700 µm leading to finger lengths of the order of 100 µm corresponding to a time scale of diffusion *ca*. 10 s. In accordance to scaling analysis, the experimental time for a complete mixing is about three seconds. It is important to note that development of fingers cannot be generalized to all the processes in which a magnetic fluid penetrates into an aqueous nonmagnetic fluid on account of the ferrofluid viscosity which is typically multiple times that of water.

In addition, magnetic field orientation has a pronounced impact on the formation of instabilities. In fact, the finger structuring is favored in the regions where the magnetic field is oblique to flow direction. In contrast, the parallel magnetic field lines between two poles have a stabilizing effect and can transmogrify fingers into parallel strips. In the downstream region, fingers are formed once again and finally the concentration gradients fade away. Such stabilizing effect of parallel magnetic fields has been previously reported by Rosensweig.[17]

II.III. Mixing with oscillating magnetic fields (OMF)

Various parameters influence nanoparticle motion in an OMF and before any attempt to deduce a mixing mechanism, it is important to clarify nanoparticle and magnetic field interactions. The response of MNPs to OMF is acutely reliant on intensity and frequency of OMF, relaxation time constant of MNPs (τ_B) and hydrodynamic time constant ($\tau_h = 1/\left|\underline{\nabla} \times \underline{\mathbf{v}}\right|$).[10, 18] When the magnetic field oscillation time scale ($\tau_{AC} = 1/f_{AC}$) exceeds the nanoparticle Brownian characteristic time or the nanofluid hydrodynamic relaxation, the magnetic field will not single out a preferred direction for a collection of rotating nanoparticles. Matter-of-factly, as soon as the magnetic field intensity falls from the amplitude peak or rises from amplitude valley to zero, in those brief moments where the field reaches nearly zero value, the magnetization vector becomes very loosely locked to the magnetic field direction and can thus be disrupted through hydrodynamic shear or randomly through Brownian relaxation. Thus, when the magnetic intensity reaches its highest algebraic value over the next quarter

of oscillation, the magnetic moment vector of each nanoparticle aligns itself anew with that of the magnetic field. Such random orientation in each half-cycle will not allow the MNPs to rotate in single direction.[18] In such case ($\tau_{AC} > \tau_h$ or $\tau_{AC} > \tau_B$, see Figures 5 (a),(b)) the measured viscosity known in the literature as positive rotational viscosity ($\Delta\eta > 0$), is inflated.[8] On the other hand, when the period of oscillation is fast enough ($\tau_B > \tau_h > \tau_{AC}$), the competing phenomena are not able to significantly deviate magnetization vector and the nanoparticles are forced to rotate in synchrony with the magnetic field. In the brief moment of zero intensity, the hydrodynamic torque will flip the nanoparticles to rotate in the same direction as the fluid vorticity. Furthermore, owing to the exerted magnetic torque, the nanoparticle angular velocity is accelerated to align its magnetization vector parallel to the magnetic field direction. This sequence replicates itself over each half-period and leads to a nonzero macroscopic angular velocity of nanoparticles.[18] In this case, energy transfer from the AC magnetic field to the fluid flow *via* rotating MNPs occurs. This oriented energy transfer decreases apparent viscosity of ferrofluid and leads to a negative rotational viscosity ($\Delta\eta<0$, see Figure 5(c)).

Rotating microparticles and nanoparticles, as theoretically and experimentally evidenced[19-21], can resemble a magnetic stirrer and can have a profound impact on mixing. If one wishes to implement mixing with OMF with a mechanism tantamount to rotating microparticles, the operating parameters should be appropriately adjusted. Normally, Brownian relaxation time of MNPs in the size of 10 nm in aqueous media, in the order of 10^{-5} s, necessitates application of OMF typically with frequencies as high as 100 kHz. Hence, moderate frequencies are practically inoperative in mixing applications. However, an oscillating field with moderate frequency can also stir magnetic fluids to promote mixing on the basis of a similar Kelvin-force driven mixing mechanism as for SMF. Whether the Kelvin force is based on application of a spatially non-uniform magnetic field or magnetic susceptibility, the governing equations of motion are those described in section 1.2.1 but in case of an OMF, the magnetic field intensity is time dependent often sine-wave like.

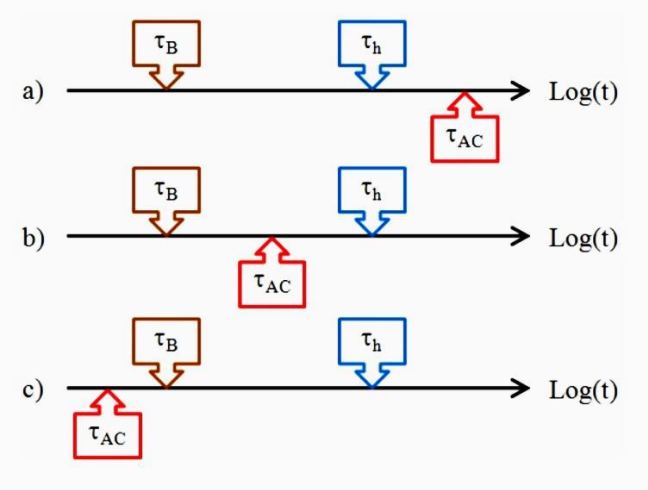

Fig 5 Impact of AC-field magnetoviscosity phenomena with respect to the relative order of Brownian, hydrodynamic and AC time scales: a)$\tau_{AC} > \tau_h > \tau_B$, $\Delta\eta > 0$; b) $\tau_h > \tau_{AC} > \tau_B$, $\Delta\eta > 0$; c) $\tau_B > \tau_h > \tau_{AC}$, $\Delta\eta < 0$.

Wen et al.[15, 22] investigated the mechanism for enhanced mixing between magnetic and nonmagnetic fluids in Y-mixers with similar characteristics as described earlier in section 1.2.2. The pathway of mixing in the observed and simulated transient evolution of concentration profiles is analogous to what has been investigated in the case of SMF. Finger shaped arrays similarly developed under the action of OMF in the regions where the oscillating field is oblique to flow direction while in the midstream the interface is stabilized and perturbed again when passing the second pole of the electromagnet. Wen et al. findings also show that a magnetic field normal to the water/ferrofluid interface can produce fingers if the magnetic field intensity passes a threshold and a critical magnetic intensity exists for the onset of instabilities on the interface. When the magnetic field intensity is less than a critical value, the narrow fingers evolve into broader shark-like fins whereby the mixing performance drops as a consequence.

Munir et al.[23] reported application of residence time distribution (RTD) analysis in theoretical characterization of ferrofluid flow in a rectangular channel under OMF. The RTD of magnetic fluid was numerically predicted while the fluid is flowing in a channel with two current carrying conductors on the top and bottom surfaces of conduit, see Figure 6.

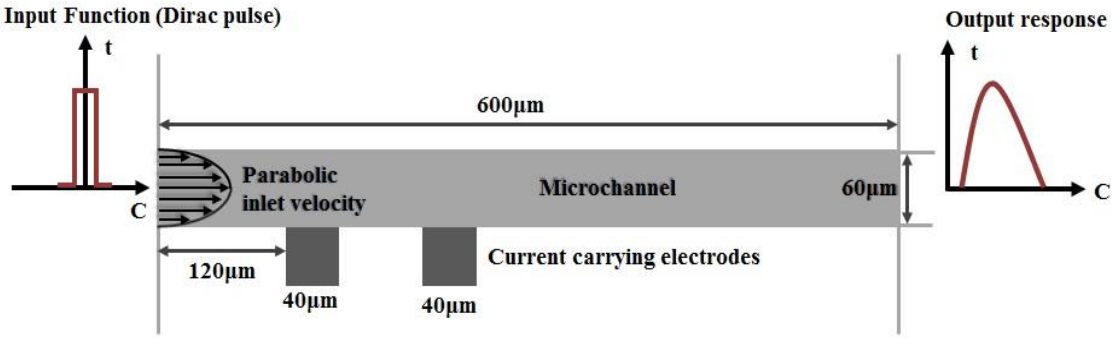

Fig 6 Schematic representation of confined space for numerical analysis of RTD (reproduced with permission from ref. 23).

Direction of current in each conductor is perpendicular to the flow direction and can be in the same or opposite direction with respect to each other. In such configuration, each conductor generates a non-uniform circular magnetic field with higher intensity near the conductor surface. Once a concentration pulse of MNPs suspension is fed into the channel, the average concentration of MNPs at a point downstream of the channel can be calculated by solving the coupled convection-diffusion and linear momentum transport equations. According to these author's simulations, the residence time distribution of the nanofluid in a magnetically-actuated system with various actuation scenario is narrower in shape, i.e., slimmer variance, in comparison to the conditions when axial dispersion is governed by diffusion and advection. The dependency of magnetic susceptibility to MNPs concentration triggers a Kelvin force and by manipulating the current direction in each conductor, periodic pulling and pushing forces on MNPs prompt secondary vertical velocity components. However, these simulations kept silent about the computed velocity profiles though in accordance with the narrower RTD signals, the magnetic field might possibly have altered the parabolic character of the velocity profile.[24]

Munir et al. approach to induce magnetic disturbances in a fluid flow undeniably requires MNPs concentration gradients. In absence of concentration gradients, thermal agitation is in permanent interference with magnetic energy to undertake nanoparticles motion and would oppose magnetic forces to harness the MNPs. Therefore, the effectiveness of a magnetic field should be quantitatively assessed in comparison to thermal perturbation of nanoparticles. To perform such analysis, a dimensionless number expressing the ratio of magnetic energy to Brownian kinetic energy can be used.[8] This ratio is prescribed by Eq.12.

$$R = \frac{\mu_0 M \pi d^3 H}{6 k_B T} \tag{12}$$

Where *d* is the diameter of MNPs. For a suspension of magnetite nanoparticles in the average size of 10 nm, the intensity of magnetic field should be larger than 100 kA/m to ensure $R \approx 1$. This analysis reveals that nanofluid flow characteristics such as RTDs cannot be manipulated magnetically using a moderate OMF. An effective mechanism of mixing even in homogeneous ferrofluids will be explained in the category of rotating magnetic fields in the section 1.2.4.

II.IV. Mixing with rotating magnetic fields (RMF)

Application of RMF in mixing with assistance of magnetic particles was first theoretically conceived by Calhoun[25]. A collection of magnetic particles can form various types of assemblies bound together by interacting magnetic dipoles. These assemblies rotate when they are subjected to RMF and can promote the mixing rate in two different regimes identified by the structure of chains. In the first regime, whenever stronger dipole interactions prevail between particles in comparison to the shear forces exerted on the assembly's body, a collection of particles leads to stable magnetic chain stirrers. In the second regime, on the contrary, the shear forces are able to overcome and weaken the dipole interactions undoing the chains which experience continual formation and break up. Demarcation between these two regimes is characterized by a dimensionless number proposed by Gao et al.[26] which accounts for the ratio of hydrodynamic torque to magnetic torque for a collection of *N* particles in a RMF rotating with frequency f:

$$R_T = \frac{16 \eta f N^3}{\mu_0 \chi_i^2 H^2 (N-1) \left(Ln\left(\frac{N}{2}\right) + 2.4N \right)} \tag{13}$$

It is experimentally shown and theoretically proven[25, 26] that rotation of particle assemblies is subject to reformation and breakup sequences for $R_T < 1$ whereby mixing times are lesser than for the conditions when $R_T > 1$. When used in typical mixing applications, this method requires mixing times in the order of several minutes. In addition, Wittbracht et al.[27] estimated effective diffusion coefficient with magnetic particle stirrers to be only 32% higher than pure diffusion.

It was argued earlier in section 1.2.1 that rotating MNPs can exchange their magnetic angular momentum (or internal angular momentum) with the surrounding fluid. In an oscillating magnetic field, the state of momentum transport is frequency dependent and also fluid vorticity is *sine qua non* a trigger for rotation. In a rotating magnetic field, in contrast, a magnetic torque is constantly exerted on the nanoparticles setting them into rotation even in the absence of fluid flow bulk advection.

Magnetically-excited angular momentum can drive the carrier fluid and produce an external angular momentum which manifests itself as a torque driven flow.[28] Besides, this macro scale effect of internal rotation of a magnetic fluid, another phenomenon pinpointed in smaller scales by Hajiani and Larachi[19] can prove to be an efficient mixing tool. The mechanism supporting this phenomenon is based on a conception that every nanoparticle will drag the surrounding fluid by means of viscous forces prompting vortex formation around each nanoparticle. Spinning of the nanoparticles causes entrainment of their neighboring fluid elements resulting in an effective reduction of the diffusion length scales. The discussion to follow provides experimental evidence in support of such postulated mechanism for the mixing ability of dispersed MNPs in a fluid carrier subject to RMF. It is first instructive to have a glimpse on the study of Gravel et al.[29] who used an optical method for the visualization of the MNP suspension stimulated by RMF. An example of microscopic images of a suspension consisting 16 nm MNPs at 0.005 volume fraction is shown in Figure 7.

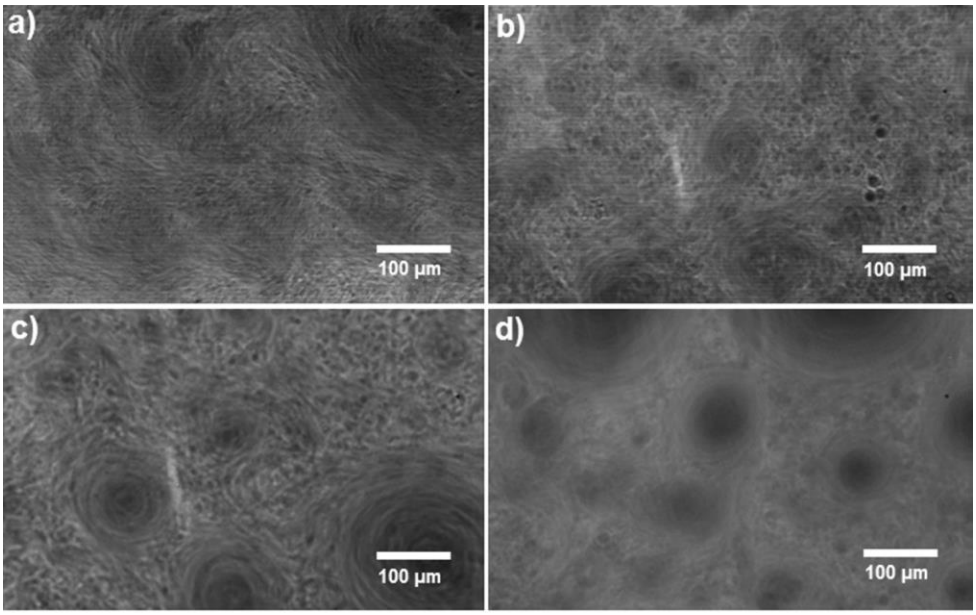

Fig 7 Optical images of magnetic suspension of 16 nm magnetite nanoparticles submitted to a uniform RMF of 31.4 kA/m with a frequency of (a) 10 Hz (b) 50 Hz (c) 100 Hz (d) 200Hz. Suspension consists of 0.005 volume fraction of MNPs (reproduced with permission from ref. 29).

Although vortices in the submicron range cannot be detected at such level of scrutiny in the image above, the coherent vortical structures in the larger scales are discernible in Figure 7. Gravel et al. work confirmed that formation of vortices and their size depends on various operating variables such as RMF frequency and intensity, and magnetic volume fraction and nanoparticle size. Prior to provide any explanation for the emergence of such vortices, it is worth mentioning that every two co-rotating

vortices when reaching a critical distance go through an elliptical deformation, diffuse into each other and grow in size. The two deformed vortices will finally form a single structure. This phenomenon known as vortex merger is strongly dependent on vortex radius, *a*, and inter-vortex separation distance, *b*. Various criteria for the merging condition as a function of *a*/*b* ratio has been reported.[30] By extension an analogy can be drawn between vortex merger at the micron scale as discussed above and the merger of vortices prompted by the rotating magnetic nanoparticles at the nanometer scale. Interestingly, as RMF frequency is increased, the coherent structures become larger in size which is conceivably due to the larger spheroids around each nanoparticle cluster as illustrated in Figure 7.

Vortex size cannot grow limitless but showcases a limiting size after a certain frequency of rotation is attained. Such growth limit may be explained by considering the act of hydrodynamic forces on the larger assembly of MNPs inside a vortex and their subsequent breakdown, a process similar to deformation of rotating chains of magnetic microparticles. Ultimately, merging and deformation reaches an equilibrium state leading to a specified distribution of vortex size. Larger MNP concentrations tantamount to reduced inter-particle distances increase the likelihood of merging. Emergence of these vortices within the MNP suspension is evocative of turbulent eddies in which motion is manifested into pseudo-turbulence by conversion of magnetic energy, via magnetic torque, into kinetic energy transferred to the carrier fluid.

Experimental studies by Hajiani and Larachi[19] unveiled that stimulated transport at such small scales in ferrofluids subject to RMF is prone to reduce significantly the diffusion time scales. For this purpose, self-diffusion coefficients of diluted ferrofluid in capillary tube have been measured by means of an electrical conductimetry method. The capillary has 1 mm inner diameter and 40 mm length with two pairs of conductivity wire electrodes located at equal distance from both ends. By injecting a brief tracer pulse at one end, the transient evolution of electrical conductivity near each probe can be monitored over time. A uniform rotating magnetic field is generated by six-current carrying coils on the periphery of a hollow cylinder and the capillary tube is placed in the bore space normal to the cylinder central axis as illustrated in Figure 8. Each pair of coils located across each other is energized with an alternating current (AC) with a specific frequency and the currents in each pair are phase shifted by $2\pi/3$ thus providing a rotating magnetic field with a rotation frequency equal to the frequency of AC currents. If two adjacent coils with the corresponding ones across them are energized with an AC current, the resulting magnetic field will be an oscillating one with the direction normal to the center axis of the magnet bore. A SMF with similar direction can also be generated if the AC current is switched to DC.

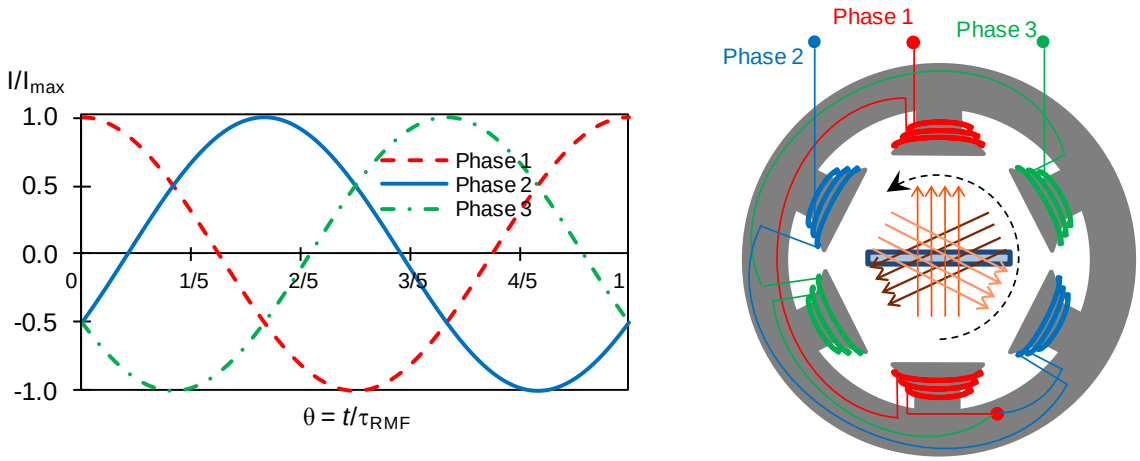

Fig 8 Schematic of 2-pole 3-phase magnetic field generator top view and the inserted capillary cell (reproduced with permission from ref. 19).

It was observed that the time required to reach equilibrium with equalized conductivities registered at both capillary ends is reduced from about 1300 min to 10 min upon enabling RMF with frequency and intensity as high as 100 Hz and 31.4 kA/m, respectively. Initiation of other mixing mechanisms, such as those induced by Kelvin force is precluded under such experiments because the injected tracer pulse consisted of the same magnetic concentration of the ferrofluid already present inside the cell. The estimated diffusion coefficient of such magnetically-actuated system neared two hundred times the normal self-diffusion coefficient of the diluted ferrofluid. Furthermore, the diffusion coefficient increases with the magnetic field rotational frequency though the enhancement tends to plateau beyond a certain frequency. This is in accordance with Gravel et al.[29] optical observations revealing that after a specified frequency, vortex growth was halted. Likewise, amplification of the magnetic field follows qualitatively a similar by strengthening the nanostirrers' agitation. Measurement of the diffusion coefficient at high frequencies as a function of RMF intensity shows an ascending trend confirming the advantageous effect of magnetic field intensity.

The concept of nanostirrers active within stagnant fluids has also been extended to dilute ferrofluids (0.001 to 0.005 volume fraction) in motion by Hajiani and Larachi[24, 31]. The authors showed that RMF active in the plane transvers to the flow direction can notably modify the flow characteristics reducing the axial dispersion coefficient (D) in laminar flow and also enhancing the lateral mixing. Dispersion was quantified by means of tracer pulse tests and by fitting an open-open axial dispersion RTD model[32]. The obtained axial dispersion coefficients were found to decrease upon enabling RMF. This can be visually picked up from the narrower residence time distributions despite Reynolds numbers corresponding to purely laminar flows. Figure 9 illustrates such dependency versus Reynolds number

for various RMF frequencies. The magnetic field parameters have also considerable effects on axial dispersion in a manner similar to that exemplified earlier in the case of self-diffusion coefficients. Similarly, higher frequencies of RMF drastically reduce axial dispersion while after a certain frequency, it does not exhibit any further reduction.

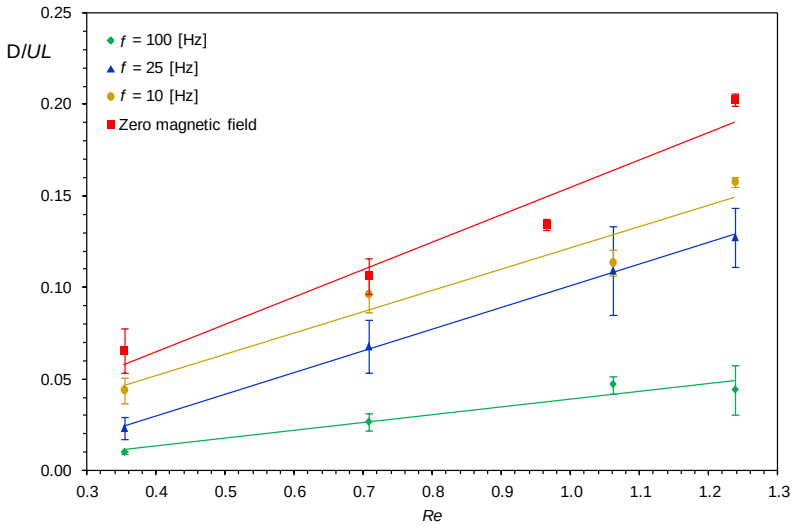

Fig 9 Effect of Reynolds number and RMF frequency on axial dispersion coefficient shown as a dimensionless number. Experiments performed with φ = 0.001, H = 31.4 kA/m (reproduced with permission from ref. 24).

II.IV.I. Comparison of RMF with OMF and SMF in lateral nanomixing of ferrofluid capillary flows

It was previously explained that low frequency OMF cannot result in any single oriented rotation of MNPs. Yet another experimental evidence of such phenomena can be observed when the capillary tube is perpendicular to OMF direction. In the range of tested frequencies, i.e., 10 to 100 Hz, no pronounced variation in axial dispersion can be observed. Undoubtedly, Brownian relaxation for *ca*. 16 nm MNPs in the order of 10 μs is notably shorter than the RMF period (0.1 to 0.01 s). The momentary zero passage of OMF will reshuffle randomly the orientation of the MNP magnetic moments thus over the whole cycle the net rotation direction of the nanoparticles is zero. Therefore a mechanism for mixing similar to RMF cannot be expected from low frequency OMF. Figure 10 portrays how RMF and OMF affect axial dispersion coefficient as a function of frequency.

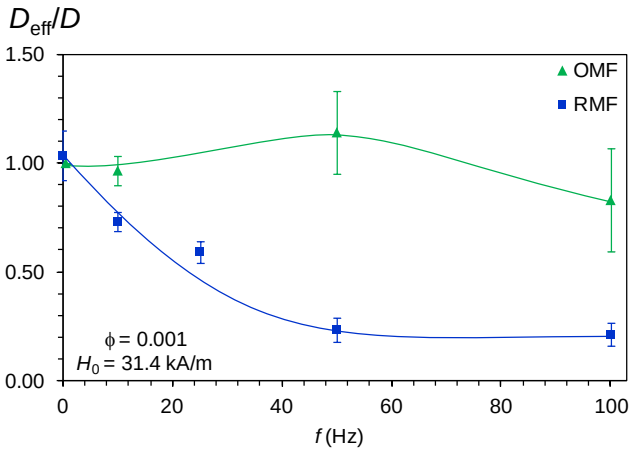

Fig 10 Ratio of axial dispersion coefficient under the effect of magnetic field (D_{eff}) to reference axial dispersion coefficient at H = 0 and φ = 0 (D) as a function of RMF and OMF frequency (reproduced with permission from ref. 31).

The effect of SMF has also been studied by Hajiani and Larachi[31] but in that case flow direction and magnetic field were set parallel to each other to investigate how competing magnetic and hydrodynamic torque affect the flow characteristics. SMF, depending on its intensity and also MNP concentration can evince different impacts on axial dispersion. In low intensity fields, the magnetic torque exerting on the nanoparticles is not strong enough to overcome the hydrodynamic torque while after a certain magnetic field intensity, RTD signals broadened corresponding to inflating axial dispersion coefficients in contrast to the effect of RMF. This dependency is depicted in Figure 11.

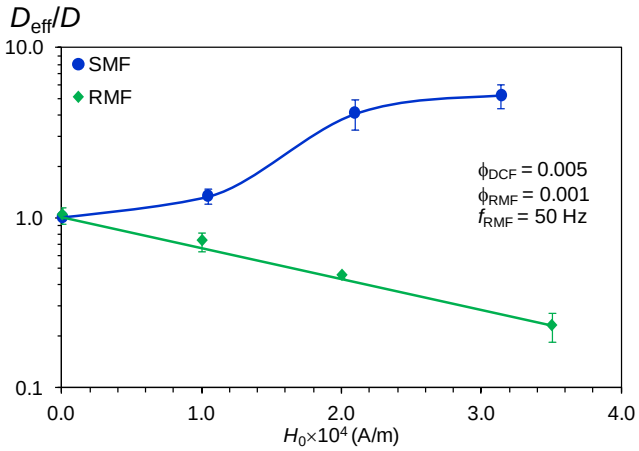

Fig 11 Relative axial dispersion evolution under RMF and SMF versus magnetic field strength. Magnetic volume fraction in RMF and SMF are 0.001 and 0.005, respectively (reproduced with permission from ref. 31).

SMF with enough strength locks the MNPs to prevent their free rotation as a result of flow vorticity. These locked nanoparticles will impede the regular sliding of fluid layers in which the MNPs are present. Therefore, fluid velocity in these layers is flattened and a zero gradient regions appear locally in the entire velocity profile. In return, the adjacent layers showcasing MNP depletion will compensate fluid mass continuity by an increased axial velocity. This would result in a protruding axial velocity profile the increased variance of which subsequently leads to inflated axial dispersion coefficients.

Alteration of the velocity profile under the action of RMF can also be conjectured since every rotating nanoparticle imposes a velocity component on the plane perpendicular to the flow direction. In addition, the reduced axial dispersion coefficient specifies a more flattened velocity profile whereas the fluid layers smear the injected tracer blob less than a parabolic distribution. Besides, the mixing ability of MNPs and their influence on velocity profile could prove promising in process intensification applications.[1]

III. Scope of thesis

The above contribution briefly introduced both theoretically and experimentally, the magnetic-field assisted mixing concept. In the subcategory of mixing with magnetic nanoparticles (MNP), the governing equations of fluid motion help gaining insights into grasping the MNPs interaction with magnetic fields and exploiting specific interactions in mixing applications. In static magnetic fields (SMF), the mixing mechanism is mainly due to the Kelvin body force as a result of inhomogeneity in magnetic field strength or material magnetic susceptibility. In oscillating magnetic fields (OMF), besides a similar mechanism to SMF, translation of magnetic energy into kinetic energy of MNPs is theoretically and experimentally proven albeit this mechanism has not been used practically in mixing applications. Rotating magnetic fields (RMF) highlight another mechanism able to perform magnetic energy conversion into kinetic energy though with technically simpler methods. Experimental evidence of RMF effectiveness in mixing applications makes it a promising tool to expand its applicability to the effervescent area of microfluidics.

We define the scope of thesis in close relevance to recent findings on the subject of scalars transport in ferrofluid subjected to external RMF. We are mainly interested to disclose properties of scalar transport in ferrofluid in presence of external magnetic field and understand the mechanisms through ferrohydrodynamic simulations. Note that we limit our studies to the transport of scalars within the interstitial fluids of a magnetic colloidal dispersion where the transport mechanisms are not yet well understood. In the first chapter, we demonstrate by experimental measurements the anisotropic

character of the enhanced mass transport in ferrofluids subjected to external magnetic stimuli. It will be shown with the aid of numerical simulations that the anomalous anisotropy of mass transport in ferrofluid is not convective in essence. By means of sensitivity analysis we will demonstrate that the effective diffusivity tensor in ferrofluids is magnetic-field dependent though its components are not yet predictable by current FHR theory. The obtained information on effective diffusion of scalars in chapter one will assist to unravel the mechanisms subtending the reduced axial dispersion in ferrofluid Poiseuille flows subjected to RMF. In this regard, in the second chapter, the contributions of advection and effective diffusion in reshaping the residence time distribution and thus altering axial dispersion are assessed by numerical and experimental methods. The set of obtained information on transport of scalars is used to develop a novel mixing method for potential applications in microreaction engineering. In the third chapter we will demonstrate how anomalous diffusion in ferrofluid may enhance mixing and micromixing by appropriate choice of magnetic field orientation. This objective is met through coupling two sets of chemical reactions to the mass transport phenomenon. The first set, an instantaneous reaction, provides information on the characteristics of mixing at micro-length scales at low Reynolds number. The second set, a parallel consecutive probe reaction set gives information on mixing at the molecular level. The significance of the obtained information is mainly relevant to applications of ferrofluids in microreaction engineering. In the fourth chapter, we will demonstrate that the concept of effective diffusion can be exploited in a magnetic medium other than viscous fluids. The experimental observations of mass transfer in a viscoelastic magnetic medium provide insights on how the viscous and elastic properties influence the effective diffusion in the presence of RMF. The information obtained from this set of experiments opens the way for magnetic applications to the concept of inter-particle mixing.

IV. Nomenclature

Latin letters	**Description**	**Units**
$\underline{\mathbf{A}}$	Exchange between internal and external angular momentum vectors	N kg m^{-5}
$\underline{\mathbf{B}}$	Magnetic flux density	kg A s^{-2}
d	Diameter of magnetic nanoparticle	m
D_i	Diffusion coefficient	m^2 s^{-1}
f	Frequency of magnetic field rotation	s^{-1}
f_0	Larmor frequency of the magnetization vector	s^{-1}
f_{AC}	Frequency of AC magnetic field	s^{-1}

$\underline{\mathbf{F}}$	External body force density	N m^{-3}
$\underline{\mathbf{F_m}}$	Kelvin body force density	N m^{-3}
$\underline{\mathbf{G}}$	Body couple density vector	Pa
$\underline{\mathbf{H}}$	Magnetic field vector	A m^{-1}
$\lvert\underline{\mathbf{H}}\rvert$	Value of magnetic field vector	A m^{-1}
I	Moment of inertia density of magnetic nanoparticles	m^2
L	Characteristic length	m
l	Scaled diffusion length	M
K	Anisotropy constant	J m^{-3}
k_B	Boltzmann's constant	J K^{-1}
$\underline{\mathbf{M}}$	Magnetization vector	A m^{-1}
$\underline{\mathbf{M}}^{\boldsymbol{e}}$	Equilibrium magnetization vector	A m^{-1}
N	Number of magnetic particles	-
p	Pressure	Pa
Re	Reynolds number	-
R_T	Dimensionless number in Eq.13	-
V_H	Hydrodynamic volume of nanoparticles	m^3
V_p	Magnetic particle core volume	m^3
t	Time	s
$\bar{t}$	Dimensionless time	-
t_m	Scaled diffusion time	s
T	Absolute temperature	K
$\underline{\mathbf{V}}$	Velocity vector	m s^{-1}
Greek letters	**Description**	**Units**
ζ	Vortex viscosity	Pa s
η	Dynamic viscosity	Pa s
η'	Shear spin viscosity	kg m s^{-1}
λ'	Bulk spin viscosity	kg m s^{-1}
μ_0	Absolute magnetic permeability of vacuum	N A^{-2}
ρ	Density	kg m^{-3}

τ	Effective relaxation time	s
τ_{AC}	AC magnetic field oscillation time scale	s
τ_b	Brownian relaxation time	s
τ_h	Hydrodynamic time scale	s
τ_n	Neelian relaxation time	s
χ_i	Initial magnetic susceptibility	-
$\underline{\boldsymbol{\omega}}$	Spin density vector	s^{-1}

V. References

1. S. Borukhova and V. Hessel, in *Process Intensification for Green Chemistry: Engineering Solutions for Sustainable Chemical Processing*, eds. K. Boodhoo and A. Harvey, John Wiley & Sons, United Kingdom, 1 edn., 2013, pp. 91-156.
2. J. Baldyga and J. R. Bourne, *Chemical Engineering Science*, 1990, **45**, 907-916.
3. A. van Reenen, A. M. de Jong, J. M. J. den Toonder and M. W. J. Prins, *Lab on a Chip*, 2014, **14**, 1966-1986.
4. K. Boodhoo and A. Harvey, in *Process Intensification for Green Chemistry: Engineering Solutions for Sustainable Chemical Processing*, eds. K. Boodhoo and A. Harvey, John Wiley & Sons, United Kingdom, 1 edn., 2013, pp. 1-31.
5. D. L. LesliePelecky and R. D. Rieke, *Chemistry of Materials*, 1996, **8**, 1770-1783.
6. N. Poudyal and J. P. Liu, *Journal of Physics D-Applied Physics*, 2013, **46**, 1.
7. R. E. Rosensweig, *Ferrohydrodynamics*, 1 edn., Dover Publications, United States of America, 1997.
8. S. Odenbach and S. Thurm, in *Ferrofluids: Magnetically Controllable Fluids and Their Applications*, ed. S. Odenbach, Springer, Germany, Editon edn., 2002, vol. 594, pp. 185-201.
9. M. I. Shliomis, *Soviet Physics Jetp-Ussr*, 1972, **34**, 1291.
10. J. C. Bacri, R. Perzynski, M. I. Shliomis and G. I. Burde, *Physical Review Letters*, 1995, **75**, 2128-2131.
11. A. Zeuner, R. Richter and I. Rehberg, *Physical Review E*, 1998, **58**, 6287-6293.
12. Q. Cao, X. Han and L. Li, *Lab on a Chip*, 2014, **14**, 2762-2777.
13. T.-H. Tsai, D.-S. Liou, L.-S. Kuo and P.-H. Chen, *Sensors and Actuators a-Physical*, 2009, **153**, 267-273.
14. G.-P. Zhu and N. Nam-Trung, *Lab on a Chip*, 2012, **12**, 4772-4780.
15. C.-Y. Wen, K.-P. Liang, H. Chen and L.-M. Fu, *Electrophoresis*, 2011, **32**, 3268-3276.
16. N. Kockmann, *Transport Phenomena in Micro Process Engineering*, 1 edn., Springer, Germany, 2008.
17. M. Zahn and R. E. Rosensweig, *Journal of Magnetism and Magnetic Materials*, 1987, **65**, 293-300.
18. M. I. Shliomis and K. I. Morozov, *Physics of Fluids*, 1994, **6**, 2855-2861.
19. P. Hajiani and F. Larachi, *Chemical Engineering and Processing*, 2013, **71**, 77-82.
20. T. G. Kang, M. A. Hulsen, P. D. Anderson, J. M. J. den Toonder and H. E. H. Meijer, *Physical Review E*, 2007, **76**.
21. Y. Gao, A. van Reenen, M. A. Hulsen, A. M. de Jong, M. W. J. Prins and J. M. J. den Toonder, *Microfluidics and Nanofluidics*, 2014, **16**, 265-274.
22. C.-Y. Wen, C.-P. Yeh, C.-H. Tsai and L.-M. Fu, *Electrophoresis*, 2009, **30**, 4179-4186.

23. A. Munir, J. Wang, Z. Zhu and H. S. Zhou, *Microfluidics and Nanofluidics*, 2011, **10**, 735-747.
24. P. Hajiani and F. Larachi, *Chemical Engineering Journal*, 2012, **203**, 492-498.
25. R. Calhoun, A. Yadav, P. Phelan, A. Vuppu, A. Garcia and M. Hayes, *Lab on a Chip*, 2006, **6**, 247-257.
26. Y. Gao, M. A. Hulsen, T. G. Kang and J. M. J. den Toonder, *Physical Review E*, 2012, **86**.
27. F. Wittbracht, A. Weddemann, B. Eickenberg, M. Zahn and A. Huetten, *Applied Physics Letters*, 2012, **100**.
28. Moskowit.R and Rosenswe.Re, *Applied Physics Letters*, 1967, **11**, 301-&.
29. O. Gravel, J. Lauzon-Gauthier, C. Duchesne and F. Larachi, *Chemical Engineering Journal*, 2015, **260**, 338-346.
30. C. Cerretelli and C. H. K. Williamson, *Journal of Fluid Mechanics*, 2003, **475**, 41-77.
31. P. Hajiani and F. Larachi, *Chemical Engineering Journal*, 2013, **223**, 454-466.
32. O. Levenspiel, *Chemical reaction engineering*, 3 edn., Wiley, USA, 1999.

Chapter 1: Anomalous anisotropic transport of scalars in dilute ferrofluids under uniform rotating magnetic fields – Mixing time measurements and ferrohydrodynamic simulations

Anomalous anisotropic transport of scalars in dilute ferrofluids under uniform rotating magnetic fields – Mixing time measurements and ferrohydrodynamic simulations

Shahab Boroun, Faïçal Larachi

Department of Chemical Engineering, Laval University, Québec, QC, Canada G1V 0A6.

Résumé

Cette étude rapporte des observations expérimentales et des simulations numériques sur le transport de scalaires dans les ferrofluides sous champs magnétiques rotatifs (CMR). Des expériences de transport de masse ont été menées dans un mélangeur en T capillaire avec un axe de rotation du champ magnétique correspondant à l'axe central du capillaire. L'amélioration significative du transport de masse a été mesurée dans la direction transversale avec l'augmentation de la fréquence du CMR et/ou de la concentration en nanoparticules magnétiques. Le contrôle directionnel par le CMR a donné lieu à des flux de transport de masse anisotropes, avec la diffusion moléculaire agissant comme seul mécanisme de transport parallèlement à l'axe du capillaire. L'importance de l'advection du ferrofluide (écoulement *spin-up*) en tant qu'amélioration du transport de masse a été examinée à la lumière du transport d'advection-diffusion et des résultats expérimentaux. Par conséquent, les équations ferrohydrodynamiques (FHD) du mouvement ont été résolues pour la limite basse de la viscosité de spin [basée sur l'interprétation de Rosensweig de l'échelle de longueur de diffusion de micro-tourbillons] et la limite supérieure rapportées par des études antérieures sur les écoulements *spin-up*. Les simulations FHD ont prédit des magnitudes de vitesses azimutales linéaires extrêmement faibles avec des tendances décroissantes à mesure que la viscosité du spin augmentait. Ces résultats étaient en désaccord avec les écoulements de ferrofluides rapportés précédemment et calculés sur la base de la théorie de la diffusion de spin. Afin de clarifier l'origine des incohérences et de confirmer la fiabilité des simulations numériques, les contraintes de champ de spin et asymétriques ont été analysées pour conclure que la petite échelle de longueur du capillaire ne pouvait pas accréditer le rôle des effets convectifs sous CMR dans l'amélioration du mélange. Les mesures du temps de mélange et l'analyse de l'équation advection-diffusion ont mis en évidence la faiblesse de la théorie FHD actuelle à décrire le transport scalaire en raison des flux de micro-convection circonférentiels secondaires à l'échelle des nanoparticules. Une approche pragmatique a donc été proposée pour estimer, à partir de mesures de temps de mélange, les coefficients de diffusion effective anisotropes

anormaux induits par la rotation des nanoparticules et pour les corréler à la fréquence de CMR et / ou à la concentration en nanoparticules.

Anomalous anisotropic transport of scalars in dilute ferrofluids under uniform rotating magnetic fields – Mixing time measurements and ferrohydrodynamic simulations

Shahab Boroun, Faïçal Larachi

Department of Chemical Engineering, Laval University, Québec, QC, Canada G1V 0A6.

1.1. Abstract

This study reports experimental observations and numerical simulations on the transport of scalars in ferrofluids under rotating magnetic fields (RMF). Mass transport experiments were conducted in a T-mixer capillary with RMF rotational axis parallel to capillary central axis. Significant mass transport enhancement was measured in the transverse direction as RMF frequency and/or magnetic nanoparticles concentration increased. RMF directional control of mass flux enhancement was anisotropic as molecular diffusion was the only transport mechanism parallel to the capillary axis. The significance of ferrofluid advection (spin-up flow) as mass transport enhancement was examined in light of the advection-diffusion transport and experimental results. Hence, the ferrohydrodynamic equations (FHD) of motion were solved for the lower spin viscosity limit [based on Rosensweig's interpretation of micro-eddies diffusion length scale], and upper limit as reported from earlier spin-up flow studies. FHD simulations predicted lower magnitudes of the linear azimuthal velocities with decreasingly trends as spin viscosity increased. These findings were in disagreement with previously reported ferrofluid flows calculated on the basis of spin diffusion theory. To clarify the inconsistency's origin and confirm reliability of numerical simulations, the spin field and asymmetric stresses were analyzed to conclude that the small length scale of the capillary could not accredit the role of spin-up flow effects *via* azimuthal velocities for the improved mixing observations. Mixing time measurements and analysis of the advection-diffusion equation pointed toward lack of current FHD theory to resolve scalar transport due to the nanoparticle-scale secondary circumferential micro-convective flows. A pragmatic approach was therefore proposed to estimate from mixing time measurements the anomalous anisotropic effective diffusion coefficients induced by rotating nanoparticles, and to correlate them to RMF frequency and/or nanoparticles concentration.

1.2. Introduction

Theoretical and experimental studies on transport phenomena of micro-polar fluids have remarkably flourished with the advent of ferrofluids. These special nanofluids consist of magnetic nanoparticles (MNP) dispersed in a carrier fluid whereby steric/electrostatic repulsive forces ensure suspension colloidal stability. In the absence of external forces and torques, the time scale of rotation of such colloidal nanoparticles is mainly governed by Brownian motion or by hydrodynamic torques from the bulk of carrier fluid[1]. However, the rotational dynamics of MNP can be manipulated by exerting external magnetic (Kelvin) body force and/or magnetic torque provided external magnetic fields are cleverly applied in terms of orientation with respect to flow geometry, intensity, spatial gradient or oscillation/rotational frequencies.[2]

Investigations on ferrofluid and magnetic field interactions unveiled magnetoviscous effects and spin-up flows as two primary momentum transport phenomena.[3,4] Seminal attempts on developing a formal framework for ferrofluid motion paved the way to deeper understanding of experimental observations relevant to momentum transport in micro-polar continua such as ferrofluids.[5,6] This mathematical framework, also known as ferrohydrodynamics (FHD)[7], accurately predicts the experimental observations on magnetoviscous effects under static [1] or oscillating magnetic fields[8]. However, with the aid of experimental observations on magnetoviscous effects, FHD underwent several amendments mainly with purpose of accurate description of the ferrofluid magnetization as a result of perturbations from equilibrium of the magnetic nanoparticles by thermal or hydrodynamic effects.[9,10]

Of equal importance as magnetoviscosity, the spin-up phenomenon or magnetic-field driven *macroscopic* flow in ferrofluids was the subject of intensive research debated both from experimental and theoretical vantage points. It has to be stressed out that spin-up phenomenon was acknowledged principally as the outcome of magnetic-field driven MNP rotation that exceeds vorticity of a sheared ferrofluid, and as such it was viewed as closely related to negative magnetoviscous effects.[8,11,12] However, spin-up phenomenon is also known to manifest itself even in initially quiescent ferrofluids.[13,14] Spin diffusion theory was initially put forward by Shliomis to explain the spin-up phenomenon considering the observed macroscopic flow in ferrofluids as an outcome of asymmetric-stress forces in curled spin fields.[15] This theory hypothesizes the contribution of couple stress diffusion in the angular momentum balance that results in a curled spin field. The diffusion of couple stress is characterized by a ferrofluid spin viscosity which is formally expressed as a product of ferrofluid viscosity and the squared average distance between magnetic nanoparticles.[3,15] Accordingly, the standard spin viscosity of a conventional ferrofluid is estimated in the order of 10^{-}

[17] kg·m/s for MNP diameter a few tens of nanometers.[3] One should keep in mind that the small value of spin viscosity is associated with the short diffusion length of MNP spin that yields a thin boundary layer the thickness of which is in the order of particle-particle distance.[3] Therefore, the classical spin diffusion theory predicts very small macroscopic flows since the spin field is almost curl-free anywhere except in the spin-field boundary layer.[17] However, studies on spin-up phenomenon for dilute ferrofluids subject to rotating magnetic fields (RMF) unveiled RMF-driven macroscopic flows to be several orders of magnitude larger than those predicted from classical spin diffusion theory.[16,17] Eventually, a modified spin diffusion theory with augmented spin viscosity gave satisfactory agreement between experimentally measured spin-up flow fields and FHD predictions.[17] However, discrepancies in experimental observations of spin-up[18] in addition to plausibility of the contribution of couple stress diffusion are still debated in the literature.[18,19]

Although the influence of external magnetic fields on the linear and internal angular velocity fields in ferrofluids is studied in the literature, the transport of scalars in ferrofluids is not yet deeply understood. Prediction of scalars transport *via* the advection-diffusion equation is heretofore validated in static magnetic fields (SMF) or oscillating magnetic fields (OMF) with frequencies lower than the reciprocal of magnetic relaxation time constant.[20-23] For these types of magnetic fields, the magnetic torque being exerted on the nanoparticles forces the MNP to rotate with an angular velocity less than ferrofluid vorticity. As a result of the mismatch between MNP spin and ferrofluid vorticity, both vortex viscosity and shear viscous dissipation contribute to dissipate external angular momentum.[3] Despite those resistive flow effects, SMF and low-frequency OMF can alternatively generate linear momentum that gives rise to magnetic-field driven advection. The mechanisms of magnetic body force generation are accounted for in the magnetic (Maxwell) stress tensor and may result either from homogenous fields applied to media having magnetic susceptibility gradients or from spatially inhomogeneous magnetic fields. While the latter mechanism increases the probability of colloidal destabilization through clustering or magnetophoresis,[24] the former attracted attention of researchers in the realm of microfluidics for rate intensification of scalars mixing between paramagnetic fluid and superparamagnetic ferrofluid.[25] Modeling of mass transport as an advection-diffusion process shows the that secondary flow resulting from the Kelvin body force is a plausible mechanism for enhanced mixing in ferrofluids.[20,21] The common approach to predict velocity fields on the basis of FHD theory assumes the external magnetic body force as an averaged quantity acting on a structured continuum essentially composed of continuous and dispersed phases. Hence, the translational movement of MNP in the force field accompanied by entrainment of the surrounding carrier fluid is manifested by ferrofluid advection as specified by a spatially-averaged velocity field which does not resolve the

micro-motions proper to each of the dispersed and continuous individual phases in the ferrofluid. Likewise, agreement between experiments and predictions from the advection-diffusion equation shows that the transport of scalars can be mathematically expressed according to FHD formulation provided the scalars are spatially averaged over the dispersed and continuous phase.

For high-frequency OMF or RMF, the rotational state of MNP can exceed the intrinsic ferrofluid vorticity thus manifesting negative magnetoviscous effects or ferrofluid spin-up flow. Experimental measurements of spin-up phenomenon for various geometries showed that notable macroscopic ferrofluid flows can also arise from uniform RMF.[13,26] Similar to the impact of ferrofluid advection driven by Kelvin body force, the spin-up phenomenon may also influence the rate of scalar transport. Heat transport enhancement by ferrofluid spin-up phenomenon is in principle also conceivable in uniform RMF.[27] However, the temperature gradients necessary for heat transfer generate magnetic susceptibility gradients that may in return trigger ferrofluid advection through the Kelvin body force. Unlike heat transfer, mass transfer experiments within the non-magnetic matrix phase of the ferrofluid lend themselves to better experimental control to eliminate such parasitic Kelvin-force driven advection provided the magnetic field is spatially uniform. Hence, enhanced mass transport was experimentally observed in dilute ferrofluids with uniform magnetic susceptibility and subject to uniform RMF.[28] One may conjecture that ferrofluid advection by spin-up phenomenon might contribute as the main mass transfer enhancement mechanism. Nevertheless, to the best of the authors' knowledge, no study has *hitherto* been conducted to corroborate (or not) the role of spin-up phenomenon in mass transfer enhancement.

In this study, we aimed at devising experimental procedures to evaluate mass transfer enhancement in dilute ferrofluids with homogeneous magnetic susceptibility in the presence of a spatially-uniform external rotating magnetic field. The main question to be addressed was if the mechanism for the observed enhancement is ascribed to ferrofluid advection arising from the spin-up phenomenon. Since recourse to conventional optical imaging techniques in ferrofluid mixing experiments is very challenging due to lack of optical contrast, mass transport phenomena were quantified through reactive mixing time measurements inside a T-mixer capillary using a previously developed electrical conductimetry technique.[29] Mixing time experiments were carried out in the so-called stop-flow RMF excitation conditions where after reaching steady-state Poiseuille flow, the ferrofluid streams were abruptly switched off simultaneously to RMF activation. Numerical solution of the combined FHD/diffusion-advection transport model helped rationalizing the convective and anisotropic diffusive signatures elicited by the magnetic field, as well as discussing the physical significance of

the linear/angular velocities, magnetic forces/couples, asymmetric stresses and magnetization in the mas transfer enhancement.

1.3. Experimental

1.3.1. Preparation of cobalt ferrite nanoparticles, and acidic and basic ferrofluids

Cobalt ferrite magnetic nanoparticles (MNP) were synthesized by a co-precipitation method according to a procedure described elsewhere.[30] In brief, Fe^{3+} and Co^{2+} ions using chloride salt precursors were precipitated at pH 9 by adding concentrated sodium hydroxide solution at 80 ºC for 15 min. A small aliquot of the resulting precipitate $CoFe_2O_4$ suspension was withdrawn, its solid content magnetically separated, washed several times with deionized water and then dried. The collected cobalt ferrite MNP powder and a surfactant-free aqueous MNP preparation thereof were characterized using a vibrating sample magnetometer (VSM) from Princeton Instrument (MicroMag model 2900) for determining the magnetization of MNP powder and ferrofluids at 298 K. The hydrodynamic diameter of MNP in the colloidal state was measured by dynamic light-scattering method by means of a Zetasizer Nano 6 (Malvern Instruments Ltd) using a 4 mW He–Ne laser at 633 nm wavelength. The remaining $CoFe_2O_4$ suspension was treated through addition of oleic acid surfactant under vigorous stirring for 15 min following which the precipitate was magnetically separated, washed several times with deionized water and sonicated for 10 min. Aqueous surfactant-stabilized colloidal suspensions of cobalt ferrite magnetic nanoparticles, referred to as ferrofluids, were then prepared for different MNP volume fractions, φ, and characterized using the same magnetic and dynamic light scattering techniques. These preparations were either acidified or alkalinized, by adding nitric acid or sodium hydroxide to yield, respectively, 0.01 N acidic or basic ferrofluid suspensions.

1.3.2. Magnet device

Rotating magnetic fields (RMF) were generated by means of a three-pair two-pole stator the coil of which was wound around a cylindrical magnet bore, 55 mm in height and 45 mm in inner diameter (Figure 1.1). A three-phase 120º-out-of-phase AC current was fed to the three coil pairs which resulted in a magnetic field inside the bore rotating with a frequency equal to that of the balanced AC currents. In the designed magnet, RMF were generated perpendicularly to the central bore axis as sketched in Figure 1.1. The intensity and frequency of RMF were adjusted by means of a variable frequency drive (ABB, ACS150, 2.2kW) coupled to a power source. The magnetic field intensity was measured by a Gaussmeter (Cryomagnetics, GM-700) and was verified to be homogeneous radially within 5 mm radial distance from bore central axis and axially along the 45 mm bore length.

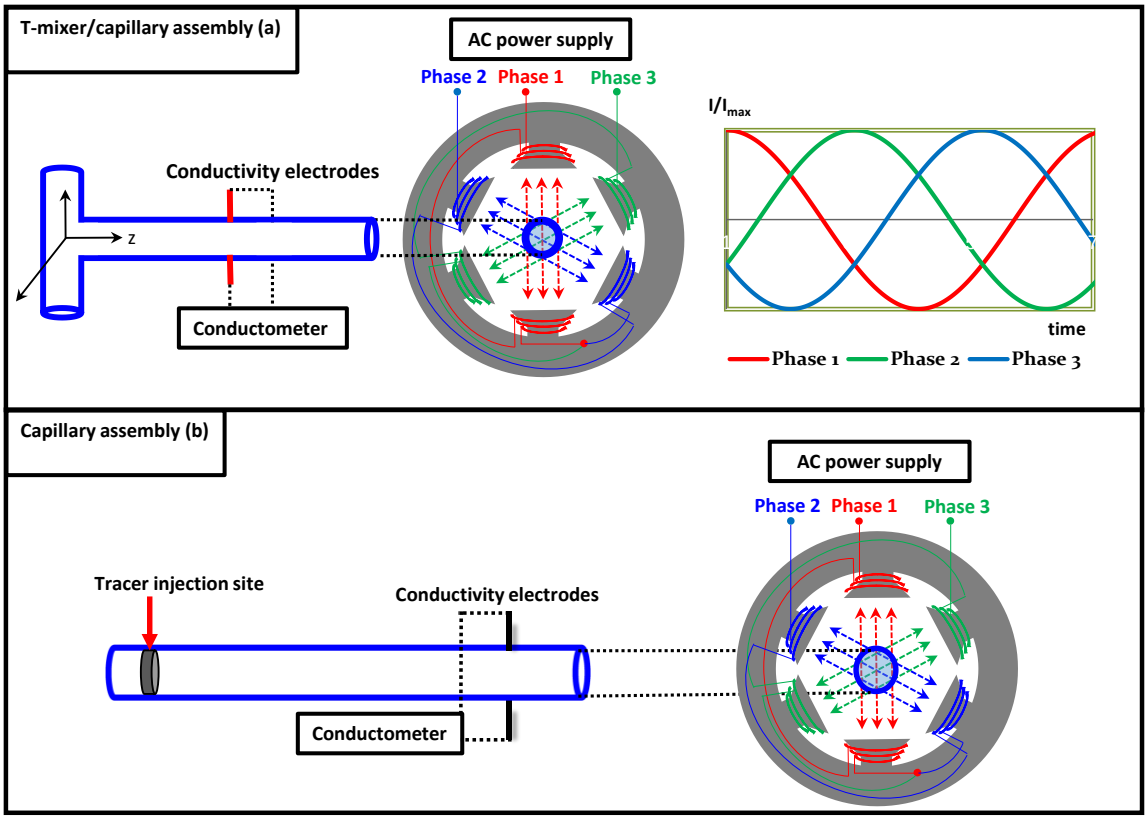

Fig 1.1 T-mixer/capillary (a) and capillary (b) magnet assemblies for quantification of transverse and axial scalar transport in rotating magnetic fields. Schematic of RMF generator, three-pair two-pole stator coils, and capillary centrally-aligner with cylindrical magnet bore in both assemblies for a perpendicular rotating magnetic field.

1.3.3. Transverse mixing via stop-flow technique

A T-mixer device terminated with a cylindrical capillary 5-cm in length and 1 mm in inner diameter (Figure 1.1a) was used for the determination of transverse diffusivities between two parallel ferrofluid streams under a particular arrangement of the rotating magnetic field. The T-mixer assembly was placed inside the magnet bore with the capillary central axis accurately aligned along the magnet bore centreline to ensure a homogeneous magnetic field rotating perpendicularly to the capillary. Each one of the T-mixer two inlets was independently connected to a precision syringe pump feeding stoichiometric acidic and basic ferrofluid streams at identical flow rates and equal MNP concentrations to ensure a *total* capillary flow rate with Re = 10 (total flow rate basis). A pair of conductivity electrodes was inserted in the capillary 3 cm downstream of the T-junction. These electrodes were connected to a conductivity-meter (Omega CDTX-90) to register the instantaneous

electrical conductivity evolution. To infer the species concentrations in response to the acid-base transient neutralization, the electrodes were pre-calibrated in order to inter-relate electrical conductivity with ferrofluid ionic strength.

The initial condition in the T-mixer/capillary assembly (Figure 1.1a) coincided with establishment of a magnetic-field-free steady-state inflow. The acidic and basic ferrofluid streams were fed collinearly and adjacently along the capillary. As they progressed towards capillary exit, their contacting interface gradually faded growing into a homogenized core. The acid-base neutralization reaction in the developing core ensured consumption of the excess reactant concentrations whereas the core thickness was entirely controlled by the transverse diffusion fluxes of proton and hydroxide ions (and their affiliated counter-ions) from the respective streams. After reaching steady-state at Re = 10, the ferrofluid streams were abruptly halted simultaneously to activation of the rotating magnetic field. Acid-base neutralization in the now stagnating ferrofluid started to be monitored to single-out and quantify in *stop-flow* the pure contribution of RMF-induced transverse mixing within the capillary. The function of stop-flow was to incapacitate unwanted mixing sources, *e.g*., Poiseuille streamwise advection and axial dispersion, to interfere with, and thus contaminate, the electrical conductivity signal changes originating from pure RMF-driven transverse mixing effects. Note that in order to highlight the role of RMF stimulation in the mixing process by means of MNPs, selection of Re = 10 for the magnetic-field-free inflow period was not arbitrary. It was tuned on the basis of two imperatives: i) inertial non-linear effects in laminar flow must, on the one hand, be minimized to avoid engulfment of the streamlines at the T-junction that would otherwise have resulted in enhanced mixing consequentially to reduced diffusion paths within the generated vortical structures[33], ii) the residence time should, on the other hand, be short enough to prevent molecular diffusion to homogenize to large extents the ferrofluid streams which would likewise have achieved high mixing levels.

1.3.4. Quantification of transverse mixing

According to Kohlrausch's law, the electrical conductivity of an electrolyte solution is barycentric with respect to the conductivities of its individual migrating ions. At sufficiently low ionic strengths, solute-solute interactions are negligible and molar conductivity of each ion may be approximated by its limiting molar conductivity. Therefore, the following relationship between ions' concentrations and solution electrolyte conductivity, κ, may be established:

$$\kappa = \sum_i C_i \nu_i \lambda_i \tag{1.1}$$

Where C_i is the concentration of *i*-type ion, ν_i is the number of ion *i* moiety in its corresponding electrolyte and λ_i is the limiting molar conductivity of ion *i* with values tabulated elsewhere.[29]
In the region where the electrodes were located in the capillary cross-section, an *exp*erimental *tr*ansient mixing index, $\Gamma_{\mathrm{tr}}^{\mathrm{exp}}$, can be defined as.[29]

$$\Gamma_{\mathrm{tr}}^{\mathrm{exp}} = \frac{\kappa_{\mathrm{max}} - \kappa_{\mathrm{exp}}}{\kappa_{\mathrm{max}} - \kappa_{\mathrm{min}}} \tag{1.2}$$

In Eq. 2, κ_{max} would be the fluid conductivity had total segregation between the acidic and basic ferrofluid streams prevailed in which case the limiting $\Gamma_{\mathrm{tr}}^{\mathrm{exp}}$ value would be zero which is always fulfilled at the capillary entrance. At the other limit, κ_{min} is the fluid conductivity should total mixedness between the acidic and basic ferrofluid streams have been achieved and whereby the limiting $\Gamma_{\mathrm{tr}}^{\mathrm{exp}}$ value would be unity. Hence, the *actually* measured conductivity over the capillary cross section, κ_{exp}, should be encompassed in-between these two limits.

Values of the time-dependent $\Gamma_{\mathrm{tr}}^{\mathrm{exp}}$ can further be rescaled with respect to the *s*teady-state mixing index, $\Gamma_{\mathrm{ss}}^{\mathrm{exp}}$, measured just before interruption of the ferrofluid streams and activation of the rotating magnetic field according to:

$$\hat{\Gamma}_{\mathrm{tr}}^{\mathrm{exp}} = \frac{\Gamma_{\mathrm{tr}}^{\mathrm{exp}} - \Gamma_{\mathrm{ss}}^{\mathrm{exp}}}{1 - \Gamma_{\mathrm{ss}}^{\mathrm{exp}}} \tag{1.3}$$

Note that unlike $\Gamma_{\mathrm{tr}}^{\mathrm{exp}}$, normalization of the "hatted" mixing index according to Eq. 3 ensures standardizing the variation domains to a *unique* [0 – 1] interval regardless of the tested experimental conditions.

1.3.5. Quantification of axial diffusive transport

A variation of the previous setup was used to quantify diffusion along the capillary axis for the same RMF arrangement. The capillary extension was first disconnected from the T-mixer head. After it was filled using as-prepared ferrofluids with known MNP concentrations, both cell ends were sealed and the capillary inserted back along the axis of the magnet bore (Figure 1.1b). A pair of conductivity electrodes was installed 2 cm downstream of an injection point whereby *ca*. 1 µL of quasi-Dirac salt tracer impulses were briefly injected into the capillary. The transient salt spread over the stagnant capillary cell was registered using a similar conductivity-meter protocol as described earlier both in presence and absence of RMF. Axial gradients of MNP concentration, due to magnetic susceptibility jumps in the injection zone, give rise to magnetic Kelvin body forces in axial direction which must

be minimized to avert artefactual secondary convective flows inside the capillary. Therefore, the tracer preparation required precautions such as dissolving the sodium chloride passive tracer (10^{-6} mole·m^{-3}) in the as-prepared ferrofluid with identical MNP volume fraction as the ferrofluid already loaded into the capillary.

1.4. Numerical Simulations

1.4.1. FHD governing equations

From the laws of continuity and of micro-polar continuum mechanics, the set of FHD governing equations consists of the incompressible form of the continuity equation, and the linear momentum and internal angular momentum balance equations, respectively:[3]

$$\underline{\nabla} \cdot \underline{\mathbf{v}} = \mathbf{0} \tag{1.4}$$

$$\frac{\partial}{\partial t}\rho\underline{\mathbf{v}} + \underline{\nabla} \cdot \left(\rho\underline{\mathbf{v}}\otimes\underline{\mathbf{v}}\right) = \underline{\nabla} \cdot \underline{\underline{\mathbf{T}^{\mathbf{m}}}} + \underline{\nabla} \cdot \underline{\underline{\mathbf{T}}} \tag{1.5}$$

$$\frac{\partial}{\partial t}\rho I\underline{\boldsymbol{\omega}} + \underline{\nabla} \cdot \left(\rho I\underline{\mathbf{v}}\otimes\underline{\boldsymbol{\omega}}\right) = \eta'\underline{\nabla} \cdot \left(\underline{\nabla}\,\underline{\boldsymbol{\omega}} + \underline{\nabla}\,\underline{\boldsymbol{\omega}}^{\mathbf{t}}\right) - \underline{\underline{\boldsymbol{\varepsilon}}} : \underline{\underline{\mathbf{T}}} + \mu_0\underline{\mathbf{M}} \times \underline{\mathbf{H}} \tag{1.6}$$

Where ρ is the ferrofluid density (kg m^{-3}), $\underline{\mathbf{v}}$ is the velocity (m s^{-1}), $\underline{\underline{\mathbf{T}}}$ is the pressure-viscous stress tensor (N m^{-2}), $\underline{\underline{\mathbf{T}^{\mathbf{m}}}}$ is the magnetic stress tensor (N m^{-2}), I is the moment of inertia of single nanoparticle per unit mass ($\approx 10^{-17}$ m^2),[31] μ_0 is the vacuum permeability (1.26×10^{-6} N A^{-2}), $\underline{\mathbf{M}}$ is the ferrofluid magnetization (A m^{-1}), $\underline{\mathbf{H}}$ is the *total* magnetic field (A m^{-1}) comprising both externally-imposed and demagnetizing fields, η' is the spin viscosity (kg m s^{-1}), $\underline{\boldsymbol{\omega}}$ is the angular velocity (s^{-1}) and $\underline{\underline{\boldsymbol{\varepsilon}}}$ is the triadic unit tensor.

The pressure-viscous tensor has symmetric and asymmetric components. The symmetric component of $\underline{\underline{\mathbf{T}}}$ is given by the conventional expression for Newtonian fluids:

$$\underline{\underline{\mathbf{T}}}^{s} = -p\underline{\underline{\mathbf{I}}} + \eta\left(\underline{\nabla}\,\underline{\mathbf{v}} + \underline{\nabla}\,\underline{\mathbf{v}}^{\mathbf{t}}\right) + \varsigma\left(\underline{\nabla} \cdot \underline{\mathbf{v}}\right)\underline{\underline{\mathbf{I}}} \tag{1.7}$$

Where p is the pressure (Pa), η and ς are, respectively, the shear and bulk viscosities of ferrofluid (kg m^{-1} s^{-1}) and $\underline{\underline{\mathbf{I}}}$ is the dyadic unit tensor. The asymmetric tensor component is expressed as:

$$\underline{\underline{\mathbf{T}}}^{a} = 2\zeta\underline{\underline{\boldsymbol{\varepsilon}}} \cdot \left(\frac{1}{2}\underline{\nabla} \times \underline{\mathbf{v}} - \underline{\boldsymbol{\omega}}\right) \tag{1.8}$$

Where ζ is the vortex viscosity (kg m^{-1} s^{-1}).

The density and shear viscosity of ferrofluid are calculated according, respectively, to the weighted mean rule of mixtures and Einstein equation:

$$\rho = 10^3(1-\varphi) + \rho^p\varphi,\ \eta = 8.9\times10^{-4}(1+2.5\varphi) \tag{1.9}$$

Where φ and ρ^p are the ferrofluid volumetric fraction and density of MNP, respectively.

The vortex viscosity is estimated according to:[3]

$$\zeta = 1.5\eta\varphi \tag{1.10}$$

The divergence of magnetic stress tensor is equivalent to the volumetric density of Kelvin magnetic force and is mathematically expressed as:

$$\underline{\nabla}\cdot\underline{\mathbf{T}}^{\mathbf{m}} = \underline{\mathbf{F}}^m = \underline{\nabla}\cdot\left(\mu_0\underline{\mathbf{H}}\otimes\underline{\mathbf{H}} - \frac{\mathbf{1}}{\mathbf{2}}\mu_0\left|\underline{\mathbf{H}}\right|^{\mathbf{2}}\underline{\mathbf{I}}\right) \tag{1.11}$$

The magnetic field and magnetic flux density are, respectively, curl free and divergence free:

$$\underline{\nabla}\cdot\left(\underline{\mathbf{H}}+\underline{\mathbf{M}}\right) = 0, \underline{\nabla}\times\underline{\mathbf{H}} = \underline{0} \tag{1.12}$$

The ferrofluid magnetization vector is shifted from its equilibrium magnetization by thermal and hydrodynamic perturbations. Hence, the magnetization relaxation is described using the usual transport equation:[3]

$$\frac{\partial\underline{\mathbf{M}}}{\partial t} + \underline{\nabla}\cdot\left(\underline{\mathbf{v}}\otimes\underline{\mathbf{M}}\right) = \underline{\boldsymbol{\omega}}\times\underline{\mathbf{M}} - \frac{1}{\tau}\left(\underline{\mathbf{M}} - \underline{\mathbf{M}}^{\boldsymbol{e}}\right) \tag{1.13}$$

Where τ is the Brownian relaxation time constant (s) and $\underline{\mathbf{M}}^{\mathbf{e}}$ is the equilibrium magnetization (A m^{-1}) expressed in the form of a Langevin relation:

$$\underline{\mathbf{M}}^{\mathbf{e}} = \varphi M_{\mathrm{d}}(\coth\alpha - \alpha^{-1})\frac{\underline{\mathbf{H}}}{\left|\underline{\mathbf{H}}\right|},\ \alpha = \frac{\pi\mu_0 M_{\mathrm{d}}\left|\underline{\mathbf{H}}\right|d^3}{\mathbf{6}k_{\mathrm{B}}T} \tag{1.14}$$

Where M_{d} is the domain-magnetization of cobalt ferrite nanoparticles (A m^{-1}), d is the nanoparticle diameter (m), k_{B} is the Boltzmann constant (1.38×10^{-23} J K^{-1}) and α is a Langevin parameter. The Brownian time constant is expressed as:

$$\tau = \frac{3V_{\mathrm{H}}\eta}{k_{\mathrm{B}}T} \tag{1.15}$$

Where V_H denotes the hydrodynamic volume of nanoparticles (m^3) and T is the temperature.

1.4.2. Scaling FHD equations for rotating magnetic fields

We first define the externally-imposed rotating magnetic (RMF) field in polar coordinates as:

$$\underline{\mathbf{H}}^{\text{ext}} = H_0 \sin(2\pi f t + \theta).\underline{\mathbf{r}} + H_0 \cos(2\pi f t + \theta).\underline{\boldsymbol{\theta}} \tag{1.16}$$

Where H_0 is the amplitude of external RMF (A m^{-1}), f is the frequency of RMF (Hz) and θ is the angle with respect to a reference pole.

It is convenient to choose the RMF angular frequency instead of frequency as a reciprocal characteristic time, $\Omega = 2\pi f$, and the capillary radius, R, as a characteristic length scale to turn the above FHD equations into their dimensionless equivalent:

$$\tilde{t} = \Omega t, \;\; \underline{\tilde{\boldsymbol{\nabla}}} = R\underline{\boldsymbol{\nabla}} \tag{1.17}$$

The FHD dependent variables, namely, linear velocity, internal spin, magnetization, magnetic field and pressure, were scaled as follows:

$$\underline{\tilde{\mathbf{v}}} = \frac{\mathbf{v}}{\Omega R}, \quad \underline{\tilde{\boldsymbol{\omega}}} = \frac{\boldsymbol{\omega}}{\Omega}, \quad \underline{\tilde{\mathbf{M}}} = \frac{\mathbf{M}}{\varphi M_d}, \quad \underline{\tilde{\mathbf{H}}} = \frac{\mathbf{H}}{H_0}, \quad \tilde{P} = \frac{P}{\eta\Omega} \tag{1.18}$$

A single magnetic nanoparticle experiencing external RMF was shown by Rosensweig [3] to maintain a lag angle, β, between $\underline{\mathbf{M}}$ and $\underline{\mathbf{H}}$ as a linear function of $\Omega\tau$ with a slope approaching unity as $\Omega\tau \longrightarrow 0$ and $\mu_0 H_0 \varphi M_d \tau / 4\zeta \longrightarrow 0$. If at low lag angle β scales as $\Omega\tau$ and with the approximation $\sin\beta \approx \beta$, the body couple density may be scaled as:

$$\rho\underline{\tilde{\mathbf{G}}} = \mu_0 H_0 \varphi M_d \Omega\tau\left(\underline{\tilde{\mathbf{M}}} \times \underline{\tilde{\mathbf{H}}}\right) \tag{1.19}$$

Introducing these transformations into the above FHD dimensional equations and rearranging after substitution of viscous and magnetic stress tensors (Eqs.7,8,11), an equivalent set of dimensionless conservation equations of motion, i.e., continuity, linear and spin balance equations, magnetization relaxation and magnetostatics is arrived at:

$$\underline{\tilde{\boldsymbol{\nabla}}} \cdot \underline{\tilde{\mathbf{v}}} = 0 \tag{1.20}$$

$$\frac{\partial \underline{\tilde{\mathbf{v}}}}{\partial \tilde{t}} + \underline{\tilde{\boldsymbol{\nabla}}} \cdot \left(\underline{\tilde{\mathbf{v}}} \otimes \underline{\tilde{\mathbf{v}}}\right) = -\frac{\eta}{\rho\Omega R^2}\underline{\tilde{\boldsymbol{\nabla}}}\tilde{P} + \frac{\eta + \zeta}{\rho\Omega R^2}\underline{\tilde{\boldsymbol{\nabla}}}^2\underline{\tilde{\mathbf{v}}} + \frac{2\zeta}{\rho\Omega R^2}\underline{\tilde{\boldsymbol{\nabla}}} \times \underline{\tilde{\boldsymbol{\omega}}} \tag{1.21}$$

$$\frac{\partial \underline{\tilde{\boldsymbol{\omega}}}}{\partial \tilde{t}} + \underline{\tilde{\boldsymbol{\nabla}}} \cdot \left(\underline{\tilde{\mathbf{v}}} \otimes \underline{\tilde{\boldsymbol{\omega}}}\right) = \frac{\eta'}{\rho I \Omega R^2} \underline{\tilde{\boldsymbol{\nabla}}}^{\mathbf{2}} \underline{\tilde{\boldsymbol{\omega}}} + \frac{2\zeta}{\rho I \Omega} \left(\underline{\tilde{\boldsymbol{\nabla}}} \times \underline{\tilde{\mathbf{v}}} - \mathbf{2}\underline{\tilde{\boldsymbol{\omega}}}\right) + \frac{\mu_0 H_0 \varphi M_d \tau}{\rho I \Omega} \underline{\tilde{\mathbf{M}}} \times \underline{\tilde{\mathbf{H}}} \tag{1.22}$$

$$\frac{\partial \underline{\tilde{\mathbf{M}}}}{\partial \tilde{t}} + \underline{\tilde{\boldsymbol{\nabla}}} \cdot \left(\underline{\tilde{\mathbf{v}}} \otimes \underline{\tilde{\mathbf{M}}}\right) = \Omega\tau\left(\underline{\tilde{\boldsymbol{\omega}}} \times \underline{\tilde{\mathbf{M}}}\right) - \left(\underline{\tilde{\mathbf{M}}} - \underline{\mathbf{e}}\right) \tag{1.23}$$

$$\underline{\tilde{\boldsymbol{\nabla}}} \cdot \left(\frac{\varphi M_d}{H_0} \underline{\tilde{\mathbf{H}}} + \underline{\tilde{\mathbf{M}}}\right) = 0 \tag{1.24}$$

$$\underline{\tilde{\boldsymbol{\nabla}}} \times \underline{\tilde{\mathbf{H}}} = \underline{0} \tag{1.25}$$

Where $\underline{\mathbf{e}}$ is a unit vector in the direction of $\underline{\mathbf{M}}^{\mathbf{e}}$. Note that for an incompressible ferrofluid, linear velocity field is divergent-free, leaving bulk viscosity as a trivial coefficient.

1.4.3. Boundary conditions

The linear and angular velocities, and magnetization vectors were set to zero at $t = 0$. The boundary conditions assume that the spin and linear velocities are zero on the capillary wall, and to satisfy axisymmetric geometry, zero gradients are imposed on the capillary centerline. The boundary conditions for the magnetostatics require that the normal component of magnetic flux density and the tangential component of magnetic field intensity are continuous on the capillary wall. Fortunately, the obstacle posed by the determination of these magnetostatics boundary conditions may be overcome by subtracting the demagnetizing field of a magnetisable material with cylindrical shape from the externally applied magnetic field:[31]

$$\underline{\tilde{\mathbf{H}}} = \underline{\tilde{\mathbf{H}}}^{\text{ext}} - \frac{\varphi M_{\text{d}}}{3H_0} \underline{\tilde{\mathbf{M}}} \tag{1.26}$$

It is straightforward to show that $\underline{\boldsymbol{\nabla}} \cdot \underline{\tilde{\mathbf{H}}}^{\text{ext}} = 0$ and at the limit when $\left|\underline{\mathbf{M}}^{\mathbf{e}}\right| H_0^{-1} \longrightarrow 0$, Eqs.24, 26 lead to:

$$\underline{\tilde{\boldsymbol{\nabla}}} \cdot \left(\frac{\varphi M_{\text{d}}}{H_0} \underline{\tilde{\mathbf{M}}} + \underline{\tilde{\mathbf{H}}}\right) \approx \underline{\tilde{\boldsymbol{\nabla}}} \cdot \underline{\tilde{\mathbf{H}}} \approx 0 \tag{1.27}$$

A similar analysis in taking the curl of Eq.26 leads to $\underline{\tilde{\mathbf{H}}}$ is also curl-free. Therefore, Eq. 26 still approximates $\underline{\tilde{\mathbf{H}}}$ over the entire geometrical domain of the capillary without violating the laws of magnetostatics. This approximation also has the advantage to decouple magnetostatics from the magnetization relaxation equation (Eq.23). In addition, it helps directly calculating $\underline{\mathbf{M}}^{\mathbf{e}}$ from the limiting Langevin function at high intensity of the external magnetic field:[3]

$$\underline{\mathbf{M}}^{\mathbf{e}} = \varphi M_{\mathrm{d}} \left(1 - \frac{1}{\alpha}\right) \frac{\underline{\mathbf{H}}}{|\underline{\mathbf{H}}|} \tag{1.28}$$

1.4.4. Scalar transport

The transport of scalars is expressed by the usual advection-diffusion species conservation equation:

$$\frac{\partial C_i^{\mathrm{r}}}{\partial t} = \underline{\boldsymbol{\nabla}} \cdot \left(\underline{\underline{\mathbf{D}}}_i \underline{\boldsymbol{\nabla}} C_i^{\mathrm{r}}\right) - \underline{\boldsymbol{\nabla}} \cdot \left(\underline{\mathbf{v}} C_i^{\mathrm{r}}\right) + R_i \tag{1.29}$$

Where C_i^{r} is the reactive tracer concentration (mole m^{-3}), R_i is the reaction rate of reactive scalars and $\underline{\underline{\mathbf{D}}}_i$ is the second-rank diffusivity tensor:

$$\underline{\underline{\mathbf{D}}}_i = \begin{bmatrix} D_{rr} & 0 & 0 \\ 0 & D_{\theta\theta} & 0 \\ 0 & 0 & D_{zz} \end{bmatrix} \tag{1.30}$$

In the T-mixer acid-base neutralization tests (Figure 1.1a), the reduction in electrical conductivity was merely the resultant of consumption of protons and hydroxides for the production of water from the encounter of the two ferrofluid streams. Therefore, Eq. 29 was solved for protons and hydroxides. The transient evolution of the computed mixing index, $\Gamma_{\mathrm{tr}}^{\mathrm{cal}}$, was obtained from the numerically predicted transient concentrations and their subsequent conversion into conductivities using Eq. 1. The boundary conditions corresponded to zero mass fluxes at the capillary wall. The initial conditions for the species concentrations were set in order to satisfy the steady-state solution of Eq. 29 for Re = 10 before the ferrofluid streams were cut-off and the magnetic field was activated. Accuracy of the calculated initial conditions was verified by comparing $\Gamma_{\mathrm{tr}}^{\mathrm{cal}}$ with $\Gamma_{\mathrm{tr}}^{\mathrm{exp}}$.

In the tests involving passive tracer dispersion in the capillary assembly (Figure 1.1b), Eq. 29 was solved under the same boundary conditions while recognizing that there are no source terms, $R_i = 0$. Tracer-free, *i.e.*, zero concentration, was assumed initially in the capillary except for the injection zone where a known amount of ferrofluid salt tracer was assigned in the form of a 1-mm thin disk with capillary radius R so that the number of moles and volume occupied by tracer at $t = 0$ initial were precisely defined.

1.4.5. Numerical method

Based on the governing equations of motion of pseudo-homogeneous micro-polar continua, for instance in the form of a set of dimensionless partial differential equations given by Eqs.20-25, and aided with the constitutive equations presented in sections 1.4.1 and 1.4.2, the FHD framework has

imposed itself over the past few decades as the tool *par excellence* in ferrofluid flow simulations. It was solved for our capillary geometry at Re = 0 with the boundary and initial conditions stated in section 1.4.3. The conservative time-dependent FHD equations, magnetization transport equation and magnetostatics were discretized using an implicit finite-volume method. The system of nonlinear equations generated from discretization was solved using an iterative Newton's method. In order to implement the initial guess, the equations were initially discretized in semi-implicit scheme by explicit discretization of magnetization relaxation equation that allows calculation of magnetization a time step earlier than linear and angular velocities. The explicitly calculated magnetization was subsequently introduced in the implicitly discretized linear and angular momentum balance equations to solve for the linear and angular velocities. Solutions by the semi-implicit scheme were used as initial guess for obtaining solutions of the complete set of equations by the implicit method. Considering the very large aspect ratio of the capillary, a fully developed axially-invariant flow assumption was adopted reducing FHD dimensionality to 2D + *t* with equations solved for their *vector components* in $\underline{\mathbf{r}}$ and $\underline{\boldsymbol{\theta}}$ directions. This resulted in radial linear velocity predicted to be zero leaving room for diffusion alone to prevail along this direction. An additional *a priori* hypothesis considered that the azimuthal component, v_θ, of the linear velocity vector was rotationally invariant. Such assumption saved treatment of the pressure-velocity coupling problem. The capillary domain was discretized using a polar cylindrical grid. Spatial resolution was verified by sequentially increasing mesh density until grid-independent vector variables are obtained which typically was reached using up to 20,000 control volumes/nodes. A combination of Matlab and Comsol Multiphysics (version 4.4) was used to solve in a decoupled manner the FHD equations and the scalar transport equation. Thus, to confront the predicted mixing indices to those determined experimentally, the advection-diffusion equation was fed with the ferrofluid velocity field obtained by first solving the FHD equations.

1.5. Results and Discussion

1.5.1. Properties of cobalt ferrite nanoparticles and ferrofluids

Analysis of the powder X-ray diffraction patterns of the prepared cobalt ferrite magnetic nanoparticles revealed formation of inverse-spinel MNP crystallites with an average size of 33 nm according to Scherrer's equation.[30] The powder's ferromagnetic response quantified at ambient temperature exhibited a magnetization hysteresis loop with saturation magnetization of 59 emu/g (Figure 1.2a) which was taken in our numerical simulations to correspond to the domain magnetization, M_d, of the cobalt ferrite nanoparticles.

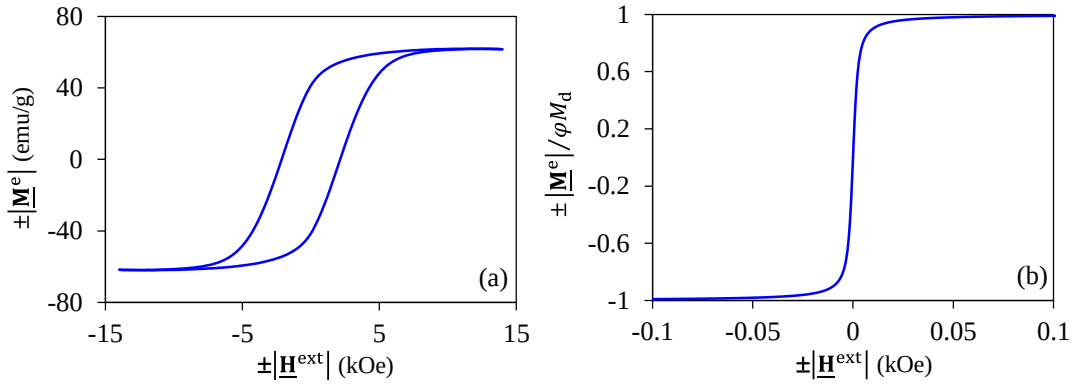

Fig 1.2 Ambient-temperature (a) equilibrium magnetization curve of powdery cobalt ferrite nanoparticles (a) and scaled equilibrium magnetization curve of cobalt-ferrite ferrofluid (φ = [0.001 – 0.004] and M_d = 295 kA/m).

There was no indication that the nanoparticles in their powdery form underwent Néelian relaxation (Figure 1.2a). Dispersion in water of the surfactant-free MNPs resulted in a unimodal bell-shaped particle size distribution with an average hydrodynamic diameter of 33.8 nm and nanoparticle sizes bracketed between 20 nm and 100 nm as measured by dynamic light scattering.[30] The dilute colloidal suspensions were prepared with MNP volume fractions between 0.001 and 0.004 (magnetic-core basis) to avert aggregation of the nanoparticles due to their permanent magnetic dipole moments. Furthermore, transitions for cobalt ferrite nanoparticles from superparamagnetism to ferromagnetism and from single-domain to multi-domain were determined to occur, respectively, near 16 nm and 100 nm particle diameters.[30] Therefore, it is reasonable to assume that within the [20 – 100 nm] range, all the cobalt ferrite nanoparticles form thermally-blocked single-domain MNPs[30,32] Lack of remnant magnetization in the composed ferrofluids (Figure 1.2b) singles out Brownian agitation as the main relaxation mechanism of the nanoparticles with an average relaxation time estimated from Eq. 15 to be *ca*. 10^{-4} s. Consequently, deviations of magnetization, both directional and in magnitude, with respect to magnetostatic equilibrium magnetization as a result of ferrofluid displacements are mainly prompted from bodily rotation of the magnetic nanoparticles. Such departures from equilibrium magnetization are accounted for in a magnetization transport equation whereby the first term and the Brownian relaxation term in Eq. 23 RHS capture the ferrohydrodynamic deviations of magnetization from the Langevin law. We are now also able to estimate $\varphi M_d/3H_0$ to be in the order of $O(10^{-3})$ $O(10^{5})$ $O(10^{-4})$ = $O(10^{-2})$ for φ varying between 0.001 and 0.004. Thus the error in approximation of $\underline{\widetilde{\mathbf{H}}}$ is lower than $O(10^{-2})$.

1.5.2. Transverse mixing via stop-flow RMF excitation

A magnetic-field-free steady-state profile of the mixing index was established along the capillary during the laminar inflow period at Re = 10. Developing from an entrance value $\Gamma_{ss}^{exp} = 0$ (Eq. 2) corresponding to impingement of the acidic and basic streams, the steady-state mixing index measured 3 cm downstream of the T-junction increased to $\Gamma_{ss}^{exp} = 0.23$. The two ferrofluid streams underwent fairly moderate interpenetration by diffusive mixing after travelling this distance. Otherwise, the theoretical limit $\Gamma_{ss}^{exp} \to 1$ would have been attained at this distance had sufficient residence time been allowed in the capillary for molecular diffusion to smooth out further the transverse concentration disparities.[29] This shortfall in mixing index is large enough to highlight the influence of magnetic field stimulation in the mixing process. Specifically, the recapture of complete mixedness was evaluated by abruptly switching flow from Re = 10 to Re = 0 (stop flow) and by comparing the mixing times and mixing index dynamics with and without magnetic field following the magnetic-field-free steady-state inflow period.

It is convenient to rescale the mixing index according to Eq. 3 to enable comparisons for different experimental conditions over the same normalized interval after flow interruption, *i.e.*, $\hat{\Gamma}_{tr}^{exp} = 0$ at $t = 0$, until complete inter-layer mixing was achieved, *i.e.*, $\hat{\Gamma}_{tr}^{exp} \to 1$ as $t \to \infty$. Also, the diffusion time scale, R^2/D, based on water self-diffusion coefficient ($D = 2.4\times10^{-9}$ m^2·s^{-1}) and capillary radius was used for time normalization. Dynamics of the rescaled mixing index, $\hat{\Gamma}_{tr}^{exp}$, immediately after flow suppression is illustrated in Figure 1.3 as a function of dimensionless time to highlight the role of pure diffusion, if it were alone to operate 3 cm downstream of the T-junction, to homogenize the species concentrations across the 1 mm diameter capillary in absence of RMF. Also, rendition of the transient mixing index assuming one-parameter first-order dynamics (solid line in Figure 1.3) captures very well the purely diffusive mixing in the henceforth stagnant ferrofluid until achievement of complete mixing ($\hat{\Gamma}_{tr}^{exp} \to 1$).

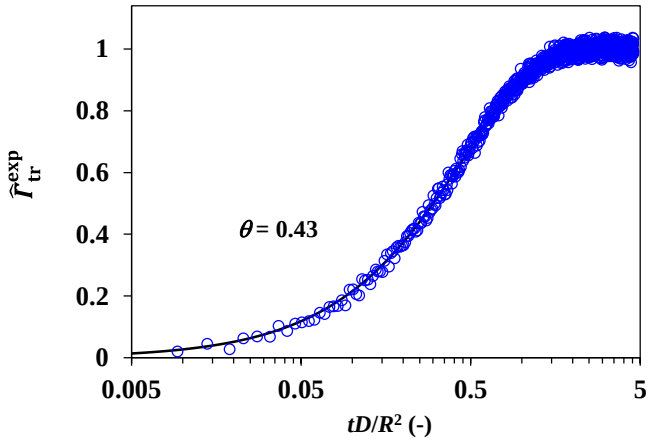

Fig 1.3 Evolution of transient magnetic-field-free response of scaled mixing index after flow interruption measured 3 cm downstream of the T junction (φ = 0.001). Solid line shows fit from a first-order dynamic model, $1 - e^{-\frac{tD}{R^2\theta}}$, with dimensionless time constant θ = 0.43.

As an example, the adjusted dimensionless time constant (θ = 0.43) echoes the contribution of pure diffusion to attain homogeneity for ferrofluids with MNP volume fraction φ = 0.001 (Figure 1.3). However, increasing MNP volume fractions up to 0.004 resulted in the same master curve of scaled mixing index (Figure 1.3) corresponding to one unique dimensionless time constant θ = 0.43 for the geometry and conditions under consideration. This finding highlights the fact that the presently tested dilute ferrofluids exhibited sufficient colloidal stability up to 0.004 MNP volume fractions to avert formation of aggregates or clusters that could have otherwise altered the diffusion phenomena during the transient mixing experiments.[34] It also suggests that as long as the external magnetic field is off, Brownian agitation by the nanoparticles does influence neither the solvent self-diffusion, *i.e.*, reaction product, nor any other scalar's diffusion.

In a second series of experiments, a magnetic-field-free steady-state inflow period similar to the above has first been set (I_{ss}^{exp} = 0.23 at 3 cm downstream of the T-junction, Re = 10). With a difference that upon switch-off of the ferrofluid feeds, a non-Fickian transverse mixing was elicited by concomitant activation of a rotating magnetic field. Dynamics of the rescaled mixing index immediately after flow suppression is inquired in terms of the influence of RMF frequency, f (figures. 4a,b), and MNP volume fraction, φ (figures. 4c,d).

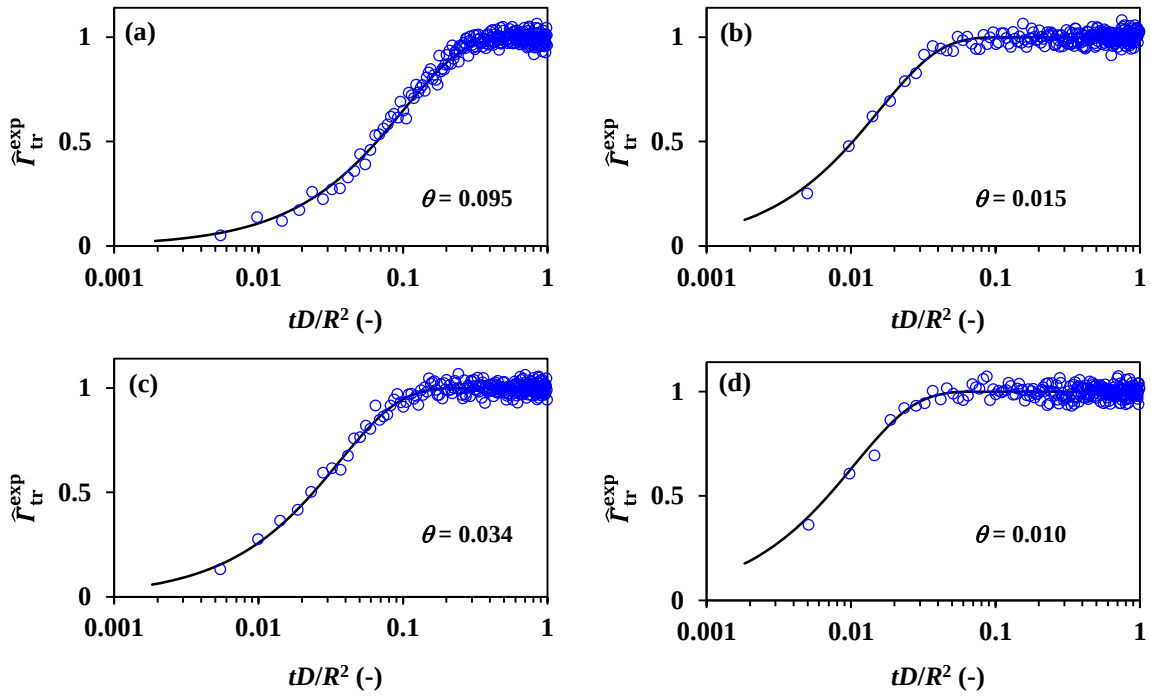

Fig 1.4 Evolution of transient response of scaled mixing index after flow interruption and RMF activation measured 3 cm downstream of the T junction: f = 50 Hz/ φ = 0.001 (a); f = 200 Hz/ φ = 0.001 (b); f = 100 Hz/ φ = 0.002 (c); f = 100 Hz/ φ = 0.004 (d). Solid lines show fit from a first-order dynamic model, $1 - e^{-\frac{tD}{R^2\theta}}$, with dimensionless time constants θ = 0.095 (a); θ = 0.015 (b) θ = 0.034 (c) θ = 0.010 (d).

In all four cases, the fitted dimensionless time constants, θ, were significantly lower in comparison to the RMF-free mixing case (Figure 1.3). Virtually, complete mixing of the two ferrofluid streams was achieved more rapidly by increasing either RMF frequency (figures. 4a,b): f = 50 and 200 Hz (φ = 0.001) or MNP volume fractions (figures. 4c,d): φ = 0.002 and 0.004 (f = 100 Hz). A 4-fold increase of RMF frequency at MNP volume fraction (φ = 0.001) resulted in more than a 6-fold contraction of the mixing characteristic time from θ = 0.095 to θ = 0.015. Whereas doubling MNP volume fraction from 0.002 to 0.004 at constant RMF frequency (f = 100 Hz) shortened the mixing characteristic time by more than a factor three from θ = 0.034 to θ = 0.010.

Despite the imposed Re = 0 condition inside the capillary, RMF intensification of the mixing dynamics is indisputable. Magnetophoretic translational movement of MNP followed by entrainment of the carrier fluid cannot be viewed as a plausible transport mechanism.[36] Also, the argument that spatial non-uniformity of RMF inside the capillary would give rise to radially or azimuthally directed

Kelvin forces is equally unsound considering the negligible spatial inhomogeneity of the magnetic field as discussed in Section 1.3.2. Therefore, such intensification can be pictured as if the magnetic nanoparticles were to act in some sort of tiny impellers. The number of stirrers, via increased MNP volume fraction, and/or their rotational speed, *via* increased RMF frequency, contribute/s to mix and homogenize the ferrofluid streams much faster than without RMF activation had molecular diffusion been the only transport mechanism to even out species concentrations ($\theta = 0.43$, Figure 1.3). The fact remains that without attempts to identify and articulate the proper mechanisms underlining the mixing observations into a physically-sound theoretical treatment; interpretations of above experiments would merely boil down to naïve and perhaps even a fantasized picture. Of specific interest for this study was an aim to highlight whether ferrofluid spin-up flow, as a *macroscopic* advection mechanism brought about by the magnetic field at Re = 0, could (or not) be at the origin of the RMF-aided MNP-driven fluid mixing in the capillary. And in the eventuality that spin-up flow is insignificant, what alternate mechanism(s) should be checked out and with what theoretical and practical implications, *hitherto* unforeseen, for the anomalous diffusive mixing resulting from magnetic field enhancement at Re = 0?

1.5.3. Assessment of spin-up flow via FHD simulations

The discussions to follow, relating to the fate of ferrofluid flow after stop-flow RMF excitation was set, are valid for all the tested MNP volume fractions and RMF frequencies. For argument's sake, FHD simulations of the ferrofluid with volume fraction $\varphi = 0.002$ subject to $f = 200$ Hz rotating magnetic field were largely analyzed with an aim at evaluating the role of spin-up flow on transverse scalar mixing. Specifically, the ferrofluid azimuthal linear velocity, v_θ, and the MNP longitudinal angular velocity, ω_z, components are the most decisive FHD model outputs to scrutinize in light of the experimental transverse mixing observations. The shadow of uncertainty surrounding which value of spin viscosity, η', to use, as this has been assigned astonishingly disparate values in the literature, was addressed in terms of sensitivity analysis of FHD predicted outputs for a lower and an upper η' limits. The lower-limit spin viscosity, *i.e.*, $\eta' = 10^{-17}$ kg·m·s^{-1}, estimated according to $\eta' = \eta d^2(\pi/6\,\varphi)^{2/3}$, is considered as a standard value in ferrofluid simulations.[3] However, an upper limit was also proposed, which in consideration of water-based ferrofluids composed of cobalt ferrite nanoparticles can be assigned the value $\eta' \approx 10^{-8}$ kg·m·s^{-1}.[17]

1.5.3.1. Role of ferrofluid azimuthal velocity on convective mixing

Ferrofluid advection driven by magnetic fields is influenced by forces stemming from the asymmetric stresses (Eq. 8) and by the Kelvin body force (Eq. 11). Because asymmetric stresses are specific to

micro-polar fluids with internal rotation, their contribution in the force balance cannot be ignored. Hence, to help rationalizing the capillary geometry under study, it is expedient to linger over the dimensionless formulation of the ferrohydrodynamic model. The ratio of forces from asymmetric stresses to inertial forces, shown in the linear momentum balance Eq. 21 as $2\zeta/\rho\Omega R^2$, is comparable in magnitude to the spin-up Reynolds number, $(\eta + \zeta)/\rho\Omega R^2$. This is due to the fact that the vortex viscosity is a linear function of the ferrofluid viscosity with a slope of 1.5 φ. These two ratios as well as the magnetic-to-inertial-forces ratio, *i.e.*, $\mu_0 H_0\ \varphi M_d/\rho\Omega^2 R^2$, in the linear momentum balance (Eq. 21) are independent of spin viscosity. Therefore, the influence of spin viscosity on the convective spin-up flow is implicitly carried through the asymmetric term, $\underline{\tilde{\nabla}} \times \underline{\tilde{\omega}}$, which propagates the η' dependence borne in the internal angular momentum balance equation (Eq. 22) up to the linear momentum balance (Eq. 21).

Owing to the magnetic field orientation (Figure 1.1a), both axial and radial directions were predicted to be convectively inactive after stop-flow RMF excitation was imposed to the capillary (results not shown). Therefore, one should expect that spiral-like trajectories of the ferrofluid at Re = 0 would be a marker for the existence of spin-up flow. Sensitivity of spin-up flow to spin viscosity was first assessed in terms of simulated ferrofluid azimuthal velocity at Re = 0. Escalating spin viscosity by nine orders of magnitude slowed down the azimuthal velocities by *ca*. two orders of magnitude (Figure 1.5a) with a tendency of the peak velocity to pull away from the capillary wall. However, casting the tangential velocities in the form of Péclet numbers using capillary radius and water self-diffusion coefficient, revealed that the convective tangential FHD effects at Re = 0 mostly remain of comparable strength with molecular diffusion of the ferrofluid solvent despite spin viscosity swept so broad an interval (Figure 1.5b).

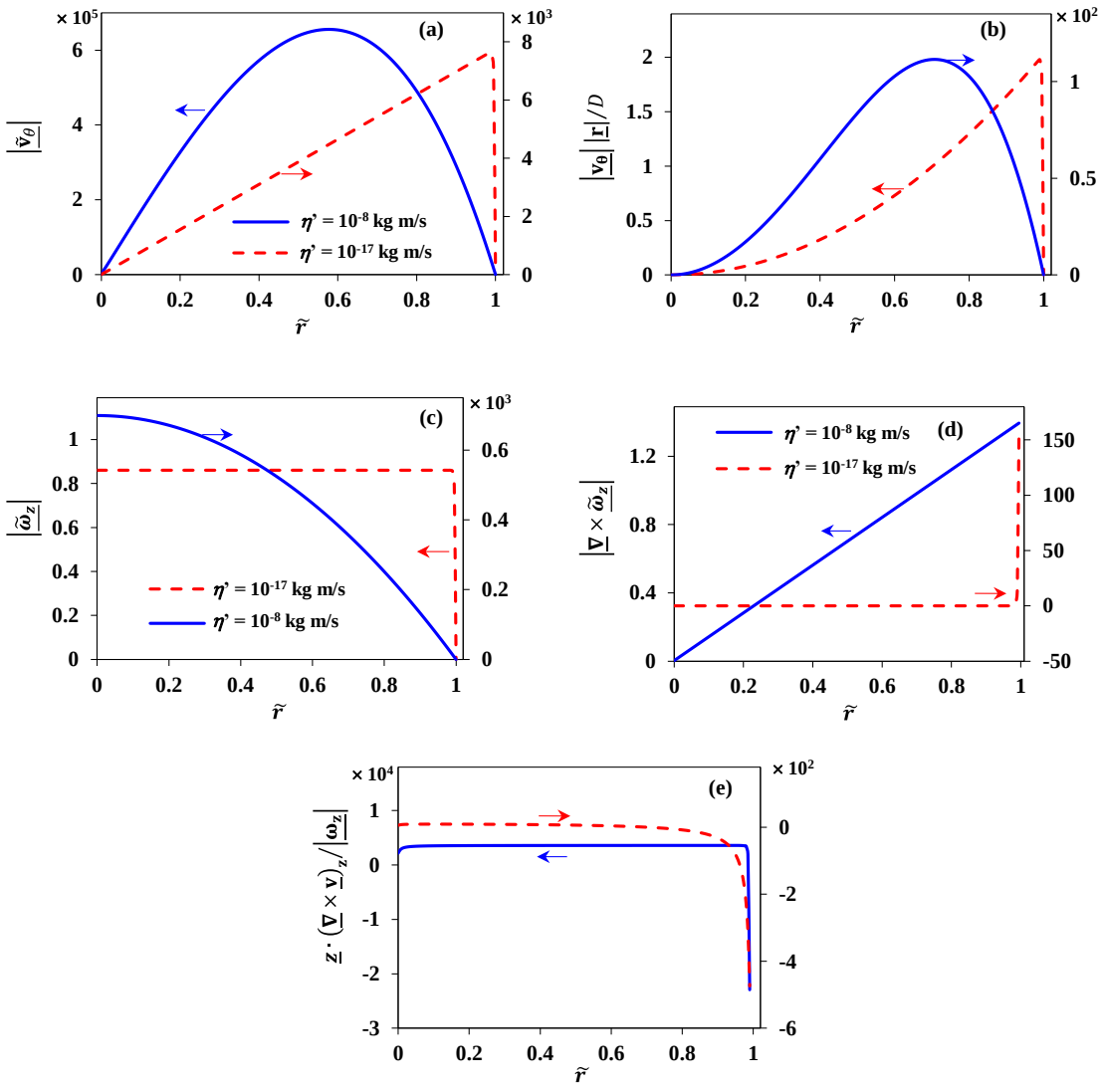

Fig 1.5 Sensitivity to spin viscosity of ferrofluid radial profiles of (a) scaled linear azimuthal velocity, (b) azimuthal Péclet number, (c) MNP axial angular velocity, (d) asymmetric-stress *z*-projection, (e) ratio of ferrofluid *z*-component vorticity to MNP axial angular velocity in the presence of RMF (f = 200 Hz, φ = 0.002).

Rinaldi and coworkers[17] have shown that using the standard value of spin viscosity in the FHD model deplorably failed to predict the measured ferrofluid tangential velocities and corresponding spin-up flow for their cm-scale cylindrical geometry. They advocated increasing spin viscosity to reinforce spin-up flow by promoting the ferrofluid tangential velocities. Only if the upper limit of spin viscosity was used that their experimentally observed spin-up flow could be predicted with consequentially higher tangential velocities. However, two key discrepancies are exposed in our ferrofluid capillary simulations at Re = 0 after increasing spin viscosity form 10^{-17} to 10^{-8} kg m s^{-1}. On the one hand,

strengthening of spin-up flow by increasing spin viscosity is not systematic but probably scale-dependent as revealed by exactly the opposite trend at our capillary scale (Figure 1.5a). On the other hand, because of the vanishingly small tangential velocity components (Figure 1.5b) predicted over a very broad range of spin viscosities, RMF excitation of ferrofluids confined to sub-mm scales at Re = 0 was unable to generate meaningful convective mixing in the transverse direction. Hence, FHD simulations preclude any significant role to be played by a convective spin-up flow mechanism to enhance transverse mixing in the capillary thus failing to support our mixing index measurements (Figure 1.4).

1.5.3.2. Role of MNP angular velocity on diffusive mixing

Alternatively, in order to substantiate the role of rotating nanoparticles in *diffusively* enhancing transverse mixing in the capillary, the impact of spin viscosity on RMF-driven MNP angular velocity is addressed next. Radial profiles of the longitudinal component of the MNP angular velocity or spin rate, $\underline{\boldsymbol{\omega}_z}$, normalized with respect to RMF angular frequency, $\Omega = 2\pi f$, showcase noticeable differences in shape and magnitude (Figure 1.5c) depending on spin viscosity. Such dissimilarity with remarkably different magnitudes for $\underline{\boldsymbol{\omega}_z}$ pleads for tangential velocities (Figure 1.5a) and asymmetric stresses (Figure 1.5d) also depending on spin viscosity as anticipated in the previous section.

At the higher spin viscosity limit, the MNP spin rate profile is parabolic and remains virtually diffusive across the capillary (Figure 1.5c). The corresponding radial profile of the asymmetric-stress *z*-projection (Figure 1.5d) varies linearly with the capillary radial coordinate giving rise to the parabolic profile of tangential velocity (Figure 1.5a). Also, the MNP angular velocity is several thousand times smaller than the imposed RMF angular frequency (Figure 1.5c). This finding implies that, in spite of an active RMF at high η', the nanoparticles behave as an idle ensemble whose rotation appears to be in effect blocked by tremendous spin viscosity excluding notable diffusive mixing effects to be gained from the MNP rotation. The ferrofluid merely reduces to a stagnant classical suspension where both fluid vorticity at Re = 0 and spin rate are virtually muzzled (Figure 1.5e). Therefore, the physical justification for the higher spin viscosity limit to prevail becomes highly questionable as neither convective mixing *via* spin-up flow (Figure 1.5a) nor diffusive mixing *via* MNP rotation (Figure 1.5c) can be invoked to interpret the experimental findings of enhanced mixing in our capillary tests (Figure 1.4).

At the lower spin viscosity limit, MNPs are able to rotate relatively freely. The scaled angular velocity, $\underline{\widetilde{\boldsymbol{\omega}}_z}$, was predicted by FHD model to reach *ca*. 86% of the angular frequency of the magnetic field (Figure 1.5c) for most of the capillary cross-section except for an abrupt decline to zero in a

narrow wall region. This finding identifies diffusive mixing stemming from rotating nanoparticles as a possible non-spin-up flow mechanism for stimulating transverse mixing provided the standard spin viscosity is adopted in FHD simulations. In the lower spin viscosity limit, excepting the wall, absence of asymmetric stresses virtually throughout the entire capillary cross-section is worth noticing (Figure 1.5d). However, the order-of-magnitude analysis of $\underline{\widetilde{\boldsymbol{\nabla}}} \times \underline{\widetilde{\boldsymbol{\omega}}}$ (Figure 1.5d) sheds light on why lower azimuthal velocities (Figure 1.5a) accompany augmented spin viscosity as a result of increased forces, albeit tiny, from the asymmetric stresses. Nevertheless, the virtually absent convective effects (Figure 1.5a) translate into practically meaningless ferrofluid vorticities when these come to be compared to the MNP angular velocities (Figure 1.5e).

1.5.3.3. Kelvin body force

Subsequent to the discussion on the asymmetric stresses *via* spin viscosity (Figure 1.5d), the contribution of the Kelvin body force is worth analyzing. The fact that the ratio of magnetic to inertial forces ($\mu_0 H_0 \varphi M_d / \rho \Omega^2 R^2$) scales as $1/R^2$ would at first glance imply that more prominent magnetic body forces are to manifest the smaller the capillary length scale. This would result in enhancement of scalar transport at microscales.[35]

Straightforward tensor/vector algebra (Appendix 1) allows rewriting the magnetic force density in the form:

$$\underline{\mathbf{F}}^m = \mu_0 \underline{\mathbf{H}} \left(\underline{\boldsymbol{\nabla}} \cdot \underline{\mathbf{H}} \right) \tag{1.31}$$

Figure 1.6a indicates that the radial profile of $\left| \underline{\mathbf{F}}^m \right|$ follows a trend similar to $\underline{\widetilde{\boldsymbol{\omega}}_{\mathbf{z}}}$ implying that magnetization can be perturbed by hydrodynamic effects related to spin viscosity. However, analysis of the ratio K_1 of magnetic force to the total forces stemming from symmetric and asymmetric viscous stresses in azimuthal direction:

$$K_1 = \frac{\underline{\boldsymbol{\theta}} \cdot \left(\underline{\boldsymbol{\nabla}} \cdot \underline{\underline{\mathbf{T}}}^m \right)}{\underline{\boldsymbol{\theta}} \cdot \left(\underline{\boldsymbol{\nabla}} \cdot \underline{\underline{\mathbf{T}}} \right)} \tag{1.32}$$

reveals the marginal contribution of Kelvin force in the momentum balance for both upper and lower limit spin viscosities (Figure 1.6b). Excepting the wall boundary condition, K_1 ratio is virtually close to zero for both spin viscosity cases to also conclude for a negligible role of magnetic force in spin-up flow. Alternatively, part of the internal angular momentum driven by magnetic body couples converts to external angular momentum with the remainder is diffusively dissipated by the couple stresses which depend on spin viscosity. However, the linear momentum generated from the

asymmetric stresses is in total balance with the viscous dissipation due to shear viscosity of the ferrofluid on account of the negligible contribution of the magnetic body force to the linear momentum balance.

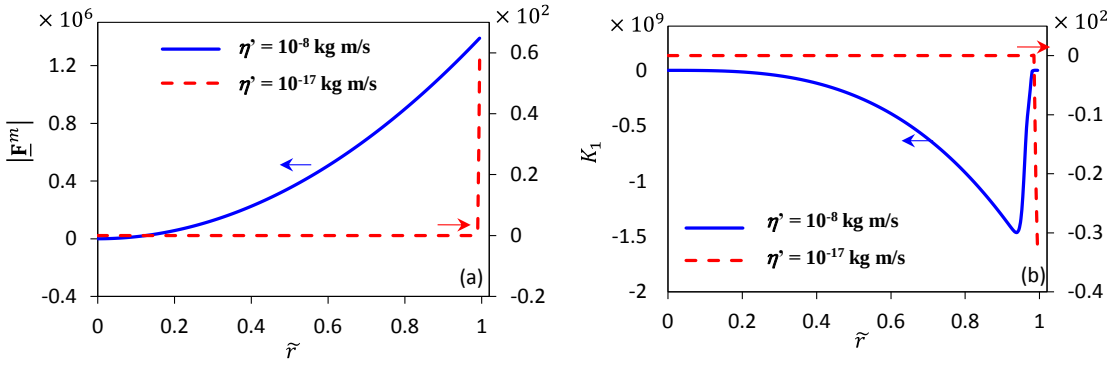

Fig 1.6 Radial distribution of magnetic body force (a) and ratio of magnetic body force to total force from symmetric and asymmetric stresses (b) in presence of RMF (f = 200 Hz, φ = 0.002).

1.5.3.4. Magnetization

It is worth reminding that the predictions of spin diffusion theory were mainly validated in the limit of low-field intensities where expression of the saturation magnetization as a linear function of applied field is valid.[17] At higher intensities, different equations of magnetization relaxation predict magnetoviscous phenomena with different characteristics.[9] However, in the limit of a Brownian relaxation setting much faster than the RMF period ($\Omega\tau$ << 1), which is largely satisfied in our investigated conditions, the equations of magnetization relaxation predict almost similar results.[9] Hence, our approach in using high-magnetic field intensities eliminates skepticism on the accuracy of implementing classical magnetization relaxation equation and its plausible influence on the velocity fields.

Numerical solution of FHD allows interpretation of the dynamic behavior of the magnetization vector, and in particular its orientation with respect to external rotating magnetic field. In addition, adequacy of the scaling factors used for the body couple density can also be verified through analysis of the lag angle between **M** and **H**. Near zero magnetic body force, as just established above, echoes uniform distribution of **M** resulting from small perturbations of the equilibrium magnetization. This alternatively points toward the fact that hydrodynamic effects from angular and linear velocities are not strong enough to perturb **M** so that the magnetization vector must inevitably keep tracking the external rotating magnetic field at an identical frequency. This expectation is evidenced from analysis

of the lag angle between **M** and **H** which confirms a very slight phase shift by less than 1° for both simulated limiting spin viscosity values (Figure 1.7a). Furthermore, had the dimensionless characteristic time $\Omega\tau$ been appropriate for scaling sin(β) then the scaled magnetic body couples would have been in the order of unity (Figure 1.7b). This would have implied fulfillment of the condition $\mu_0 H_0 \varphi M_d \tau / 4\zeta \longrightarrow 0$ and which appears not to be the case in our conditions.

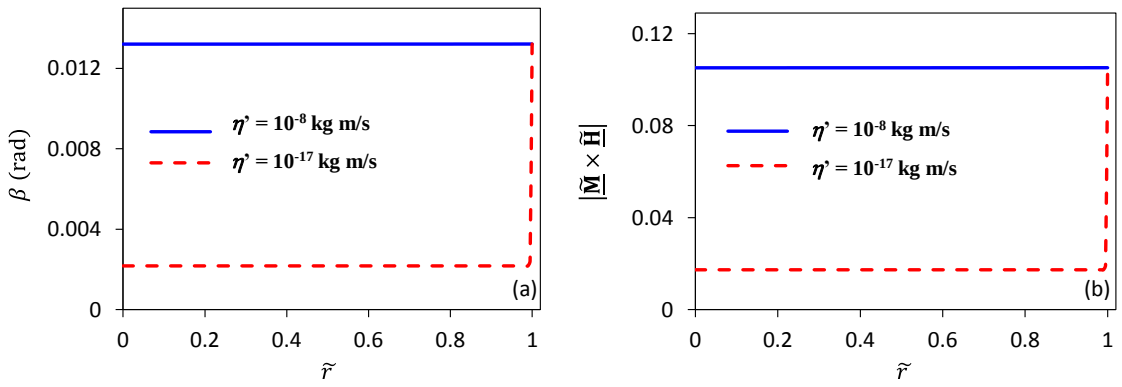

Fig 1.7 Radial distributions of lag angle between magnetic field and magnetization vectors (a) and scaled magnetic body couple (b) in presence of RMF (f = 200 Hz, φ = 0.002).

The small perturbation of magnetization from equilibrium is mathematically consistent with the phenomenological model of relaxation since $\tilde{\boldsymbol{\omega}} \times \tilde{\mathbf{M}}$ scales with $\Omega\tau < 1$. Consequently, the dynamics of $\tilde{\mathbf{M}}$ is mainly governed by the Brownian relaxation expressed in the second term of Eq.25 RHS rather than from hydrodynamic perturbations. When η' = 10^{-8} kg m s^{-1}, the frequency of the Brownianly-relaxing rotating magnetic nanoparticles or equivalently their magnetic moments –which are locked within MNP– was predicted to be drastically silenced as compared with the RMF angular frequency (Figure 1.5c). This behavior is bluntly inconsistent with the predicted quasi-collinearity of the magnetization vector with the rotating magnetic field (Figure 1.7a) which implies rotation of the former at quasi diapason with the latter. From a physical point of view, this result seems to be odd in consideration of the fact that the magnetization vector represents an average of the magnetic moment vectors of the suspended nanoparticles per unit volume of the colloidal suspension. Such contradiction is virtually lifted had the standard (lower limit) spin viscosity been used (Figure 1.5c). It is finally worth reminding that experimental validation of spin diffusion theory down to the micro length scales as explored in our study has *hitherto* been ignored. Nevertheless, we take the predictive role of FHD for granted in the calculation of the macroscopic flows, inclusive of their spin-up flow component, and pursue our analysis of the mixing experiments to predict the anomalous diffusion highlighted in Figure 1.4.

1.5.3.5. RMF frequency and MNP concentration

The peak azimuthal velocities, $v_{\theta max}$, plotted as a function of RMF frequency, f, and MNP volume fraction, φ, are shown in Figure 1.8.

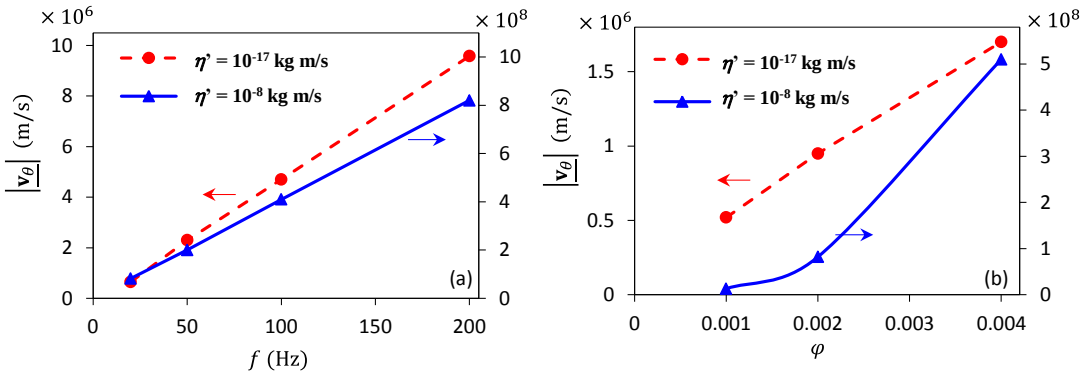

Fig 1.8 Variation of azimuthal velocity maxima in presence of RMF (a) as a function of RMF frequency (φ = 0.002) and (b) MNPs volume fraction (f = 200 Hz).

At constant MNP fraction, $v_{\theta max}$ increases linearly with RMF frequency (Figure 1.9a) with an expected tendency to be lower, typically by the same two orders of magnitude as observed above (Figure 1.5a), the larger the spin viscosity. The linear behaviour of $v_{\theta max}$ with respect to φ is observable only for $\eta' = 10^{-17}$ kg m/s (Figure 1.8b). These simple behaviors can be rationalized from analysis of the linear and angular momentum balance, and magnetization transport equations (Eqs. 21-23). At very low values of spin viscosity, the internal angular momentum balance equation (Eq. 22) reduces to:

$$3\eta\left(\underline{\tilde{\nabla}} \times \underline{\tilde{\mathbf{v}}} - \mathbf{2}\underline{\tilde{\boldsymbol{\omega}}}\right) = -\mu_0 H_0 M_d \tau \underline{\tilde{\mathbf{M}}} \times \underline{\tilde{\mathbf{H}}} \tag{1.33}$$

Eq. 33 is independent of η' and φ. Considering negligible dependence of viscosity of dilute colloids on φ, Eq. 33 yields $\underline{\tilde{\boldsymbol{\omega}}}$ as a function of RMF intensity. Since Eq. 23 is also independent of φ, Eq. 21 predicts tangential velocity to scale linearly with MNP volume fraction.

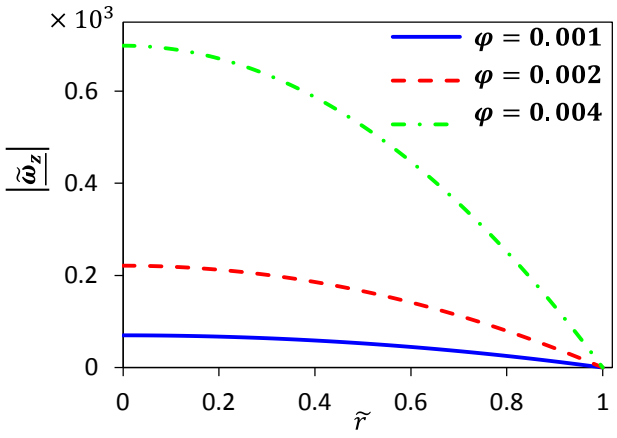

Fig 1.9 Radial distribution of scaled axial internal angular velocity in presence of RMF (f = 200 Hz) for different MNP volume fractions.

At higher spin viscosity, $v_{\theta max}$ is a nonlinear function of φ (Figure 1.8b). Since the contribution of spin diffusion in internal angular momentum balance is not excluded at higher η', Eq. 22 maintains a dependency with respect to φ. Likewise, the radial profile of $|\underline{\tilde{\boldsymbol{\omega}}_z}|$ as a function of φ (Figure 1.9) reflects a consistent dependency with respect to MNP volume fraction. Consequently, $\underline{\tilde{\nabla}} \times \underline{\tilde{\boldsymbol{\omega}}}$ must be φ-dependent leading to $|\underline{\tilde{\mathbf{v}}}|$ from Eq. 21 to become a nonlinear function of φ (Figure 1.8b). In spite of the rotationally slowed down MNPs due to high spin viscosity value, the FHD simulations predict counter-intuitively increased MNP angular velocities with increasing MNP volume fractions.

The FHD framework predicts promotion of ferrofluid advection as MNP concentration or RMF frequency is increased for both spin viscosity limits. However, one has to be cautious that although these trends appear to align qualitatively with the experimentally observed dynamics of the transverse mixing indices in response to f and φ changes (Figure 1.4), they do not sustain sufficiently strong convective effects in favor of an efficient spin-up flow.

1.5.3.6. Scale effect and spin-up flow

The elements of understanding drawn from above FHD simulations tend to disqualify spin-up flow as being a major mechanism behind the enhanced mixing measurements. In that respect, inflating spin viscosity above its standard value in an attempt to increase tangential velocities revealed effectless. We will now examine to which extent the capillary length scale may have upset the antagonism between convective mixing *via* $\underline{\mathbf{V}_\theta}$ and diffusive mixing *via* $\underline{\boldsymbol{\omega}_z}$, leaning towards prevalence of the latter at the expense of the former at a small scale. For the purpose of illustration, the influence of scale dependency is assessed in terms of radial profiles of angular and azimuthal

velocities at three capillary radii: R (= 0.5 mm), 10R and 100R for η' = 10^{-8} kg·m·s^{-1} (figures. 10a,b) and η' = 10^{-17} kg·m·s^{-1} (figures. 10c,d).

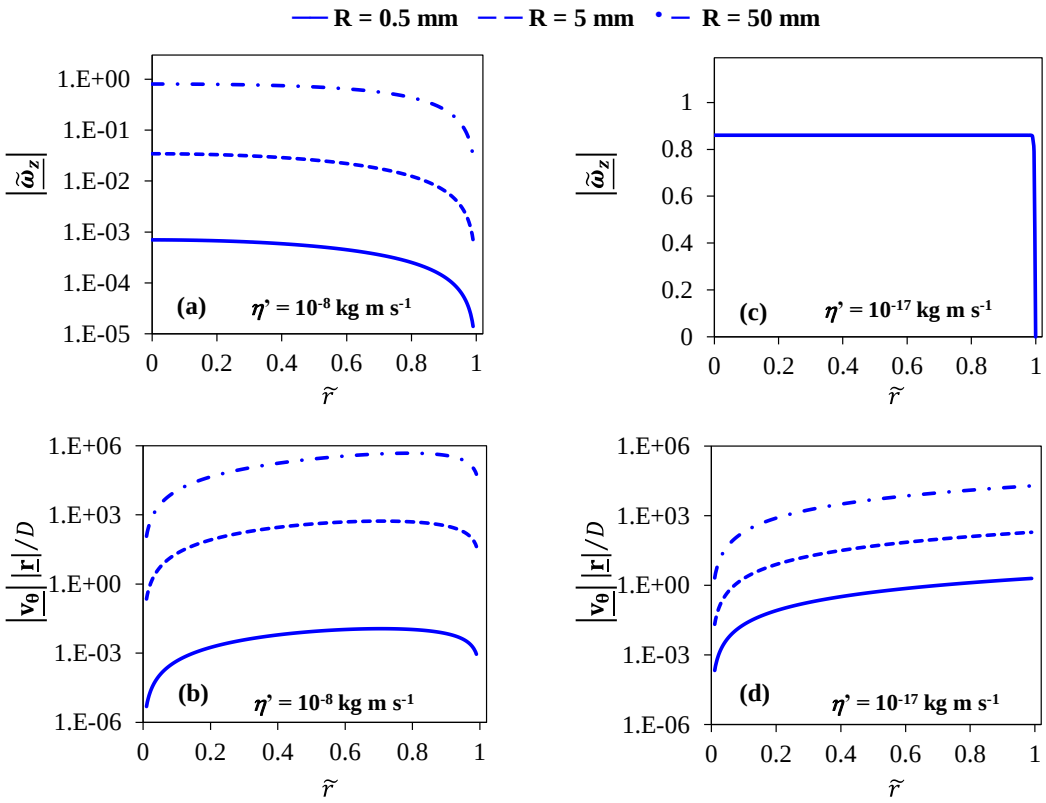

Fig 1.10 Sensitivity to channel size and spin viscosity of ferrofluid radial profiles of (a,c) MNP axial angular velocity, (b,d) azimuthal Péclet number in the presence of RMF (f = 200 Hz, φ = 0.002).

At the higher spin viscosity limit, enlargement of capillary radius by a factor 100 tended to inflate the MNP angular velocity by more than three orders of magnitude reaching, for the biggest channel, an upper limit nearing *ca*. 81 % of the angular frequency of the rotating magnetic field (Figure 1.10a). Nanoparticles rotating with frequencies very close to RMF frequency for the larger capillaries would certainly have resulted in a meaningful contribution of dispersive mixing. Correspondingly, escalation of the azimuthal velocity as predicted by the FHD model is even more significant as indicated by the huge Péclet numbers reached from increasing capillary radius to 5 mm and then to 50 mm (Figure 1.10b). As pinpointed by Rinaldi and coworkers,[17] as far as tangential velocity is concerned, its trend is coherent with the significant reinforcement of spin-up flow the larger the capillary size.

At the lower spin viscosity limit, the radial profiles of the longitudinal angular velocity are indifferent to channel scale (Figure 1.10b). MNPs can rotate fairly freely approaching for most of the capillary

cross-section *ca*. 86% of the RMF angular frequency. The contribution of dispersive mixing through rotating nanoparticles is omnipresent and constant regardless of scale. However, the tendency for spin-up flow through its ferrofluid tangential velocity is to gain in importance with increased capillary size (Figure 1.10d). Spin-up flow follows gradation with channel scale similar to FHD simulations with $\eta' = 10^{-8}$ kg·m·s^{-1}, though leading to lower tangential velocities (figures. 10b,d).

In summary, if spin viscosity $\eta' = 10^{-8}$ kg·m·s^{-1} were to prevail, increasing channel scale would have actuated both convective and dispersive mixing to play significant roles (figures. 10a,b) in the capillary transverse mixing. Nevertheless, the fact that none of these two mechanisms has been active for R = 0.5 mm capillary (figures. 5a,c) casts doubts on the legitimacy of the higher spin viscosity limit in microgeometry ferrofluid flows. On the contrary, adopting the standard spin viscosity in FHD simulations sparks conflicts neither with the enhanced mixing observations at the smaller capillary scale upon RMF excitation nor with the extra mixing to be gained from an additional convective contribution to reinforce spin-up flow upon scale enlargement. Furthermore, for Brownianly-relaxing magnetic nanoparticles, the standard spin viscosity led to consistent predictive behaviors for MNP angular velocity and for the quasi-collinearity of rotating magnetic field and magnetization vectors.

1.5.4. FHD model confrontation to mixing index experiments

1.5.4.1. Failure of isotropic diffusion tensor

The experimental transient response of the rescaled mixing index under RMF excitation at f = 200 Hz and φ = 0.004 is confronted to the solution of the advection-diffusion equation (Eq. 29) using the FHD-computed velocity field. For this set of RMF frequency and MNP concentration, the highest azimuthal linear velocities were predicted by the FHD model (Figure 1.8). Since the transport of scalars occurs in the interstitial (non-magnetic) carrier fluid, one first scenario was hypothesized in which an isotropic diffusion tensor (Eq. 30) based on the water self-diffusion coefficient was used in the numerical simulations. Of course, this assumption ignores the fact that magnetic nanoparticles rotating under the action of RMF bring about nanoparticle-level motion which cannot presently be resolved by current FHD models.

Definitely, the duration for establishment of the mixing index plateau predicted by FHD is not in accordance with the observed trend of mixing index. FHD simulations in this case predict mixing time before achieving complete mixing much longer than the one determined experimentally (Figure 1.11). This is due to the sluggish spin-up flow (figures. 5,8) which leads to an insignificant $\underline{\nabla} \cdot \left(\underline{\mathbf{v}} C_i^r\right)$ term *vis-à-vis* the diffusion term in Eq. 29 if the in-fluid extra-diffusive effects due to nanoparticles' rotation are ignored. The mixing index simulations concur to a lack of sensitivity by the model to

both magnetic field excitation and spin viscosity level (Figure 1.11). Hence without meaningful spin-up flow effects, molecular diffusion alone fails to explain the measured mixing index dynamics.

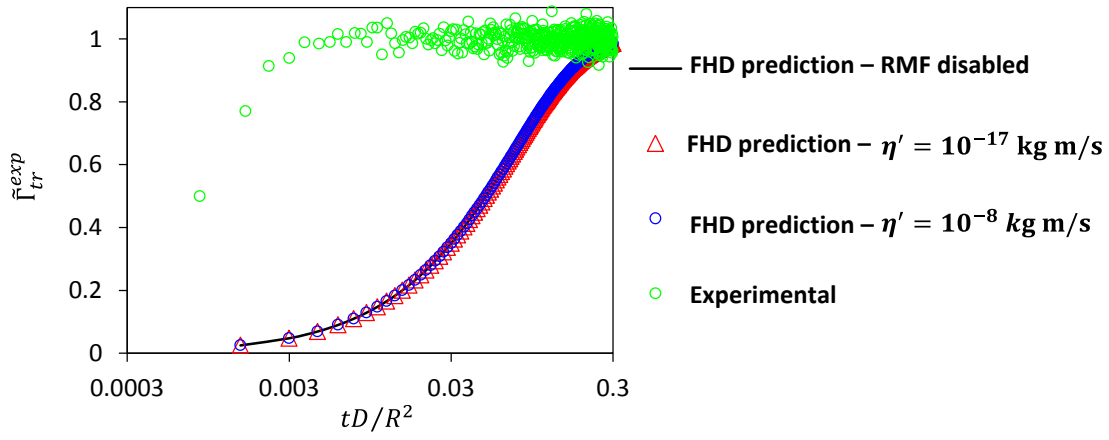

Fig 1.11 Experimental and simulated transient response of scaled mixing index with and without RMF excitation (f = 200 Hz, φ = 0.004).

Although the spin rate of individual MNP has *hitherto* not been measured directly, measurements of the magnetization vector under low-frequency RMF unveiled that its rotational dynamics is similar to the applied rotating magnetic field.[37,38] As the magnetic moment of the cobalt-ferrite nanoparticles in Brownian ferrofluids keeps locked within the nanoparticle crystal structure, MNPs rotating close to the RMF frequency would be highly plausible as predicted from above FHD simulations using the standard spin viscosity (Figure 1.5c). Hence, MNP rotation would invalidate prevalence of molecular diffusion transport in the carrier fluid by virtue of the non-slip boundary condition on the MNP surface. The entrained fluid around MNP should plausibly give rise to circumferential micro-convective phenomena in the interstitial fluid thus substantially influencing the transfer rate of scalars which the advection-diffusion equation (Eq. 29), using an isotropic tensor, fails to capture. Unfortunately, these circumferential micro-convective phenomena are not resolved in the current FHD formulation preventing fully predictive capabilities for the anomalous anisotropic effective diffusion coefficients induced by the longitudinal component of the MNP angular velocity (Figure 1.5c). A rigorous mathematical description of this phenomenon is beyond the scope of the present study which in itself represents a formidable task left to theoreticians and future research works. Nevertheless, we will show next that scalar transport in ferrofluids governed by dispersive mixing, instead of spin-up flow (convective) mixing, as alluded to it above is indeed anisotropic in nature and also sensitive to external RMF.

1.5.4.2. Determination of effective diffusivity tensor

We assume that the transport of scalars still obeys Eq. 29 by now replacing the components of diffusivity tensor by effective diffusivities in radial, azimuthal and axial directions:

$$\underline{\underline{\mathbf{D}}}^{\boldsymbol{e}} = \begin{bmatrix} D_{rr}^{e} & 0 & 0 \\ 0 & D_{\theta\theta}^{e} & 0 \\ 0 & 0 & D_{zz}^{e} \end{bmatrix} \tag{1.34}$$

This tensor is meant to represent transport of scalars *via* the combined action of molecular diffusion and so-called micro-convective phenomena induced by RMF in the interstitial fluid by the rotating magnetic nanoparticles. Because of the negligible contribution of spin-up flow in the transport of scalars (Figure 1.11), both radial and azimuthal components of effective diffusivity have been assumed equal and lumped into one single effective diffusion coefficient, D_{tr}^{e}, to capture mass transport enhancement in the direction *transverse* to that of RMF rotation:

$$D_{rr}^{e} = D_{\theta\theta}^{e} = D_{tr}^{e} \tag{1.35}$$

Furthermore, on account of the arrangement of the capillary inside the magnet bore and resulting magnetic field orientation (Figure 1.1), the axial effective diffusive coefficient cannot be enhanced and therefore D_{zz}^{e} should stick close to the solvent molecular diffusion coefficient, D, whereas the convective axial velocity component is zero during the stop-flow RMF excitation. To prove this expectation, Figure 1.12a shows the experimentally measured transient tracer concentration response in the absence of RMF in axial diffusion experiment, following the pulse-injection quantification protocol of axial diffusive transport described in Section 1.3.5 for the modified setup illustrated in Figure 1.1b.

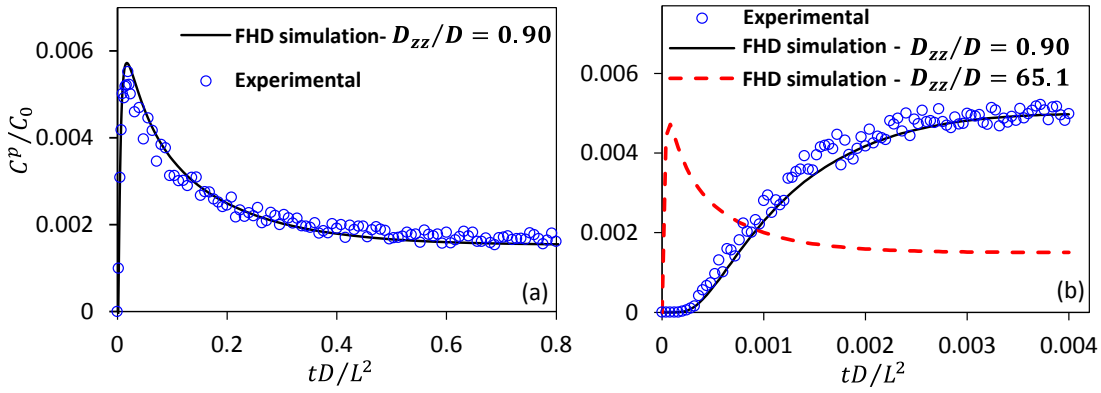

Fig 1.12 Experimental and calculated transient response of passive tracer concertation in (a) absence of RMF and (b) presence of RMF (f = 200 Hz, φ = 0.004).

The axial effective diffusive coefficient, D_{zz}^{e} = 0.90D, was fitted by minimizing the sum of quadratic residuals between the measured tracer concentration and the one predicted from solving Eq. 29 for species diffusion. This value is very close to the solvent diffusion coefficient which is to be expected as RMF is disabled. Similar fit for axial diffusion experiment in the presence of f = 200 Hz RMF is shown in Figure 1.12b for the same ferrofluid suspension (φ = 0.004). The concentration of tracer is measured in the first 2,000 second of experiment to avoid overheating of the magnet core which may influence the measurement accuracy of the conductivity probes. The solid line in Figure 1.12b shows the solution of advection-diffusion equation for D_{zz}^{e} = 0.90D proving that axial diffusion is not perturbed by the presence of magnetic field and confirming experimentally that RMF enhancement of scalar transport does not take place in the longitudinal capillary direction. To make sure that axial dispersion is idle under RMF excitation, the simulation has been repeated by assuming an isotropic effective diffusion corresponding to D_{zz}^{e} = 65.1D (= D_{tr}^{e}). This value, voluntarily taken as the highest D_{tr}^{e} value quantified in the case of transverse effective diffusion coefficient to be discussed next, predicts a diffusion profile (red dotted line) plateauing much more quickly than the observed one.

Let us therefore turn our attention to the quantification of the effective diffusion coefficient, D_{tr}^{e} in the transverse capillary plane. For each given experiment at fixed MNP volume fraction and RMF frequency, it is possible to optimize a single D_{tr}^{e} by minimizing the objective function $\left(\Gamma_{tr}^{cal} - \Gamma_{tr}^{exp}\right)^2$ following the same procedure as described for the axial effective diffusive coefficient, D_{zz}^{e}. The optimized D_{tr}^{e} values, scaled with respect to the solvent diffusion coefficient, are plotted in Figure 1.13 to demonstrate the influence of RMF frequency and MNP concentration.

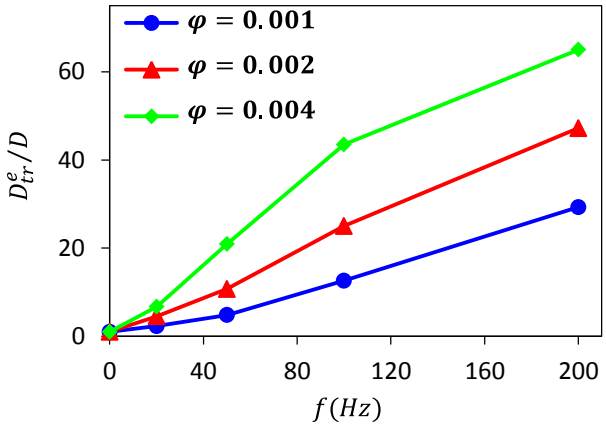

Fig 1.13 Transverse component effective diffusivity tensor as function of RMF frequency and MNP volume fraction.

The goodness-of-fit of the predicted dynamics of the rescaled mixing index in terms of the influence of RMF frequency, f, and MNP volume fraction, φ (figures. 14c,d) on the effective diffusivity tensor

can be appreciated from figures. 14a,b and figures. 14c.d, respectively. The effective diffusivities estimated from experimental mixing index experiments support the hypothesis of preferential enhancement of scalar transport in ferrofluid by local entrainment of fluid at nanometric scales in the transverse capillary plane. One may attribute the observed enhanced mass transport sensitivity to f and φ to the following postulated mechanism. The kinetic energy of spinning MNP is constantly counterbalanced by viscous dissipation in the sheared interstitial fluid. Since the kinetic energy of MNP depends on the squared angular velocity, higher RMF frequency intensifies elongation of sheared fluid inside the oblate spheroid[28] around individual spinning nanoparticles. The increase of D_{tr}^{e} with RMF frequency (Figure 1.13) also supports contraction of the mixing characteristic times from $\theta = 0.43$ (no RMF, Figure 1.3) to $\theta = 0.095$ (f = 50 Hz, Figure 1.4a) and $\theta = 0.015$ (f = 200 Hz, Figure 1.4b). At higher MNP concentration, more regions of the carrier fluid are involved in this elongation process ultimately resulting in smaller diffusion paths. Similarly, the increase of D_{tr}^{e} with MNP volume fraction (Figure 1.13) is coherent with the shortened mixing characteristic times under RMF excitation down to $\theta = 0.034$ (φ = 0.002, Figure 1.4c) and $\theta = 0.010$ (φ = 0.004, Figure 1.4d). Therefore, we may alternatively generalize our observation by stating that a uniform RMF enhances the scalars transport merely in the transverse direction to RMF rotation axis whilst RMF is neutral in terms of transport in axial direction.

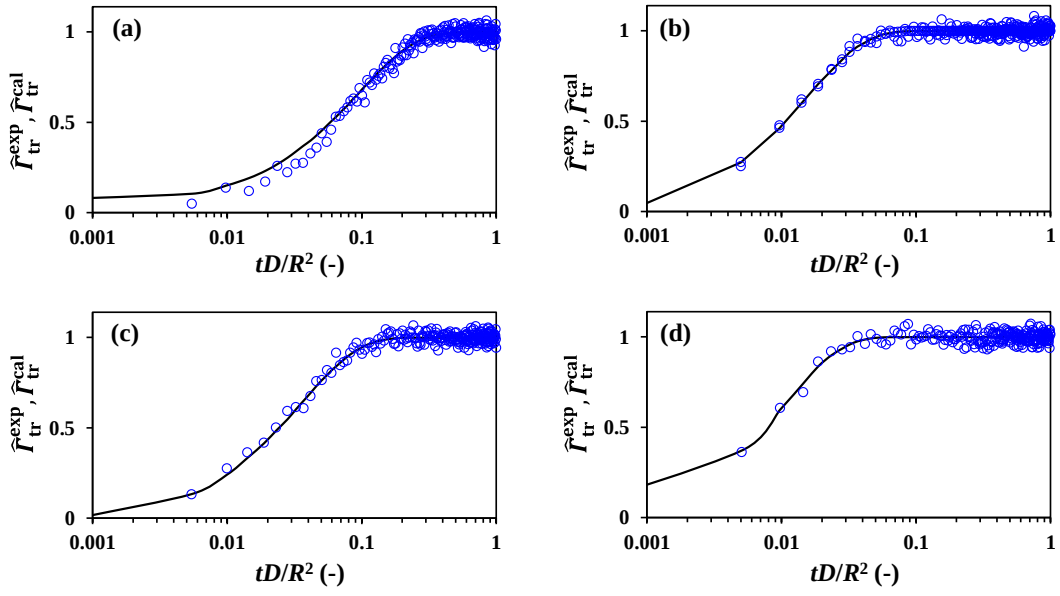

Fig 1.14 Measured transient response of scaled mixing index after flow interruption and RMF activation: f = 50 Hz/ φ = 0.001 (a); f = 200 Hz/ φ = 0.001 (b); f = 100 Hz/ φ = 0.002 (c); f = 100 Hz/ φ = 0.004 (d). Solid lines show model predictions with fitted values of effective diffusivities.

1.6. Conclusion

Reactive mixing time measurements were carried out in conjunction with ferrohydrodynamic (FHD) simulations to identify and quantify the mechanisms of mass transport of a ferrofluid inside a T-mixer capillary experiencing externally uniform rotating magnetic fields (RMF). Experiments were conducted in the so-called stop-flow RMF excitation conditions where after reaching steady-state Poiseuille flow, the ferrofluid streams were abruptly switched off simultaneously to RMF activation to assess the convective and diffusive signatures elicited by the magnetic field. The RMF was generated perpendicularly to the central axis of the capillary to provide directional control of the mass flux enhancement over the capillary cross-section while preserving invariance of the mass flux in the direction parallel to RMF rotation axis. RMF intensification of the mixing dynamics was remarkable due to enhancement of the transverse mass transport rate with respect to pure molecular diffusion as the RMF frequency and/or the concentration of magnetic nanoparticles (MNP) was increased.
Numerical solution of the capillary FHD model under stop-flow RMF excitation helped demarcating the contributions stemming from ferrofluid advection (spin-up flow) and from the anomalous anisotropic mass transport induced by the rotating magnetic nanoparticles. Analysis of the linear azimuthal velocities in mm-scale capillaries showed that in contrast with previous literature studies, FHD predicts ineffectually small linear velocities whose trend tends to dwindle as the spin viscosity is increased above its classically admitted value of 10^{-17} kg·m/s for water-based ferrofluids. Such discrepancy is shown to originate due to the small length scale of the capillary in comparison to the diffusion length scale of the couple stresses when spin viscosity is 10^{-8} kg·m/s. Analysis of forces and stresses showed that the Kelvin body force is negligible and asymmetric stresses are the only contributing momentum source for driving ferrofluid in azimuthal direction. However, the asymmetric stresses were too weak to trigger sufficient convective mixing to reflect the degree of mixing achieved experimentally.

Solution of the advection-diffusion equation using the FHD velocity field and an isotropic molecular diffusion tensor failed to describe the transient transverse mass transport problem. Therefore, ferrofluid advection or spin-up flow was, on the one hand, ruled out as a possible mixing mechanism in small-scale capillaries. An effective diffusivity tensor was, on the other hand, determined by fitting solution of the advection-diffusion equation to the experimental mixing data. The transverse component of the effective diffusivity tensor took into account the anomalous mass transport induced by the rotation of the magnetic nanoparticles in the rotating magnetic field. The component of effective diffusivity in the transverse direction showed a notable dependence with respect to RMF frequency and MNP concentration. Furthermore, due to the directional control by RMF orientation,

the advection-diffusion equation predicted mass transport with an effective diffusivity in axial direction virtually equal to the solvent self-diffusion coefficient for the studied magnet-capillary configuration.

Our experimental observations and analysis of the advection-diffusion equation point toward insufficiency of current FHD theory to resolve the nanoparticle-scale secondary circumferential micro-convective flows preventing fully predictive capabilities because of the anomalous anisotropic effective diffusion coefficients induced by rotating MNPs. Therefore, a more comprehensive mathematical description accounting for this enhancement phenomenon is awaiting and will open up opportunities for theoreticians and future research to unveil new fundamental understanding and modeling approaches in the field of process intensification *via* magnetic fields.

Acknowledgments

The authors gratefully acknowledge the Natural Sciences and Engineering Research Council of Canada and the Canada Research Chair on Sustainable Energy Processes and Materials for their financial support.

1.7. Nomenclature

Latin letters	Description	Unit
C_i	Concentration of ion *i*	mol m^{-3}
C_i^r	Reactive tracer concentration	mol m^{-3}
d	Nanoparticle diameter	m
D	Water self-diffusion coefficient	m^2 s^{-1}
D_{rr}	Component of diffusivity tensor in $\underline{\mathbf{r}}$ direction	m^2 s^{-1}
$D_{\theta\theta}$	Component of diffusivity tensor in $\underline{\boldsymbol{\theta}}$ direction	m^2 s^{-1}
D_{zz}	Component of diffusivity tensor in $\underline{\mathbf{z}}$ direction	m^2 s^{-1}
D_{rr}^e	Component of effective diffusivity tensor in $\underline{\mathbf{r}}$ direction	m^2 s^{-1}
D_{tr}^e	Component of effective diffusivity tensor in transverse direction	m^2 s^{-1}
$D_{\theta\theta}^e$	Component of effective diffusivity tensor in $\underline{\boldsymbol{\theta}}$ direction	m^2 s^{-1}
D_{zz}^e	Component of effective diffusivity tensor in $\underline{\mathbf{z}}$ direction	m^2 s^{-1}
$\overline{\overline{\mathbf{D}^e}}$	Second ranked effective diffusivity tensor	m^2 s^{-1}
$\overline{\overline{\mathbf{D}_i}}$	Second ranked diffusivity tensor	m^2 s^{-1}
f	Frequency of RMF	s^{-1}
$\underline{\mathbf{F}}^m$	Kelvin magnetic force density	N m^{-3}
$\underline{\mathbf{H}}$	Magnetic field intensity vector	A m^{-1}
$\underline{\widetilde{\mathbf{H}}}$	Scaled magnetic field intensity vector	-
$\underline{\mathbf{H}}^{ext}$	External magnetic field intensity vector	A m^{-1}
H_0	Amplitude of external RMF	A m^{-1}
$\underline{\widetilde{\mathbf{G}}}$	Scaled body couple density	-
I	Moment of inertia of single nanoparticle per unit mass	m^2

$\underline{\underline{\mathbf{I}}}$	Dyadic unit tensor	-
k_{B}	Boltzmann constant	J K^{-1}
K_1	Ratio of magnetic force to viscous force	-
$\underline{\mathbf{M}}$	Magnetization vector	A m^{-1}
$\underline{\widetilde{\mathbf{M}}}$	Scaled magnetization vector	-
M_d	Magnitude of domain magnetization vector	A m^{-1}
$\underline{\mathbf{M}}^{\boldsymbol{e}}$	Equilibrium magnetization	A m^{-1}
p	Pressure	N m^{-2}
$\tilde{P}$	Scaled pressure	-
$\underline{\mathbf{r}}$	Unit vector in radial direction	-
R	Capillary radius	m
Re	Reynolds number	-
R_i	Reaction rate of reactive scalars	mol m^{-3} s^{-1}
t	Time	s
$\tilde{t}$	Scaled time	-
T	Temperature	K
$\underline{\underline{\mathbf{T}}}$	Pressure-viscous stress tensor	N m^{-2}
$\underline{\underline{\mathbf{T}}}^{a}$	Antisymmetric component of stress tensor	N m^{-2}
$\underline{\underline{\mathbf{T}}}^{\mathbf{m}}$	Maxwell stress tensor	N m^{-2}
$\underline{\underline{\mathbf{T}}}^{s}$	Symmetric component of stress tensor	N m^{-2}
$\underline{\mathbf{v}}$	Linear velocity vector	m s^{-1}
$\underline{\tilde{\mathbf{v}}}$	Scaled linear velocity vector	-
V_H	Hydrodynamic volume of nanoparticles	m^3

Greek letters	**Description**	**Unit**
α	Langevin parameter	-
β	Lag angle between $\underline{\mathbf{M}}$ and $\underline{\mathbf{H}}$ vectors	-
$\Gamma_{\mathrm{tr}}^{\mathrm{cal}}$	Transient mixing index (calculated)	-
$\Gamma_{\mathrm{tr}}^{\mathrm{exp}}$	Transient mixing index (experimental)	-
$\underline{\underline{\boldsymbol{\varepsilon}}}$	Triadic unit tensor	-
ζ	Vortex viscosity	kg m^{-1} s^{-1}
η	Shear viscosity of ferrofluid	kg m^{-1} s^{-1}
η'	Spin viscosity	kg m s^{-1}
θ	Angle or dimensionless characteristic time	-
$\underline{\boldsymbol{\theta}}$	Unit vector in azimuthal direction	-
κ	Electrical conductivity	S m^{-1}
λ_i	Limiting molar conductivity of ion *i*	S m^2 mol^{-1}
μ_0	Vacuum permeability	N A^{-2}
ν_i	Number of ion *i* in its corresponding electrolyte formula	-
ρ	Ferrofluid density	kg m^{-3}
ρ^p	MNP density	kg m^{-3}
ς	Bulk viscosity of ferrofluid	kg m^{-1} s^{-1}
τ	Brownian relaxation time constant	s
φ	Volumetric fraction of MNP	-
Ω	Angular velocity of RMF	s^{-1}
$\underline{\boldsymbol{\omega}}$	Internal angular velocity vector	s^{-1}
$\underline{\widetilde{\boldsymbol{\omega}}}$	Scaled internal angular velocity vector	-
$\underline{\widetilde{\boldsymbol{\omega}}}_{\boldsymbol{z}}$	Scaled internal angular velocity vector in $\underline{\mathbf{z}}$ direction	-

1.8. References

1. M. I. Shliomis, *Soviet Physics Jetp-Ussr*, 1972, **34**, 1291.
2. S. Odenbach, *Colloids and Surfaces a-Physicochemical and Engineering Aspects*, 2003, **217**, 171-178.
3. R. E. Rosensweig, *Ferrohydrodynamics*, 1 edn., Dover Publications, United States of America, 1997.
4. S. Odenbach and S. Thurm, *Ferrofluids: Magnetically Controllable Fluids and Their Applications*, 2002, **594**, 185-201.
5. J. S. Dahler and L. E. Scriven, *Nature*, 1961, **192**, 36-&.
6. D. W. Condiff and J. S. Dahler, *Physics of Fluids*, 1964, **7**, 842-854.
7. R. E. Rosensweig, *Journal of Chemical Physics*, 2004, **121**, 1228-1242.
8. J. C. Bacri, R. Perzynski, M. I. Shliomis and G. I. Burde, *Physical Review Letters*, 1995, **75**, 2128-2131.
9. M. I. Shliomis, *Physical Review E*, 2001, **64**.
10. Martseny.Ma, Y. L. Raikher and M. I. Shliomis, *Zhurnal Eksperimentalnoi I Teoreticheskoi Fiziki*, 1973, **65**, 834-841.
11. A. P. Krekhov, M. I. Shliomis and S. Kamiyama, *Physics of Fluids*, 2005, **17**.
12. M. I. Shliomis and K. I. Morozov, *Physics of Fluids*, 1994, **6**, 2855-2861.
13. I. Torres-Diaz, C. Rinaldi, S. Khushrushahi and M. Zahn, *Journal of Applied Physics*, 2012, **111**.
14. A. D. Rosenthal, C. Rinaldi, T. Franklin and M. Zahn, *Journal of Fluids Engineering-Transactions of the Asme*, 2004, **126**, 198-205.
15. V. M. Zaitsev and M. I. Shliomis, *J. Appl. Mech. Tech.Phys.*, 1969, **10**, 696.
16. A. Chaves, M. Zahn and C. Rinaldi, *Physics of Fluids*, 2008, **20**.
17. I. Torres-Diaz, A. Cortes, Y. Cedeno-Mattei, O. Perales-Perez and C. Rinaldi, *Physics of Fluids*, 2014, **26**.
18. S. Khushrushahi and M. Zahn, *Journal of Magnetism and Magnetic Materials*, 2011, **323**, 1302-1308.
19. S. Feng, A. L. Graham, J. R. Abbott and H. Brenner, *Journal of Fluid Mechanics*, 2006, **563**, 97-122.
20. G.-P. Zhu and N. Nam-Trung, *Lab on a Chip*, 2012, **12**, 4772-4780.
21. Z. M. Wang, V. B. Varma, H. M. Xia, Z. P. Wang and R. V. Ramanujan, *Physics of Fluids*, 2015, **27**.
22. C.-Y. Wen, K.-P. Liang, H. Chen and L.-M. Fu, *Electrophoresis*, 2011, **32**, 3268-3276.
23. A. Munir, J. L. Wang, Z. Z. Zhu and H. S. Zhou, *Ieee Transactions on Nanotechnology*, 2011, **10**, 953-961.
24. S. S. Leong, Z. Ahmad and J. Lim, *Soft Matter*, 2015, **11**, 6968-6980.
25. T.-H. Tsai, D.-S. Liou, L.-S. Kuo and P.-H. Chen, *Sensors and Actuators a-Physical*, 2009, **153**, 267-273.
26. A. Chaves, C. Rinaldi, S. Elborai, X. He and M. Zahn, *Physical Review Letters*, 2006, **96**.
27. F. Fadaei, A. M. Dehkordi, M. Shahrokhi and Z. Abbasi, *Appl. Therm. Eng.*, 2017, **116**, 329-343.
28. P. Hajiani and F. Larachi, *Chemical Engineering and Processing*, 2013, **71**, 77-82.
29. S. Boroun and F. Larachi, *Aiche Journal*, 2017, **63**, 337-346.
30. S. Boroun and F. Larachi, *Soft Matter*, 2017, **13**, 6259-6269.
31. B. A. Finlayson, *Physics of Fluids*, 2013, **25**.
32. S. Monz, A. Tschope and R. Birringer, *Phys Rev E Stat Nonlin Soft Matter Phys*, 2008, **78**, 021404.
33. A. Fani, S. Camarri and M. V. Salvetti, *Physics of Fluids*, 2013, **25**.

34. J. C. Bacri, A. Cebers, A. Bourdon, G. Demouchy, B. M. Heegaard, B. Kashevsky and R. Perzynski, *Physical Review E*, 1995, **52**, 3936-3942.
35. X. Y. Chen and L. Zhang, *Microchimica Acta*, 2017, **184**, 3639-3649.
36. A. Munir, J. Wang, Z. Zhu, H.S. Zhou, *Microfluidics and Nanofluidics*, 2011, **10**, 735-747.
37. T. Yoshida, K. Enpuku, J. Dieckhoff, M. Schilling and F. Ludwig, *Journal of Applied Physics*, 2012, **111**.
38. J. Dieckhoff, M. Schilling and F. Ludwig, *Applied Physics Letters*, 2011, **99**.

Chapter 2: Residence time distribution of passive scalars in magnetic nanofluid Poiseuille flow under rotating magnetic fields

Residence time distribution of passive scalars in magnetic nanofluid Poiseuille flow under rotating magnetic fields

Shahab Boroun, Faïçal Larachi

Department of Chemical Engineering, Laval University, Québec, QC, Canada G1V 0A6.

Résumé

Les mécanismes de transport diffusif et convectif, régissant la distribution des temps de séjour (DTS) d'un écoulement capillaire type Poiseuille pour des nanofluides magnétiques (ferrofluides) sous à un champ magnétique rotatif (CMR) uniforme externe, ont été étudiés à la fois expérimentalement et numériquement. Les DTS mesurées ont tendance à se contracter, se rapprochant d'un écoulement piston sous excitation de CMR, raccourcissant le temps d'élution et raidissant la courbe de percée tout en retardant le temps de percée lorsque la fréquence du champ magnétique et / ou la concentration en nanoparticules magnétiques augmente(nt). Les simulations ferrohydrodynamiques (FHD) prédisent l'apparition d'un écoulement azimutal convectif secondaire mais n'ayant qu'une incidence mineure quant à expliquer l'impact du champ magnétique sur l'évolution des DTS sous l'hypothèse d'un transport diffusif isotrope. L'origine de l'anisotropie dans le transport diffusif scalaire a été élucidée en analysant les propriétés de rotation des nanoparticules magnétiques par rapport à la vorticité du ferrofluide et de l'arrangement de champ magnétique. Par conséquent, la détermination indépendante d'un tenseur de diffusion anisotrope mesuré pour les ferrofluides au repos sous excitation CMR a permis d'améliorer le caractère prédictif des simulations FHD des DTS en écoulement de Poiseuille.

Residence time distribution of passive scalars in magnetic nanofluid Poiseuille flow under rotating magnetic fields

Shahab Boroun, Faïçal Larachi

Department of Chemical Engineering, Laval University, Québec, QC, Canada G1V 0A6.

2.1. Abstract

The diffusive and convective transport mechanisms governing the residence time distribution (RTD) of magnetic nanofluid (ferrofluid) capillary Poiseuille flows under external uniform rotating magnetic field (RMF) were investigated both experimentally and numerically. The measured RTDs tend to shrink, thus approaching plug flow under RMF excitation, by shortening the elution time, stiffening the breakthrough rise and delaying the breakthrough time as RMF frequency and/or magnetic nanoparticle concentration increase(s). Ferrohydrodynamic (FHD) simulations predict inception of secondary convective azimuthal flows but which failed to explain the impact of magnetic field on RTD evolution under the assumption of isotropic diffusion transport. The origin of anisotropy in scalar diffusive transport was elucidated by analyzing the rotational properties of magnetic nanoparticles with respect to ferrofluid vorticity and RMF arrangement. Therefore, independent determination of an anisotropic effective diffusion tensor measured for RMF-excited quiescent ferrofluids led to improved FHD simulations of RTD without penalizing model predictive power.

2.2. Introduction

Enthrallment for research on the motion of ferrofluids under external magnetic fields has been unfading since the pivotal works of Shliomis[1,2] and Rosensweig,[3,4] more than half a century ago. The nonconforming properties of transport phenomena stemming from the interaction of ferrofluids with magnetic fields paved the way to various innovative discoveries and applications of ferrofluids.[5,6] Early ferrofluid dynamic studies were mainly devoted to elucidation of the phenomenon of magnetoviscosity impelled by exchanges of internal angular momentum of the magnetic nanoparticles (MNP) with the ferrofluid linear momentum.[4] Apart from the large body of studies on momentum transport in ferrofluid, the transport of scalars is also increasingly contemplated with emphasis on microfluidic applications.[7] Owing to the ferrofluid remote controllability by a variety of magnetic fields, conversion and delivery of nanometrically-focused magnetic energy into heat/kinetic energy using chemically and biologically benign nanoparticles is formidably expanding the event horizon of potential applications in the realm of chemical synthesis, biomedicine and physics, to name just a few.[8-12]

Fluid flow in microchannel geometries is largely dominated by viscous forces which often necessitate travel of long distances for a scalar to achieve homogenization by the only active *crosswise* mixing mechanism fulfilled by molecular diffusion in laminar linear flows.[10] The second shortcoming in microfluidics, besides the mixing problem, arises because of non-uniform, usually bell-shaped, radial velocity profile which embodies the familiar axial dispersion. Axial dispersion translates in a distribution of reaction or processing times which may result in a detrimental polydispersity in terms of quality of final product. From a reaction engineering point of view, poor mixing and high axial dispersion both can considerably deteriorate conversion and selectivity of chemical reactions.[8,13]

The concept of active mixing based on the magnetic field excitation of ferrofluids is one possible route to overcome these shortcomings. Mixing in this concept can be achieved through multiple physical mechanisms as reviewed recently in the literature.[11,12] A conventional category of mixing mechanism in ferrofluids relies on exploiting the magnetic Kelvin body force which can be generated in two circumstances: by applying i) homogeneous magnetic fields to magnetic media endowed with gradient magnetic susceptibility such as systems associating superparamagnetic and paramagnetic fluid flows;[8] ii) gradient magnetic fields to magnetic media with uniform magnetic susceptibility. The latter modality requires high-intensity magnetic fields to estrange the magnetic nanoparticles from the hold of the random thermal motion,[3] although at the cost of colloidal destabilization at high magnetic field intensities.[14]

Among the various types of magnetic fields, rotating magnetic fields (RMF) offer interesting properties in dilute ferrofluids with homogeneous magnetic susceptibility even at low intensity and frequency. It has been experimentally observed that the mass transport rate in quiescent ferrofluids exposed to uniform RMF is tremendously enhanced.[15] In addition, axial dispersion of a ferrofluid Poiseuille flow is reduced upon application of a uniform RMF perpendicularly to flow direction.[16,17] The reduced axial dispersion is attested from the narrower residence time distributions (RTD) with their shapes becoming closer to a Gaussian symmetric distribution. These experimental observations suggest potential application of uniform RMF for manipulation of flow patterns and scalar transport in microfluidic devices. However, the mechanisms behind RTD restructuring for dilute ferrofluid Poiseuille flows subjected to uniform RMF are not clearly understood. In particular, delineating the turfs of convective and diffusive contributions as well as the proper configuration for each ought to be scrutinized in more details. The anomalous effective diffusivity of *stagnant* dilute ferrofluids in response to rotating magnetic fields has been experimentally studied[15,18] and proven to be anisotropic in nature.[18] Anisotropy reflects in scalar diffusion mainly enhanced in a direction transverse to the rotation axis of RMF leaving the remaining direction under the grip of molecular diffusion. On the other hand, the existence of asymmetric stresses resulting from the mismatch between ferrofluid vorticity and MNP rotation rate may give rise to secondary macroscopic flows, generally known as spin-up phenomenon.[2] Spin-up flow is the outcome of curled internal angular velocity field that generates stresses directed normal to the internal angular velocity. Extensive research on spin-up phenomenon has shown that macroscopic flows driven by low frequency and low intensity RMF can be activated in various geometries.[19,20] More specifically, an azimuthal convective flow is triggered assuming synchronized rotation of MNP in a cylindrical geometry with RMF directed transverse to the vessel centerline. These two concepts of effective anisotropic diffusivity and spin-up phenomenon can be viewed as the main transport mechanisms behind restructuring the residence time distribution of ferrofluid Poiseuille flows.

In this contribution, the authors aim at identifying and quantifying the transport mechanisms responsible for the reduction of axial dispersion in capillary ferrofluid Poiseuille flows brought about by application of a rotating magnetic field. Residence time distribution measurements were carried out with dilute ferrofluids composed of Brownian magnetic nanoparticles to objectify the role of RMF frequency and MNP concentration on how passive scalars are transported in ferrofluid flows. The transient tracer concentrations along the capillary were simulated by solving the advection-diffusion transport within the FHD framework to assist in our quest for analyzing the RMF-driven rotational properties of magnetic nanoparticles and secondary convective flows and their impact on RTDs.

2.3. Experimental

2.3.1. Magnet device

A rotating magnetic field (RMF) was generated by a two-pole stator winding with three pairs of coils around the periphery of a cylindrical magnet bore. The bore dimensions were 55 mm in height and 45 mm in inner diameter. A three-phase AC current, 120º out of phase, fed the three coil pairs so that the resultant magnetic field inside the bore rotated with a frequency equal to that of the balanced AC currents. This configuration generates RMF directed perpendicular to the central bore axis as sketched in Figure 2.1. The intensity and frequency of RMF were adjusted by means of a variable frequency drive (ABB, ACS150, 2.2kW) coupled to a power source. The intensity of resultant magnetic field, measured by a Gaussmeter (Cryomagnetics, GM-700), was verified to be spatially homogeneous both radially within 5 mm radial distance from the bore central axis, and axially along a 45 mm height excepting the top and bottom sections of the magnet bore.

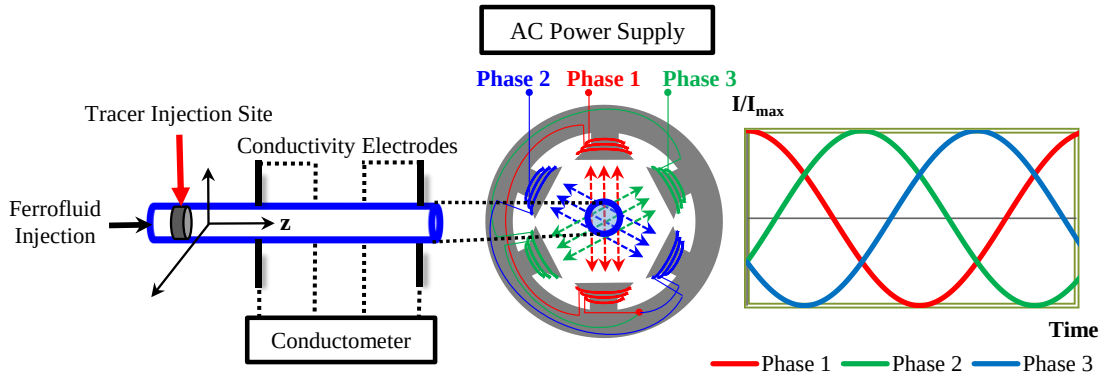

Fig 2.1 Capillary tube/magnet assembly for quantification of RTD in rotating magnetic fields: Schematics of RMF generator, three-pair two-pole stator coils, and capillary centrally-aligned with cylindrical magnet.

2.3.2. Synthesis and characterization of Cobalt ferrite nanoparticles and ferrofluid

Cobalt ferrite MNP were synthesized by co-precipitation method according to a procedure described elswehere.[21] In brief, Fe^{3+} and Co^{2+} ions in an alkaline solution were precipitated at pH 9 by adding concentrated sodium hydroxide solution. The resultant precipitate was maintained at 80ºC for 15 min. A small portion of the suspension was collected and its solid content was magnetically separated, washed several times by deionized water and dried prior to be used for magnetometry analysis. After several washing and MNP separation steps, the pH of the suspension was adjusted around 9 by sodium hydroxide solution and subsequently sonicated for 15 min. The MNP volumetric fractions in the

resultant colloidal dispersion, also referred to as ferrofluid, were adjusted MNP from 0.001 to 0.004. Magnetic characterization of both MNP powders and prepared ferrofluids was carried out using a vibrating sample magnetometer (VSM) from Princeton Instrument (MicroMag model 2900) at 298 K. The hydrodynamic diameter of MNP in the colloidal state was measured by dynamic light-scattering method by means of a Zetasizer Nano 6 (Malvern Instruments Ltd) using a 4 mW He–Ne laser at 633 nm wavelength.

2.3.3. Residence time distribution tests

Laminar Poiseuille ferrofluid flows were monitored in a cylindrical capillary, 1 mm in inner diameter, by means of residence time distribution (RTD) tests. The capillary was placed inside the magnet bore so that their central axes were superimposed. The capillary was equipped with a syringe port for injection of tracer impulsions and two conductivity electrodes, placed 2 and 5 cm downstream of the injection site for concentration measurements. The schematic of capillary and magnetic field orientation is shown in Figure 2.1. The conductivity electrodes were connected to a conductometer (Omega CDTX-90) to continuously measure the cross-sectionally averaged tracer concentrations following release of a brief tracer pulse upstream of the capillary. The tracer was prepared by dissolving precisely-weighted amounts of sodium chloride (10^{-5} mole m^{-3}) in a marker ferrofluid with identical MNP concentration as the main ferrofluid stream flowing in the capillary. This stream was fed into the capillary by a syringe pump at a constant flow rate corresponding to $\mathrm{Re} = 1$ and superficial velocity of 10^{-3} m s^{-1}. The tracer was injected in the ferrofluid stream after steady-state was reached in presence or absence of RMF. The measured concentrations at two points are related to the ferrofluid flow impulse response or RTD by the classical convolution integral:[13]

$$C_2(t) = \int_0^t C_1(t - t')\, E(t') dt' \tag{2.1}$$

Where C_1 and C_2 are the cross-sectionally averaged tracer concentrations at first and second measurement points along the capillary, respectively. The system's residence time distribution can be retrieved from the transfer function in the frequency domain of the Fourier transforms of C_1 and C_2 time series and then back to the time-domain using classical treatments of the convolution theorem:[13]

$$E(t) = \mathcal{F}^{-1}\big(\mathcal{F}\big(C_2(t)\big)/\mathcal{F}\big(C_1(t)\big)\big) \tag{2.2}$$

Where $\mathcal{F}$ and $\mathcal{F}^{-1}$ are the Fourier transform operators between time and frequency domains.

2.4. Ferrohydrodynamic model

From the laws of continuity and of micro-polar continuum mechanics, the set of FHD governing equations consists of the incompressible form of the continuity equation, and the linear momentum and internal angular momentum balance equations, respectively:[3]

$$\frac{\partial}{\partial t}\rho\underline{\mathbf{v}} + \underline{\boldsymbol{\nabla}}\cdot\left(\rho\underline{\mathbf{v}}\otimes\underline{\mathbf{v}}\right) = \underline{\boldsymbol{\nabla}}\cdot\underline{\underline{\mathbf{T}^{\mathbf{m}}}} + \underline{\boldsymbol{\nabla}}\cdot\underline{\underline{\mathbf{T}}} \tag{2.3}$$

$$\frac{\partial}{\partial t}\rho I\underline{\boldsymbol{\omega}} + \underline{\boldsymbol{\nabla}}\cdot\left(\rho I\underline{\mathbf{v}}\otimes\underline{\boldsymbol{\omega}}\right) = \eta'\underline{\boldsymbol{\nabla}}\cdot\left(\underline{\boldsymbol{\nabla}}\,\underline{\boldsymbol{\omega}} + \underline{\boldsymbol{\nabla}}\,\underline{\boldsymbol{\omega}}^{\mathbf{t}}\right) - \underline{\underline{\boldsymbol{\varepsilon}}} : \underline{\underline{\mathbf{T}}} + \mu_0\underline{\mathbf{M}}\times\underline{\mathbf{H}} \tag{2.4}$$

$$\underline{\boldsymbol{\nabla}}\cdot\underline{\mathbf{v}} = \mathbf{0} \tag{2.5}$$

Where $\underline{\mathbf{v}}$ is the velocity field (m s^{-1}), $\underline{\underline{\mathbf{T}}}$ the pressure-viscous stress tensor (N m^{-2}), $\underline{\underline{\mathbf{T}^{\mathbf{m}}}}$ the Maxwell stress tensor (N m^{-2}), $\underline{\mathbf{M}}$ the magnetization (A m^{-1}), $\underline{\mathbf{H}}$ the magnetic field (A m^{-1}), $\underline{\boldsymbol{\omega}}$ the internal angular velocity (s^{-1}) and $\underline{\underline{\boldsymbol{\varepsilon}}}$ is the triadic unit tensor, and where ρ is the ferrofluid density (kg m^{-3}), η' its spin viscosity (kg m s^{-1}), I the moment of inertia for a single nanoparticle per unit mass ($\approx 10^{-17}$ m^2) and μ_0 the vacuum permeability (1.26×10^{-6} N A^{-2}).

The ferrofluid stress tensor consists of symmetric and asymmetric terms. The symmetric component of $\underline{\underline{\mathbf{T}}}$ is given by the conventional expression for a Newtonian fluid:

$$\underline{\underline{\mathbf{T}}}^{\mathrm{s}} = -p\underline{\underline{\mathbf{I}}} + \eta\left(\underline{\boldsymbol{\nabla}}\,\underline{\mathbf{v}} + \underline{\boldsymbol{\nabla}}\,\underline{\mathbf{v}}^{\mathbf{t}}\right) + \varsigma\left(\underline{\boldsymbol{\nabla}}\cdot\underline{\mathbf{v}}\right)\underline{\underline{\mathbf{I}}} \tag{2.6}$$

Where p is the pressure (Pa), η and ς are the ferrofluid shear and bulk viscosities (kg m^{-1} s^{-1}) and $\underline{\underline{\mathbf{I}}}$ is the dyadic unit tensor.

The asymmetric component is expressed as:

$$\underline{\underline{\mathbf{T}}}^{\mathrm{a}} = 2\zeta\underline{\underline{\boldsymbol{\varepsilon}}}\cdot\left(\frac{1}{2}\underline{\boldsymbol{\nabla}}\times\underline{\mathbf{v}} - \underline{\boldsymbol{\omega}}\right) \tag{2.7}$$

Where ζ is the vortex viscosity (kg m^{-1} s^{-1}) and where the ferrofluid density and shear viscosity are calculated according to the weighted-mean mixtures rule and Einstein equation:

$$\rho = 1000(1-\varphi) + \rho^{\mathrm{p}}\varphi, \qquad \eta = 8.9\times10^{-4}(1+2.5\varphi) \tag{2.8}$$

Where ρ^{p} and φ are the MNP density and MNP volumetric fraction in the ferrofluid, respectively. The vortex viscosity is estimated according to:[3]

$$\zeta = 1.5\eta\varphi \tag{2.9}$$

The divergence of Maxwell stress tensor is equivalent to the volumetric density of Kelvin magnetic force and is expressed as:

$$\underline{\nabla} \cdot \underline{\mathbf{T}}^{\mathbf{m}} = \underline{\mathbf{F}}^{\mathrm{m}} = \underline{\nabla} \cdot \left(\mu_0 \underline{\mathbf{H}} \otimes \underline{\mathbf{H}} - \frac{1}{2} \mu_0 |\underline{\mathbf{H}}|^2 \underline{\mathbf{I}} \right) \tag{2.10}$$

In a non-conducting material, magnetic field and magnetic flux density should, respectively, be curl-free and divergence-free:

$$\underline{\nabla} \cdot \left(\underline{\mathbf{H}} + \underline{\mathbf{M}} \right) = 0 \tag{2.11}$$

$$\underline{\nabla} \times \underline{\mathbf{H}} = \underline{\mathbf{0}} \tag{2.12}$$

Deviations of the magnetization vector with respect to the equilibrium magnetization by thermal or hydrodynamic perturbations are accounted for by means of a phenomenological magnetization relaxation transport equation:

$$\frac{\partial \underline{\mathbf{M}}}{\partial t} + \underline{\nabla} \cdot \left(\underline{\mathbf{v}} \otimes \underline{\mathbf{M}} \right) = \underline{\boldsymbol{\omega}} \times \underline{\mathbf{M}} - \frac{1}{\tau} \left(\underline{\mathbf{M}} - \underline{\mathbf{M}}^{\boldsymbol{e}} \right) \tag{2.13}$$

Where τ is the Brownian relaxation time constant (s) and $\underline{\mathbf{M}}^{\boldsymbol{e}}$ is the equilibrium magnetization (A m^{-1}) expressed by the Langevin relation:

$$\underline{\mathbf{M}}^{\mathbf{e}} = \varphi M_{\mathrm{d}} (\coth \alpha - \alpha^{-1}) \frac{\underline{\mathbf{H}}}{|\underline{\mathbf{H}}|}, \alpha = \frac{\pi \mu_0 M_{\mathrm{d}} |\underline{\mathbf{H}}| d^3}{6 k_{\mathrm{B}} T} \tag{2.14}$$

Where M_{d} is the domain magnetization of cobalt ferrite nanoparticles (A m^{-1}), d is the nanoparticle diameter (m), k_{B} is the Boltzmann constant (1.38×10^{-23} J K^{-1}), α is the Langevin parameter and T is the temperature. The Brownian time constant is estimated by:

$$\tau = \frac{3 V_H \eta}{k_B T} \tag{2.15}$$

Where V_H denotes the hydrodynamic volume of nanoparticles (m^3).

2.4.1. Scalar transport

Transport of scalars is expressed by the classical advection-diffusion equation:

$$\frac{\partial C}{\partial t} = \underline{\nabla} \cdot \left(\underline{\mathbf{D}} \, \underline{\nabla} C \right) - \underline{\nabla} \cdot \left(\underline{\mathbf{v}} C \right) \tag{2.16}$$

Where C is the passive tracer concentration (mole m^{-3}) and $\underline{\mathbf{D}}$ is the second-rank anisotropic diffusivity tensor (m^2 s^{-1}), defined as:

$$\underline{\underline{\mathbf{D}}} = \begin{bmatrix} D_{\mathrm{rr}} & 0 & 0 \\ 0 & D_{\theta\theta} & 0 \\ 0 & 0 & D_{\mathrm{zz}} \end{bmatrix} \tag{2.17}$$

After solving the FHD (Eqs. 3-15) and passive scalar transport (Eq. 16) equations, the mixing cup concentrations obtained from flow-rate weighted concentration over the capillary cross-section were used to calculate numerically the predicted RTD using Eq. 2.

2.4.2. Boundary and initial conditions

The velocity boundary conditions are such that spin and linear velocities are zero on the capillary wall. To satisfy cylindrical symmetry condition, the vector variables are assumed continuous and gradient-free on the capillary central axis. The initial values of azimuthal and radial linear velocities, axial and radial internal angular velocities and magnetization vectors were zero. The initial conditions of axial linear, azimuthal angular velocities and pressure were obtained by solving the steady-state Poiseuille flow in the absence of RMF.

The boundary conditions for magnetostatics are such that the normal component of magnetic flux density and tangential component of magnetic field intensity are continuous on the wall:

$$\underline{\mathbf{n}} \cdot \underline{\mathbf{H}}_{\mathrm{in}} = \underline{\mathbf{n}} \cdot \underline{\mathbf{H}}_{\mathrm{out}} \tag{2.18}$$

$$\underline{\mathbf{n}} \times \underline{\mathbf{H}}_{\mathrm{in}} = \underline{\mathbf{n}} \times \underline{\mathbf{H}}_{\mathrm{out}} \tag{2.19}$$

$\underline{\mathbf{H}}_{\mathbf{out}}$ and $\underline{\mathbf{M}}_{\mathbf{out}}$ are not known and their experimental determination is formidably complicated. Fortunately, the obstacle in determination of boundary conditions of magnetostatics may be overcome by subtracting the demagnetizing field of a magnetisable material with cylindrical shape from the externally applied magnetic field:[22]

$$\underline{\mathbf{H}} = \underline{\mathbf{H}}^{\mathrm{ext}} - \frac{\varphi M_{\mathrm{d}}}{3H_0} \underline{\mathbf{M}} \tag{2.20}$$

Where $\underline{\mathbf{H}}^{\mathrm{ext}}$ is the externally applied uniform RMF expressed by:

$$\underline{\mathbf{H}}^{\mathrm{ext}} = H_0 \sin(2\pi f t + \theta) \cdot \underline{\mathbf{r}} + H_0 \cos(2\pi f t + \theta) \cdot \underline{\boldsymbol{\theta}} \tag{2.21}$$

With H_0 is the RMF amplitude (10^3 kA m^{-1}), f RMF frequency (s^{-1}) and θ angular position.

The concentration boundary conditions in radial direction are zero flux on the wall and zero-gradient on capillary central axis. In axial direction, the concentration at capillary inlet is approximated by a brief rectangular impulse function and a at capillary outlet, a Danckwerts open boundary condition was imposed, i.e., concentration continuity.[23] The initial concentration was zero for the entire domain.

2.4.3. Numerical solution

The conservative time-dependent FHD equations, including magnetostatics and transport of magnetization, were discretized using an implicit finite difference method. The system of nonlinear equations generated from discretization was solved by a Newton's iterative method. In order to implement initial guesses, the equations were initially discretized in semi-implicit scheme by explicit discretization of the magnetization transport equation to allow calculation of the magnetization a time step earlier than the linear and internal angular velocities. The explicitly calculated magnetization was subsequently introduced in the implicit discretized linear and angular momentum balance equations to obtain the linear and angular velocities. The solution of semi-implicit scheme was used as the initial guess for solution of the complete set of equations by the implicit method. The large diameter-to-length aspect ratio allows simplifying solution of the vector components in $\underline{\mathbf{r}}$ and $\underline{\boldsymbol{\theta}}$ directions by assuming axially invariant vector fields. Preliminary calculations showed that activation of the magnetic field had no influence on the axial linear velocity component as determined form the initial condition. The linear azimuthal velocity exhibited negligible angular dependency and the radial velocity component is zero under any circumstances. Accordingly, the pressure-velocity coupling was solved by using the pressure drop obtained from the classical Poiseuille flow of ferrofluid flow in the absence of magnetic field. The capillary was discretized using a polar cylindrical grid with mesh density increased sequentially until grid independence was achieved for the predicted vector variables. A combination of Matlab and Comsol Multiphysics (version 4.4) was used to solve in a decoupled manner the FHD equations and the scalar transport equation after the velocity field was imported into Comsol from the Matlab FHD solution.

2.5. Results and discussion

2.5.1. Magnetic properties of MNP and ferrofluid

The crystallographic study of cobalt ferrite nanoparticles confirms formation of an inverse spinel of crystalline cobalt-ferrite with 33 nm average crystallite size.[21] These MNP are in ferromagnetic state at ambient temperature as evidenced by the magnetometric measurements shown in Figure 2.2a. The magnetization curve demonstrates a hysteresis loop with a saturation magnetization of 59 emu g^{-1} also taken as the domain magnetization of cobalt ferrite nanoparticles in our numerical calculations.

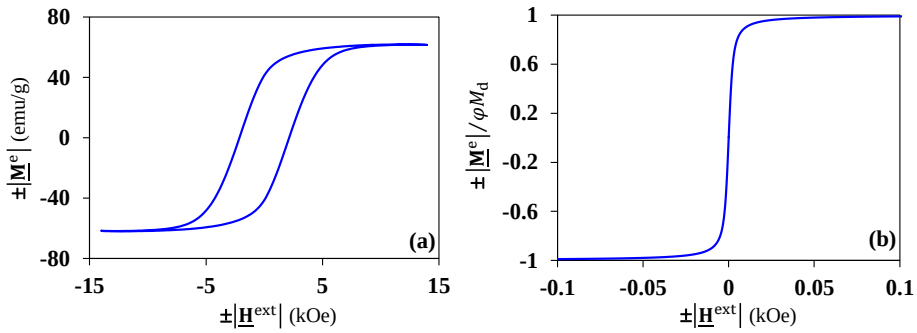

Fig 2.2 Ambient-temperature (a) equilibrium magnetization curve of powdery cobalt ferrite nanoparticles (a) and dimensionless equilibrium magnetization curve of cobalt-ferrite ferrofluid (φ = [0.001 – 0.004] and M_d = 295 kA/m).

The hydrodynamic diameter of the surfactant-free MNP dispersed in water exhibits polydispersity with an average diameter of 33.8 nm and minimum size of approximately 20 nm.[21] Thus, it may be safe to assume that all the nanoparticles are in a thermally-blocked state since the critical diameter of transition from superparamagnetism to ferromagnetism is less than 16 nm for cobalt-ferrite nanoparticles.[24,25] Accordingly, the magnetization relaxation equation remains valid for ferrofluids with cobalt ferrite nanoparticles since the hydrodynamic perturbation of magnetization from equilibrium occurs via averaged bodily spin rate of MNP in a unit volume of ferrofluid.[26] Although MNPs show no sign of Néelian relaxation in the dry powdery state, superparamagnetism is the prevailing mechanism of relaxation in the dispersed state as evidenced by the zero remnant magnetization in Figure 2.2b. The Brownian relaxation time estimated from the MNP hydrodynamic diameter and Eq. 15 is in the order of 10^2 μs.

2.5.2. Tracer dispersion in ferrofluid Poiseuille flow - RMF disabled

First and foremost, the simulated residence time distribution obtained from solution of the advection-diffusion equation combined with the FHD equations (Eqs. 3-17) was compared to the measured RTD for the ferrofluid Poiseuille flow in absence of RMF excitation. The purpose of such comparison was to demonstrate the validity of our hypothesis on describing the actual non-Dirac impulse concentration function at the inlet boundary as a rectangular perturbation as well as to test model predictability and accuracy without magnetic field.

To simulate the theoretical ferrofluid RTD at zero magnetic field intensity, the ferrofluid spin viscosity was assigned two limiting values when solving Eqs. 3-17. The lower limit, or standard value, is determined on the basis of Rosensweig's interpretation of spin viscosity in accordance with the diffusion length of the internal angular momentum which is approximately equal to the average

distance between MNP.[3] It is calculated from $\eta' = \eta d^2(\pi/6\varphi)^{2/3}$ to be of the order of 10^{-17} kg m s^{-1}.[3] This classical interpretation of spin diffusion has been found to underestimate the cylindrical spin-up phenomenon for a Brownian ferrofluid.[26] A spin viscosity several orders of magnitude higher than the standard one, has also been proposed for a cobalt-ferrite based ferrofluid. We assume $\eta' = 10^{-8}$ kg m s^{-1} as an upper limit based on Torres-Diaz et al.[26] report on spin viscosity to match measured cylindrical spin-up flows in uniform RMF with FHD predictions.

Solving the FHD equations under disabled RMF invariably predicts the same fully-developed Poiseuille flow parabolic velocity profile for both values of spin viscosity at $\mathrm{Re} = 1$. However, the magnitude of internal angular velocity vector of the nanoparticles in azimuthal direction, ω_θ, is sensitive to variations of spin viscosity. The radial distribution of ω_θ scaled by the ferrofluid half-vorticity $\left(0.5\Omega_\theta = 0.5\underline{\boldsymbol{\theta}} \cdot (\underline{\nabla} \times \underline{\mathbf{V}})\right)$ is shown for both values of η' for a dilute ferrofluid with MNP volume fraction $\varphi = 0.004$ (Figure 2.3a). In absence of magnetic field, the average rotation rate (or internal angular velocity) of MNP, ω_θ, is naturally expected to be in synchrony with the angular velocity of the dilute ferrofluid given by half its vorticity.[3] This is indeed what the simulations predict for η' = 10^{-17} kg m s^{-1} as the scaled ω_θ is unity over the entire radial positions as if $\underline{\underline{\mathbf{T}}}^{\mathrm{a}} \approx \underline{\underline{\mathbf{0}}}$ (Eq. 7), except at the wall where $\omega_\theta = 0$ is imposed as a boundary condition. In contrast, for η' = 10^{-8} kg m s^{-1}, the internal angular velocity is smaller than the ferrofluid angular velocity by at least three orders implying, contrary to expectation for dilute suspensions,[3] practically non-rotating nanoparticles, *i.e.*, $\underline{\underline{\mathbf{T}}}^{\mathrm{a}} \neq \underline{\underline{\mathbf{0}}}$ (Eq. 7). The hindered rotation of MNPs would be reminiscent of positive magnetoviscosity akin to that observed for ferrofluids under static magnetic fields.[1,3] Let us analyze the soundness of positive rotational viscosity in absence of magnetic field on the basis of the shear stress on the capillary wall.

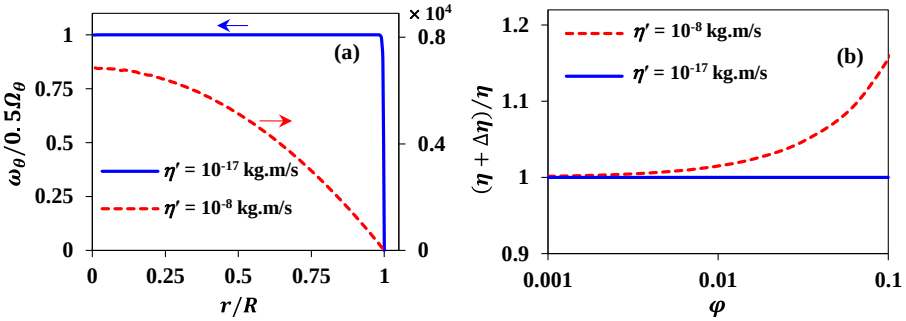

Fig 2.3 Effect of spin viscosity on (a) the radial profile of MNP angular velocity component normalized by ½ azimuthal vorticity component of the ferrofluid (φ = 0.004) and (b) on the ferrofluid rotational viscosity as a function of MNP volume fraction for a ferrofluid Poiseuille flow ($Re = 1$, RMF disabled).

The shear stress acting on a wall unit surface area from the ferrofluid is expressed by:

$$\underline{\mathbf{T}}^{\mathbf{w}} = \underline{\mathbf{n}} \cdot \left(\underline{\underline{\mathbf{T}}}^{\mathrm{s}} + \underline{\underline{\mathbf{T}}}^{\mathrm{a}} \right) \tag{2.22}$$

where $\underline{\mathbf{n}}$ is the normal vector to the surface on which the stress tensor $\underline{\underline{\mathbf{T}}}$ is applied. In Poiseuille ferrofluid fully-developed flow, vorticity and MNP spin are in azimuthal direction. Thus, by referring to Eqs. 6,7, one can write:

$$\underline{\underline{\mathbf{T}}}^{\mathrm{s}} = -\eta \Omega_{\theta} \underline{\mathbf{r}}\, \underline{\mathbf{z}} \tag{2.23}$$

$$\underline{\underline{\mathbf{T}}}^{\mathrm{a}} = \zeta (\Omega_{\theta} - 2\omega_{\theta}) \left(\underline{\mathbf{z}}\, \underline{\mathbf{r}} - \underline{\mathbf{r}}\, \underline{\mathbf{z}} \right) \tag{2.24}$$

The normal vector on capillary inner wall surface is $-\underline{\mathbf{r}}$, thus, the shear stress on the wall is:

$$\underline{\mathbf{T}}^{\mathbf{w}} = (\zeta(\Omega_{\theta} - 2\omega_{\theta}) + \eta\Omega_{\theta})\underline{\mathbf{z}} = \Omega_{\theta}(\eta + \Delta\eta)\underline{\mathbf{z}} \tag{2.25}$$

Where $\Delta\eta$ is the rotational viscosity (kg m^{-1} s^{-1}) defined as:

$$\Delta\eta = \frac{\zeta(\Omega_{\theta} - 2\omega_{\theta})}{\Omega_{\theta}} \tag{2.26}$$

Eq. 26 is valid for a ferrofluid whether external body forces/couples are present or not.[3] Therefore, for a ferrofluid flow description in absence of external magnetic field, the FHD equations should restore the Navier-Stokes equation admitting solely Eq. 6 as the symmetric stress tensor contribution. Thus, for a ferrofluid Poiseuille flow without RMF, the shear stress on the wall must alternatively be expressed as:

$$\underline{\mathbf{T}}^{\mathbf{w}} = \eta\Omega_{\theta}\underline{\mathbf{z}} \tag{2.27}$$

The ratio of FHD wall stress (Eq. 25) to that from Navier-Stokes equation (Eq. 27) reduces to the viscosity ratio, $(\eta + \Delta\eta)/\eta$, as a measure of the mismatch between MNP spin and fluid vorticity. Figure 2.3b illustrates sensitivity of $(\eta + \Delta\eta)/\eta$ to MNP volume fraction and spin viscosity when no magnetic field is applied to the ferrofluid Poiseuille flow. The viscosity ratio for η' = 10^{-17} kg m s^{-1} is independent of MNP concentration and implies dormant asymmetric stresses. Figure 2.3a attests for perfect synchronicity between MNP and ferrofluid rotations, *i.e.*, $\Omega_{\theta} = 2\omega_{\theta}$ ($\Delta\eta = 0$). On the contrary, for η' = 10^{-8} kg m s^{-1}, the effective viscosity progressively deviates from the ferrofluid intrinsic viscosity echoing an asymmetric stress that gains in strength as MNP concentration increases. It is worthy of notice that suppression of MNP rotation with respect to vorticity as manifested in dilute ferrofluids (Figure 2.3a) would be undetectable from wall shear-stress-based rotational viscosity measurements. However, even if lack of rotational viscosity in the dilute range

up to $\varphi \approx 0.004$ (Figure 2.3b) would not permit discrimination between the two spin viscosity values, an asymmetric stress associated with $\eta' = 10^{-8}$ kg m s^{-1} would yet significantly block MNP rotation with respect to ferrofluid vorticity (Figure 2.3a). Hence, one could have assigned purely spurious positive magnetoviscous contribution, whose manifestation is questionable in the absence of external magnetic body couples, to the ferrofluid suspension had the upper spin viscosity limit been chosen. Therefore, we will rely in our simulations of the ferrofluid capillary Poiseuille flow on the assumption of validity of the standard spin viscosity.

A typical magnetic-field-free experiment represented by the measured tracer concentrations is shown in Figure 2.4a. The resultant RTD (solid line, Figure 2.4b) obtained from deconvolution (Eq. 2) has an asymmetric shape with a coefficient of variance CoV = 0.2. Repeat RTD tests for identical conditions led to the 95% confidence-interval envelope indicated by the light blue shade in Figure 2.3b. The dashed line shows solution of the advection-diffusion equation obtained by setting the diffusion tensor components equal to the tracer diffusion coefficient of sodium chloride at 25 ºC (D_t = 1.5·10^{-9} m^2/s)[27] in all three directions. The theoretical prediction of advection-diffusion is not precisely superimposed on the experimental RTD. The mismatch may be attributed to slight tailing effects observed in both concentration signals that relatively broadens the confidence interval of the experiment. The observed tails are ascribed to small dead zones inevitably forming onto the machined capillary inner wall to allow insertion of the conductivity electrodes. Nevertheless, the predicted RTD falls within the confidence interval of the measured mean RTD attesting for an acceptable accuracy of both our experimental and numerical procedures.

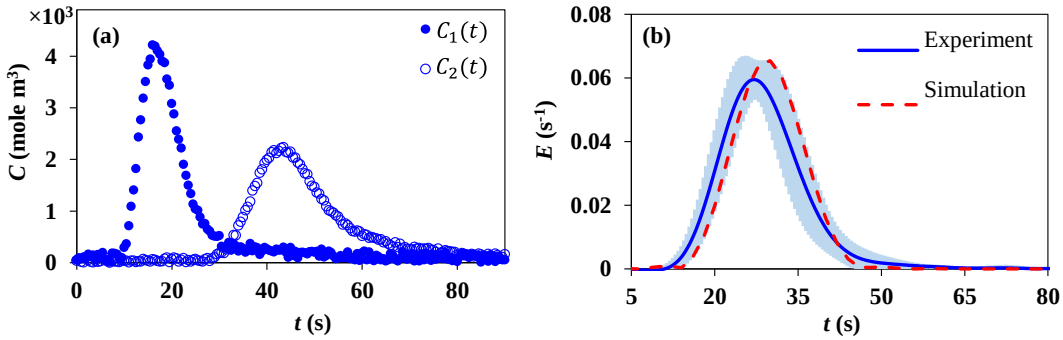

Fig 2.4 (a) Transient tracer concentration signals measured at two downstream points along capillary and (b) corresponding experimental (solid line) and simulated (dashed line) RTD for magnetic-field-free ferrofluid Poiseuille flow ($\varphi = 0.004$, $Re = 1$). Light blue shade shows 95% confidence level for repeat tests.

2.5.3. Tracer dispersion in ferrofluid Poiseuille flow - RMF enabled

The tracer concentration transients undergo remarkable changes upon application of rotating magnetic fields to the ferrofluid Poiseuille flow (Figure 2.5). As an example, increasing RMF frequency to f = 50 Hz and then 100 Hz tends to narrow down the transient concentration signals at a given measurement position as compared with the signals acquired without magnetic field. The bell-shaped curves evolved towards more symmetric Gaussians at both measurement points with increasing RMF frequency. A tracer breakthrough time can be defined as the earliest time for detection of the passage of tracer nearby the sensor. RMF activation retards tracer breakthrough but also accelerates tracer elution resulting in the narrower shapes of the signals at both measurement points (Figure 2.5). This observation points out to the altered ferrofluid residence time distribution upon activation of the magnetic field.

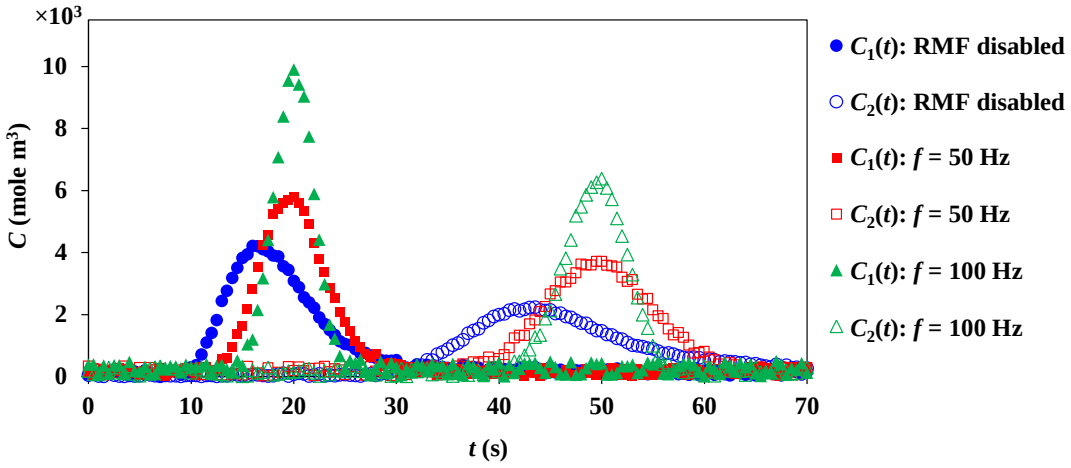

Fig 2.5 Influence of rotating magnetic field frequency on the transient tracer concentration signals measured at two downstream points along capillary for a ferrofluid Poiseuille flow (H_0 = 10^3 kA/m, φ = 0.004, Re = 1).

In the classical view of laminar Poiseuille flow, axial dispersion of the tracer is the outcome of laminar velocity profile and molecular diffusion. The axial velocity component smears the tracer in axial direction according to its magnitude on a specific streamline, *i.e.*, faster tracer transport close to capillary center and longer tracer residence time towards the wall. However, advection transport gives rise to lateral concentration gradients with faster tracer-rich regions near the centerline traveling downstream to become enclaved into the more sluggish tracer-poor regions. The resulting disparities in tracer concentration trigger molecular diffusion, especially in the lateral direction, to smooth out

concentration gradients. Similar smearing effects are expected in the axial direction resulting in stiff/gentle take-off of the RTD curves near the breakthrough time controlled by the amplitudes of centerline velocity, axial diffusion coefficient and depleting power of transverse diffusion to expel radially outwards the tracer.

We have recently determined that *stagnant* ferrofluids in a capillary exhibit anisotropic diffusive transport under stop-flow RMF excitation.[18] This anisotropy is highly sensitive to the capillary arrangement inside the magnet bore and the resulting magnetic field orientation (Figure 2.1). The effective diffusivity in the transverse direction ($D_{\mathrm{rr}} = D_{\theta\theta} = D_{\mathrm{trans}}$) was found to markedly increase by at least an order of magnitude with respect to the tracer molecular diffusion coefficient depending on MNP content in the ferrofluid and RMF frequency (Figure 2.6). However, in the direction normal to RMF rotation axis, the axial effective diffusion coefficient remained approximately the same as the tracer diffusion coefficient ($D_{\mathrm{zz}} = D_{\mathrm{t}}$).[18] These experimental observations on pre-existing anisotropic diffusion in stagnant ferrofluids attributed to rotating magnetic fields imply also possible prevalence of anisotropic diffusive transport in Poiseuille ferrofluid flow in the presence of RMF thus, altering the shape of the tracer concentration signals (Figure 2.5). On the other hand, it is *a priori* not implausible that the externally-imposed RMF may also induce secondary ferrofluid flows as a result of asymmetric stresses. These can alter the ferrofluid velocity field to enhance the tracer convective transport. For instance, if convective transport is enabled in the transverse capillary direction, then distinction between the convective and diffusive mechanisms becomes necessary. In order to gain insights on the role of these two mechanisms and to which extent they affect the ferrofluid RTDs under RMF excitation, it is instructive to solve the FHD equations aided with the advection-diffusion tracer transport equation. To preserve the approach's predictive power, no fitting parameter will be attempted in comparing the FHD-simulated and measured RTDs. To accomplish such task, the constitutive closure for effective diffusion tensors as determined from independent RMF-excited quiescent ferrofluids[18] and the standard spin viscosity as justified above will be implemented in the ferrohydrodynamic/scalar transport model (Eqs. 3-17).

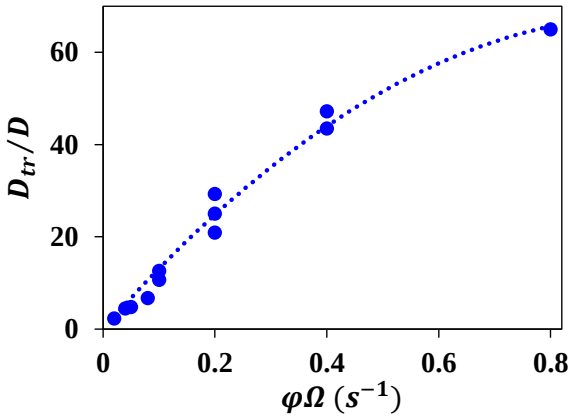

Fig 2.6 Transverse effective diffusivity as function of RMF frequency and MNP volume fraction for water-based cobalt ferrite ferrofluid (range $H_0 = 10^3$ kA/m, φ = [0.001-0.004], f = [0-200] Hz).

2.5.4. Magnetization and magnetic body couple density

Rotation of the magnetic field coerces the magnetic nanoparticles to incessantly re-orientate their magnetic moments constraining the ferrofluid magnetization vector to track the ever-changing magnetic field in order to achieve in-phase synchronicity. Brownian agitation and ferrofluid flow, *e.g.*, vorticity, are the two disruptive factors that frustrate attainment of the equilibrium magnetization. This gives rise to a magnetic body couple density, $\rho\underline{\mathbf{G}} = \mu_0\underline{\mathbf{M}} \times \underline{\mathbf{H}}$ (Eq. 4) which reflects in a lag angle, β, between the magnetization and magnetic field vectors. According to the magnetization transport equation, Eq. 10, the dynamics of lag angle is a measure of the time scale for the linear and angular velocities, and the magnetization vectors to reach steady state. Moreover, assessment of this angle is crucial for analysis of the magnetic body couple density in terms of in-phase ($\sin\beta = 0 \;\forall\; t$) or out-phase ($\sin\beta = \text{Cst} \neq 0 \;\forall\; t$) synchronicity, or simply lack of synchronicity, *i.e.*, $\sin\beta\,(t)$.

Typical simulated dynamics of the lag angle is exemplified upon activation of RMF with frequency of 200 Hz and MNP volume fraction of 0.004 (Figure 2.7). A maximal lag is reached after 25 μs due to MNP inertia that impedes magnetization in-phase tracking of the magnetic field. However, the lag angle ultimately plateaus towards a lower value of 0.0024 rad implying that the frequency of the steady-state magnetization vector is locked onto the RMF frequency while $\underline{\mathbf{M}}$ being slightly lagging behind $\underline{\mathbf{H}}$ as a result magnetic torque. The time required for reaching a ferrohydrodynamic steady-state is of the order of the Brownian agitation time scale, *ca.* 100 μs (Figure 2.7). This duration is deemed brief in comparison with the observational time for tracer elution in the RTD tests (Figure 2.5) to assume that tracer transport occurs essentially under steady-state ferrohydrodynamic conditions.

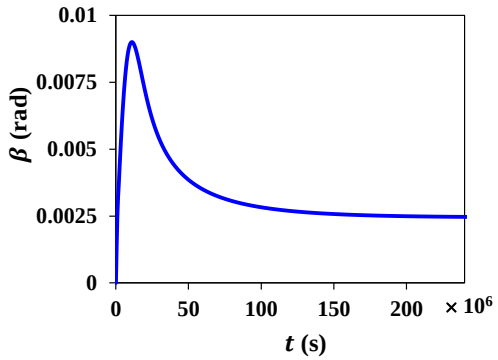

Fig 2.7 Transient response of angle between magnetization and magnetic field intensity vectors (H_0 = 10^3 kA/m, φ = 0.004, Re = 1).

Contour plots in the capillary cross-section of the instantaneous radial, azimuthal and axial projections of the magnetization vector scaled by the amplitude of equilibrium magnetization vector are discussed for the sake of illustration for RMF frequency f = 200 Hz and MNP fraction ϕ = 0.004 (Figures 8a,c,e). The angular distributions of scaled magnetization components at r/R = ½ are shown in Figures 8b,d,f.

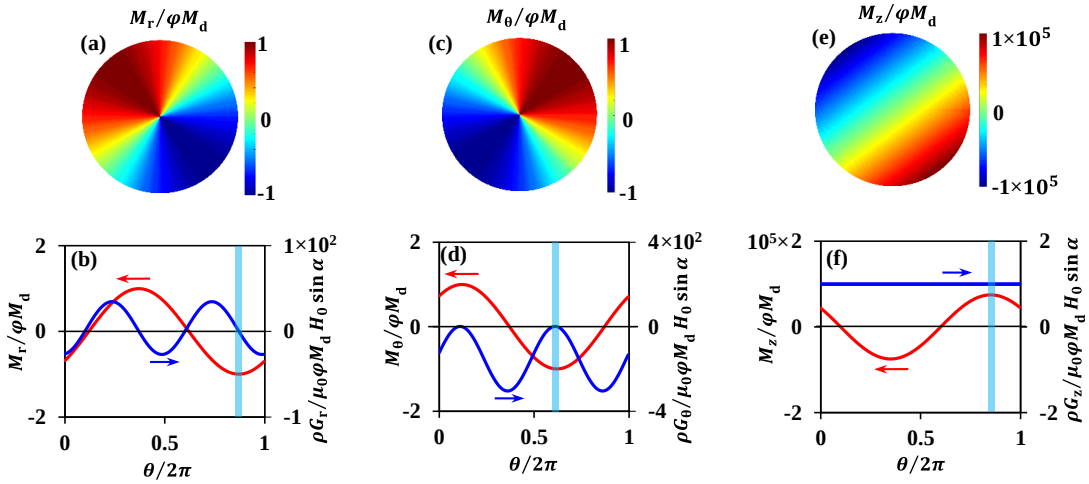

Fig 2.8 Plots of dimensionless magnetization spatial distribution in capillary cross-section and angular distribution of dimensionless magnetization and dimensionless magnetic body couple components in (a,b) radial, (c,d) azimuthal, and (e,f) axial directions (Simulation results at H_0 = 10^3 kA/m, f = 200 Hz, φ = 0.004, Re = 1).

The radial and azimuthal magnetization components are essentially gradient-free in the radial direction (Figures 8a,c). Moreover, although both components bear the sinusoidal behavior of the

applied rotating magnetic field (Figures 8b,d), M_r and M_θ are out-of-phase by $\pi/2$ as expected from the radial and azimuthal RMF components. Numerical simulations predict a component of magnetization in axial direction which varies in both radial (Figure 2.8e) and azimuthal directions (Figure 2.8f). Interestingly, development of axial magnetization defies the fact that the applied RMF has no axial component ($H_z = 0$). Since M_z component cannot be the result of magnetic field component in axial direction, a likely interpretation for the emergence of this component is azimuthal hydrodynamic torque whereby the magnetization vector and ferrofluid vorticity are mutually orthogonal. The ferrofluid vorticity is exclusively in azimuthal direction so that an azimuthally directed magnetization vector cannot yield any axial component as a result of hydrodynamic torque. It can be observed that M_z is remarkably smaller than M_r and M_θ pointing toward the fact that in comparison to magnetic torque, the hydrodynamic torque is not strong enough to shift the axis of MNP rotation to a great extent. On the other hand, M_z and M_r peak positions coincide at the same angular coordinate (vertical bars in Figures 8b,f).

The angular distributions of scaled magnetic body couple in radial, azimuthal and axial directions at r/R = ½ are also shown in Figures 8b,d,f for the same conditions. G_z component is invariant with respect to θ while the remaining $\underline{\mathbf{G}}$ components are sinusoidal functions of angular position. We argued that perturbation of M_r by the ferrofluid vorticity produces an M_z component that oscillates with angular positions. One should have observed an oscillatory behaviour of G_z similar to G_θ and G_r since $\rho G_z = \mu_0(M_r H_\theta - M_\theta H_r)$. However, the hydrodynamic perturbations of M_r and M_θ are too weak thus yielding G_z that is invariant with respect to angular coordinate. The value of G_r averaged over angular positions is zero whereas the scaled G_θ oscillates approximately between zero and -3 yielding non-zero averaged value. Manifestation of body couples in radial and azimuthal directions results from hydrodynamic perturbations of magnetization and from inception of M_z component since $\rho G_r = -\mu_0 M_z H_\theta$ and $\rho G_\theta = \mu_0 M_z H_r$. Note that the lag angle between $\underline{\mathbf{M}}$ and $\underline{\mathbf{H}}$ is very small so that M_z resulting from M_r at its peak magnitude couples to the magnetic field vector slightly ahead of the radial component of magnetization. The resultant body couple forms an angle β with azimuthal axis having a negligible radial component. Thus, zero G_r in addition to G_θ minima coincide with M_r extrema. This is schematically illustrated in Figure 2.9a showing formation of small angle between the body couple vector and azimuthal axis. Where the G_θ cancels the M_θ is extremal (vertical bar in Figure 2.8d) in accordance with the instance of parallel fluid vorticity and magnetization (Figure 2.9b).

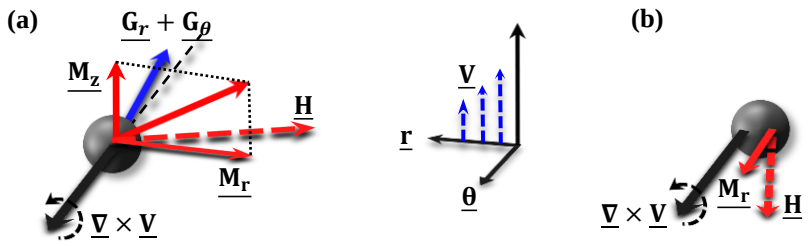

Fig 2.9 Schematic representation of relative orientation of magnetization, magnetic field, vorticity and magnetic body couple vector components when radial component of magnetization is (a) normal or (b) parallel to ferrofluid vorticity

The numerical results show that in ferrofluid Poiseuille flow subjected to transverse uniform RMF, transverse body couple vector components are produced in addition to axial component. The magnitude of resultant hydrodynamic torque is not comparable to magnetic torque because of the low Re number value in our problem. Therefore, the spin of MNP is mainly in axial direction tantamount to situation of nanoparticles in ferrofluid cylindrical spin-up phenomenon.[26] Another outcome of strong axial magnetic body couple is the MNP resistance to ferrofluid vorticity through azimuthal body couple. The averaged value of G_θ over each RMF rotation cycle is non-zero, subsequently impeding MNP synchronized rotation with vorticity and thus triggering positive magnetoviscous effect. Nevertheless, in treating the problem of dilute ferrofluid flow, the magnetoviscous phenomenon remains inconsequential and imposes negligible rotational viscosity as discussed above (Figure 2.3b).

2.5.5. Linear and angular velocities in ferrofluid Poiseuille flow - RMF enabled

We have shown above that the magnetic body couples alter the state of internal angular velocities of MNP by bringing about directional and amplitude deviations pulling the nanoparticles from synchronized rotation with the ferrofluid angular velocity due to pure vorticity as in the absence of magnetic field. The linear velocities are expected to be influenced by coupling of angular and linear momentum balance equations. The whole set of velocity vectors in dimensionless forms is illustrated in Figure 2.10 (f = 200 Hz, φ = 0.004, Re =1). If in absence of RMF the nanoparticles are able rotate at diapason with the ferrofluid angular velocity, $0.5\underline{\boldsymbol{\theta}} \cdot \left(\underline{\boldsymbol{\nabla}} \times \underline{\mathbf{V}}\right)$, (Figure 2.3a), a plot of ω_θ scaled with ferrofluid half-vorticity (Figure 2.10a) shows that under RMF excitation the spin of MNP is drastically suppressed in the azimuthal direction ($\omega_\theta << 1$). Use of the same standard spin viscosity in both instances is worth reminding and signifies that the rotating magnetic field frustrates the natural propensity of the nanoparticle to obey the vorticity directional constraint. The azimuthal MNP spin component, ω_θ, is radially uniform except near the wall where the asymmetric stresses in axial

direction are expected to emerge. It was explained earlier that this component of asymmetric stress has negligible impact on the axial linear velocity component.

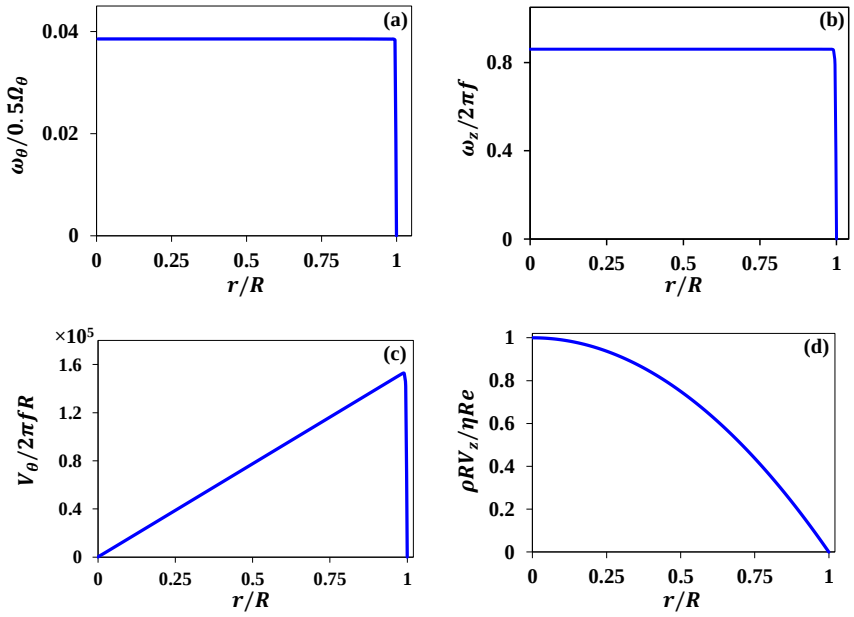

Fig 2.10 Dimensionless internal angular velocities and dimensionless linear velocities in (a,c) azimuthal and (b,d) axial directions (Simulation results at $H_0 = 10^3$ kA/m, f = 200 Hz, φ = 0.004, Re = 1).

The strong magnetic body couple in axial direction determines the angular motion of MNP whereas the axial MNP spin component, ω_z, is very close to the angular frequency of the rotating magnetic field (Figure 2.10b). The radial profile of scaled ω_z is radially uniform except near the capillary wall sharing in that respect similar behavior as its ω_θ component. The asymmetric stress in azimuthal direction is foreseen to be generated in the MNP spin boundary layer producing linear momentum in azimuthal direction and triggering spin-up macroscopic flows. The azimuthal linear velocity (Figure 2.10c) attests for the existence of asymmetric stresses as a result of spin diffusion in the MNP thin boundary layer due to ω_z rotating component of the nanoparticles. The radial profile of axial velocity component (Figure 2.10d) is parabolic with maximum velocity ($V_{\max} = \eta \mathrm{Re}/\rho R$) on the capillary centreline. Since the MNP volumetric fraction is in the order of 10^{-3}, the ferrofluid effective viscosity $\eta + \Delta\eta$ is virtually identical with the ferrofluid intrinsic viscosity. This results in axial velocity radial profiles under RMF excitation identical with classical fully-developed parabolic profile without magnetic field.

According to the numerical results and based on existence of an azimuthal velocity component, the streamlines of ferrofluid Poiseuille flow in presence of RMF presumably have a helical shape with a degree of torsion increasing outwards from capillary centreline to wall. However, torsion of the streamlines declines to zero on the wall since azimuthal velocity declines to zero (Figure 2.10c). Apart from the anisotropic diffusive transport as evidenced under stop-flow RMF excitation,[18] emergence of a tangential velocity component in the RMF-excited Poiseuille flow is also likely to contribute in reshaping the transient tracer concentration behaviour (Figure 2.5). In the next section, we will quantify these two contributions and simulate the transient tracer concentrations along the capillary by solving the coupled advection-diffusion transport within the FHD framework. The contributions of spin-up phenomenon and effective diffusivity will be assessed through comparisons of experimental and theoretical residence time distributions.

2.5.6. Simulated versus experimental RTDs - RMF enabled

Solutions of the advection-diffusion equation coupled to FHD equations are compared in terms of RTDs for two cases assuming isotropic and anisotropic diffusivities. The residence time distribution measurements were carried out at two different RMF frequencies (f = 50, 200 Hz) and MNP volume fractions (φ = 0.001, 0.004), Figures 11a-d. The solid lines represent the average RTD for a given f/φ set and the light blue shades allow assessing the scatter in the repeated RTD measurements in the form of envelopes with 95% confidence level. The dotted lines show the simulated RTDs for an isotropic diffusion tensor $\underline{\underline{\mathbf{D}}} = D_{\mathrm{t}}\underline{\mathbf{I}}$ and the dashed lines are obtained from the anisotropic diffusion tensor with components as defined earlier, *i.e.*, $D_{\mathrm{rr}} = D_{\theta\theta} = D_{\mathrm{trans}}$ and $D_{\mathrm{zz}} = D_{\mathrm{t}}$. Model prediction assuming isotropic $\underline{\underline{\mathbf{D}}}$ agrees relatively well with experimental RTD only for the lowest f/φ values (Figure 2.11a). However, the model predictive power tends to degrade with increasing RMF frequency and/or MNP content in the ferrofluid (Figures 11b-d). The reason for deviations is the important change in the measured RTDs as a function of f/φ that the lack of sensitivity of the predicted RTDs with isotropic $\underline{\underline{\mathbf{D}}}$ fails to describe. The *CoV* of simulated RTDs remains constant around 0.2 for all four cases, whereas that of the measured RTDs decreased from 0.29 (Figure 2.11a) to 0.17 (Figure 2.11d). In addition, inception of a secondary flow induced by the rotating magnetic field reflects in negligible lateral tracer dispersion with marginal impact on the RTD since the calculated *CoV* with or without RMF remained virtually unchanged. It can be inferred that the convective V_θ component remains very low in the tested experimental ranges. Therefore, it can be concluded that scalar transport via spin-up flow is insignificant.

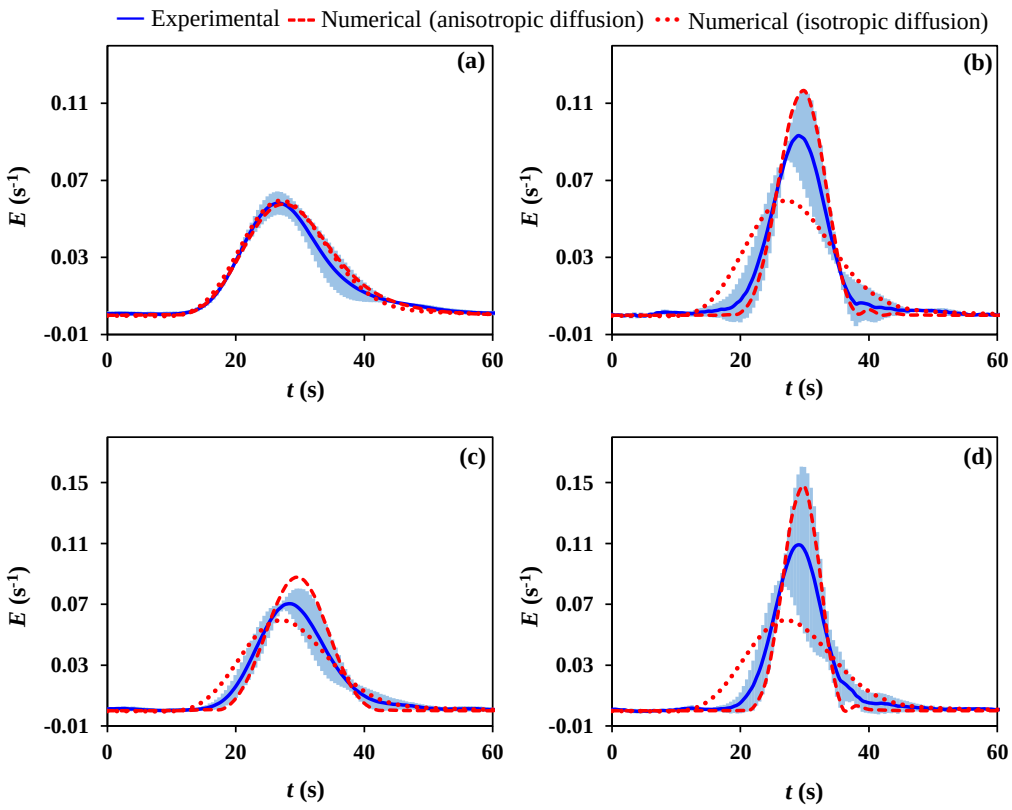

Fig 2.11 Experimental and numerical RTDs obtained for ferrofluid Poiseuille flow (Re = 1) in presence of external RMF ($H_0 = 10^3$ kA/m): (a) f = 50 Hz/ φ = 0.001; (b) f = 200 Hz/ φ = 0.001; (c) f = 50 Hz/ φ = 0.004; (d) f = 200 Hz/ φ = 0.004.

Description of RMF-induced scalar transport by means of an anisotropic effective diffusivity tensor $\underline{\underline{\mathbf{D}}}$ is attempted next to account for the effect of RMF frequency and MNP content on the shape of RTDs. The predicted RTDs are narrower in shape and closer to Gaussian symmetry as RMF frequency or MNP concentration is increased (Figure 2.11). This is tantamount to reduction of axial dispersion in the ferrofluid Poiseuille flow in presence of RMF which is even furthered the higher the frequency and/or the MNP content. The model predictions also remain within the confidence intervals of the experimental RTDs (Figure 2.11), accrediting the depiction of enhanced tracer transverse diffusivity as the main factor in reducing axial dispersion and narrowing the residence time distributions. Note that the effective diffusivity components in the direction normal to RMF rotation axis are a function of f/φ (Figure 2.6), *i.e.*, $D_{\mathrm{rr}} = D_{\theta\theta} = D_{\mathrm{trans}}$ and $D_{\mathrm{zz}} = D_{\mathrm{t}}$. The anisotropic diffusion in ferrofluid is consistent with the observed stretching of breakthrough times under RMF. As a matter of fact, the enhanced mass transport in the transverse direction results in the accelerated depletion of tracer content for the faster centerline streamlines and in flattening the radial

concentration profile. It is thus by expelling more tracer outwards toward the slower streamlines in direction of the capillary wall that contributes to stretching out the breakthrough times. Moreover, the higher the RMF frequency and/or MNP content, the more flattened the radial concentration profiles and thus the longer breakthrough time. Likewise, similar enhanced transverse diffusive transport accelerates the slower tracer initially located near the wall by kicking it out inwards toward the faster streamlines. This is evidenced from the accelerated elution of the longest tracer residence times (Figure 2.11). The combined outcome of RMF-stimulated transverse diffusive transport is manifested in steeper RTD front and back tail and narrower variance as a result of a tracer swarm that is shorter in length with more uniform radial concentration profile.

We must point out an important consequence stemming from the comparison between experimental and theoretical RTD prediction with the aid of FHD framework. The macroscopic convective flows driven by the asymmetric stresses arising from magnetic fields are predicted to be extremely weak. Therefore, spin-up phenomenon cannot be put forward to explain the observed changes in the RTD patterns under rotating magnetic fields. More importantly, the current FHD framework is still too simplified to be able to resolve the nanoparticle-level interstitial transport of scalars that predominantly occurs in the immediate neighbourhood of the individual magnetic nanoparticles. Motion of the interstitial fluid phase in the ferrofluid plausibly undergoes significant deformation and shearing under RMF because of no-slip boundary condition of the interface of fluid and MNP. The MNP angular and linear momentum are constantly exchanged in the presence of external body forces and couples. The exchanged momentum between fluid and MNP gives rise to motion of the fluid with conceivably complex patterns as a result of combined Brownian motion with linear/angular motion proper to the magnetic nanoparticles. Failure in the predictability of current FHD theory for flow problems involving transport of scalars coupled with momentum transport calls for development of more comprehensive formulations capable of resolving the motion in both discrete and continuous phase. An ersatz to this limitation was proposed through recourse to an anisotropic diffusivity tensor which is implemented in the advection-diffusion equation. Provided an independent determination of this tensor is possible the predictive and explanative character of FHD theory is preserved.

2.6. Conclusion

We have observed experimentally that application of external uniform rotating magnetic fields directed perpendicular to Brownian ferrofluid Poiseuille flow reduces axial dispersion and narrows down the residence time distribution by shortening the elution time, stiffening the breakthrough rise and delaying the breakthrough time. Comparatively to the classical RTD in laminar Poiseuille flow

without magnetic field, the increase in RMF frequency and MNP concentration led to narrower RTDs suggesting enhanced transverse mixing aiding ferrofluid Poiseuille flow to approach a plug flow pattern under magnetic field excitation.

Numerical FHD simulations unveiled inception of secondary convective azimuthal flows resulting from RMF-induced asymmetric stresses in the ferrofluid flow. The MNP spin field evolved from the classical one-dimensional vorticity field without magnetic fields, to a two-dimensional field. A strong MNP axial rotation rate nearing the angular frequency of the rotating magnetic field emerged simultaneous to drastic blockage of the nanoparticle rotation in the natural azimuthal direction dictated by the ferrofluid vorticity. Nevertheless, FHD simulations predict no meaningful magnetoviscous effects over the low MNP concentration range investigated. The ferrofluid axial velocity component remains unchanged with respect to the classical Poiseuille velocity parabolic profile whether RMF is enabled or not.

Coupled solution of FHD equations with the advection-diffusion equation using an isotropic tracer diffusivity tensor demonstrated the marginal role of secondary convective azimuthal flows in modifying the shape of the residence time distributions. Advection of ferrofluid in the azimuthal direction was indeed predicted to be effectless on the simulated RTDs whose coefficients of variation kept indifferent upon changes of magnetic field frequency or magnetic nanoparticle concentration. Description of RTDs under magnetic field using independent constitutive closure for an anisotropic effective diffusion tensor determined from RMF-excited quiescent ferrofluids along with assumption of standard spin viscosity led to improved RTD predictions by the coupled ferrohydrodynamic/scalar transport model. Anisotropy in diffusive transport is accounted for because of enhanced diffusion of scalars in the transverse capillary direction explaining shape changes of the RTDs. Plausibly tied to the small scale of the capillary, spin-up phenomenon failed because of the marginal convective effects to predict RTD changes.

Acknowledgments

The authors gratefully acknowledge the Natural Sciences and Engineering Research Council of Canada and the Canada Research Chair on Sustainable Energy Processes and Materials for their financial support.

2.7. Nomenclature

Latin letters	Description	Unit
C	Concentration	mole m^{-3}
d	Nanoparticle diameter	m

D_{t}	Tracer diffusion coefficient	$m^2\ s^{-1}$
D_{rr}	Component of diffusivity tensor in $\underline{\mathbf{r}}$ direction	$m^2\ s^{-1}$
$D_{\theta\theta}$	Component of diffusivity tensor in $\underline{\boldsymbol{\theta}}$ direction	$m^2\ s^{-1}$
D_{zz}	Component of diffusivity tensor in $\underline{\mathbf{z}}$ direction	$m^2\ s^{-1}$
D_{trans}	Component of effective diffusivity tensor in transverse direction	$m^2\ s^{-1}$
$\underline{\underline{\mathbf{D}}}$	Second ranked effective diffusivity tensor	s^{-1}
E	Residence time distribution function	$m^2\ s^{-1}$
f	Frequency of RMF	s^{-1}
$\underline{\mathbf{F}}^m$	Kelvin magnetic force density	$N\ m^{-3}$
$\underline{\mathbf{T}}^w$	Wall shear stress vector	$N\ m^{-2}$
G_r	Radial Magnetic body couple mass density vector magnitude	$N\ kg^{-1}$
G_z	Axial magnetic body couple mass density vector magnitude	$N\ kg^{-1}$
G_θ	Azimuthal magnetic body couple mass density vector magnitude	$N\ kg^{-1}$
$\underline{\mathbf{H}}$	Magnetic field intensity vector	$A\ m^{-1}$
$\underline{\mathbf{H}}^{\mathrm{ext}}$	External magnetic field intensity vector	$A\ m^{-1}$
H_{r}	Radial magnetic field intensity vector magnitude	$A\ m^{-1}$
H_{z}	Axial magnetic field intensity vector magnitude	$A\ m^{-1}$
H_{θ}	Azimuthal magnetic field intensity vector magnitude	$A\ m^{-1}$
$\underline{\underline{\mathbf{I}}}$	Dyadic unit tensor	-
k_{B}	Boltzmann constant	$J\ K^{-1}$
$\underline{\mathbf{M}}$	Magnetization vector	$A\ m^{-1}$
M_{d}	Magnitude of domain magnetization vector	$A\ m^{-1}$
M_{r}	Radial magnetization vector magnitude	$A\ m^{-1}$
M_{z}	Axial magnetization vector magnitude	$A\ m^{-1}$
M_{θ}	Azimuthal magnetization vector magnitude	$A\ m^{-1}$
$\underline{\mathbf{M}}^{\mathbf{e}}$	Equilibrium magnetization	$A\ m^{-1}$
$\underline{\mathbf{n}}$	Unit surface normal vector	-
p	Pressure	$N\ m^{-2}$
$\underline{\mathbf{r}}$	Unit vector in radial direction	-
R	Capillary radius	m
Re	Reynolds number	-
t	Time	s
T	Temperature	K
$\underline{\underline{\mathbf{T}}}$	Pressure-viscous stress tensor	$N\ m^{-2}$
$\underline{\underline{\mathbf{T}}}^{\mathrm{a}}$	Antisymmetric component of stress tensor	$N\ m^{-2}$
$\underline{\underline{\mathbf{T}}}^{\mathbf{m}}$	Maxwell stress tensor	$N\ m^{-2}$
$\underline{\underline{\mathbf{T}}}^{\mathrm{s}}$	Symmetric component of stress tensor	$N\ m^{-2}$
$\underline{\mathbf{v}}$	Linear velocity vector	$m\ s^{-1}$
V_{H}	Hydrodynamic volume of nanoparticles	m^3
V_{max}	Maximum velocity of Poiseuille flow	$m\ s^{-1}$
V_{θ}	Azimuthal linear velocity vector magnitude	$m\ s^{-1}$
$\underline{\mathbf{z}}$	Unit vector in axial direction	-

Greek Letters	**Description**	**Unit**
α	Langevin parameter	-

β	Angle between $\underline{\mathbf{M}}$ and $\underline{\mathbf{H}}$ vectors	-
$\Delta\eta$	Rotational viscosity	kg m^{-1} s^{-1}
$\underline{\underline{\boldsymbol{\varepsilon}}}$	Triadic unit tensor	-
ζ	Vortex viscosity	kg m^{-1} s^{-1}
η	Shear viscosity of ferrofluid	kg m^{-1} s^{-1}
η'	Spin viscosity	kg m s^{-1}
θ	Angle	-
$\underline{\boldsymbol{\theta}}$	Unit vector in azimuthal direction	-
μ_0	Vacuum permeability	N A^{-2}
ρ	Ferrofluid density	kg m^{-3}
ρ^p	MNP density	kg m^{-3}
ς	Bulk viscosity of ferrofluid	kg m^{-1} s^{-1}
τ	Brownian relaxation time constant	s
φ	Volumetric fraction of MNP	-
Ω	Angular velocity of RMF	s^{-1}
Ω_θ	Vorticity in azimuthal direction	s^{-1}
$\underline{\boldsymbol{\omega}}$	Internal angular velocity vector	s^{-1}
ω_θ	Magnitude of internal angular velocity vector in azimuthal direction	s^{-1}

2.8. References

1. Shliomis MI. Effective viscousity of magnetic susspensions. *Soviet Physics Jetp-USSR* 1972;34:1291-1294.

2. Bacri JC, Perzynski R, Shliomis MI, Burde GI. Negative-viscousity effect in a magnetic fluid. *Physicsl Review Letters.* 1995;75:2128-2131.

3. Rosensweig RE. *Ferrohydrodynamics* (1 ed). United States of America: Dover Publications; 1997.

4. Rosensweig RE. Continuum equations for magnetic and dielectric fluids with internal rotations. *Journal of Chemical Physics.* 2004;121:1228-1242.

5. Odenbach S. Recent progress in magnetic fluid research. *Journasl of Physics of Condensed Matter.* 2004;16: 1135-1150.

6. Rinaldi C, Chaves A, Elborai S, He XW, Zahn M. Magnetic fluid rheology and flows. *Current Opinion in Colloid & Interface Science.* 2005;10:141-157.

7. Yang RJ, Hou HH, Wang YN, Fu LM. Micro-magnetofluidics in microfluidic systems: A review. *Sensors and Actuators B Chemical.* 2016;224:1-15.

8. Boroun S, Larachi F. Enhancing liquid micromixing using low-frequency rotating nanoparticles. *AIChE Journal.* 2017;63:337-346.

9. Bitar A, Kaewsaneha C, Eissa MM, et al. Ferrofluids: From Preparation to Biomedical Applications. *Journal of Colloid Science in Biotechnology.* 2014;3:3-18.

10. Ottino JM, Wiggins S. Introduction: mixing in microfluidics. *Philosophical Transactions of the Royal Society A: Mathematical, Physical and Engineering Sciences.* 2004;362:923-935.

11. Boroun S, Larachi F. Role of magnetic nanoparticles in mixing, transport phenomena and reaction engineering - challenges and opportunities. *Current Opinion in Chemical Engineering.* 2016;13:91-99.

12. Boroun S, Larachi F. Prospects of Magnetic Nanoparticles for Magnetic Field-Assisted Mixing of Fluids with Relevance to Chemical Engineering. In: Stefanidis G, Stankiewicz A. *Alternative Energy Sources for Green Chemistry*. United Kingdom: The Royal Society of Chemistry, 2016:198-226.

13. Levenspeil O. *Chemical Reaction Engineering* (2 edn). United States of America: Wiley; 1972.

14. Faraudo J, Andreu JS, Camacho J. Understanding diluted dispersions of superparamagnetic particles under strong magnetic fields: a review of concepts, theory and simulations. *Soft Matter* 2013;9:6654-6664.

15. Hajiani P, Larachi F. Giant effective liquid-self diffusion in stagnant liquids by magnetic nanomixing. *Chemical Enginnering and Processing: Process intensification.* 2013;71:77-82.

16. Hajiani P, Larachi F. Controlling lateral nanomixing and velocity profile of dilute ferrofluid capillary flows in uniform stationary, oscillating and rotating magnetic fields. *Chemical Engineering Journal.* 2013;223:454-466.

17. Hajiani P, Larachi F. Reducing Taylor dispersion in capillary laminar flows using magnetically excited nanoparticles: Nanomixing mechanism for micro/nanoscale applications. *Chemical Engineering Journal.* 2012;203:492-498.

18. Boroun S, Larachi F. Anomalous anisotropic transport of scalars in dilute ferrofluids under uniform rotating magnetic fields – Mixing time measurements and ferrohydrodynamic simulations. Submitted to *Chemical Engineering Journal.* 2019.

19. Torres-Diaz I, Rinaldi C, Khushrushahi S, Zahn M. Observations of ferrofluid flow under a uniform rotating magnetic field in a spherical cavity. *Journal of Applied physics.* 2012;111 07B313.

20. Chaves A, Zahn M, Rinaldi C. Spin-up flow of ferrofluids: Asymptotic theory and experimental measurements. *Physics of Fluids* 2008;20:053102.

21. Boroun S, Larachi F. Tuning mass transport in magnetic nanoparticlefilled viscoelastic hydrogels using low-frequency rotating magnetic fields. *Soft Matter* 2017;13:6259-6269.

22. Finlayson BA. Spin-up of ferrofluids: The impact of the spin viscosity and the Langevin function. *Physics of Fluids* 2013;25:073101.

23. Danckwerts PV. Continous flow systems – Distribution of residence times. *Chemical Engineering Science.* 1953;2:1-13.

24. Hoh JC, Yaacob, II. Polymer matrix templated synthesis: Cobalt ferrite nanoparticles preparation. *Journal of Material Research.* 2002;17:3105-3109.

25. Monz S, Tschope A, Birringer R. Magnetic properties of isotropic and anisotropic $CoFe_2O_4$-based ferrogels and their application as torsional and rotational actuators. *Physical review. E, Statistical, nonlinear, and soft matter physics.* 2008;78:021404.

26. Torres-Diaz I, Cortes A, Cedeno-Mattei Y, Perales-Perez O, Rinaldi C. Flows and torques in Brownian ferrofluids subjected to rotating uniform magnetic fields in a cylindrical and annular geometry. *Physics of Fluids* 2014;26:012004.

27. Harned HS, Hildreth CL. The differential diffusion coefficents of lithium and sodium chlorides in dilute aqueous solution at 25 degrees. *Journal of American Chemical Society.* 1951;73:650-652.

Chapter 3: Enhancing liquid micromixing using low-frequency rotating nanoparticles

Enhancing liquid micromixing using low-frequency rotating nanoparticles

Shahab Boroun, Faïçal Larachi

Department of Chemical Engineering, Laval University, Québec, QC, Canada G1V 0A6

Résumé

L’excitation de nanofluides magnétiques par des champs magnétiques rotatifs a été proposée comme un outil performant de mélange de liquides avec des fonctionnalités de micromélange améliorées. Une étude comparative a été réalisée pour évaluer l'indice de mélange dans des mélangeurs de type T pour les fluides magnétiques et non-magnétiques soumis à des champs magnétiques statiques (CMS), oscillants (CMO) et rotatifs (CMR). L'excitation par CMR a révélé des indices de mélange supérieurs avec de fortes dépendances par rapport à la fréquence du champ magnétique et au contenu en nanoparticules magnétiques. L'impact des types de champs magnétiques sur le micromélange a ensuite été examiné pour des nombres de Re faibles à modérés à l'aide de la réaction de Villermaux-Dushman et du modèle de micromélange IEM. Les temps de micromélange déduits par IEM étaient remarquablement plus courts de près de 4 ordres de grandeur par rapport aux excitations CMO et CMS, et sans champ magnétique. La stratégie de mélange proposée est prévue pouvoir compléter les dispositifs microfluidiques innovants avec des outils et des méthodes de mélange utiles pour le diagnostic du couplage entre la vitesse de transport des espèces et la cinétique intrinsèque.

Enhancing liquid micromixing using low-frequency rotating nanoparticles

Shahab Boroun, Faïçal Larachi

Department of Chemical Engineering, Laval University, Québec, QC, Canada G1V 0A6

3.1. Abstract

Magnetic nanofluid actuation by rotating magnetic fields was proposed as a high-performance tool for liquid mixing with enhanced micromixing features. A comparative study was conducted to evaluate the mixing index in T-type mixers of magnetic and non-magnetic fluids subject to static (SMF), oscillating (OMF) and rotating (RMF) magnetic fields. RMF excitation unveiled superior mixing indices with strong dependences to magnetic field frequency and content of magnetic nanoparticles. The impact of magnetic field types on micromixing was further examined at low and moderate Re numbers using the Villermaux-Dushman reaction and IEM micromixing model. The IEM-inferred micromixing times were remarkably shorter by nearly 4 orders of magnitude in comparison with OMF and SMF excitations, and without magnetic field. The proposed mixing strategy is foreseen to complement innovative microfluidic devices with valuable mixing tools and methods for the diagnosis of the coupling between transport and intrinsic kinetics.

3.2. Introduction

Microfluidic devices for the purpose of mixing, a.k.a. micromixers, have been widely explored in the literature over the past decade. Almost every application in the realm of microfluidics such as micro-analysis, detection, chemical synthesis, emulsification and gas absorption takes advantage of mixing at the microscale. In this respect, efforts for the development of new micromixers with superior mixing characteristics are legion in the literature. A key point in the development of new mixing devices is to understand the dynamics of mixing in order to enable rational tuning of the design/operating parameters to a desired state of mixing. For this purpose, several methods of characterization have so far been developed, such as dilution and spreading of colored or fluorescent species monitored by imaging techniques[1] or computational methods to decipher the governing mechanisms of diffusion-convection phenomena.[2] Mixing which is known to be controlled by molecular diffusion at the microscale can be prompted by increasing the concentration gradients and reducing the diffusion path in micro-structured micromixers, *i.e.*, passive mixing, or by eliciting formation of smaller fluid length scales using external energy stimuli, *i.e.*, active mixing.[3] The importance of mixing arises when it is accompanied by molecular-level phenomena such as a chemical reaction. It is well established that the rate of molecular events is intimately related to the rate at which molecular-level mixing is accomplished.[4-6] Since mixing index alone is not a comprehensive metric of how molecular-level mixing and other micromixer phenomena may interact with each other, researchers introduced the concept of micromixing as a more relevant indicator.[4]
The concept of micromixing originally emerged in studies of large-scale reactors for prediction of product quality, *e.g.*, estimation of conversion and selectivity of chemical reactions[4] or particle size distribution in reactive precipitation.[7] With the advent of chemical processing at the microscale, micromixing studies percolated into the realm of micro-reaction engineering.[8] Numerous studies have revealed that the signature of micromixing has a profound influence on the selectivity and yield of chemical reactions in micromixers where, if inadequately deployed, poor mixing will result in a drastic reduction in product quality.[9-11] This may be a serious concern for chemical reaction systems where micromixing and reaction characteristic times are of the same magnitude. Therefore, product distribution is not solely determined by the reaction kinetics as the micromixing rate also comes into play.[12-14]

A plethora of microfluidic devices has been devised for micromixing in micro-reaction applications where various mixing principles have been implemented.[3,8] Among the ones with fascinating potential concern microfluidics mixing based on the excitation of magnetic nanoparticles (MNP) by a magnetic field. Appealing attributes to ascribe to such active mixing based on external magnetic

fields are circumvention of the challenging manufacturing methods encountered in the fabrication of passive mixers with complex patterns and reduction of fabrication costs thereof. Magnetic-field mixing attractiveness also arises from its simplicity and ease in remote controllability.[15] Simplicity in manipulation and flexibility in the generation of various types of magnetic fields also makes magnetic-field driven mixing an attractive tool in microfluidics.[16] Furthermore, from a reaction engineering perspective, magnetic nanoparticles, as a bridge between homogeneous and heterogeneous catalysis, may be propelled into new realms of applications where both chemical reactions and manipulation of transport phenomena can be merged into the very same single nano-objects. Magnetic micro-particles as well as colloidal MNP dispersions, known as ferrofluids, have previously been utilized for mixing purposes in micro-devices in several experimental and theoretical studies.[2,17-22] The mixing mechanisms put forward are mostly based on the activation of a magnetic body force (Kelvin force) in static and oscillating magnetic fields[17-19] or from inducing a bulk fluid movement by means of a collective motion of magnetic micro-particles.[20-22] In addition to those magnetic mixing approaches, our group has recently demonstrated the capability of rotating magnetic fields (RMF) in the actuation of magnetic nanofluids to promote molecular diffusion.[23] Attempts to unveil the mass transport mechanism based on the spinning effect of MNPs have been highlighted in a series of experimental studies.[23-25] For instance, it has been shown that the apparent self-diffusion coefficient of a magnetic nanofluid subject to RMF can be enhanced by a factor 10^2 at moderate magnetic field frequency and intensity.[23] These findings clearly point out to potential applications of magnetic fields in scalar transport phenomena.

The present authors hypothesize that the observed stimulated transport properties of magnetic nanofluids in rotating magnetic fields can also be beneficial for enhancing mixing and micromixing in microfluidic configurations. In this regard, this study presents the first measurements on the mixing index and micromixing times for two miscible streams seeded with MNPs and mixed in T-type mixer under static (SMF), oscillating (OMF) and rotating (RMF) magnetic fields. A novel and facile electrical conductimetry method was developed for the characterization of mixing index *via* an acid-base neutralization reaction while micromixing was investigated by means of implementation of the Villermaux-Dushman chemical and analysis of the micromixing times using the interaction-by-exchange-with-the-mean (IEM) model.

3.3. Experimental

3.3.1. Nanofluid preparation

Water-based magnetic nanofluids were prepared by dispersing in water trisodium-citrate surfacted magnetic nanoparticles synthesized using well-established Fe^{2+} and Fe^{3+} co-precipitation protocols. Magnetic characterization was carried out using an alternating gradient magnetometer (MicroMag model 2900, Princeton Instrument) at 298 K for determining both nanoparticle and nanofluid magnetizations. The distribution of hydrodynamic diameters of MNPs in the colloidal dispersion was measured by a dynamic light scattering method by means of a Zetasizer Nano 6 (Malvern Instruments Ltd) using a 4 mW He-Ne laser at 633 nm wavelength. The synthesis procedure of MNPs, the nanofluid preparation, and the characterizations of magnetization and size distribution are provided with full details in the Appemdix.2.

3.3.2. Magnet device

Various magnetic fields were generated by a two-pole stator winding with 3 pairs of coils around the periphery of a cylindrical magnet bore. The bore dimensions were 55 mm in height and 45 mm in inner diameter. Uniform static (SMF), oscillating (OMF) and rotating (RMF) magnetic fields can be generated inside the magnet bore according to the types of currents fed to the coils. For generating SMF, two adjacent coil pairs are fed by a DC current source (Agilent Tech, N8739A) whose intensity is adjustable from a power source generating controllable magnetic field intensities (Figure 3.1a). For an OMF, two adjacent coil pairs are fed by a 50 Hz AC current using an AC variable frequency drive (Invertek Drives, Optidrive E2) with adjustable current (Figure 3.1b). The root-mean-square (rms) of OMF intensity was classically calculated for a sine wave, $H_{rms} = H_{amplitude}/\sqrt{2}$. Finally, all 3 coil pairs are fed by a 3-phase AC current, 120° out of phase, for RMF excitation so that the resultant magnetic field inside the bore rotates with a frequency equal to that of the balanced AC currents. The intensity and frequency of RMF are adjusted by means of a variable frequency drive (ABB, ACS150, 2.2kW) coupled to a power source (Figure 3.1c). In all three configurations, the magnetic field direction was perpendicular to the central bore axis as sketched in Figures 3.1a-c.

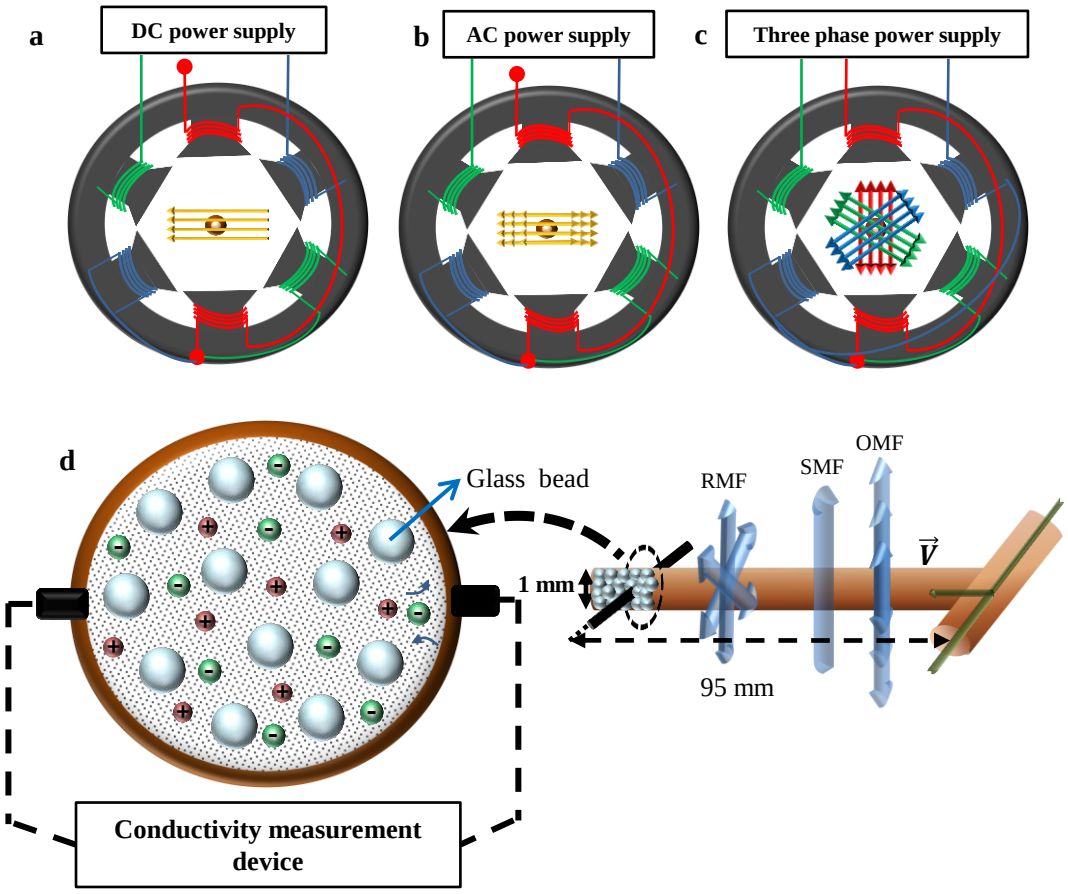

Fig 3.1 Schematic representation of magnet, mixing device and conductivity electrodes. The magnet can generate a) SMF when energized by DC power supply, b) OMF when energized by AC power source and c) RMF when energized by a three-phase power supply. d) Possible configurations of mixing device relative to three types of magnetic fields. Conductivity electrodes are in contact with the fluid passing through a bed of glass beads while anions and cation periodically migrate between electrodes excited with AC current.

3.3.3. Mixing device

The device used for the mixing studies consisted of a 1-mm ID tubular glass capillary tube. A T-junction was mounted on one tube end to serve as feeding section by bringing into contact two separate fluid streams to be mixed with each other along the capillary tube. The total length of the T-junction/tube assembly was 95 mm. The capillary was equipped with a pair of stainless steel electrical conductivity electrodes installed 10 mm upstream of the tube outlet (Figure 3.1d). The tube length was filled over a distance of 20 mm from the outlet with spherical glass beads around 116 μm in diameter. The role of the glass bead segment is to liken the radial velocity and concentration profiles to those of a quasi-plug flow in the region where electrical conductivity measurements are acquired.

By ensuring transverse velocity and concentration gradients are smoothed out in the measurement region substantially simplifies the quantitative calibration procedure of the probes as well as retrieval of concentrations from the electrical conductivity measurements. Referred to in short as conductivity, the electrical conductivity of the fluid was measured continuously by means of an electrical conductivity meter (Omega CDTX-90) connected to the electrodes pair. To minimize unwanted electrochemical reactions and alteration of the electrodes, a 50-Hz AC current was applied to the electrodes. For all the mixing experiments, the capillary tube was set parallel to the central axis of the magnet bore so that the applied magnetic fields in above three configurations were normal to the flow direction (Figure 3.1).

3.3.4. Model reaction systems

3.3.4.1. Acid-base neutralization for probing mixing index

For the mixing studies, a method was developed for evaluating the extent of mixedness on the basis of measured conductivities to retrieve conversions of a model neutralization reaction between a strong base and a strong acid. For this purpose, separate streams of equimolar solutions of nitric acid and sodium hydroxide (1 mM) were simultaneously fed through the T-junction at equal flow rates by means of a two-piston precision syringe pump. The basic stream was prepared (See Appendix.2) by dilution of a stock nanofluid (φ = 0.1 mass fraction of surfactant-coated MNPs) with a sodium hydroxide solution of appropriate concentration to result into a magneto-basic colloidal dispersion with MNP mass fractions in the [0.01 – 0.05] range. Because of stability issues of the acidic stream, this latter was kept as MNP-free stream. This configuration enabled investigations of mixing in the capillary tube of an acidic solution and a magneto-basic suspension. In view of the following statements, the degree of mixedness can be attributed to the conversion of the neutralization reaction: i) acid-base neutralization is instantaneous whereby each proton reacts with hydroxide anion right upon an effective collision; ii) effective collision of reactants is to be understood according to Danckwert's perfectly mixed conditions. That is to be at minimum scale of segregation where the mass exchange between two points is dominated by diffusion and the concentrations of reactants at each point are equal satisfying the condition of zero intensity of segregation; iii) Kohlrausch's law is valid at the utilized dilution level and the molar conductivity of each electrolyte component is equal to its limiting molar conductivity:

$$\Lambda_j \approx \Lambda_j^0 \;\&\; \kappa_j \approx C_j \Lambda_j^0 \tag{3.1}$$

In Eq.1, Λ_j denotes the conductivity of electrolyte j.

Since the measured conductivity is an outcome of the conductivities of nitric acid, sodium hydroxide and produced salt, *i.e.*, sodium nitrate electrolytes, the chemical conversion of the neutralization reaction can be interpreted as an index for mixing quality. In this regard, three situations are plausible for equimolar streams of acid and base at equal flow rates:

i) Perfect mixing: leads to a minimum conductivity (κ_{min}) where only sodium nitrate contributes to electrical conductivity. It is straightforward to show that the solution conductivity is equal to $NaNO_3$ conductivity times half the molar concentration of either acid or base:

$$\kappa_{min} = \frac{1}{2} C \Lambda^{\circ}_{NaNO_3} \tag{3.2}$$

ii) Total segregation: Parallel configuration of two streams with no mixing and zero reaction conversion is assumed in total segregation conditions. This assumption facilitates demonstration of the effect of various parameters such as residence time, Re number and magnetic field stimuli on the mixing phenomenon between the two streams. The reactants conductivity κ_{max} is the average conductivity of the two adjacent streams:

$$\kappa_{max} = \frac{C}{2}\left(\Lambda^{\circ}_{HNO_3} + \Lambda^{\circ}_{NaOH}\right) \tag{3.3}$$

iii) Partial mixing: In the intermediate situation where some of the protons and hydroxides are converted into water molecules, the measured electrical conductivity ($\kappa_{min} \leq \kappa_{measured} \leq \kappa_{max}$) is contributed by the unreacted protons and hydroxides as well as the produced sodium nitrate.
A mixing index, α, varying between 1 (best-case scenario) and 0 (worst-case scenario) can be defined according to the three cases above:

$$\alpha = \frac{\kappa_{max} - \kappa_{measured}}{\kappa_{max} - \kappa_{min}} \tag{3.4}$$

In Eq.4, κ_{max} and κ_{min} are estimated using the known limiting conductivities of the individual cations and anions. It is worth reminding that the measured electrical conductivities being cross-sectionally averaged entail that the mixing quality calculated from Eq.4 is clueless about the *spatial* mixing information.

The use of Kohlrausch's law for estimation of electrolyte conductivities was verified as detailed in the Appendix.2 where conductivities of individual acidic solution and magneto-basic suspension were also measured in the mixing device and compared with their limiting molar conductivities.

3.3.4.2. Villermaux-Dushman reaction for probing micromixing

The mixing index as defined above remains clueless with regard to the impact of micromixing on the product distribution. Hence, the Villermaux-Dushman reaction system which consists of a set of two competitive reactions is the standard method used to probe the relationship between product selectivity and micromixing. The first reaction is an *instantaneous* neutralization of borate anions with protons:

$$\mathrm{H^+ + H_2BO_3^- \overset{K_1}{\leftrightarrow} H_3BO_3} \tag{3.5}$$

$$pK_1 = 9.2 \tag{3.6}$$

Whereas the second one corresponds to iodine dismutation also known as Dushman reaction:[12]

$$\mathrm{6H^+ + IO_3^- + 5I^+ \rightarrow 3I_2 + 3H_2O} \tag{3.7}$$

For which the irreversible rate equation is given by:

$$r = k[\mathrm{IO_3^-}][\mathrm{H^+}]^2[\mathrm{I^-}]^2 \tag{3.8}$$

Where the rate constant *k* depends on the solution ionic strength, I_s:[26]

$$\log_{10} k = \begin{cases} 9.28105 - 3.664\sqrt{I_s} & I_s > 0.166\ mol/L \\ 8.383 - 1.5115\sqrt{I_s} + 0.23689 I_s & I_s < 0.166\ mol/L \end{cases} \tag{3.9}$$

Iodine is in instantaneous equilibrium with iodide (I^-) and triiodide (I_3^-) anions according to:

$$I_2 + I^- \overset{K_2}{\leftrightarrow} I_3^- \tag{3.10}$$

$$\log_{10} K_2 = \frac{555}{T} + 7.355 - 2.575\, log_{10}\, T \tag{3.11}$$

In the instance of fast micromixing where the characteristic time of homogenization of ions at diffusional subrange, *i.e.*, micromixing time, is shorter than that of the Dushman dismutation reaction (Eq.7), the majority of protons are consumed by the instantaneous neutralization reaction (Eq.5). Conversely, for longer micromixing times, the slow distribution of ions leads to concentrated zones of protons in borate-depleted aggregates contributing to the accumulation of larger amounts of triiodide ions. Hence, higher triiodide concentrations for a specific initial concentration of reactants implicitly indicate poor micromixing feature.

For probing experimentally the relationship between micromixing and the various types of implemented magnetic fields, two separate streams were simultaneously fed through the T-junction by means of a two-piston syringe pump under controlled equal volumetric flow rates. The first stream

consisted of a mixture solution of boric acid, potassium iodide, potassium iodate, sodium hydroxide and MNPs whereas the second was a sulfuric acid solution at lower pH with a deficient number of protons based on the required stoichiometric amount for borate neutralization reaction (Eq.5). For the reason stated earlier regarding colloidal stability for the acid-base reaction system, preparation of magnetic sulfuric acid dispersions was not possible as the resultant nanofluid rapidly agglomerated during the course of experiment.

The reacted stream at the capillary outlet was collected in vials and the triiodide concentration was measured by UV-vis spectrometer (Varian-Cary 300) where according to Beer-Lambert law, the concentration of triiodide was monitored by measuring its absorbance at 353 nm wavelength.[14] To allow analysis of a transparent solution prior to spectrophotometric measurements, the magnetic nanoparticles were separated magnetically from the sampled effluent. Also, for speeding up the MNP magnetic separation, sodium chloride was added to destabilize the sampled colloidal dispersion. Each cycle of sample collection, separation of MNPs and concentration measurement was repeated three times to make sure steady-state conditions were achieved. As explained elsewhere, it was crucial to maintain the measured triiodide concentrations in a range whereby the optical density had to be constrained for variations between 0.1 and 2.5.[14] Various mixing strategies and operating parameters resulted in triiodide concentrations with absorbances out of this validity range. Hence, four different sets of reactant concentrations were tuned by trial and error in order to control the rate of Dushman reaction and to identify the best conditions to fulfill the restriction on the absorbance range. These concentration sets are listed in Table 4.1.

3.4. Results and Discussion

3.4.1. Acid-base neutralization for probing mixing index without magnetic field

Figure 3.2 shows the characteristic trough-like evolution of the mixing index, α, of acidic and magneto-basic streams (MNP mass fraction, φ = 0.05) in the T-mixer as a function of Re number when the magnetic field is disabled. At very low Reynolds numbers (Re ~ 1) mixing is complete as the residence time of the two streams down to the measurement point is long enough to achieve perfect mixing. At this condition, mixing between the parallel streams is controlled by molecular diffusion. Mixing index then deteriorates with increasing Re reaching its lowest values at moderate Re numbers [10 - 200] as a result of the reducing residence times. However, as Re is further increased (Re > 200), α starts climbing over again on the onset of a vortex flow prompting collisions between streamlines in the T-junction.[27] The streamlines from the two individual streams periodically protrude into one another giving rise to eddy like patterns whose characteristic size is equal to the tube

diameter. By mutually engulfing into the incipient eddies, the two streams undergo stretching and elongation of their filaments. As a result, in an Eulerian reference frame, more concentration gradients emerge and eventually the continuous deformation process yields shorter length scales for diffusional transport.[28] Such reduction in length scale is responsible for the rapid mixing at higher Reynolds numbers. Our observed experimental trends of mixing index are in qualitative agreement with numerical simulations of mixing in similar geometries over a similar range of Re numbers.[27] Since mixing index was at its lowest for Re in the range [10 - 200], the mixing experiments under magnetic field stimulation were performed at Re = 10 to better contrast the effects of various parameters (magnetic field type, intensify, frequency, MNP concentration) on the mixing index.

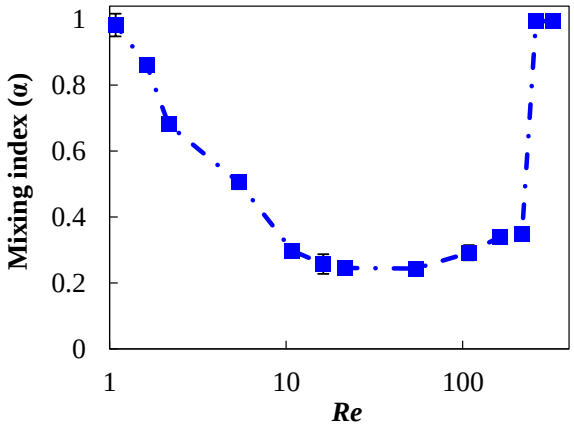

Fig 3.2 Mixing index as a function of Re number and magnetic field disabled. Experiments carried out with MNP mass fraction φ = 0.05. Vertical bars show repeat-test standard-deviations.

3.4.2. Acid-base neutralization for probing mixing index with magnetic field enabled

3.4.2.1. Observations under SMF

Figure 3.3a depicts the mixing indices as a function of MNP mass fraction, φ, in the magneto-basic suspension at a constant intensity of static magnetic field (H = 53 kA/m). A tepid response of mixing to SMF stimulation is observed at low φ values; however, mixing index at φ = 0.05 is notably higher in comparison with the one measured without magnetic field. As shown in Figure 3.3b for φ = 0.05, the mixing index is further improved upon application of a higher-intensity SMF. This figure also suggests that if SMF intensity > 90 kA/m were applied, accomplishment of perfect mixing would have been possible though this limit was above the specification of our designed magnet. The increasing trend of mixing index as a function of φ and H parameters is to be rationalized through a

mechanism for enhanced mixing governed by the Kelvin body force which directly depends on both parameters.

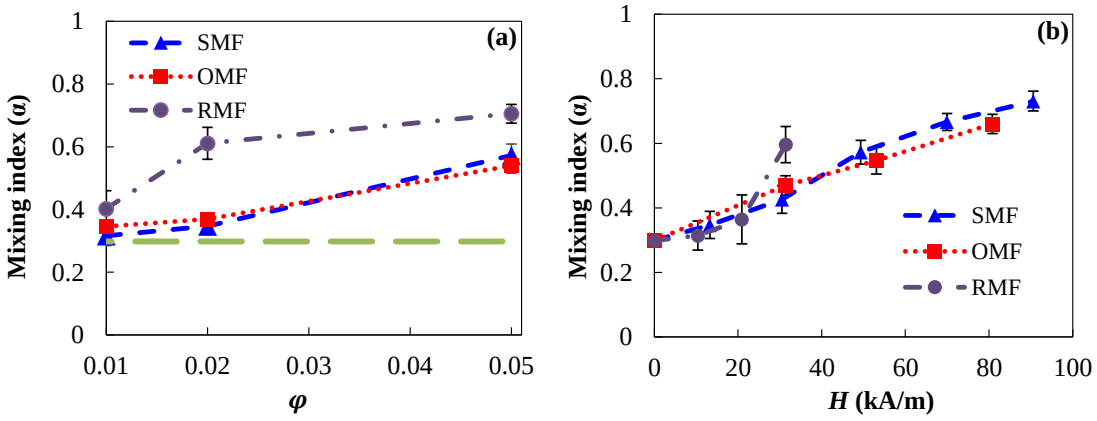

Fig 3.3 a) Mixing index as a function of φ in SMF (H = 49.3 kA/m), OMF (H = 53 kA/m) and RMF (H = 31.4 kA/m, f = 25 Hz): α with OFF magnetic field is shown as dashed line. b) Mixing index as a function of H in SMF, OMF and 25 Hz RMF (φ = 0.05). Vertical bars show repeat-test standard-deviations.

For a magnetic material subject to a *uniform* magnetic field, the Kelvin body force vector is expressed as:[19]

$$\mathbf{F_m} = \frac{1}{2}\mu_0 \mathrm{H}^2 \boldsymbol{\nabla}\chi \tag{3.12}$$

In Eq.12, μ_0 and χ are the vacuum permeability and the nanofluid magnetic susceptibility, respectively. According to the law of superparamagnetic magnetization of a colloidal ferrofluid, χ can be written as:[29]

$$\chi = \frac{dM}{dH} = \varphi' M_b \frac{dL_\beta}{dH} \tag{3.13}$$

Where L_β, M_b and φ' are, respectively, the Langevin function, the domain magnetization of MNPs, and their volume fraction in nanofluid. Eq.13 reveals that at constant magnetic field, magnetic susceptibility is directly proportional to MNP volume fraction. Recalling that the acidic solution stream is initially deprived of MNPs, increasing MNP fraction in the magneto-basic suspension will inevitably lead to increased spatial gradients of the magnetic susceptibility crosswise of the capillary tube. Clearly, such gradient is initially normal to the flow direction. Numerical simulations[19,30] related the governing mechanisms of enhanced mixing to a magnetic body force being exerted oblique to the flow direction on a sheared fluid. Such obliquity stems from a gradient of the magnetic susceptibility

which alters the uniaxial velocity profile by inducing secondary flows and velocity components collinear with the direction of the magnetic body force. This secondary flow generates patterns that break flow symmetry and consequently the superparamagnetic and non-magnetic fluids are brought into contact over a shorter mean distance between two fluid segments thus the shorter mixing times.

It should be emphasized that in contrast to the conventional imaging techniques employed in the characterization of ferrofluid mixing and which rely on a grayscale analysis of MNP concentration, the presently utilized method of mixing characterization is independent of MNP content. It signifies that mixing is achieved when the hydroxide ions in the host nanofluid and the protons in the acidic stream are reacting and where the presence of MNPs is not *sine qua non* condition for the determination of the mixedness level. It further confirms that the bodily acting character of the Kelvin force on a magnetic nanofluid drives the entire nanofluid suspension and not exclusively the magnetic nanoparticles.[29]

3.4.2.2. Observations under OMF

The results of mixing index as a function of MNP mass fraction and rms intensity in OMF are also exposed in Figure 3.3. It should be noted that currents and voltages applied in generating SMF and OMF were purposely adjusted to yield equal SMF and rms OMF intensities. Similar to SMF, both φ and H operating parameters promote as they increase the mixing indices. Interestingly, mixing indices as a function of φ and H are almost identical to those obtained upon applying SMF. The dominant mechanism of an OMF-excited mixing is believed to be tantamount to that prevailing under SMF with similar direction of the Kelvin body force acting on the magnetic fluid. This similarity has been confirmed by numerical investigations of microfluidic mixing between a ferrofluid and a paramagnetic fluid under SMF and OMF excitations.[30] It should be pointed out that mixing enhancement *via* negative magnetoviscothinning mechanism, in which magnetic energy translates into kinetic energy gained by the nanofluid, is not plausible in our experimental conditions as we have previously studied the effect of low-frequency OMF on magnetoviscosity of a sheared ferrofluid.[25]

3.4.2.3. Observations under RMF

Figures 3.3 and 3.4 describe the effects on the mixing index of intensity (H), MNP mass fraction (φ) and frequency (f) of the rotating magnetic field (RMF). It can be observed that upon increasing one factor at a time, all three parameters improve the mixing index. Contrary to SMF or OMF, application of RMF at frequencies higher than 50 Hz enabled attaining perfect mixing for comparable magnetic field intensities and MNP mass fractions (Figure 3.4).

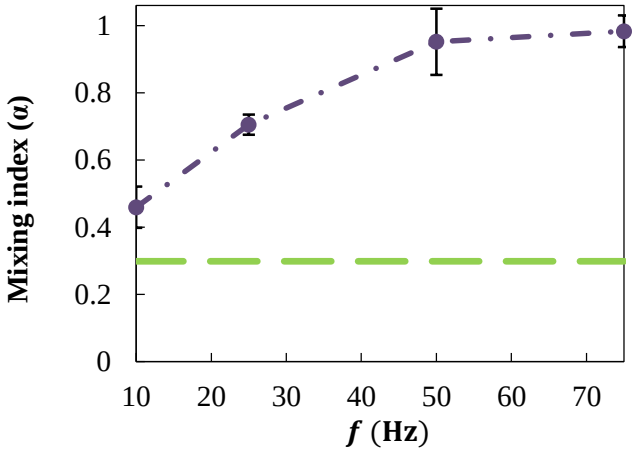

Fig 3.4 Mixing index as a function of frequency at H = 31.4 kA/m and φ = 0.05: with OFF magnetic field is shown as dashed line. Vertical bars show repeat-test standard-deviations.

Although Kelvin forces resulting from spatial gradients of the magnetic susceptibility also manifest when a uniform RMF is applied, the observed enhancement of mixing index cannot be attributed to the sole action of this body force. This is exemplified in Figure 3.5 where it is instructive to compare mixing indices at equal MNP volume fraction and almost identical magnetic field intensities for the three types of magnetic fields. Therefore, interpretation of the remarkable mixing behavior under RMF requires identification and explanation of the various phenomena which take part in the course of fluids homogenization.

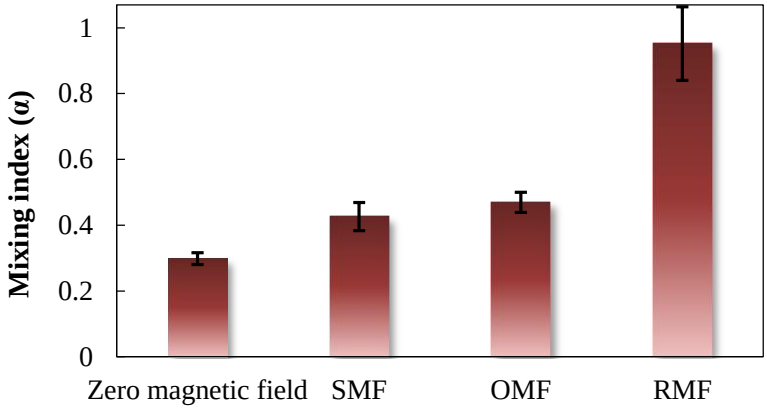

Fig 3.5 Mixing index without magnetic field (reference condition) compared with that of RMF (31.4 kA/m, 50 Hz), SMF (30.5 kA/m) and OMF (31.4 kA/m). Vertical bars show repeat-test standard-deviations.

In the early stages of mixing, the scale of segregation between the two streams is reduced by the action of two dominant bulk fluidic motions. The first draws its source from the Kelvin force and the

relevant mixing mechanism outlined earlier in the case of SMF or OMF. The second source of motion is elicited by the external angular momentum in the magnetic nanofluid possibly through a spin up of the flow in the azimuthal direction.[31] This external angular momentum is an outcome of the constant exchange between MNPs angular momentum and the linear momentum of the nanofluid.[31] MNP angular momentum manifests itself as an internal rotation of the fluid sub-continuum at a rate ($\boldsymbol{\omega}$), which is bodily coupled to the volumetric externally-exerted magnetic torque ($\mu_0 \mathbf{M} \times \mathbf{H}$) and subject to surface couples determined by the spin viscosity.[32] Apart from inherent inertia in the axial direction of the sheared flow, both magnetic torque and Kelvin force driving the fluids motion break each stream into smaller segments thus reducing the scale of segregation. It is likely that the Kelvin force alone cannot reduce in a marked manner the scale of segregation associated with very short diffusion times; otherwise mixing indices of similar levels would have been achieved as in the case of SMF and OMF excitations (Figure 3.5). In addition, mixing cannot be attributed exclusively to spin up effect since it has been shown that ferrofluids with no free surface in uniform RMFs do not exhibit notable tangential bulk flows.[33] A mechanism accountable for such mixing amplification is giant molecular diffusion in magnetic nanofluids subject to RMF.[23] The augmented diffusion inside magnetic fluid media under RMF compensates for the long diffusion times associated with the length scales between two fluid segments resulting globally in rapid homogenization rates. The magnetic fluid segments become presumably diluted in terms of MNP content which can alter the dynamics of mixing over time. The function of rotating MNPs is not halted notwithstanding such dilution. There is thus still a potential for the MNPs to penetrate into the non-magnetic stream to enhance mass transport. However, the efficacy of this mode would anyhow by hampered by the lower pH of the acidic stream which would compromise, as alluded to earlier, colloidal MNP stability.

The observed enhancement of mixing as a function of H, φ and f may also benefit from the interpretations put forward by Hajiani and Larachi in their studies of Taylor dispersion of capillary nanofluid flows.[24,25] From a physical point of view, numerous experimental and theoretical studies have also demonstrated more vigorous bulk movement of a ferrofluid at higher intensities of rotating magnetic fields besides the stronger Kelvin force which can accelerate fluid break-up at the early stages of mixing. Furthermore, according to figure A2.2 (Appendix.2), our tested MNPs exhibit some size polydispersity. MNPs belonging to the lower-end of the size distribution should require larger external magnetic torques to oppose Brownian agitation to be able to smoothly track the rotating pattern of the RMF and thus to function as nanostirrers. Furthermore, the volume of fluid where mass transport is dominated by intrinsic molecular diffusion shrinks down as MNP concentration is raised leading to mass transport dominated by nano-stirring effects. Similarly, by increasing RMF

frequency, the fluid spheroidal shells surrounding each rotating nanoparticle are likely to grow in size resulting in fluid volumes spared by MNP stirring in retreat.

3.4.3. Villermaux-Dushman reaction for probing micromixing with magnetic field enabled

The results above and interpretations thereof highlighted the role of magnetic fields, and especially RMF as the most influential magnetic field stimulation to noticeably intensify the overall mixing performances by means of rotating MNPs. This section proposes to further investigate the MNP-driven mixing mechanisms through micromixing studies to gain more insights on the rate of diffusional transport. The aim here is to specifically highlight prominent features of magnetic fields to generate small scales for mass transport in comparison with those commonly reported in absence of magnetic fields.

The most important preliminary condition to be met for conducting Villermaux-Dushman reactions is that reactants and products alike must be present in a completely homogenized state (or perfect mixing) at the exit section of the mixing device. This is a crucial point as partially mixed reactants might undergo a sequence of post-mixing alterations inherent to the sampling protocol down to the sample collection vials. As uncontrollable as this sequence may be, post-mixing alterations are likely to corrupt reproducibility of the results under similar experiments. Therefore, the first step is to identify which flow rates are able to achieve a complete mixing which is independent of parameters other than Re number. According to Figure 3.2, the mixing index at *Re* = 1 and 260 is 1 without magnetic field; it will remain so *a fortiori* under application of a magnetic field. Therefore, experiments at these *Re* numbers – referred to as low-Re and moderate-Re tests – are retained to unveil distinct diffusional transport features influencing the micromixing signature under magnetic fields.

3.4.3.1. IEM model for interpretation of micromixing phenomena

Since product concentration is not solely a function of micromixing time because of the multitudinous initial concentration sets explored in our experimental procedure, accounting for triiodide concentration for micromixing comparisons results in inadequate interpretations. Furthermore, it is necessary to translate experimental results into a generic parameter which allows comparisons between dissimilar studies. In this respect, applying a micromixing model to convert product concentrations into micromixing times circumvent such ambiguities.[14] A simplified interaction-by-exchange-with-the-mean (IEM) model was used for the interpretation of the micromixing results.[14,34,35] This model assumes that reactions take place in a subrange where the last stage of

mixing occurs through molecular diffusion between the two fluid segments to be mixed. Each segment is subject to continuous mass exchange over the length scale of the subrange and governed by molecular diffusion mechanism. While primary micromixing models such as engulfment-deformation-diffusion (EDD) are mostly based on calculating concentration distributions accompanied by reaction in the viscous subrange,[36] in the simplified IEM model used here, a uniform distribution of components is assumed inside each segment. By expressing reactant and product mass balances for each segment, a set of ordinary differential equations is yielded to express the rate of consumption/production as a function of micromixing time (t_m):[34]

$$\frac{dC_{1,i}}{dt} = \frac{1}{t_m}\left(\langle C_i \rangle - C_{1,i}\right) + R_{1,i} \tag{3.14}$$

$$\frac{dC_{2,i}}{dt} = \frac{1}{t_m}\left(\langle C_i \rangle - C_{2,i}\right) + R_{2,i} \tag{3.15}$$

In Eqs. 14,15, $\langle C_i \rangle$ is the ith-component concentration, averaged over both segment volumes. By solving these differential equations for all the components participating in the reactions, the product concentrations as a function of t_m are obtained for each of the specified initial concertation sets shown in Table 3.1. The kinetics of Villermaux-Dushman reaction is critically influenced by the range of adopted reactant concentrations and type of acid.[37,38] Therefore, the kinetics must be selected with great care for accurate micromixing calculations. In our experimental procedures, the utilized concentration sets were in agreement with those used in Guichardon et al.[26] for estimation of the kinetics as expressed in Eq.8. A detailed derivation and solution of the model is available in the Appendix.2.

It will be shown that each experimentally measured UV absorbance for the various concentration sets can be attributed to a unique micromixing time calculated from the IEM model. It is worth reminding that these theoretically inferred micromixing times are conjectured to represent a good estimation of the order of magnitude of t_m.[34]

Figure 3.6 portrays solutions of the IEM model for the various initial concentration sets summarized in Table 3.1.

Table 3.1 Concentration sets for micromixing studies by Villermaux-Dushman reaction

	Concentration set			
C (mol/L)	1	2	3	4
$[H^+]$	0.06	0.03	0.015	0.0075
$[I^-]$	0.032	0.032	0.016	0.008
$[IO_3^-]$	0.006	0.006	0.003	0.0015
$[OH^-]$	0.09	0.09	0.045	0.0225
$[H_3BO_3]$	0.09	0.09	0.045	0.0225

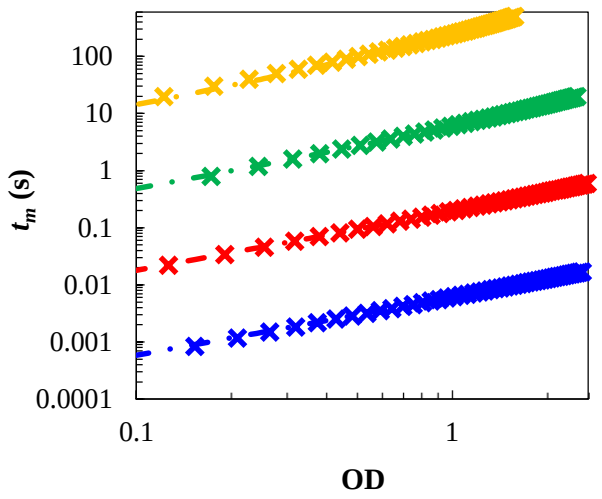

Fig 3.6 Inferred micromixing as a function of UV absorbance for the tested utilized concentration sets 1 to 4 (identified, respectively, with blue, red, green and yellow markers).

The model predictions are cast in terms of micromixing time as a function of UV absorbance which represents the concentration of triiodide anion. As discussed earlier, it can be seen that for each concentrations set, a distinct span of t_m is allocated for the valid range of UV absorbance between 0.1 and 2.5. It is worthy of notice that the t_m spans do not overlap with each other for similar UV absorbance ranges. Therefore, for each concentration set of Table 4.1, an experimentally determined UV absorbance is uniquely assigned to a micromixing time according to Figure 3.6 which will be used as the main descriptor of micromixing phenomena with and without magnetic field excitations.

3.4.3.2. Low-Re micromixing

Figure 3.7 depicts the variations of t_m as a function of H under SMF, OMF and RMF at MNP mass fraction of 0.05. Long micromixing times, in the order of magnitude of 10^2 s, are characteristic of the tests conducted with a disabled magnetic field. They indicate formation of iodine by virtue of reaction (Eq.7) whose characteristic time becomes comparable with the system's micromixing time. This was also the reason for using very dilute reactant concentrations from the fourth set to prevent formation of high triiodide concentrations.

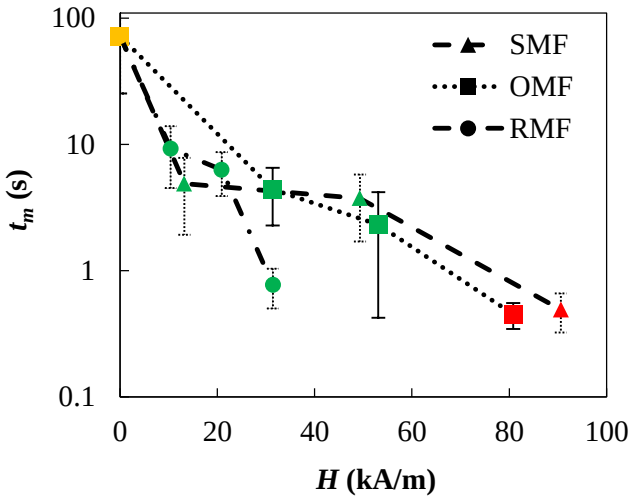

Fig 3.7 Illustration of t_m as a function of SMF, OMF and RMF intensities. While in the absence of magnetic field, large micromixing times are obtained, application of SMF, OMF or RMF leads to a reduction of t_m by approximately 3 orders of magnitude. The corresponding colors (see Figure 3.6) represent the concentration sets of Table 3.1.

Upon excitation with moderate SMF and OMF up to about 50 kA/m, t_m is dramatically reduced by two orders of magnitude around 1 s and which can be reduced further down to 10^{-1} s by increasing the magnetic field intensity (Figure 3.7). Provided they are assigned equal magnetic field intensities, both OMF and SMF exhibit comparable micromixing times. This finding supports commonness of the mixing mechanism originating under both uniform low-frequency OMF and SMF conditions as discussed earlier in terms of mixing index of the acid-base reaction.

Micromixing time can be manipulated by means of two main controlling parameters of the diffusional transport, *i.e.*, diffusion path or diffusion coefficient. A collapse of the micromixing time is due to a flow pattern modified by the Kelvin body force which induces deformations of the two streams. This results into a reduction of the segregation scales hence decreasing the diffusion times even though the diffusion coefficient keeps unaltered. Furthermore, from a practical point of view, the simplicity that lies in the implementation of Kelvin-force driven mixing for SMF and OMF may hold promises for the stimulation of micromixing as revealed from the response of the Villermaux-Dushman system.

The Villermaux-Dushman system was also implemented under uniform RMF to assess the effects of MNP mass fraction, and intensity and frequency of the magnetic field (figures 7 and 8). As can be seen, whichever H, f or φ is increased results in a descending trend of the micromixing time. In the lower range of H, f or φ, the drop in t_m is in the same order of magnitude as under SMF and OMF excitations. However, towards the upper range of MNP mass fraction and RMF frequency, t_m

underwent a reduction from 10^2 s to 10^{-2} s (Figure 3.8). Such 4-order-of-magntiude reductions of micromixing time at a constant Reynolds number are remarkable and confirm substantial shrinkage of the domains with prevalence of pure diffusion as in the case of disabled magnetic field. For such substantially shortened micromixing times, the diffusion of protons into the neighboring magneto-basic suspension segment should be extremely fast so that the majority of protons are preferentially consumed by the instantaneous acid-base equilibrium-limited protonation of borate anions (Eq.5). However, being MNP-free, the acidic segments are sites of slower counter-diffusion of ions from the nanofluid segments towards the proton-rich acidic segments with subsequent formation of more triiodide ions (Eq.10). One strategy to further lessen the system's micromixing time down to the millisecond could be through seeding also the acidic stream with stabilized MNP colloidal suspensions.

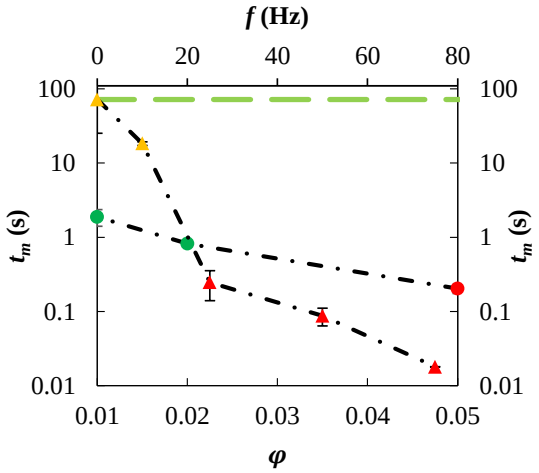

Fig 3.8 Illustration of t_m as a function of RMF frequency (φ = 0.05 and H = 31.2 kA/m) and MNP mass fraction (H = 31.2 kA/m and f = 25 Hz). Micromixing time in absence of magnetic field is shown as dashed line. The corresponding colors (see Figure 3.6) represent the concentration sets of Table 3.1.

3.4.3.3. Moderate-Re micromixing

The Villermaux-Dushman system was also implemented at Re = 260 in the absence of magnetic field, and under SMF (H = 30.52 kA/m) and RMF (H = 31.4 kA/m) for a magneto-basic suspension with 0.05 mass fraction of MNP. In the absence of magnetic field, inception of eddies in the engulfment regime bring the acidic and basic streams into contact over shorter length scales resulting in a micromixing time around 0.2 s which is notably shorter than t_m (~ 10^2 s) for the above low-Re run. Enabling SMF did not lead to prominent improvement of micromixing with t_m slightly sliding to 0.1 s.

However, the micromixing time measured under RMF dropped down to 8 ms resulting in its contraction by four orders of magnitudes similarly to the low-Re runs. Manifestly, rotating magnetic fields offer a *superior* micromixing strategy where the synergistic association between the classical instability-driven eddies and those that are magnetically-driven further promote the micromixing rate.

3.5. Conclusion

Mixing of dilute magnetic nanofluid and non-magnetic fluids was investigated using a capillary T-type mixer under various types of magnetic field from the standpoints of mixing index and micromixing. Mixing index was monitored experimentally using a conductometry method which revealed that by increasing SMF and OMF intensity and MNP mass fraction led to higher mixing indices. These were ascribed to spatial gradients in magnetic susceptibility and ensuing activation of the Kelvin body force. Unlike OMF and SMF, RMF proved to be far more efficient a tool for magnetic mixing purposes. At high Reynolds numbers where the Kelvin force at moderate SMF or OMF intensity could not bring mixing times shorter than the mean residence time of fluids, a complete homogenous state was accomplished by utilizing RMF transverse to the flow direction. The unique advantage of RMF over SMF and OMF was attributed to the rotating MNPs which were speculated to induce a non-convective mixing mechanism whereby an enhanced apparent molecular diffusion reduces the time scale of mass transport.

For the first time, the impact of magnetic-field assisted mixing was demonstrated for micromixing applications by means of the Villermaux-Dushman reaction and micromixing times inferred from the IEM model. This test reaction system revealed the superior micromixing features of rotating magnetic fields for their stimulated rotation of magnetic nanoparticles. The estimated micromixing times under RMF were considerably lower than those of mixing by pure diffusion (without magnetic field) or under SMF and OMF. Micromixing was highly sensitive to the intensity and frequency of RMF as well as to the MNP content of the nanofluid. Where application of SMF at moderate Re numbers had negligible effect on micromixing, RMF experiments led to dramatically shorter micromixing times in the order of a few milliseconds. The active mixing technique developed in this study proved to be a valuable tool in the analysis of the coupling of transport and intrinsic kinetics at the molecular level.

Acknowledgments

The authors gratefully acknowledge the Natural Sciences and Engineering Research Council of Canada and the Canada Research Chair on Sustainable Energy Processes and Materials for their financial support.

3.6. Nomenclature

Latin letters	**Description**	**Units**
C	Concentration	mol/L
D	Diffusion coefficient	m^2/s
f	Frequency	Hz
$\mathbf{F_m}$	Kelvin force density vector	N/m^3
H	Magnetic field intensity	A/m
k	Reaction 7 rate constant	$L^4\,mol^{-5}\,s^{-1}$
K_1	Reaction 5 equilibrium constant	L/mol
K_2	Reaction 10 equilibrium constant	L/mol
L_β	Langevin function	-
M	Magnetization of magnetic nanofluid	A/m
M_b	Magnetization of bulk MNPs	A/m
R	Rate of reaction	$mol\,L^{-1}\,s^{-1}$
Re	Reynolds number	-
t	Time	s
t_m	Micromixing time	s
Greek letters	**Description**	**Units**
α	Mixing index	-
κ	electrical conductivity	S/m
Λ	Molar conductivity	$S\,m^2\,mol^{-1}$
Λ_0	Limiting molar conductivity	$S\,m^2\,mol^{-1}$
μ_0	Absolute magnetic permeability of vacuum	N/A^2
φ	MNP mass fraction	-
φ'	MNP volume fraction	-
χ	Magnetic susceptibility	-
$\boldsymbol{\omega}$	Spin density vector	Rd/s

3.7. References

1. J. Aubin, M. Ferrando and V. Jiricny, *Chemical Engineering Science*, 2010, **65**, 2065-2093.
2. Z. M. Wang, V. B. Varma, H. M. Xia, Z. P. Wang and R. V. Ramanujan, *Physics of Fluids*, 2015, **27**.
3. V. Hessel, H. Lowe and F. Schonfeld, *Chemical Engineering Science*, 2005, **60**, 2479-2501.
4. J. Baldyga and R. Pohorecki, *Chemical Engineering Journal and the Biochemical Engineering Journal*, 1995, **58**, 183-195.
5. J. R. Bourne, *Organic Process Research & Development*, 2003, **7**, 471-508.
6. C.-H. Chang, B. K. Paul, V. T. Remcho, S. Atre and J. E. Hutchison, *Journal of Nanoparticle Research*, 2008, **10**, 965-980.
7. J. F. Chen, C. Zheng and G. T. Chen, *Chemical Engineering Science*, 1996, **51**, 1957-1966.
8. K. Jahnisch, V. Hessel, H. Lowe and M. Baerns, *Angewandte Chemie-International Edition*, 2004, **43**, 406-446.
9. K. K. Coti, Y. Wang, W.-Y. Lin, C.-C. Chen, Z. T. F. Yu, K. Liu, C. K. F. Shen, M. Selke, A. Yeh, W. Lu and H.-R. Tseng, *Chemical Communications*, 2008, 3426-3428.
10. A. Nagaki, M. Togai, S. Suga, N. Aoki, K. Mae and J. Yoshida, *Journal of the American Chemical Society*, 2005, **127**, 11666-11675.
11. K. Midorikawa, S. Suga and J.-i. Yoshida, *Chemical Communications*, 2006, 3794-3796.
12. P. Guichardon and L. Falk, *Chemical Engineering Science*, 2000, **55**, 4233-4243.

13. J. R. Bourne, F. Kozicki and P. Rys, *Chemical Engineering Science*, 1981, **36**, 1643-1648.
14. J.-M. Commenge and L. Falk, *Chemical Engineering and Processing*, 2011, **50**, 979-990.
15. R. J. Yang, H. H. Hou, Y. N. Wang and L. M. Fu, *Sensors and Actuators B-Chemical*, 2016, **224**, 1-15.
16. Q. Cao, X. Han and L. Li, *Lab on a Chip*, 2014, **14**, 2762-2777.
17. T.-H. Tsai, D.-S. Liou, L.-S. Kuo and P.-H. Chen, *Sensors and Actuators a-Physical*, 2009, **153**, 267-273.
18. C.-Y. Wen, C.-P. Yeh, C.-H. Tsai and L.-M. Fu, *Electrophoresis*, 2009, **30**, 4179-4186.
19. G.-P. Zhu and N. Nam-Trung, *Lab on a Chip*, 2012, **12**, 4772-4780.
20. I. Petousis, E. Homburg, R. Derks and A. Dietzel, *Lab on a Chip*, 2007, **7**, 1746-1751.
21. Y. Gao, A. van Reenen, M. A. Hulsen, A. M. de Jong, M. W. J. Prins and J. M. J. den Toonder, *Microfluidics and Nanofluidics*, 2014, **16**, 265-274.
22. Y. Gao, J. Beerens, A. van Reenen, M. A. Hulsen, A. M. de Jong, M. W. J. Prins and J. M. J. den Toonder, *Lab on a Chip*, 2015, **15**, 351-360.
23. P. Hajiani and F. Larachi, *Chemical Engineering and Processing*, 2013, **71**, 77-82.
24. P. Hajiani and F. Larachi, *Chemical Engineering Journal*, 2012, **203**, 492-498.
25. P. Hajiani and F. Larachi, *Chemical Engineering Journal*, 2013, **223**, 454-466.
26. P. Guichardon, L. Falk and J. Villermaux, *Chemical Engineering Science*, 2000, **55**, 4245-4253.
27. A. Soleymani, E. Kolehmainen and I. Turunen, *Chemical Engineering Journal*, 2008, **135**, S219-S228.
28. T. Solomon, in *Transport and Mixing in Laminar Flows: From Microfluidics to Oceanic Currents*, ed. R. Grigoriev, John Wiley & SonsJohn Wiley & Sons, Germany, Editon edn., 2012.
29. R. E. Rosensweig, *Ferrohydrodynamics*, 1 edn., Dover Publications, United States of America, 1997.
30. C.-Y. Wen, K.-P. Liang, H. Chen and L.-M. Fu, *Electrophoresis*, 2011, **32**, 3268-3276.
31. I. Torres-Diaz, A. Cortes, Y. Cedeno-Mattei, O. Perales-Perez and C. Rinaldi, *Physics of Fluids*, 2014, **26**.
32. A. Chaves, C. Rinaldi, S. Elborai, X. He and M. Zahn, *Physical Review Letters*, 2006, **96**.
33. S. Khushrushahi and M. Zahn, *Journal of Magnetism and Magnetic Materials*, 2011, **323**, 1302-1308.
34. L. Falk and J. M. Commenge, *Chemical Engineering Science*, 2010, **65**, 405-411.
35. X. Guo, Y. Fan and L. Luo, *Chemical Engineering Journal*, 2013, **227**, 116-127.
36. J. Baldyga and J. R. Bourne, *Chemical Engineering Journal and the Biochemical Engineering Journal*, 1989, **42**, 83-92.
37. A. Kolbl, V. Desplantes, L. Grundemann and S. Scholl, *Chemical Engineering Science*, 2013, **93**, 47-54.
38. A. Kolbl and S. Schmidt-Lehr, *Chemical Engineering Science*, 2010, **65**, 1897-1901.

Chapter 4: Tuning Mass Transport in Magnetic Nanoparticle-filled Viscoelastic Hydrogels using Low-Frequency Rotating Magnetic Fields

Tuning Mass Transport in Magnetic Nanoparticle-filled Viscoelastic Hydrogels using Low-Frequency Rotating Magnetic Fields

Shahab Boroun, Faïçal Larachi

Department of Chemical Engineering, Laval University, Québec, QC, Canada G1V 0A6

Résumé

Cette étude examine la réponse de nanoparticules magnétiques (NPM), dispersées dans un hydrogel viscoélastique, à un champ magnétique rotatif externe (CMR) dans le but de développer une nouvelle classe de matériaux magnéto-sensibles dotés de propriétés de transport de masse ajustables. Les ferrogels ont été préparés par réticulation chimique et polymérisation de l'acrylamide dans des dispersions colloïdales de NPM de ferrite de cobalt bloquées thermiquement. Les mesures d'aimantation des ferrogels imbibés ont révélé un état intermédiaire entre ferromagnétisme et superparamagnétisme par l'atténuation des boucles d'hystérèse et par la réduction de l'aimantation rémanente. L'analyse quantitative des données d'aimantation a révélé la coexistence entre NPM hydrodynamiquement libres sensibles à la relaxation Brownienne et des NPM mécaniquement bloquées. Une analyse rhéologique a montré que l'inclusion de NPM dans la matrice polymère altère de manière significative l'élasticité du ferrogel. À des taux de réticulation chimiques faibles, les NPM améliorent l'élasticité par la formation de réticulations physiques entraînées par la réduction de la fraction de NPM libres. Lorsque le taux de réticulation augmente, le réseau de polymères présente une plus grande tendance au blocage de NPM. Les coefficients de diffusion effectifs, à la fois dans les hydrogels et les ferrogels exempts de particules, ont été obtenus en mesurant la cinétique de libération d'un composé modèle en absence et en présence de CMR externe à basse fréquence. Les résultats expérimentaux ont montré que la conversion de l'énergie magnétique en énergie cinétique par le mouvement de rotation des NPM libres dans le CMR augmente le transport de masse à condition que des NPM libres hydrodynamiquement soient disponibles dans les ferrogels. L'efficacité de l'excitation par CMR a montré une corrélation avec la densité de NPM libres. Des expériences de libération à intensité CMR constante et à différentes fréquences ont révélé une augmentation des diffusivités effectives lorsque la fréquence était augmentée de 10 à 75 Hz.

Tuning Mass Transport in Magnetic Nanoparticle-filled Viscoelastic Hydrogels using Low-Frequency Rotating Magnetic Fields

Shahab Boroun, Faïçal Larachi

Department of Chemical Engineering, Laval University, Québec, QC, Canada G1V 0A6

4.1. Abstract

This study investigates the response of magnetic nanoparticles (MNPs), dispersed in a viscoelastic hydrogel, to an external rotating magnetic field (RMF) for the purpose of developing a new class of magneto-responsive materials with tunable mass transport properties. Ferrogels were prepared by chemical cross-linking and polymerization of acrylamide in colloidal dispersions of thermally blocked MNPs of cobalt ferrite. Magnetization measurements of ferrogels at swollen state revealed transitional state from ferromagnetism to superparamagnetism through shrinkage of the hysteresis loops and reduction of remanent magnetization. Quantitative analysis of magnetization data indicated the existence of hydrodynamically free MNPs, susceptible to Brownian relaxation along with blocked ones. It was found through rheological analysis that inclusion of MNPs within the polymer matrix significantly alters the ferrogel's elasticity. At low chemical crosslinking ratios, MNPs improve elasticity through formation of physical crosslinks ensued by reduction in fraction of free MNPs. As the crosslinking ratio was increased, the polymer network showed tendency toward blockage of more MNPs. Effective diffusion coefficients in both particle-free hydrogels and ferrogels were obtained by measuring the kinetics of release of a model compound in the absence and presence of external low-frequency RMF. Experimental results showed that conversion of magnetic energy to kinetic energy by rotational movement of free MNPs in RMF escalates mass transport provided that hydrodynamically free MNPs are available within the ferrogels. The effectiveness of excitation by RMF showed correlation with the density of free MNPs. Release experiments at constant RMF intensity and various frequencies revealed augmentation of the effective diffusivities as the frequency was increased from 10 to 75 Hz.

4.2. Introduction

The fascinating aspects of nano-scaled magnetic materials such as superparamagnetism, dispersion in other phases and modifiable surface chemistry accelerated their applications in a wealth of diverse fields.[1] More specifically, thanks to the unique response of MNPs to various types of external magnetic fields, numerous mechanisms for magnetic manipulation of transport phenomena are also being discovered by now.[2] In the light of that knowledge, design and development of magneto-responsive materials with tunable transport properties is frenetically pursued both as academic and applied research.[3, 4] The concept of magnetic field controlled transport phenomena was instigated by the discovery of magnetoviscous effects in colloidal MNP dispersions also christened after the neologism "ferrofluids".[5] It was eventually extended from colloidal systems to a broader category of soft matters and solid phases, among which the hydrogels, as cross-linked hydrophilic polymer networks, became a common choice thanks to their tunable properties such as viscoelasticity, polymer network conformation and chemistry of macromolecules.[6] Hydrogels seeded with MNPs are commonly termed ferrogels and through suitably tuned magnetic properties, their application as magneto-responsive materials in microfluidics, microencapsulation, controlled release, membrane and heterogeneous catalysis is conceivable.[6-8]

The response of MNPs to various external magnetic fields inspired researchers to develop smart ferrogels with diverse properties. In a static magnetic field (SMF), MNPs can be pinned into the continuum through the resistive act of magnetic body couples against external hydrodynamic torques and thermal energy.[9,10] At certain dilution levels of MNPs, formation of one-dimensional chainlike assemblies[11] in external SMF can give rise to anisotropic mass diffusivity, a mechanism exploited for magnetically triggered permeation applications.[12-14] In gradient SMF, the magnetic body force on MNPs can be transferred to the polymer network, giving rise to macroscale matrix deformations.[15] Upon judicious adjustment of gradient SMF direction, ferrogel contraction with subsequent repulsion of liquid from the constricted pore space can be utilized as a mechanism of triggered release for drug-delivery purposes.[16] In contrast to magnetoviscous phenomenon in SMF, an oscillating magnetic field has the fascinating feature of converting magnetic energy into *kinetic* energy.[17] Note that the dynamics of Brownian motion of colloidal MNPs is characterized by very short time scales in the order of milliseconds or less. Thus, if the periods of the applied OMF are in the order $\leq$ 1 ms (consistent with frequencies $\geq$ 1 kHz) then the sinusoidal magnetic torque can single out distinctive a rotational direction of MNPs.[18] The kinetic energy of MNPs in high-frequency OMF is shown to be capable of modulating the permeability of MNPs-filled membranes.[19,20] In addition, heating of superparamagnetic nanoparticles dispersed in thermo-responsive hydrogels by high-frequency OMF

can induce reversible volume changes in hydrogel nano-composites, a mechanism also extensively used for triggered release applications.[21]

In contrast to OMF, rotating magnetic fields (RMF) are endowed with distinctive characteristics which are temporal and spatial variations of magnetic field direction while a magnetic body subject to RMF *uninterruptedly* experiences a magnetic torque. Therefore the magnetic body can be constantly coupled to a moderate intensity RMF without perturbation by thermal energy.[10] This opens up an opportunity to use every low-frequency RMF even in the order of 10^1 Hz to bring MNPs into rotational movements. The manipulation of momentum transport in ferrofluids by low-frequency RMF has a long precedent in experimental and theoretical studies.[5] In specific case of scalar transport, the possibility of enhancement in self-diffusion coefficients of a dilute ferrofluid by the a so-called nano-stirring act of rotating MNPs was experimentally observed.[22] Although Brownian motion of MNPs is definitely harnessed in a moderate intensity RMF, nano-stirring mechanism requires sufficiently strong magnetic torques to overcome the resisting viscous torque that is constantly exerted on rotating MNPs by virtue of the carrier fluid viscosity which is intrinsic to it. However, in conventional-oil based or water-based ferrofluids nano-stirring mechanism can be conveniently activated since the magnetic torque from moderate intensity RMF overcomes the viscous torque if MNPs rotation frequency is low.[23]

Nanoparticles in hydrogel nano-composites are also susceptible to Brownian motion stemming from thermal energy of water and the flexible macromolecules. Nevertheless, Brownian motion of nanoparticles can be halted by coupling to the polymer network structure.[24] The energy required for decoupling of MNPs by external magnetic fields is strongly dependent on the network elasticity.[25] As a result, implementation of nano-stirring in viscoelastic media is not foreseen as a straightforward task.

In this respect, this article aims at investigating the possibility of triggering a new nano-stirring mechanism in viscoelastic media where elastic stresses also play role. Neutral acrylamide (AM) is selected as the building block of the ferrogel to minimize possible ionic[26] or covalent[27] interactions with the magnetic nano-inclusions. The magnetization state of MNPs is also probed to demonstrate its impact on the response of nanoparticles to external RMF. Finally, species release experiments are implemented to establish the relationship between the response of ferrogels to the RMF characteristics and the magnetization state of ferrogels. In contrast to existing mechanisms of triggered release in SMF and OMF, the principal motivation of this work is to identify a new nanoscale non-thermal transport mechanism for development of magneto-responsive materials with tunable transport properties.

4.3. Materials and Methods

Cobalt ferrite nanoparticles were synthesized by moderate temperature coprecipitation of Fe^{3+} and Co^{2+} ions in an alkaline solution. Water at pH 9, adjusted by NaOH, was added to a weighed amount of dried nanoparticles and the suspension was sonicated by means of an ultrasonic bath for 15 min. The resultant colloidal dispersion is referred to as ferrofluid. The prepared stock ferrofluid was diluted to the desired levels of MNPs mass fraction (φ) for preparation of ferrogels.

Hydrogel samples were prepared by free radical polymerization of neutral acrylamide (AM) monomers using N,N'-methylene*bis*acrylamide (MBAA) as a cross-linker. The molar cross-linking ratio, defined as the molar concentration of MBAA to that of AM in pregel solution, was varied from 0.002 to 0.006 by adjusting the concentration of MBAA. A hydrogel synthesized in the selected weight fraction of monomer and the range of cross-linking ratio is homogeneous.[28,29]
The procedure for preparation of ferrogel samples is the same as hydrogels but the polymerization was performed in a ferrofluid with adjusted φ. The hydrogels or ferrogels having 0.002, 0.003, 0.004 and 0.006 cross-linking ratios were denoted as G2, G3, G4 and G6, respectively. By molding the pregel solution, the final hydro/ferrogel was obtained in the form of identical cylinders, 4 mm in inner diameter and 50 mm in length.

The swelling ratios (*SR*) of the cylindrically shaped samples were estimated by dividing the weight of total absorbed water to the weight of the dried sample. The volumetric fractions of MNPs in the swollen ferrogels (Φ) were calculated knowing their volume obtained from density and initial mass fraction in pregel solution and final volume of the hydro/ferrogel samples obtained from their known initial volume and measured amount of water in the swelling process.

XRD measurements were performed on a Rigaku D-Max-Ultima III instrument using nickel-filtered Cu K α radiation with wavelength of 1.5406 Å and step size of 0.04°. The hydrodynamic diameter of MNPs in the colloidal state (d_p) and corresponding zeta potential were measured by a light-scattering method by means of a Zetasizer Nano 6 (Malvern Instruments Ltd) using a 4 mW He-Ne laser at 633 nm wavelength.

Magnetic characterization was carried out using in a vibrating sample magnetometer (VSM) from Princeton Instrument (MicroMag model 2900) at 298 K for determining the magnetizations of MNPs and ferrogels. The magnetization (*M*) of each sample was calculated by dividing the measured magnetic moments by the mass of magnetic nanoparticles in the sample as determined form the known mass fraction of MNPs in the pregel solution.

Dynamic mechanical tests (DMT) on the swollen samples were performed using an ARES rheometer from TA Instruments. The frequency sweep test was performed at ambient temperature at constant strain amplitude. The linear viscoelastic range was previously determined from a strain amplitude sweep test at constant frequency of 1 Hz before each frequency sweep test. The samples used for DMT analysis were obtained by molding the pregel solution in a 50 ml beaker followed by washing and swelling steps as explained by details in appendix 3. Superficial water in the samples was removed by delicate task wipers prior to each test. Parallel plates of 40 mm diameter (sandblasted/serrated) were used in order to prevent slippage of the samples.

The effective diffusion coefficients (*D*) of rhodamine B in the samples were determined by measuring the kinetics of release into a stirred receiver solution of finite volume.[30] The receiver solution was water at pH 9, circulated with a peristaltic pump at constant rate within a closed loop. The theoretical analytical concentration of the solute as a function of time was obtained from solving the transport problem of solute diffusion from infinite circular cylinder to a well-stirred solution of finite volume. By taking *D* as the iterated variable, the root-mean squares error between experimental and theoretical concentrations of rhodamine B was minimized and *D* values corresponding to each release experiment were determined.

Rotating magnetic field (RMF) used in the release experiments were generated by a two-pole stator winding with 3 pairs of coils around the periphery of a cylindrical magnet bore (Figure 4.1).

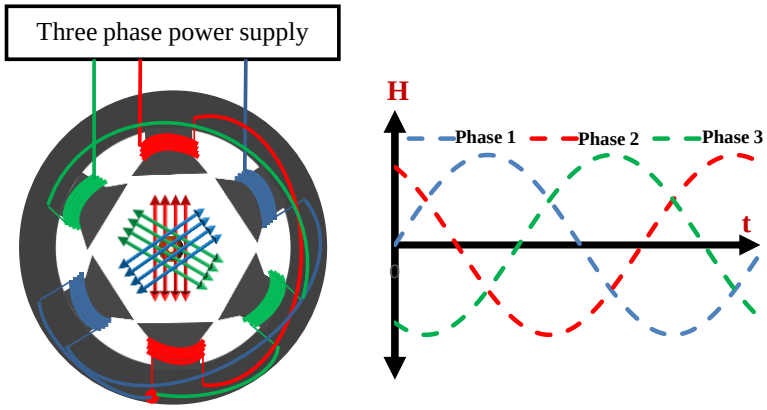

Fig 4.1 Schematic illustration of the magnet device used for the generation of RMF: the alternative currents fed to each pair of coils have shifted phases so that the magnetic field inside the bore rotates in synchrony with the currents frequency.

The bore dimensions were 55 mm in height and 45 mm in inner diameter. All three pairs of coils were fed by a 3-phase AC current, 120°out of phase, so that the resultant magnetic field inside the bore rotates with a frequency equal to that of the balanced AC currents. The intensity and frequency of

RMF are adjusted by means of a variable frequency drive (ABB, ACS150, 2.2kW) coupled to a power source. The magnetic field direction is perpendicular to the central bore axis. For release experiments in RMF, the plastic tube filled with sample and glass beads was placed inside the magnetic field generator as its longitudinal central axis coincided with the central axis of magnet bore. More details on the experimental procedures and setups can be found in appendix 3.

4.4. Results and Discussion

4.4.1. Characteristics of Cobalt-Ferrite Nanoparticles

The XRD patterns of MNPs, shown in Figure 4.2a, confirm formation of an inverse spinel of crystalline cobalt-ferrite with 33 nm average crystallite sizes as estimated from Scherrer formula. These MNPs are in ferromagnetic state at ambient temperature as evidenced by the magnetometric measurements illustrated in Figure 4.2b. The magnetization curve demonstrates hysteresis loop with saturation magnetization (M_s) of 61 emu/g. The reduced remanent magnetization (M_r) defined as the ratio of remanent magnetization to M_s is 0.73 which is below the theoretical value of 0.831 for single-domain cubic anisotropy.[15] The size distribution of MNPs at φ = 0.05, as shown in Figure 4.2c, exhibits polydispersity with average diameter of 33.8 nm. It is also evident that at mass fractions of MNPs higher than 0.05, the spectrum of scattered light intensity is broadened. This is due to formation of aggregates stemming from interacting permanent magnetic dipoles within the crystal structure. In view of these considerations, φ = 0.05 was selected as the maximum mass fraction for preparation of the pre-gel solutions to prevent formation of aggregates. The minimum size of nanoparticles as revealed from scattered light intensity is around 20 nm. Thus, it may be safely assumed that all the nanoparticles are in thermally-blocked state since the critical diameter of transition from superparamagnetism to ferromagnetism is less than 16 nm for cobalt-ferrite.[15,31] The transition from single-domain to multi-domain state in cobalt-ferrite nanoparticles occurs at around 100 nm.[32] Therefore, existence of small amounts of nanoparticles larger than 100 nm, as evident from the spectrum of scattered light intensity, could be the reason why M_r< 0.831. This fact does not conflict with the assumption regarding thermally-blocked states of MNPs since multi-domain magnetic nanoparticles slightly larger than the transition size still preserve large domains with significant magnetic anisotropy energy.[33]

pH dependence of zeta potential of MNPs dispersed in water is illustrated in Figure 4.2d. The nanoparticles electric potential around -36 mV at pH 9 on their slipping plane relative to the bulk of solution endows them with acceptable colloidal stability in the time scale of several hours without necessitating recourse to surfactants. This is the reason for implementation of ferrogel synthesis at

pH around 9 to avoid aggregation and subsequent sedimentation of nanoparticles during solution preparation and gelation steps.

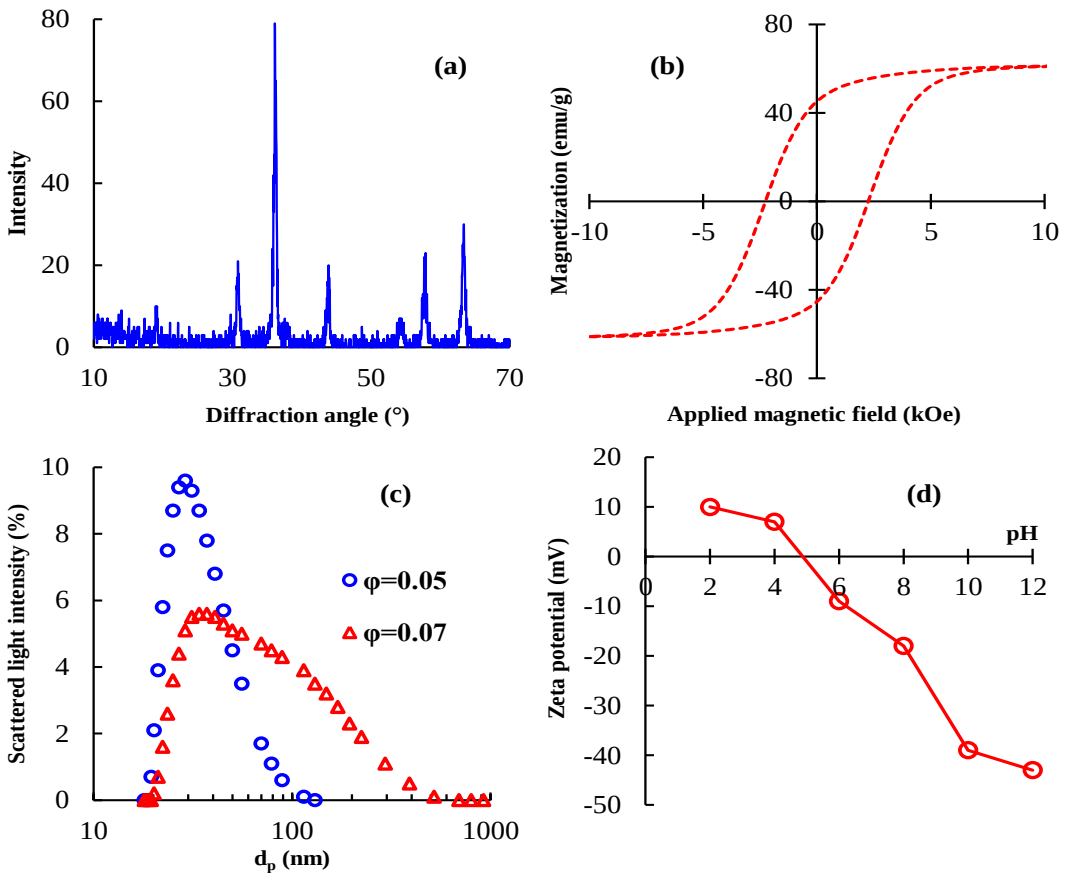

Fig 4.2 XRD pattern of cobalt-ferrite MNPs (a). Magnetization of powdery (dry) MNPs measured at ambient temperature (b). Hydrodynamic size distribution of MNPs measured by dynamic light scattering method (c). Zeta potential of MNPs in colloidal state as a function of pH at φ = 0.05 (d).

4.4.2. Characteristics of Hydro/Ferrogels

The magnetization state of MNPs dispersed in ferrogels is obtained by magnetometry of ferrogel samples. Figure 4.3 shows the magnetization curves of G2 and G6 ferrogels as extrema of cross-linking ratios. It might be inferred that the thermal energy of water molecules in the swollen ferrogels can give rise to random bodily movement of seeded MNPs thus resulting in superparamagnetic state of ferrogels tantamount to the magnetic state of ferrofluids. Nevertheless, the Langevin-type magnetization as a characteristic signature of superparamagnetism is not observable in Figure 4.3 for all the G2 and G6 samples.

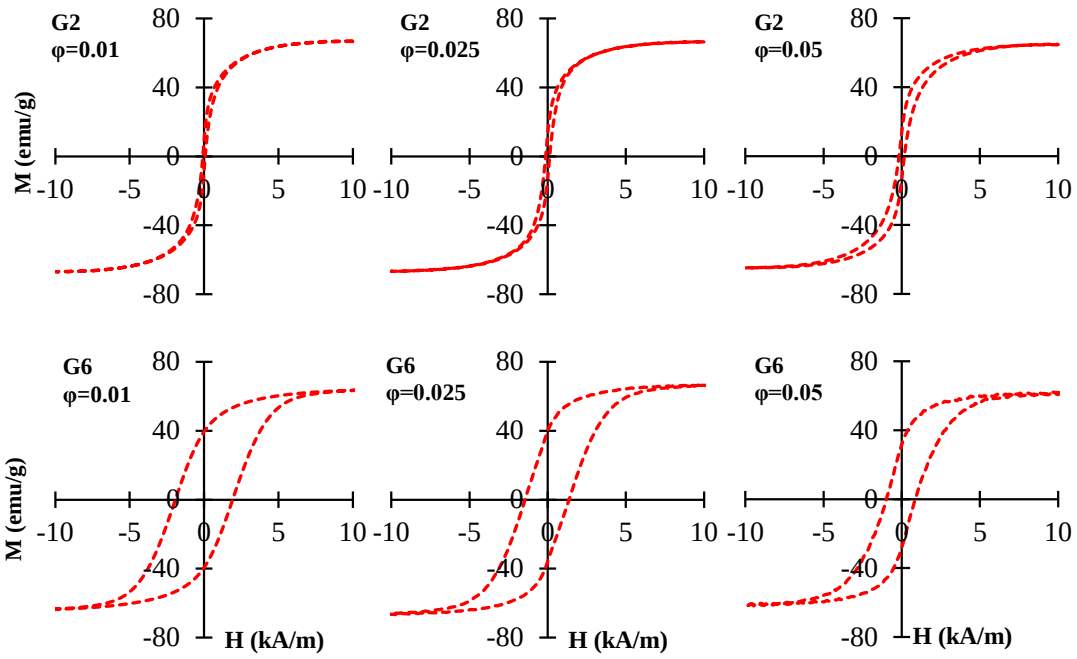

Fig 4.3 Magnetization of G2 (top) and G6 (bottom) ferrogels measured at ambient temperature. All the M-H curves show hysteresis loops identified by the remanent magnetization and coercivity noticeable at every mass fraction of MNPs. The M_r values calculated for the ferrogels, as demonstrated in Figure 4.4, are less than 0.73 ruling out plausibility of MNPs relaxation.

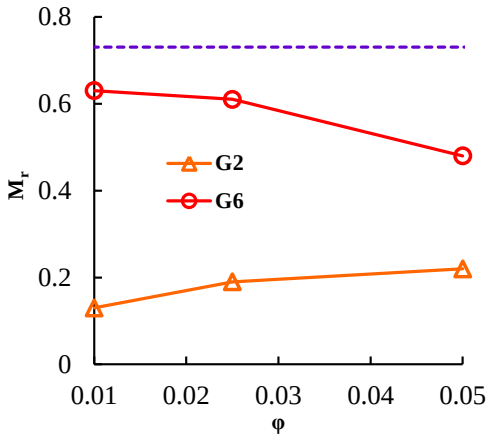

Fig 4.4 Reduced remanent magnetization of G2 and G6 ferrogels: M_r of powdery MNPs is shown as a dashed line.

This observation indicates that magnetic moments in swollen ferrogels should have been partially relaxed through a specific mechanism in the absence of external fields; otherwise M_r values of ferrogels in zero-magnetic fields should have been the same as powdery (dry) MNPs. A hard nano-

magnet is not susceptible of Néelian relaxation below its Curie temperature due to the high anisotropic energy barrier of magnetic moments. Nevertheless, magnetization of a collection of thermally blocked MNPs in colloidal state undergoes relaxation once the external applied magnetic field is disabled. This relaxation mechanism, known as Brownian relaxation, is due to random bodily movement of nanoparticles induced from thermal energy of the carrier fluid molecules and is characterized by a time scale expressed as:[23]

$$\tau_b = \frac{3V_H\eta}{k_BT} \tag{4.1}$$

where T is temperature, V_H denotes the hydrodynamic volume of the nanoparticle, k_B is the Boltzmann constant and η is the dynamic viscosity of the carrier fluid. Eq.1 expresses the resistive nature of hydrodynamic viscous stress on thermal perturbation induced by the carrier fluid. Therefore, a collection of hard MNPs is merely susceptible to Brownian relaxation if the nanoparticles are not hydrodynamically blocked. Perturbation of magnetic moments inside the crystal lattice is not the governing mechanism of the observed reduction of M_r since the cobalt-ferrite nanoparticles were proven to be thermally blocked. Therefore, existence of a number of hydrodynamically free MNPs, susceptible to Brownian relaxation, remains the plausible mechanism. This implies that these nanoparticles are free to be perturbed by Brownian motion of the surrounding water molecules in the swollen ferrogels or even possibly by the PAM flexible chains. The observed shrinkage in hysteresis loops was also reported in various studies on solid matrices including permanent nano-magnets which was mainly attributed to mechanical rotation of MNPs.[34-36] Tejada et al.[37] also brought evidence for mechanical rotation in systems exhibiting shrinkage in their hysteresis loop by performing electron spin resonance studies on MNPs confined in polymeric cavities. In order to quantify the amount of hydrodynamically free and blocked MNPs, it is assumed that the free nanoparticles manifest their magnetization through the Langevin law of superparamagnetism while the blocked ones preserve their hysteresis loop as demonstrated in Figure 4.2b. The magnetic moment vector can be decomposed into magnetic moments of free ($\mathbf{m_f}$) and blocked ($\mathbf{m_b}$) MNPs, so that the global magnetic moment can be compounded as:

$$\mathbf{m} = \mathbf{m_b} + \mathbf{m_f} \tag{4.2}$$

By defining magnetization as the magnetic moment per unit mass, one can write:

$$\mathbf{M}w_t = \mathbf{M_b}w_b + \mathbf{M_f}w_f \tag{4.3}$$

where w_b and w_f are, respectively, the masses of blocked and free MNPs according to $\mathbf{M_b}$ and $\mathbf{M_f}$ the corresponding magnetization vectors. Thus, the total magnetization can be written in terms of mass fractions of free and blocked nanoparticles denoted by X_f and X_b, respectively.

$$\mathbf{M} = \mathbf{M}_\mathrm{b} X_b + \mathbf{M}_\mathrm{f} X_f \tag{4.4}$$

At zero applied fields, the superparamagnetism state of free nanoparticles implies zero values for $\mathbf{M}_\mathrm{f}$ because of the randomly oriented magnetic moments that yield an average zero magnetization. Thus, one expects that:

$$X_b = \frac{M}{M_b} \; @ \; H = 0 \tag{4.5}$$

Where M_b is the magnitude of $\mathbf{M}_\mathrm{b}$ vector equal to 44.5 emu/g as obtained from the magnetization curve of the powdery (dry) MNPs. Finally, by measuring the magnetization of ferrogels and determining the remanent magnetization at zero applied fields X_b is deduced. Figure 4.5 illustrates the variation of X_b as a function of cross-linking ratio and φ.

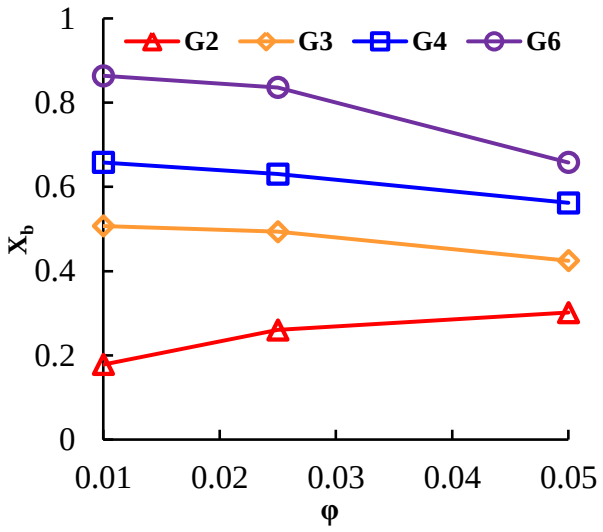

Fig 4.5 Mass fraction of blocked MNPs in ferrogels calculated from Eq.5.

The G2 ferrogels have the lowest mass fractions of blocked nanoparticles at every mass fraction of MNPs. The observed lower fraction of blocked nanoparticles in ferrogels having lower cross-linking ratio points out to a mechanism of MNPs coupling to the polymeric backbone that impedes their Brownian relaxation. The studies on dynamics of nanoparticles in hydrogel nano-composites attests that in addition to viscous stresses, the viscoelastic medium imposes additional elastic stress on the nanoparticles when these are entrapped within a poral space of smaller size.[24,38] It is probable that in

all the ferrogel samples, a fraction of MNPs is entrapped in smaller pores according to a mechanical blockage, otherwise the Langevin-type of magnetization should have been manifested. Furthermore, the theory of swelling of cross-linked hydrogels predicts a contraction of the pore space by increasing the density of effective reticulations. To gain more quantitative information on the pore structure of the samples, the average length of pore space in hydrogel or mesh size (ξ) was experimentally estimated from DMT analysis. By assuming the polymer chains as entropic springs, the average network spacing or mesh size is estimated by:[39]

$$\xi = \sqrt[3]{\frac{k_B T}{G'}} \tag{4.6}$$

where G´ is the storage modulus. As demonstrated in Figure 4.6a, hydrogels with various cross-linking ratios exhibit virtually frequency-independent storage moduli. The calculated values of ξ for G´ values at 1 Hz show a descending trend as the cross-linking ratio increases (Figure 4.6b). The mesh size values implicitly allude to the capability of hydrogels to host nanoparticles without blockage provided that $\xi < d_p$.[38,40,41] However, as shown in Figure 4.5, G2 hydrogel as the softest sample with large network spacing of 72 nm manifests blockage of MNPs. X_b values also increase as more MNPs are included. A peculiarity can be also identified in G6 samples since G6 hydrogel has an average mesh size of 20 nm, slightly larger than the minimum particle size identified by light scattering, whereas nearly 14 wt% of MNPs are still mechanically free at φ = 0.01. The propensity in reduction of X_b at higher φ is also discernible as the cross-linking ratio increases. This is most notable in G6 ferrogels where X_b, in contrast to G2, drastically drops from 0.86 to 0.65 when φ is increased from 0.025 to 0.05.

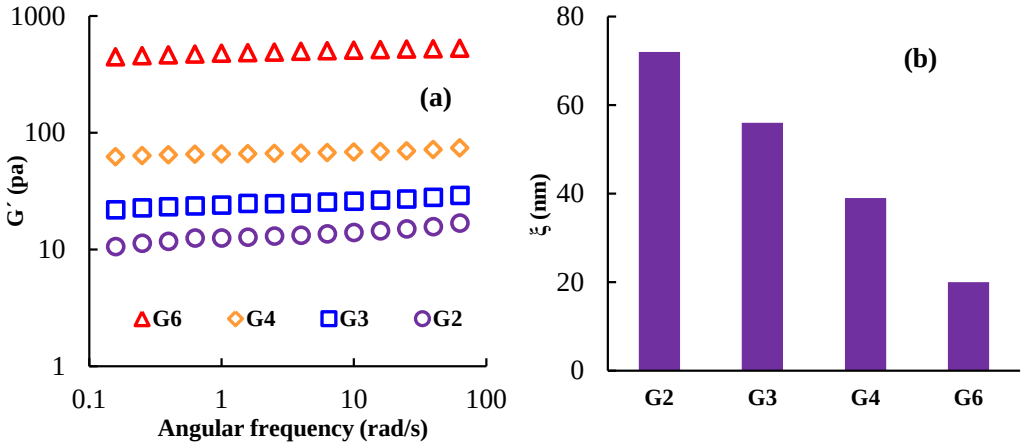

Fig 4.6 Storage modulus of hydrogels measured at constant strain amplitude (a) and corresponding ξ calculated from Eq.6 using G´ values measured at 1 Hz (b).

It might be inferred that existence of blocked MNPs in G2 ferrogels is due to the size polydispersity in nanoparticles and network spacing that results in entrapment of larger particles in smaller pores. Nevertheless, further scrutiny by DMT analysis on G2 and G6 ferrogels reveals substantial transformation in the structure of polymer chains upon their seeding by MNPs. Figure 4.7 shows the storage modulus enhancement factor defined as the ratio of the measured G´ to that of hydrogel of the same chemical cross-linking ratio (G_0´).

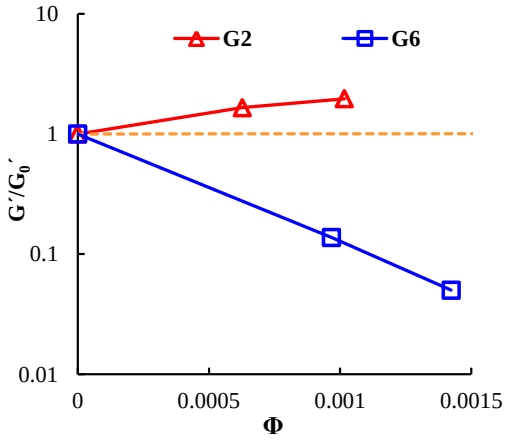

Fig 4.7 Storage modulus enhancement factors of G2 and G6 samples: mass fractions of MNPs in ferrogels are converted to volume-based fractions to compare experimental results with theoretical values shown as dashed line.

The enhancement factor monotonically increases by addition of more MNPs in G2. These experimental values are compared to the theoretical values of storage modulus enhancement ratio for passive particles dispersed in viscoelastic media calculated by:[42]

$$\frac{G'}{G_0'} \approx 1 + 2.5\Phi + 14.1\Phi^2 \qquad (4.7)$$

The higher modulus enhancement factor *vis-à-vis* the theoretical prediction (shown as a dashed line in Figure 4.7) rules out a merely passive presence of MNPs and, on the contrary, attests for their participation in the improvement of elasticity *via* specific interactions with the polymeric matrix. The anomalous enhancement in elasticity is attributed to adsorption of PAM chains on the nanoparticles during the network formation followed by their entanglement leading to the formation of *physical* cross-linking nodes.[43] G2 ferrogels also should have lower ξ values since the storage modulus is lower than that of G2 hydrogel. Thus, more MNPs are possibly entrapped in the resultant smaller mesh space beside those forming physical cross-links. It should be stressed that neutral PAM

mainly establishes interactions to the oxide surfaces *via* hydrogen bonds between the surface hydroxyl groups and the carbonyl functional groups belonging to the polymeric chains.[26,27] However, the affinity of PAM adsorption on the hydroxylated surfaces by hydrogen bonding is low as confirmed by the adsorption isotherms of PAM on iron oxide nanoparticles.[27] Furthermore, according to the zeta potential data of cobalt-ferrite nanoparticles, formation of hydrogen bonds are even less favorable in our samples since the polymerization step is performed at basic pH where the majority of the hydroxyl groups are deprotonated, leaving an electron-rich oxide surface. Therefore, participation of the entire MNPs in the formation of physical cross-links does not seem plausible. The hypothesis of formation of elastic nodes aided by MNPs also can explain the observed ascending trend of X_b in G2 ferrogels (Figure 4.5). By addition of more MNPs, PAM adsorption capacity of nano-inclusions increases and consequently entanglement of chains on the nanoparticles surface becomes more probable to promote formation of physical cross-links. It should be emphasized that the nano-scale torsion stemming from the magnetic torques on elastically coupled nanoparticles cannot be refuted since the elastic stress in some regions can be sufficiently low to be overcome by the magnetic torque.[25] Deeper scrutiny on this subject is left for future studies.

Dynamic mechanical tests performed on G6 ferrogels also unveil another mode of restructuring in the polymer as inferred from the modulus enhancement factors shown in Figure 4.7. In contrast to G2, addition of MNPs reduces G' to values lower than those for G6 hydrogel. The intrinsic mesh size of G6 hydrogel is smaller than the average nanoparticle size, thus during the network formation, regions depleted from cross-linkers are inevitably generated to host the largest nanoparticles. At constant chemical cross-linker concentration, the polymerization in other regions proceeds with higher density of cross-linkers with higher probability of their heterogeneous distribution.[44] The heterogeneity in the cross-linker density reduces the concentration of elastically-effective cross-links. The lower $G´$ values in G6 ferrogels as compared to the hydrogel is due to deteriorating impact of heterogeneities on elasticity.[45] Therefore, existence of multimodality in mesh size distribution of ferrogels becomes more plausible as the cross-linking ratio increases. The length scale of cross-linker depleted regions generated in stiff hydrogel nano-composites can be even larger than the size of nanoparticles.[46] Galicia et al.[28] also performed neutron scattering spectroscopies on PAM nano-composites and confirmed the existence of regions larger than the length scale of nano-inclusions when the pore space volume is almost equal to the nanoparticle volume. Therefore, it is probable that in G2 ferrogels a fraction of largest MNPs, entrapped in the low cross-linker density regions, gain hydrodynamic freedom. The weight fraction of blocked nanoparticles is even more pronounced at higher mass fractions of MNPs. It is likely that at larger φ, the particle-filled pores become large

enough to be interconnected and form larger pore space encompassing more free nanoparticles. Nevertheless, even with substantial reduction in elasticity of G6 ferrogels, X_b values are higher than those of G2. Note that the existence of MNPs as elastic nodes cannot be neglected but its impact on elasticity improvement cannot dominate the deteriorating effect of heterogeneous distribution of chemical cross-linkers and formation of larger mesh space.

Results obtained from the DMT studies suggest dissimilar influences of MNPs on the magnetization and elasticity of ferrogels. These impacts should also manifest themselves in the swelling equilibrium of ferrogels as the elasticity has a decisive role in the water uptake capacity. Figure 4.8 shows the swelling ratio, *SR*, of ferrogels of various cross-linking ratios and MNPs mass fractions.

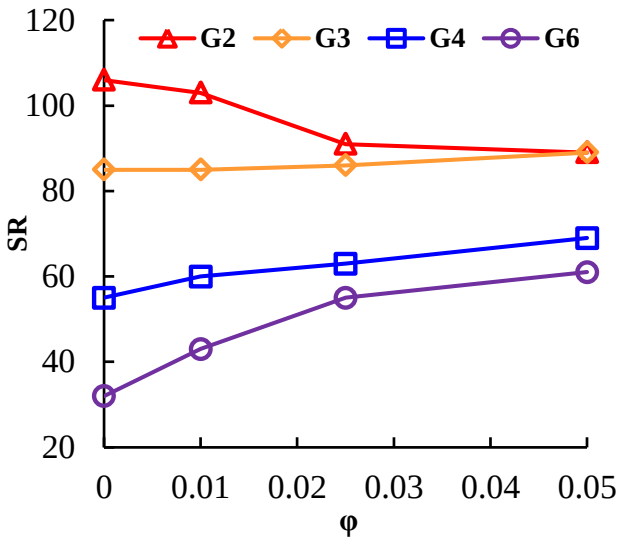

Fig 4.8 Swelling ratios of hydrogels and ferrogels as a function of φ values.

The softest samples exhibit the highest amount of absorbed water since the low density of chemical cross-linkers reduces the elastic forces which counterbalance the osmotic pressure of mixing between water and PAM. Interestingly, the observed trends of swelling data follow the trends obtained for the mass fraction of blocked particles in the ferrogels. The swelling ratio of the softest ferrogel declines as more MNPs are added which further supports the hypothesis of nanoparticles participation in the formation of physical cross-links. In contrast to the soft ferrogels, the stiff samples show ascending trend by addition of more nanoparticles. Similar to X_b trends, the impact of MNPs mass fraction on the swelling ratio is more significant at higher cross-linking ratios confirming the substantial restructuring of polymer chains when the network spacing is smaller than the average size of nano-inclusions.

4.4.3. Intrinsic Diffusional Mass Transport in Hydro/Ferrogels

The measured effective diffusion coefficients of rhodamine B in hydrogel and ferrogel samples in the absence of external magnetic field are shown in Figure 4.9.

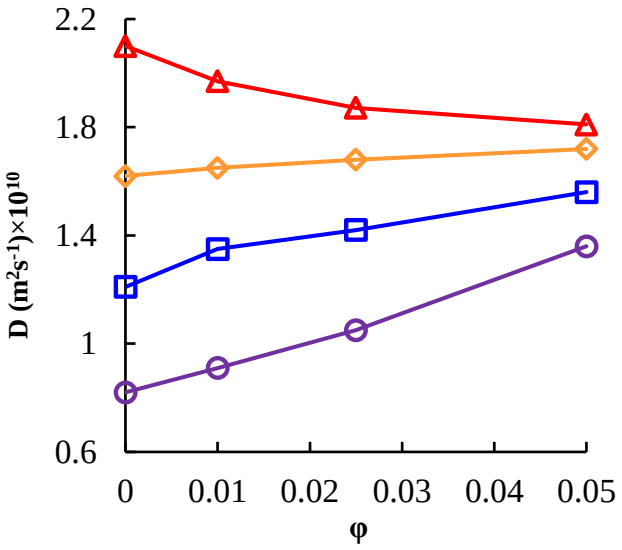

Fig 4.9 Estimated effective diffusion coefficients of rhodamine B in hydrogel and ferrogel samples.

The G2 samples demonstrate descending trend of D as φ increases. By increasing the density of chemical cross-linker, the slopes of the curves demonstrate gradual transition from negative to positive values. It has been discussed that a fraction of nanoparticles exhibits affinity toward formation of physical cross-links as evidenced by rheological and swelling data of G2. Accordingly, reduction of diffusion coefficients in the softest samples is an expected behavior as the density of reticulations is increased *via* physical cross-linking. According to the previous discussions on the structure of G6 ferrogels, the heterogeneous distribution of chemical cross-linkers provide regions of lower cross-linker density with lower resistance to mass diffusion. The polymer chains in these regions are more flexible thanks to the reduced number of elastic nodes which subsequently impose less hydrodynamic drag on solute transport. Therefore, it is not unanticipated to observe increased values of D in the stiffer ferrogels when more MNPs are seeded. In G6 samples, a drastic enhancement in D is apparent when φ increases from 0.025 to 0.05. In agreement with the previous discussion, existence of percolating paths that developed from interconnections of the regions of low cross-linking density may explain this anomalous augmentation. The obtained trends of diffusion coefficients conform to the deduced structures of ferrogels as discussed above.

4.4.4. Mass Transport in Hydro/Ferrogels under RMF

Figure 4.10a shows the variations of effective diffusion coefficient enhancement factor (*E*) when an external RMF with rotation frequency of 10 Hz and an intensity equal 31.4 kA/m was applied during the release experiment.

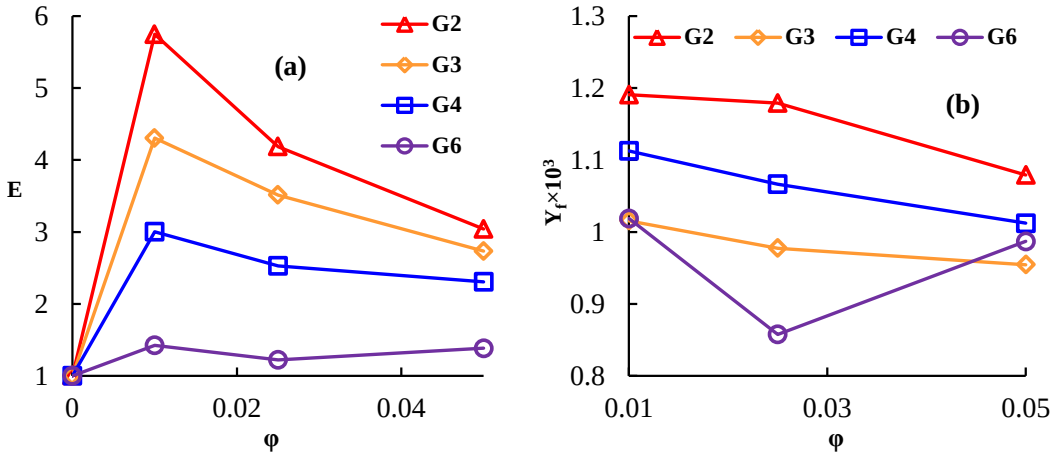

Fig 4.10 Effective diffusion coefficient enhancement factors in presence of 31.4 kA/m RMF with 10 Hz rotation frequency (a). Scaled mass of mechanically free MNPs (b).

The enhancement factor is defined as the ratio of diffusion coefficient measured in presence of external RMF to the value obtained under zero magnetic field conditions. It is evident that application of external RMF enhances the diffusional transport in all ferrogel samples but the effect of external RMF becomes less significant as the density of chemical cross-linker increases. One might conceive that the number of free MNPs determines the effectiveness of the nano-stirring mechanism. Therefore, the scaled mass fraction of free MNPs (Y_f) defined as the ratio of the free MNPs mass to the total mass of swollen cylindrical ferrogels is taken as a quantitative criterion for free MNPS. It is straightforward to calculate Y_f from the fraction of free MNPS ($1\text{-}X_b$), the initial mass of MNPs in pregel solution and the swelling data. It is interesting that the trends of *E*, as shown in Figure 4.10b, mirror those of Y_f for the range $0.01 < \varphi < 0.05$. This result suggests that there is a correlation between the amount of free nanoparticles and the enhancement factor for diffusion. In order to explain this correlation, the mechanism of mass transport intensification should be addressed in details.

The mechanism of mass transport intensification can be explained based on the ability of free MNPs to convert magnetic energy into kinetic energy by their rotational movement as driven by RMF.[10,22,47] The magnetic torque gives rise to rotational movement of the free MNPs being hydrodynamically coupled to the surrounding fluid *via* viscous shear. A specific volume of fluid in the vicinity of the

rotating nanoparticles is sheared and mixed by the viscous coupling of angular momentum. The synchronized act of the whole free MNPs generates a finite nano-stirred volume with intensified mass transport that results in an augmentation of the effective diffusion coefficient. However, in a swollen hydrogel, besides the intrinsic diffusivity of a solute in water, the impact of the polymeric backbone on the effective diffusivity cannot be neglected. Amsden[48] showed that the frictional drag force exerted from flexible chains of polymer on solute molecules can explain the diffusional transport in a homogenous hydrogel. Thus, rotating MNPs may also contribute to the mass transport enhancement mechanism by compensating for the frictional drag force of the polymer chains *via* momentum transport from rotating nanoparticles. It should be noted that the extensive research on the response of colloidal MNPs to uniform RMF has also proven the existence of magnetic torque-driven flows.[49] Since the magnetic torque-driven convective flow *via* transformation of internal angular momentum to linear momentum is only validated in viscous fluids, it is highly unlikely that convective flows can be invoked as contributing mechanism for ferrogels.

Thus, at higher density of MNPs, the individual rotating nanoparticles reflect into shortened length scales over which mass is transported *via* intrinsic diffusion owing to the increased total volume of mixed volumes. In addition, at constant rotational rate of nanoparticles the angular momentum per unit mass of free MNPs also increases. This further translates in intensifying the counteraction of magnetic field driven angular momentum against the frictional drag of polymer chains.

It is worth noting that the enhancement factors for G6 ferrogels are also less than expected since Y_f at φ = 0.01 and 0.05 are almost higher than the corresponding values of G4 ferrogels. This peculiarity can be explained by referring to the theory of diffusion in heterogeneous hydrogels. In heterogeneous hydrogels, the diffusional transport is explained by the obstruction theory.[48] Accordingly, the regions of higher cross-linking density develop impenetrable chains that increase the path length of diffusional transport. According to our premise regarding the heterogonous nature of the stiffest ferrogels, the free MNPs are mainly encompassed in low cross-link density regions. It is plausible that the exerted magnetic torque on the blocked MNPs is not strong enough to overcome the elastic forces in the highly cross-linked regions to give rise to any conformational rearrangements of chains nearby the obstacles. However, the observed slight enhancement factor is due to rotation of free MNPs in the larger mesh spaces with minimal impact on rate intensification of mass transport. This observation highlights the dominating role of rotating nanoparticles in compensating the frictional drag of polymer chains over their role in generating the nano-stirred zones.

Figure 4.11 shows the variation of E in G2, G3 and G4 ferrogel samples as a function of RMF frequency. Over the entire range of frequencies, the samples with higher Y_f demonstrate higher E, in agreement with the previous discussion.

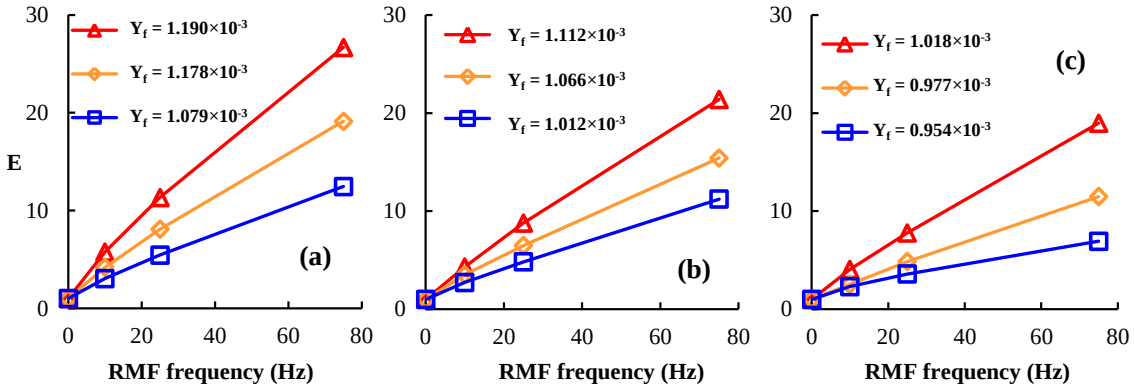

Fig 4.11 Enhancement factors of effective diffusion coefficient in G2 (a), G3 (b) and G4 (c) ferrogels as a function of RMF frequency: RMF intensity = 31.4 kA/m in all experiments.

All the samples, regardless of the cross-linking ratio or amount of free MNPs, show responsiveness to frequency of RMF. It is evident from the trends in Figure 4.11 that by increasing the frequency the effective diffusivities are augmented. The response of ferrogels to RMF frequency can be explained in the framework of ferrohydrodynamics formulation relevant to the problem of colloidal MNPs response to homogeneous RMF. It is theoretically and experimentally validated that the average magnetization vector tracks a homogenous RMF with a specific lag angle that varies as a function of frequency and amplitude of applied magnetic field.[50] Taking this fact into account, Rosensweig[23] showed that the dimensionless ratio of magnetic torque to viscous drag torque, P, exerted on MNPs body in the absence of bulk fluid motion determines the average spin rate of nanoparticles. This parameter is expressed as:

$$P = \frac{\mu_0 M_f H \tau}{6\eta\phi} \tag{4.8}$$

where μ_0 is vacuum permeability and η is the viscosity of the carrier fluid. When P is sufficiently large (>2), the ratio of average rotation rate of free MNPs (ω) to RMF angular velocity remain constant in the RMF frequencies less than the reciprocal of the Brownian relaxation time, τ. For a water-based magnetic colloid, τ is estimated to be in the order of 10^{-5} s for d_p ca. 10^1 nm in size. Although the flexible polymer chains contribute to the viscous stress exerted on the nanoparticles, η can be roughly assumed equal to the viscosity of water. The magnetization of hydrodynamically free MNPs at H = 31.4 kA/m is estimated from the Langevin magnetization law:[23]

$$M_f = \phi M_d L_\beta \quad (4.9)$$

where M_d is the domain magnetization of cobalt-ferrite equal to M_s determined from magnetization measurements on powdery (dry) MNPs and L_β is the Langevin function. Finally, one can calculate P to be in the order of 10^2 for mechanically free MNPs for a swollen ferrogel. From this rough estimation, it can be concluded that by increasing the frequency of RMF, ω also linearly increases. This implies that at higher frequencies, higher angular momentum is gained by the nanoparticles, which is simultaneously transferred to the surrounding. As a final remark, an augmentation of diffusion coefficients solely due to thermal effects is not a plausible mechanism since the transformation of magnetic energy to thermal energy is not possible at such low frequencies.[51]

The predominant aspect of the investigated mechanism is the response of ferrogels to external RMF generated by a basically designed magnet working at very low frequencies and intensities. Furthermore, the rate of mass transport within ferrogels can be controlled by tuning the frequency of RMF. The thus discovered *controllable* mass transport property of ferrogels in response to RMF opens up new opportunities to develop viscoelastic materials that are suitable for controlled permeation purposes in the field of microencapsulation or microfluidics.

4.5. Conclusion

Intensification of scalar transport in hydrogel media loaded with magnetic nano-inclusions subject to low-frequency rotating magnetic fields (RMF) necessitates the existence of hydrodynamically free MNPs. In contrast to viscous media, excitation of MNPs by RMF in viscoelastic hydrogel is influenced by the network physical parameters, such as mesh size, elasticity, and polymer-nanoparticle interactions. These parameters substantially alter the hydrodynamic freedom of nanoparticles. Thus in contrast to MNPs dispersions in viscous media, the properties of hosting viscoelastic media should be judiciously adjusted for the purposes of mass transport intensification.
Quantitative analysis of magnetization measurements for thermally blocked cobalt-ferrite MNPs hosted in *neutral* PAM hydrogels showed that higher mass fractions of hydrodynamically free MNPs can be obtained provided a soft ferrogel with low chemical cross-linkers ratio is formulated. This is mainly due to entrapment of MNPs in larger mesh spaces with less elastic coupling to the network. Non-covalent interactions between cobalt-ferrite surface and PAM functional groups bring about inevitable participation of MNPs in the formation of physical crosslinks ensued by the contraction of mesh space. Such phenomena increase the likelihood of MNPs blockages. Although the fraction of

free MNPs becomes lower as the cross-linking ratio increases, the very stiff hydrogels experience deterioration of their elastic properties resulting in the existence of some free MNPs.

The estimated values of effective diffusivities in absence and presence of external rotating magnetic field indicates that mass transport in a ferrogel containing free MNPs can be intensified by excitation in RMF. The effectiveness of RMF excitation can be also increased if the density of free MNPs becomes higher. However, achieving this goal by a method of ex-situ inclusion of MNPs inside the network structure is impractical. The reason behind is the significant magnetic dipole-dipole interactions among MNPs in the pre-gel solution at higher initial mass fractions which give rise to the formation of large aggregates. The fascinating properties of the discovered mechanism of mass transport enhancement reside in the fact that the diffusivity is simply controllable with the magnetic field frequency. In contrast to the pulsatile responsiveness in SMF and OMF, the frequency dependent diffusivity is advantageous for developing magneto-responsive materials with remote tunable mass transport properties.

Acknowledgments

The authors gratefully acknowledge the Natural Sciences and Engineering Research Council of Canada and the Canada Research Chair on Sustainable Energy Processes and Materials for their financial support. The assistance of Professor Rodrigue in the Chemical Engineering Department (Laval University) for implementation of the rheological tests is gratefully appreciated.

4.6. Nomenclature

Latin letters	**Description**	**Units**
D	Effective diffusion coefficient	m^2/s
E	Effective diffusion coefficient enchantement factor	-
G'	Storage modulus	Pa
H	Magnetic field	A/m
k_B	Boltzmann's constant	J/K
L_β	Langevin function	-
$\mathbf{m}$	Magnetic dipole vector	Am^2
$\mathbf{m_b}$	Blocked MNPs magnetic dipole vector	Am^2
$\mathbf{m_f}$	Free MNPs magnetic dipole vector	Am^2
$\mathbf{M}$	Magnetization vector	Am^2/kg
$\mathbf{M_b}$	Blocked MNPs Magnetization vector	Am^2/kg
$\mathbf{M_f}$	Free MNPs Magnetization vector	Am^2/kg
M	Magnitude of magnetization vector	A/m
M_b	Magnitude of blocked MNPs magnetization vector	A/m
M_f	Magnitude of free MNPs magnetization vector	A/m
M_r	Reduced remanent magnetization	-

P	Dimensionless number in Eq. 4.8	-
T	Absolute temperature	K
V_H	Hydrodynamic volume of nanoparticles	m^3
w_b	Mass of blocked MNPs	kg
w_f	Mass of free MNPs	kg
w_t	Total mass of MNPs	kg
X_b	Mass fraction of blocked MNPs	-
X_f	Mass fraction of free MNPs	-
Y_f	Mass of free MNPs scaled to total mass of swollen ferrogel sample	-
Greek letters	**Description**	**Units**
η	Dynamic viscosity	Pa s
μ_0	Absolute magnetic permeability of vacuum	N/A^2
ξ	Mesh size	m
T	Brownian relaxation time	s
φ	Mass fraction of MNPs	-
Φ	Volume fraction of MNPs	-
ω	Magnitude of spin vector	rad/s

4.7. References

1. A. H. Lu, E. L. Salabas and F. Schuth, *Angew. Chem., Int. Ed.*, 2007, **46**, 1222-1244.
2. S. Boroun and F. Larachi, *Curr. Opin. Chem. Eng.*, 2016, **13**, 91-99.
3. I. Torres-Diaz and C. Rinaldi, *Soft Matter*, 2014, **10**, 8584-8602.
4. F. Ridi, M. Bonini and P. Baglioni, *Adv. Colloid Interface Sci.*, 2014, **207**, 3-13.
5. C. Rinaldi, A. Chaves, S. Elborai, X. W. He and M. Zahn, *Curr. Opin. Colloid Interface Sci.*, 2005, **10**, 141-157.
6. A. Doring, W. Birnbaum and D. Kuckling, *Chem. Soc. Rev.*, 2013, **42**, 7391-7420.
7. F. Hapiot, S. Menuel and E. Monflier, *ACS Catal.*, 2013, **3**, 1006-1010.
8. A. K. Hauser, R. J. Wydra, N. A. Stocke, K. W. Anderson and J. Z. Hilt, *J. Controlled Release*, 2015, **219**, 76-94.
9. S. Odenbach, *Colloids Surf., A*, 2003, **217**, 171-178.
10. P. Hajiani and F. Larachi, *Chem. Eng. J.*, 2013, **223**, 454-466.
11. J. Faraudo, J. S. Andreu and J. Camacho, *Soft Matter*, 2013, **9**, 6654-6664.
12. T. Y. Liu, S. H. Hu, D. M. Liu and S. Y. Chen, *Langmuir*, 2006, **22**, 5974-5978.
13. T.-Y. Liu, T.-Y. Chan, K.-S. Wang and H.-M. Tsou, *RSC Adv.*, 2015, **5**, 90098-90102.
14. A. M. Al-Baradi, O. O. Mykhaylyk, H. J. Blythe and M. Geoghegan, *J. Chem. Phys.*, 2011, **134**, DOI: 10.1063/1.3557496.
15. S. Monz, A. Tschope and R. Birringer, *Phys. Rev. E: Stat., Nonlinear, Soft Matter Phys.*, 2008, **78**, DOI: 10.1103/PhysRevE.78.021404.
16. C. A. Cezar, S. M. Kennedy, M. Mehta, J. C. Weaver, L. Gu, H. Vandenburgh and D. J. Mooney, *Adv. Healthcare Mater.*, 2014, **3**, 1869-1876.
17. A. Zeuner, R. Richter and I. Rehberg, *Phys. Rev. E*, 1998, **58**, 6287-6293.
18. J. C. Bacri, R. Perzynski, M. I. Shliomis and G. I. Burde, *Phys. Rev. Lett.*, 1995, **75**, 2128-2131.
19. S. H. Hu, C. H. Tsai, C. F. Liao, D. M. Liu and S. Y. Chen, *Langmuir*, 2008, **24**, 11811-11818.
20. Z. H. Lu, M. D. Prouty, Z. H. Guo, V. O. Golub, C. Kumar and Y. M. Lvov, *Langmuir*, 2005, **21**, 2042-2050.
21. N. S. Satarkar, D. Biswal and J. Z. Hilt, *Soft Matter*, 2010, **6**, 2364-2371.

22. P. Hajiani and F. Larachi, *Chem. Eng. Process.*, 2013, **71**, 77-82.
23. R. E. Rosensweig, *Ferrohydrodynamics*, Dover Publications, United States of America, 1997.
24. S. Rose, A. Marcellan, D. Hourdet, C. Creton and T. Narita, *Macromolecules*, 2013, **46**, 4567-4574.
25. V. M. Kalita, A. A. Snarskii, D. Zorinets and M. Shamonin, *Phys. Rev. E*, 2016, **93**, DOI: 10.1103/PhysRevE.93.062503.
26. Y. Samoshina, A. Diaz, Y. Becker, T. Nylander and B. Lindman, *Colloids Surf., A*, 2003, **231**, 195-205.
27. M. J. McGuire, J. Addai-Mensah and K. E. Bremmell, *J. Colloid Interface Sci.*, 2006, **299**, 547-555.
28. J. A. Galicia, F. Cousin, E. Dubois, O. Sandre, V. Cabuil and R. Perzynski, *Soft Matter*, 2009, **5**, 2614-2624.
29. N. Gundogan, O. Okay and W. Oppermann, *Macromol. Chem. Phys.*, 2004, **205**, 814-823.
30. B. A. Westrin, A. Axelsson and G. Zacchi, *J. Controlled Release*, 1994, **30**, 189-199.
31. J. C. Hoh and Yaacob, II, *J. Mater. Res.*, 2002, **17**, 3105-3109.
32. N. Poudyal and J. P. Liu, *J. Phys. D: Appl. Phys.*, 2013, **46**, DOI: 10.1088/0022-3727/46/4/043001.
33. U. Jeong, X. W. Teng, Y. Wang, H. Yang and Y. N. Xia, *Adv. Mater.*, 2007, **19**, 33-60.
34. E. del Barco, J. Asenjo, X. X. Zhang, R. Pieczynski, A. Julia, J. Tejada, R. F. Ziolo, D. Fiorani and A. M. Testa, *Chem. Mater.*, 2001, **13**, 1487-1490.
35. E. De La Cruz-Montoya and C. Rinaldi, *J. Polym. Sci., Part B: Polym. Phys.*, 2011, **49**, 1163-1172.
36. M. Solzi, C. Pernechele, G. Calestani, M. Villani, M. Gaboardi and A. Migliori, *J. Mater. Chem.*, 2011, **21**, 18331-18338.
37. J. Tejada, R. D. Zysler, E. Molins and E. M. Chudnovsky, *Phys. Rev. Lett.*, 2010, **104**, DOI: 10.1103/PhysRevLett.104.027202.
38. V. Adibnia and R. J. Hill, *Macromolecules*, 2014, **47**, 8064-8071.
39. P. B. Laxton and J. C. Berg, *Langmuir*, 2008, **24**, 9268-9272.
40. P. S. Bhosale, J. Chun and J. C. Berg, *Langmuir*, 2011, **27**, 7376-7379.
41. P. S. Bhosale and J. C. Berg, *Langmuir*, 2010, **26**, 14423-14426.
42. E. Guth, *J. Appl. Phys.*, 1945, **16**, 20-25.
43. V. Adibnia, S. M. Taghavi and R. J. Hill, *Rheol. Acta*, 2017, **56**, 123-134.
44. L. Benguigui and F. Boue, *Eur. Phys. J. B*, 1999, **11**, 439-444.
45. A. K. Denisin and B. L. Pruitt, *ACS Appl. Mater. Interfaces*, 2016, **8**, 21893-21902.
46. M. Yanagioka and C. W. Frank, *Langmuir*, 2009, **25**, 5927-5939.
47. S. Boroun and F. Larachi, *AIChE J.*, 2017, **63**, 337-346.
48. B. Amsden, *Macromolecules*, 1998, **31**, 8382-8395.
49. I. Torres-Diaz, A. Cortes, Y. Cedeno-Mattei, O. Perales-Perez and C. Rinaldi, *Phys. Fluids*, 2014, **26**, DOI: 10.1063/1.4863201.
50. T. Yoshida, K. Enpuku, J. Dieckhoff, M. Schilling and F. Ludwig, *J. Appl. Phys.*, 2012, **111**, DOI: 10.1063/1.3688254.
51. R. E. Rosensweig, *J. Magn. Magn. Mater.*, 2002, **252**, 370-374.

Conclusion and suggestions for future works

I. Conclusion

In this PhD thesis, experimental and theoretical studies on the transport of scalars in ferrofluids/ferrogels subjected to external magnetic fields unveiled new properties on mass transport processes. The principle phenomena were further studied through numerical simulations to understand the underlying mechanisms. We can summarize our findings as follows:

- In the first chapter, we have shown that a dilute ferrofluid, subjected to external RMF exhibits anomalous diffusion which is also anisotropic. The mass transport rate in ferrofluid in a direction perpendicular to the rotation axis of external RMF is a function of RMF frequency and MNP concentration. Increasing both parameters in the range of experimented conditions monotonically enhances the mass transport rate. On the other hand, mass transport flux in the direction parallel to RMF rotation axis remains unaffected with respect to mere intrinsic molecular diffusion. The numerical solution of the advection-diffusion equation coupled to FHD transport equations informed on the insignificant contribution of ferrofluid advection in the rate intensification of mass transport in presence of RMF. Our observations vouch for effective ferrofluid diffusivities as a diagonal tensor quantity with the transverse components being strong functions of magnetic field and ferrofluid magnetic content.

- In the second chapter, we experimentally examined the variations of axial dispersion in a capillary Poiseuille flow for a Brownian ferrofluid subjected to transverse uniform RMF. The axial dispersion in Brownian ferrofluids is reduced by application of external RMF similar to previously reported observations for ferrofluid having bimodality in relaxation mechanism, *e.g.*, with magnetite nanoparticles. The transport of a passive tracer and resulting RTD were simulated in the framework of FHD. Solution of the advection-diffusion equation with intrinsic molecular diffusion does not predict the experimental RTD observations while RMF is activated as the tracer flux in the transverse direction is governed by molecular diffusion. In fact, the concept of effective diffusion explored in the first chapter is able to explain the experimental observations regarding reduced axial dispersion. The solution of advection-diffusion equation by means of an effective diffusivity tensor taking into account RMF effects shows acceptable agreement between model prediction and experimentally measured RTD. We also concluded that FHD theory is still deficient to predict transport processes occurring in the interstitial fluid of a magnetic colloidal dispersion.

- In the third chapter, we exploited the concept of anomalous diffusion for application in chemical reaction engineering. The mixing of reactive scalars in ferrofluid subjected to external RMF is more pronounced in comparison to SMF and OMF and also magnetic field-

free conditions. Although mixing experiments were performed in systems of paramagnetic/ superparamagnetic flows, the Kelvin force driven convection from the inherent magnetic susceptibility gradient has been found to have a marginal role in the mixing enhancement under RMF. Studies of mixing in molecular scale, a.k.a micromixing, through coupling of a model chemical reaction to the mixing phenomenon showed that by applying RMF, the molecular diffusion rate is substantially enhanced. A chemical reaction in ferrofluid proceeds with a rate closer to the intrinsic reaction rate and with less sensitivity to the rate of mixing between reactants at low RMF frequency.

- In the last chapter, we showed that the concept of anomalous diffusion can be exploited in a medium other than colloidal dispersions where elastic forces are also present along with viscous forces. A viscoelastic medium loaded with MNP exhibits enhanced mass transport rate when exposed to external RMF. However, the enhancement factor especially depends on viscoelastic properties, such as, mesh size, elasticity, and polymer-nanoparticle interactions. In contrast to MNPs dispersions in viscous media, properties of the hosting viscoelastic media should be judiciously adjusted for the purpose of mass transport intensification. The existence of hydrodynamically free MNP in the ferrogel is crucial to manifest enhanced mass transport in RMF. Magnetometry analysis showed that higher mass fractions of hydrodynamically free MNPs is obtained provided a soft ferrogel with low chemical cross-linkers ratio is prepared. The estimated values of effective diffusivities in absence and presence of external rotating magnetic field indicate that mass transport in a ferrogel containing free MNPs can be intensified under RMF excitation. The effectiveness of RMF excitation can be also increased if the number density of free MNPs or frequency of RMF is increased.

II. Suggestions for future work

Before closing this thesis, the following suggestions for future work are listed based on the experimental and theoretical studies achieved so far:

- The RMF driven macroscopic flows are relatively substantial as experimentally measured and reported in the literature. The spin-diffusion theory in microscale in contrast predicts scale-dependent but negligible spin up flows. The experimental validation of such finding from spin-diffusion theory at microscales is ought to be verified to test accuracy of FHD spin-up flow predictions.

- The augmented values of spin viscosity, previously proposed to explain spin-up phenomenon at macroscale, result in contradictions when extended to ferrofluid Poiseuille flow problems

at the microscale. This calls for the necessity to measure confidently this ferrofluid flow property in capillary Poiseuille flows subject to RMF and further verify predictions of spin-diffusion theory at microscale.

- The framework of FHD is unable to predict the transport of scalars in interstitial fluid when ferrofluid is subjected to RMF. This shortcoming in current theoretical knowledge relevant to ferrofluid motion calls for a more comprehensive theory with ability to explain our experimental observations. This might be achieved by developing ferrofluid flow models able to discriminate the motion of the dispersed and the continuous phases while expressing the exchange of vector and scalar properties in the presence of external forces/couples.

- The concept of reduced axial dispersion finds one of its potential applications in micro-reactor engineering. It is of notable interest to couple a chemical reaction set to the problem of ferrofluid Poiseuille flow and probe the impact of external RMF on conversion and selectivity of chemical reactions.

- As we have shown in chapter three, the selectivity of a probe reactive system with sensitivity to external magnetic stimuli can be remotely manipulated. There are a number of heterogeneous catalytic reactions whose selectivities are indeed mixing dependent. The MNP being easily separable and reusable, their surface properties can be tailored for proper catalytic active sites for subsequent utilization in chemical reactions. We may envision a catalytic microreactor whereby the MNP assist in both catalysing and mixing processes. This concept may facilitate reuse of costly and sensitive catalysts for mixing-sensitive reactions.

- The majority of studies in connection with ferrofluids use magnetite as a dispersed phase. Magnetite nanoparticles in a range less than 30 nm in diameter exhibits bimodality in their relaxation mechanism. It expected that only a fraction of magnetite nanoparticles with hard dipoles contribute through RMF-driven mixing mechanism. A comparative mixing study between magnetite and hard nano-magnet may give some clues on how different relaxation mechanisms play a role in the response of MNP to external magnetic fields.

- In chapter four, the proven concept of mixing in ferrogel points toward a fact that mixing by MNP might be possible even in solid macroscopic particles provided that mechanically-free MNP are present. This concept is of major importance in multiphase chemical processing where the solid phase resistance to scalar transport is a substantial barrier for process intensification purposes. The idea may be initiated by seeding a porous material with MNP and probe inter-particle mixing in presence of external magnetic stimuli.

Appendix.1

From Eq. 1.11 we have

$$\underline{\mathbf{F}}^{m} = \underline{\boldsymbol{\nabla}} \cdot \left(\mu_0 \underline{\mathbf{H}} \otimes \underline{\mathbf{H}} - \frac{\mathbf{1}}{\mathbf{2}} \mu_0 \left| \underline{\mathbf{H}} \right|^{\mathbf{2}} \underline{\mathbf{I}} \right) \tag{A1.1}$$

With the aid of

$$\underline{\boldsymbol{\nabla}} \cdot \left(\underline{\mathbf{H}} \otimes \underline{\mathbf{H}} \right) = \underline{\mathbf{H}} \cdot \underline{\boldsymbol{\nabla}}\, \underline{\mathbf{H}} + \underline{\mathbf{H}} \left(\underline{\boldsymbol{\nabla}} \cdot \underline{\mathbf{H}} \right) \tag{A1.2}$$

And

$$\underline{\boldsymbol{\nabla}} \cdot \left(\frac{\mathbf{1}}{\mathbf{2}} \mu_0 \left| \underline{\mathbf{H}} \right|^{\mathbf{2}} \underline{\mathbf{I}} \right) = \underline{\boldsymbol{\nabla}} \left(\frac{\mathbf{1}}{\mathbf{2}} \mu_0 \left| \underline{\mathbf{H}} \right|^{\mathbf{2}} \right) \tag{A1.3}$$

Then Eq. 1.11 is rewritten

$$\underline{\mathbf{F}}^{m} = \mu_0 \underline{\mathbf{H}} \cdot \underline{\boldsymbol{\nabla}}\, \underline{\mathbf{H}} + \mu_0 \underline{\mathbf{H}} \left(\underline{\boldsymbol{\nabla}} \cdot \underline{\mathbf{H}} \right) - \underline{\boldsymbol{\nabla}} \left(\frac{\mathbf{1}}{\mathbf{2}} \mu_0 \left| \underline{\mathbf{H}} \right|^{\mathbf{2}} \right) \tag{A1.4}$$

Since

$$\frac{\mathbf{1}}{\mathbf{2}} \underline{\boldsymbol{\nabla}} \left(\underline{\mathbf{H}} \cdot \underline{\mathbf{H}} \right) = \underline{\boldsymbol{\nabla}} \left(\frac{\mathbf{1}}{\mathbf{2}} \left| \underline{\mathbf{H}} \right|^{\mathbf{2}} \right) = \underline{\mathbf{H}} \cdot \underline{\boldsymbol{\nabla}}\, \underline{\mathbf{H}} + \underline{\mathbf{H}} \times \left(\underline{\boldsymbol{\nabla}} \times \underline{\mathbf{H}} \right) \text{ and } \underline{\boldsymbol{\nabla}} \times \underline{\mathbf{H}} = \underline{\mathbf{0}} \tag{A1.5}$$

Then we can rewrite Eq. 1.11

$$\underline{\mathbf{F}}^{m} = \mu_0 \underline{\mathbf{H}} \cdot \underline{\boldsymbol{\nabla}}\, \underline{\mathbf{H}} + \mu_0 \underline{\mathbf{H}} \left(\underline{\boldsymbol{\nabla}} \cdot \underline{\mathbf{H}} \right) - \mu_0 \underline{\mathbf{H}} \cdot \underline{\boldsymbol{\nabla}}\, \underline{\mathbf{H}} = \mu_0 \underline{\mathbf{H}} \left(\underline{\boldsymbol{\nabla}} \cdot \underline{\mathbf{H}} \right) \tag{A1.6}$$

Appendix.2

MNP synthesis procedures and preparation of the magnetic nanofluid

MNPs were synthesized by coprecipitation of Fe^{2+} and Fe^{3+} ions from a 2.5 mL aqueous solution containing 0.5 M of $FeCl_2$ and 1 M of $FeCl_3$ by controlled addition of 25 mL solution of 0.32 M ammonium hydroxide under nitrogen atmosphere. The precipitate was magnetically collected and washed several times with deionized water to remove excess ammonium hydroxide. The powder was dried for 24 h under nitrogen atmosphere at 60˚C and then mixed with a 1 wt% solution of trisodium citrate in an ultrasonic bath at 60˚C for 2 h. The particles were then precipitated with acetone and washed with deionized water. The precipitation and washing steps were repeated several times to remove excess sodium citrate from the suspension. The MNPs were dried at ambient conditions under nitrogen atmosphere and subsequently weighed and suspended in specified amounts of water to yield a stock suspension containing 10wt% of MNPs. The suspension was placed in an ultrasonic bath for 1 h for disaggregation of the particles, finally forming a stable ferrofluid. The prepared stock ferrofluid was diluted to desired levels for the subsequent experiments.

Magnetization of MNPs and ferrofluid

Figure A2.1 illustrates magnetization of MNPs and ferrofluid as a function of the applied field magnetic field. The hysteresis observed in the magnetization curve of MNPs confirms their ferromagnetic character whereas the ferrofluid exhibits super-paramagnetic behavior with zero coercivity in its magnetization curve.

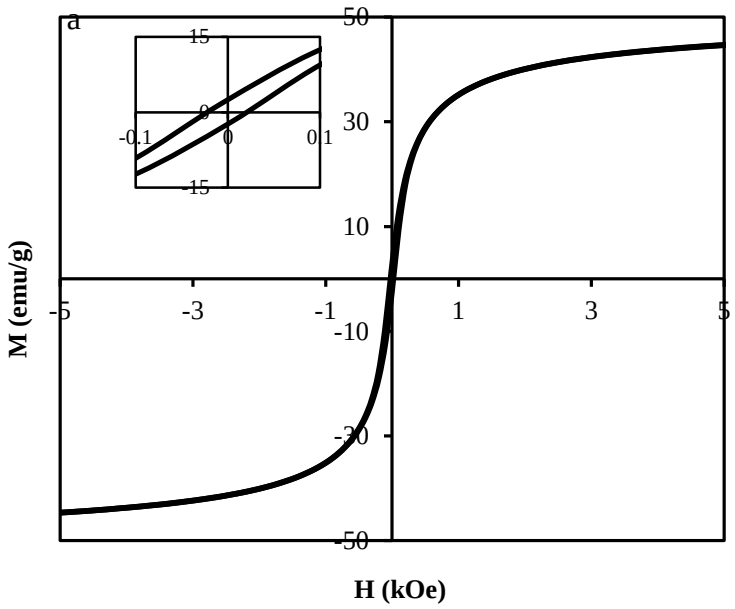

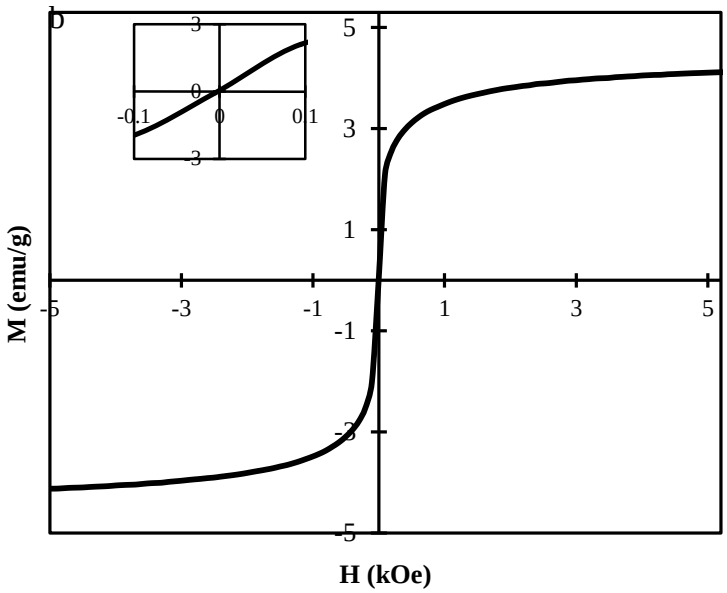

Fig A2.1 Magnetization of a) MNPs and b) ferrofluid containing 10wt% of MNPs dispersed in water with trisodium citrate as a function of applied field magnetic field at 298 K. Inset: low-field details.

Measurement of MNP size distribution by DLS method

Figure A2.2 portrays the MNP particle size distribution with 5% volume fraction MNP dispersed in water. Curve confirms some polydispersity in MNP size distribution.

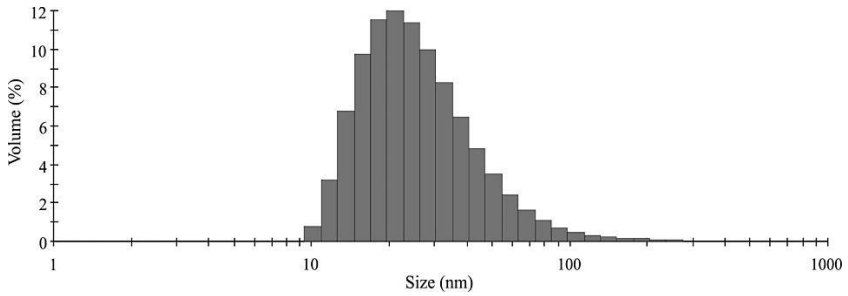

Fig A2.2 Particle size distribution of MNPs measured by DLS method. Volume based mean hydrodynamic diameter = 36.3 nm.

Pertinence of Kohlrausch's law in conductivity measurement

Prior to utilization of the conductometry method for assessment of mixing, the Kohlrausch's law at the tested dilution levels was first verified. For this purpose, the calculated conductivities based on Kohlrausch's law were compared to those calculated by Onsager equation that accounts for higher-ionic strength deviations. In contrast to Kohlrausch's law, Onsager's equation takes two parameters into account to predict relaxation and electrophoretic effects on ionic mobility:[1]

$$\Lambda = \Lambda_0 - (A + B\Lambda_0)\sqrt{C} \qquad \text{(A2.1)}$$

Where A and B for aqueous solutions at 25ºC are 60.2 and 0.229, respectively. The second term in Eq. A2.1 RHS becomes marginal in diluted conditions resulting in an almost valid linear relationship between conductivity and concentration (see Eq. 3.1 in manuscript text).

The results in Table A2.1 show that the values obtained from Onsager`s equation have approximately 1% error relative to the limiting conductivities. Furthermore, experimentally measured conductivities of individual electrolytes do not show any significant deviation from their limiting conductivities, indicating satisfactory estimation of concentrations from Kohlrausch's law. The higher experimentally measured conductivities of neutralized and magneto-basic solutions than their limiting molar conductivities are possibly due to presence of surfactant molecules in the carrier fluid. κ_{max} and κ_{min} in Eqs. 2-4 (see manuscript text) were determined to be, respectively, 335.1 and 60.7 μS/cm by using the limiting conductivities in Table A2.1. Therefore, the mixing efficiencies from Eq. 3.4 can be calculated from the experimentally measured electrical conductivity, $\kappa_{measured}$.

Table A2.1 Limiting theoretical (from Eq. A2.1) and experimental values of conductivities ($mS.cm^2/L$) for three 1 mM electrolyte solutions (95% confidence intervals on measured conductivities)

Component	Limiting conductivity[1]	Conductivities by Onsager's equation	Experimentally measured conductivities
HNO_3	421	416.6	418.6 ± 3.7
NaOH	249.2	245.4	257.1 ± 4.1
$NaNO_3$	121.5	118.7	127.3 ± 2.6

Solution procedure of ordinary differential equations of IEM model

According to Eq. 3.14 and 3.15 (see manuscript text), for each species two ordinary differential equations should be solved simultaneously. Since there are six individual components participating in reactions Eqs. 5,7 & 10, a set of twelve ODEs must be solved as initial-valued problem. The concentration of each species is set to a variable according to the following order : $A \equiv IO_3^-$, $B \equiv I^-$, $C \equiv H^+$, $D \equiv I_2$, $E \equiv H_2BO_3^-$, $F \equiv I_3^-$. The corresponding ODEs for each component become:

$$\frac{dA_i}{dt} = -R_{1,i} + \frac{\langle A_i \rangle - A_i}{t_m} \tag{A2.2}$$

$$\frac{dB_i}{dt} = -5R_{1,i} - R_{3,i} + R_{4,i} + \frac{\langle B_i \rangle - B_i}{t_m} \tag{A2.3}$$

$$\frac{dC_i}{dt} = -6R_{1,i} - R_{2,i} + \frac{\langle C_i \rangle - C_i}{t_m} \tag{A2.4}$$

$$\frac{dD_i}{dt} = 3R_{1,i} - R_{3,i} + R_{4,i} + \frac{\langle D_i \rangle - D_i}{t_m} \tag{A1.5}$$

$$\frac{dE_i}{dt} = -R_{2,i} + \frac{\langle E_i \rangle - E_i}{t_m} \tag{A2.6}$$

$$\frac{dF_i}{dt} = -R_{4,i} + R_{3,i} + \frac{\langle F_i \rangle - F_i}{t_m} \tag{A2.7}$$

Where i = 1,2 correspond to concentration or reaction in segments 1 and 2. A serious difficulty lies in the treatment of R_2, R_3 and R_4 reaction rates. These reaction rates are associated with instantaneous reactions which are notably faster in comparison to the other reactions, hence turning the involved

ODEs into stiff ones. To remove stiffness from this set of ODEs, a variable transformation is adopted as shown below:[2]

$$U = C - E \quad \text{(A2.8)}$$

$$Z = B - D \quad \text{(A2.9)}$$

$$W = B + F \quad \text{(A2.10)}$$

From straightforward algebraic operations (S.4-S.6), (S.3-S.5), (S.3+S.7) yields the resultant ODEs:

$$\frac{dU_i}{dt} = -6R_{1,i} + \frac{\langle U_i \rangle - U_i}{t_m} \quad \text{(A2.11)}$$

$$\frac{dZ_i}{dt} = -8R_{1,i} + \frac{\langle Z_i \rangle - Z_i}{t_m} \quad \text{(A2.12)}$$

$$\frac{dW_i}{dt} = -5R_{1,i} + \frac{\langle W_i \rangle - W_i}{t_m} \quad \text{(A2.13)}$$

$$\frac{dA_i}{dt} = -R_{1,i} + \frac{\langle A_i \rangle - A_i}{t_m} \quad \text{(A2.14)}$$

Another set of ODEs similar to Eqs. S.11-S.14 should be taken into account for the second stream. A code in Matlab was written to solve the two sets of ODEs by a second-order Rung-Katta method. Each concentration set in Table 3.1 (see manuscript text) is used separately as initial conditions and for each set an appropriate range of t_m was selected and discretized into 50 values. Therefore, for each concentration set a 4×50 matrix is generated consisting A, U, Z and W, as a function of t_m. Since I_3^- is in instantaneous equilibrium with I^- and I_2, its concentration is calculated by:

$$F = K_B BD \quad \text{(A2.15)}$$

By substituting F and D by W-B and B-Z, Eq. A1.15 becomes a second order algebraic equation that gives B according to:

$$B = \frac{Z - 1/K_B + \sqrt{(Z - 1/K_B)^2 + 4W/K_B}}{2} \quad \text{(A2.16)}$$

Therefore for each trialed t_m a specific F and concentration set is attributed. By utilizing:

$$F = [I_3^-] = \varepsilon OD \quad \text{(A2.17)}$$

The optical densities, OD, corresponding to F values were calculated to plot figure 6 for each concentration set (ε was determined to be 26103 mol/L from the calibration data).

References

1. Atkins PW. *Physical chemistry* (6 edition). New York, Freeman, 1999.

2. Yang HJ, Chu GW, Zhang JW, Shen ZG, Chen JF. Micromixing efficiency in a rotating packed bed: Experiments and simulation. *Industrial & Engineering Chemistry Research.* 2005;**44**,7730-7737.

Appendix.3

Synthesis of Cobalt-Ferrite Nanoparticles

Cobalt-ferrite nanoparticles were synthesized by moderate temperature coprecipitation of Fe^{3+} and Co^{2+} ions in an alkaline solution. For this purpose, an aqueous solution of $FeCl_3$ (0.02 mM) and $CoCl_3$ (0.04 mM) was prepared and heated up to 55°C. After temperature stabilization, 2 M NaOH solution was added dropwise to the vigorously stirred solution at constant rate of 1 mL/min. The volumetric ratio of metal-bearing solution to caustic solution was 1.5. After formation of a brown precipitate, the temperature of suspension was raised to 85°C and the suspension was stirred for 30 min under reflux conditions at constant temperature. Afterwards, the black precipitate as final product was magnetically separated and washed several times with deionized water and dried 24 h at 80°C. The density of dried MNPs was 4.547 g/cm^3 measured by an Ultrapyc 1200e gas pycnometer (Quatachrome Instruments) where nitrogen was the gas phase. Finally, water at pH 9 adjusted by NaOH was added to a weighed amount of dried powder and the suspension was sonicated by means of an ultrasonic bath for 15 min. The resultant colloidal dispersion is denoted as ferrofluid. The prepared stock ferrofluid was diluted to the desired levels of MNPs mass fraction (φ) for preparation of ferrogels.

Synthesis of Hydrogels

Hydrogel samples were prepared by free radical polymerization of AM monomers using N,N'-methylenebisacrylamide (MBAA) as cross-linker, ammonium persulfate (APS) as initiator and tetramethylethylenediamine (TEMED) as catalyst. The pregel solution containing 6 wt% AM, cross-linker and catalyst was bubbled with argon while under vigorous mixing. Afterward, solution of 1 wt% APS was added to the pregel solution to initiate the polymerization. The volumetric ratio of TEMED, APS solution and monomer solution was kept 1/10/100, accordingly. By adjusting the concentration of MBAA, the molar cross-linking ratio, defined as the molar concentration of MBAA to that of AM, was varied.

Synthesis of Ferrogels

The procedure for preparation of ferrogel samples is the same as hydrogels but the monomer, cross-linker and TEMED were initially dissolved in a ferrofluid with adjusted φ. Sonication in the ultrasonic bath was utilized as a mixing means to prevent aggregation of MNPs in the magnetic stirrer. The pregel solutions of hydrogels and ferrogels were poured into plastic tubes 4 mm in inner diameter and 50 mm in length right after addition of the initiator, so that obtaining the final gel in the form of cylinders. All the samples were subsequently immersed in deionized water for 4 days and the supernatant water was replaced every 12 h to remove the unreacted chemicals.

Determination of Swelling Ratio

In order to obtain the swelling ratios (*SR*), the cylindrically shaped samples were immersed in water at pH 9 for 10 days and their final weights at equilibrium swelling were recorded. The amount of water in swollen state is calculated by subtracting the PA and MNPs weights from the final weight. The samples were subsequently dried for 24 h at 80°C and then weighed again. *SR* was calculated by dividing the calculated weight of total absorbed water to the weight of the dried sample.

Determination of Effective Diffusion Coefficient from Release Kinetics

The receiver solution used in the release experiments was water at pH 9, circulated with a peristaltic pump at constant rate of 10 mL/min within a closed loop. The cylindrical shaped samples were previously equilibrated with imbibition solution of 50 mM rhodamine B for 4 days. The concentration of solute in sample was assumed 50 mM since the volume of imbibition solution was much larger

than the sample volume. Afterwards, the imbibed sample was placed in the central axis of a plastic tube with inner diameter of 22 mm and the tube was connected to the closed loop of the circulating solution. The space between the sample and inner wall of plastic tube was filled with glass beads of 1 mm in diameter, holding the sample in vertical position. The glass beads also help to eliminate radial concentration profiles that might establish in the space between the inner wall of plastic tube and peripheral surface of the sample. The concentration of released rhodamine B into the circulating solution was continuously measured by a UV-Vis spectrophotometer (Stellarnet Inc, model Black Comet) equipped with an optical cell designed for in-flow measurements. A vigorously stirred container with ventilation to atmosphere was placed prior to the optical cell to remove bubbles and possible concentration gradients in the outlet stream of the plastic tube. For determination of *D*, the analytical solution to the problem of solute diffusion from infinite circular cylinder to a well stirred solution of finite volume was utilized. The concentration of solute in the solution is expressed according to (L. Haggerty, J. H. Sugarman, R. K. Prudhomme, *Polymer*, 1988**, 29**, 1058-1063.):[1]

$$\frac{\mathrm{C(t)}}{\mathrm{C_\infty}} = 1 - \sum_{\mathrm{n=1}}^{\infty} \frac{4\alpha(1+\alpha)}{4 + 4\alpha + \alpha^2 \mathrm{q_n^2}} \exp(-\mathrm{Dtq_n^2/r^2}) \qquad \text{(A3.1)}$$

Where t is time, r is the radius of the sample, $C(t)$ is the concentration in the solution and C_∞ is the final concentration in the solution, q_n are the positive roots of equation:

$$2\mathrm{J_1(q)} + \alpha \mathrm{q J_0}(q) = 0, \ \alpha = \frac{\text{solution volume}}{\text{sample volume}} \times K \qquad \text{(A3.2)}$$

Where K is the partition coefficient defined as the ratio of equilibrium concentration of rhodamine B solution in contact with the sample (C_∞^s). The K values were determined by immersing the imbibed samples in water at pH 9 until the concentration of solute in water reaches a constant value. The equilibrium concentration inside the sample was simply calculated from the known mass of water in the sample. C_∞ was also calculated according to the obtained K values. After swelling, sample expansion in the axial direction was negligible, so that the radius of sample was calculated assuming sample expansion only in radial direction. The initial radius was set to 2 mm equal to the inner radius of the plastic tube. The Diffusion coefficients were estimated by plotting $C(t)$ as the function of t and minimizing the root-mean squares error between experimental and theoretical data by iterating on the values of D.

Procedure of Vibrating Sample Magnetometry

Magnetic characterization was carried out in a vibrating sample magnetometer (VSM) from Princeton Instrument (MicroMag model 2900) at 298 K for determining magnetizations of MNPs and ferrogels. The external magnetic field (H) applied from the instrument had a maximum value of 14 kOe. Swollen samples were weighed and then put into a hollow cylinder made of silicone rubber mounted and fixed on the VSM vibrating probe by means of silicon grease. The cylinder was capped with a plastic sheet to prevent evaporation of water during the experiment. The magnetization (M) of each sample was calculated by dividing the measured magnetic moments by the mass of magnetic nanoparticles in the sample, determined form the known initial amount of MNPs in the pregel solution. The amount of MNPs in the pregel solution and swollen samples are identical since the nanoparticles did not diffuse out of the ferrogel samples during the swelling process as verified by magnetometry of supernatant liquids during swelling process.

References

1. L. Haggerty, J. H. Sugarman, R. K. Prudhomme, *Polymer*, 1988**, 29**, 1058-1063.

Appendix.4

The role of magnetic nanoparticles in mixing, transport phenomena and reaction engineering - Challenges and opportunities

The role of magnetic nanoparticles in mixing, transport phenomena and reaction engineering - Challenges and opportunities

Shahab Boroun, Faïçal Larachi

Department of Chemical Engineering, Laval University, Québec, QC, Canada G1V 0A6

Abstract

Practicality of tailoring the physical chemistry of magnetic nanoparticles (MNPs) has opened up fascinating paths for magnetism into the realm of chemical engineering. Such outgrowth is accredited to the MNPs unique behavior when these are excited under external magnetic fields. This commentary serves as an usher for readers interested in this emerging research field in which the potential of magnetic nanoparticles to modify or improve transport phenomena, mixing and chemical reaction is exposed. With a focus on MNPs and their stabilized colloidal dispersions, the mechanisms whereby intensification is achieved *via* momentum, mass and heat stimulations are discussed in priority.

Introduction

Since Gilbert's XVIIth century "*De Magnete*" scholarly treatise, enthrallment for the science of magnetism has been unfading, and invention in the past century of synthetic magnetic fluids, a.k.a. ferrofluids, led to a paradigm shift especially at unlocking new domains of applications to unprecedented levels [1,2]. Exploiting the unique properties of **m**agnetic **n**ano**p**articles (MNP) is actively pursued in many engineering fields, let alone these unusual nano-objects are still vividly scrutinized in physics and medicine [1]. This widespread interest is ascribed to the peculiar behavior and properties MNPs manifest upon exposure to external magnetic fields. With the advent of ferrofluids as stabilized MNP colloidal dispersions and owing to decades of theoretical studies and experimental verifications, the journey into the realm of magnetism science took an unexpected turn expanding into new domains of applications [1] and particulalry in chemical engieering. In this regard, this commentary attempts to modestly fill in a gap by introducing to the chemical engineering readership the current state of research in the emerging field of transport phenomena intensification by means of magnetic nanoparticles and ferrofluids under external magnetic fields. After introducing some backgrounds on MNP properties and momentum transport in ferrofluids, the concepts of momentum control, mixing and mass transfer control, then finally heat transfer control will be discussed in distinct sections. For each section, the spotlight will be put on some selected findings deemed promising from the recent literature. In particular, we did not refrain from referring to single and potentially pioneering works as the emphasis is to demonstrate current trends in research. However, despite its brevity, this account covers numerous applications of MNPs backed, when necessary, with references providing fundamental knowledge and theories on the subjects discussed.

Background

If analysis of force and stress in magnetic materials is well-established in magnetostatics, the advent of colloidal magnetic fluids initiated development in recent decades of a fluid mechanics branch dedicated to study the dynamics of ferrofluids or ferrohydrodynamics (FHD) [2]. Prior to presentation of the relevant research work, it is essential to clearly grasp specificity of momentum transport in ferrofluids subject to external magnetic fields. Though detailed explanation of FHD goes beyond this work's scope, introducing some basic principles to rationalize the mechanisms proper to MNP is deemed necessary.

Superparamagnetic nanoparticles under an external magnetic field exhibit considerable magnetization stemming from a lattice-wise resultant of the collective organization of individual magnetic moments

within MNPs. Upon removal of magnetic field, magnetization decays over time as a result of thermal agitation of these aligned magnetic moments. This process is characterized by a Néelian relaxation time [3]

$$\tau_n = f_0 \exp\left(\frac{KV_p}{k_B T}\right) \tag{A4.1}$$

Where k_B is Boltzmann's constant, V_p is MNP magnetic core volume, K is an anisotropy constant, f_0 is the Larmor frequency of the magnetic moment in the nanoparticle anisotropic field, and T is the absolute temperature.

Néelian relaxation in ferrofluids competes with a Brownian relaxation mechanism whereby the individual MNPs are being permanently assaulted and knocked by neighboring entities in the carrier fluid. The resulting rotational diffusion has a characteristic time [1]

$$\tau_b = \frac{3V_H \eta}{k_B T} \tag{A4.2}$$

Where V_H denotes the MNP hydrodynamic volume including surfactant layer and η is the carrier fluid dynamic viscosity. Brownian relaxation results in the manifestation of superparamagnetism in ferrofluids even when containing hard MNPs (ferromagnets) with negligible Néelian relaxation.

Derivation of the linear and angular momentum balance equations of a ferrofluid rests on simultaneous consideration of surface stresses and moments thereof, body couples exerting in the form of magnetic torque and also surface couples [2,4]

$$\rho \frac{\mathbf{Du}}{\mathbf{D}t} = -\boldsymbol{\nabla} p + \rho \mathbf{F} + 2\zeta \boldsymbol{\nabla} \times \boldsymbol{\omega} + (\zeta + \eta)\boldsymbol{\nabla}^2 \mathbf{u} \tag{A4.3}$$

$$\rho I \frac{\mathbf{D}\boldsymbol{\omega}}{\mathbf{D}t} = \mu_0 \mathbf{M} \times \mathbf{H} + 2\zeta(\boldsymbol{\nabla} \times \mathbf{u} - 2\boldsymbol{\omega}) + (\lambda' + \eta')\boldsymbol{\nabla}\boldsymbol{\nabla}.\boldsymbol{\omega} + \eta' \boldsymbol{\nabla}^2 \boldsymbol{\omega} \tag{A4.4}$$

Where ρ is the fluid density, **ω** is the spin density vector, p is the hydrodynamic pressure, ζ is the vortex viscosity, **F** is the sum of gravitational and magnetic body forces ($\mathbf{F_m}$), λ' is the bulk spin viscosity, η' is the shear spin viscosity, μ_0 is the vacuum permeability, **M** is the magnetization vector and **H** is the magnetic field vector. Eqs.A4.3,4 express the ferrofluid motion when MNPs exchange angular momentum with the surrounding fluid; however, in the absence of momentum exchange –for instance when magnetic and hydrodynamic torques on MNPs are mutually orthogonal vectors– the linear momentum balance suffices to describe the fluid motion [2]. The magnetic body force on a magnetically polarized body can be expressed as [2]

$$\mathbf{F_m} = \mu_0 (\mathbf{M}.\boldsymbol{\nabla})\mathbf{H} \tag{A4.5}$$

Substituting in Eq.A4.5 magnetization assumed to be linearly function of magnetic susceptibility (χ_i) leads after some vector algebra manipulations to

$$\mathbf{F_m} = \frac{\mathbf{1}}{\mathbf{2}} \mu_0 |\mathbf{H}|^2 \boldsymbol{\nabla}(\chi_i) + \frac{\mathbf{1}}{\mathbf{2}} \mu_0 \chi_i \boldsymbol{\nabla}(\mathbf{H}.\mathbf{H}) \tag{A4.6}$$

Ferrofluid magnetization is traditionally described by a relaxation-reorientation equation [5]

$$\frac{\mathbf{DM}}{\mathbf{D}t} = \boldsymbol{\omega} \times \mathbf{M} + \tau^{-1}(\mathbf{M} - \mathbf{M_0}) \tag{A4.7}$$

Let us turn our attention onto how ferrofluids interact with external magnetic fields. Einstein viscosity formulation of dilute nanofluids adopts a realistic view that equalization of nanoparticles rotation to fluid vorticity occurs at very short time lapses [5]. However, if the nanoparticle rotation does not

match with fluid vorticity, the emergence of a friction force triggers additional rotational viscosity [6]. This is reflected in the second term on Eq.A4.4 RHS which expresses the exchange rate of momentum between fluid vorticity and the average internal rotation rate of MNPs in the sub-continuum [2]. By prompting **M**-**H** directional mismatch as a result of fluid vorticity, the magnetic character of the fluid nano-inclusions manifests in the form of a magnetic torque to oppose MNP free rotation. With magnetic field direction set normal to fluid vorticity, a positive magnetoviscosity effect tantamount to an increased ferrofluid effective viscosity is enabled [7, 8]. By their ability to curtail disruption of the "magnetic" coherence due to Brownian agitation, oscillating (OMF) and rotating (RMF) magnetic fields, unlike static magnetic fields (SMF), offer a remarkable advantage. For instance, Brownian agitation can be nullified upon enabling OMF oscillation periods below the Brownian relaxation time thus ensuring *undisrupted* OMF-synchronized rotation of MNPs [9]. In the case of rotating fields, such restriction is even unnecessary as an MNP feels constantly a *finite* magnetic torque regardless of the RMF frequency. To the discontent of Brownian agitation, such magnetic field actuation ensures that the nanoparticles keep spinning even at low RMF frequencies [10,11].

Momentum Transfer Control

Decades of improvements and experimental verifications have evolved FHD into a mature framework proving reliability and accuracy of FHD for computational studies under various types of magnetic fields [12], and laminar and turbulent flows [13,14]. The concept of hydrodynamic control is illustrated by both theoretical and experimental works that showcase in this regard the capacity of MNPs to modify the flow characteristics in the presence of various types of magnetic fields.

To curb wall flow channeling in porous media suffering low tube-to-particle diameter ratios, a chemical engineering concept of magnetic field-assisted hydrodynamic control was proposed [7,15,16]. The concept's premise acknowledges the fact that the high-permeability near-wall region is the site of highest fluid flow vorticity thereby prompting flow short-circuiting alongside the tube wall. For this purpose spatially averaged continuity, linear and internal angular momentum balances, magnetization relaxation equation, and Maxwell flux and Ampere-Maxwell laws were numerically solved for a 3-D axisymmetric geometry (Figure A4.1a). Numerical simulations have shown that by judicious orientation of a gradient static magnetic field with respect to an isothermal ferrofluid flow in porous media, wall channeling can indeed be minimized. By prompting magneto-viscothickening conditions near the wall, the expected idea consists in hindering the flow there by a reversal of MNP spin vectors with respect to the natural fluid vorticity vector. The porous medium was subject to a static magnetic field with both upward and downward gradients with respect to flow direction. An important finding from the simulations is the dramatic reduction of angular velocity (or spin) of MNPs alongside the wall region translating in an augmented resistive force that flattened the radial profile of the axial linear velocity component of the ferrofluid flow. Despite intrinsically higher wall-region permeability, such radial profiles bear more resemblance to plug flow the higher the positive gradient magnetic field as portrayed in Figure A4.1b.

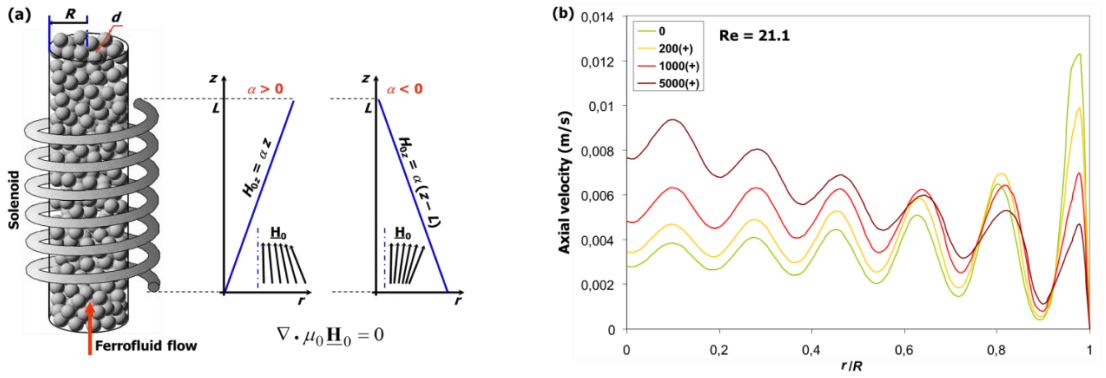

Fig A4.1 (a) Schematic of a porous medium for the wall channeling study under gradient SMF [16]; (b) Radial profiles of axial linear velocity at the bed exit (z = L). Values of α in legend box refer to applied magnetic field gradient [7].

Manipulation of residence time distribution (RTD) is of great importance in chemical processes for establishing uniform processing times may be crucial to produce high-quality products. Hajiani and Larachi recently expanded the concept of hydrodynamic tuning into ferrofluid flows subject to low frequency (<100 Hz) transverse uniform rotating magnetic fields for manipulation of RTD. In a series of experimental studies [17-19], they investigated the effect of uniform RMF transverse to a capillary *laminar* flow of dilute ferrofluids. Analysis of tracer pulse tests revealed that RMF drastically reduced the RTD variance which is to be mirrored with reduction of axial dispersion coefficient and therefore resulting in reshaping the laminar parabolic velocity profile into a flatter close-to-plug flow profile (Figure A4.2). Conversely, enabling a positive magnetoviscous regime through imposition of static magnetic fields was shown to result in broadened RTD responses whereby the inflating axial dispersions were ascribed to stem from the retarded spin of MNPs.

Another momentum transport mechanism has also been numerically predicted for manipulation of RTD patterns in laminar capillary ferrofluid flow subject to gradient low frequency OMF [20]. This mechanism is based on the oscillatory magnetophoretic movement of MNPs in an oblique direction with respect to fluid flow. The simulation results suggested the possibility of achieving narrower RTD patterns in various magnetic field stimulation scenarii. The postulated mechanism is based on assuming that OMF can bring about linear momentum exchange between the oscillating MNPs and the surrounding fluid. It should be pointed out that from a practical point of view, aggregation of nanoparticles due to magnetic dipole-dipole interactions under applied magnetic field may impair the feasibility of this magnetophoresis concept. Informative theoretical [21] or experimental [22,23] accounts are available in the literature to help construction of more realistic mathematical frameworks on the stability of ferrofluids in gradient fields as well as on the dynamics of magnetophoresis. Nonetheless, until now the pinpointed mechanism of momentum transport in gradient OMF has not been validated experimentally.

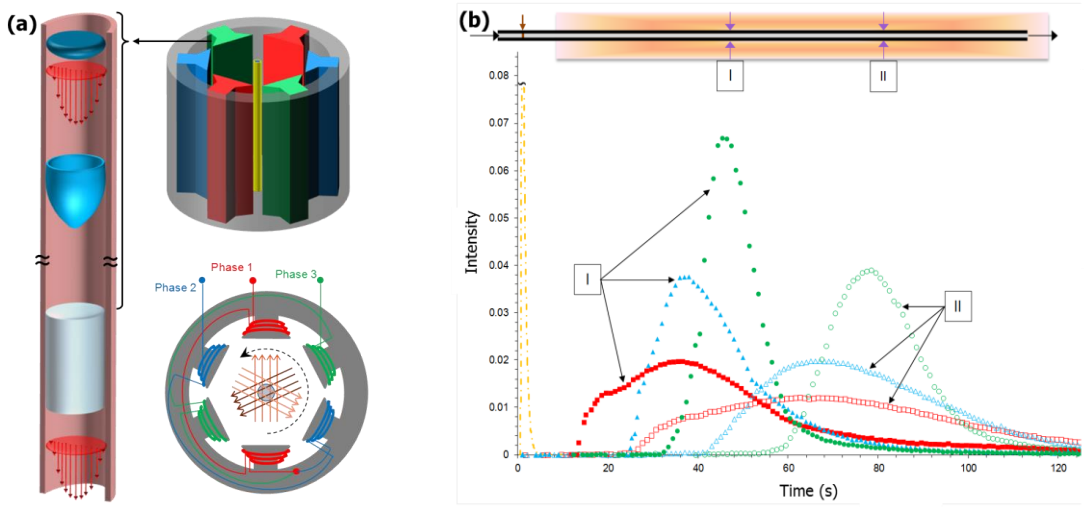

Fig A4.2 RTD alteration by external rotating magnetic field: (a) Schematic representation of tracer dispersion in a capillary Poiseuille flow with laminar velocity profile and orientation of uniform RMF; (b) Inlet (■) and outlet (□) conductivity responses without magnetic field are notably narrowed (○,●) and (Δ,▲) by application of a 50 Hz RMF transverse to ferrofluid flow (MNP volume fraction 0.0025) corresponding, respectively, to 10.4 and 36.5 kA/m magnetic field intensities [17].

MNPs have also been explored for hydrodynamic tuning in fluidized beds after the pioneering work of Rosensweig [24] in developing the concept of magnetically stabilized beds (MSB) and extending its use to industrial units [25]. The bubble-free operation in fluidized beds, as a result of the stabilizing effect of external magnetic fields, has technological interest in the reduced gas bypassing in catalytic reactions. Currently, a branch of expanding knowledge in MSB is moving toward development of magnetic catalysts that serve for reaction and stabilization simultaneously. By utilization of magnetic catalysts, increased conversion and selectivity stemming from the attenuation of the bypassing phenomenon in MSB are reported in the literature [26-28]. It should be noted that the chaotic mixing in conventional fluidized beds creates isothermal conditions that suits well for exothermic reactions, whereas MSBs reportedly suffer from lower heat transfer coefficients [29]. An additional constraint to envisage in this area is the fact that Curie temperature of magnetic materials restricts MSB versatility to an implementation which excludes high-temperature operations.

Mixing and Mass Transfer Control

The interaction between mixing and chemical reactions is now a well-studied subject both in macro- and microscale reaction engineering [30,31]. In addition, utilization of MNPs with tailored surface chemistry for the development of magnetic (bio)-catalysts, has many technical and economic advantages [32]. Therefore, developing chemical processes benefitting from MNPs for both reaction and transport is undoubtedly an appealing endeavor. Here, we describe the potential of magnetic nanoparticles in mixing and mass transport intensification *via* several possible mechanisms.

A magnetic body force, as expounded in Eq.A4.6, can be put into action in the presence either of magnetic susceptibility gradient –even under uniform magnetic field– or gradient magnetic field –even at constant susceptibility–. Empowered with such a driving force and provided this latter is properly implemented; “miscible” mixing of nonmagnetic fluids with magnetic ones is possible. Owing to the latter’s facile protrusion into the former nonmagnetic regions results into smaller length scales for molecular diffusion (figure A4.3a) thus yielding intimate mixing [33]. Micromixer prototypes exploiting this mechanism have been developed more than a decade ago and are now

widely deployed in microfluidics though reaction engineering applications are still awaiting [34-37,38].

A number of studies have been reported on mixing under OMF where the governing mixing mechanism is identical to that from SMF [35,39]. Furthermore, a distinct mixing mechanism based on MNP magnetophoretic transport under gradient OMF has also been identified theoretically [40]. Simulations predicted the inception of swirling and asymmetric patterns the origin of which has been ascribed to momentum exchange between MNPs and the sheared fluid.

Contrary to OMF-stimulated mixing, a limited number of studies have been devoted to the intensification of interphase mass transfer under oscillating magnetic fields. However, discrepancies regarding the capability of low-frequency OMF for interphase mass transfer intensification have not been resolved. Coherent with the theory of magnetoviscosity, the effect of low-frequency OMF on mass transfer enhancement in gas-liquid systems was found insignificant [41,42]. Yet, contradictory reports on enhanced mass transfer in gas-liquid [43,44] and liquid-liquid [45] systems shed doubts on this view. Further scrutiny to clarify such inconsistencies requires more detailed investigations. Although the concept has *hitherto* not been put in practice, prompting negative magnetoviscosity regime is another field of opportunity for scalar transport in sheared ferrofluids.

Unlike the rationale built around Eq.A4.6 for OMF, RMF-stimulated mixing takes place even with homogeneous magnetic field and gradientless ferrofluid magnetic susceptibility [46]. It was experimentally shown that ferrofluid self-diffusion coefficients can be amplified by a few orders of magnitude for frequencies as low as 100 Hz. Optical imaging of dilute ferrofluids under RMF [47] undoubtedly revealed manifestation of vortical patterns induced by the rotating MNPs. Reminiscent of turbulent eddies, these vortices can notably enhance mass transport and mixing (figure A4.3b). This unique nano-stirring method was further implemented for the intensification of interphase gas-liquid mass transfer in the Taylor bubble flow regime [41] where an increase of liquid-side volumetric mass transfer coefficients between oxygen bubbles and ferrofluid were reported. It should be a rigorous mathematical formulation of scalar transport in ferrofluids under RMF is yet another untreated FHD problems.

Last but not least, near-surface mixing stimulation is becoming a practical concept thanks to magnetism. Though, as explained above, the response of MNPs to low-frequency OMF solicitations is severely impaired by the nanoparticle Brownian relaxation dynamics, it has recently been shown experimentally that MNPs decorating solid surface bounds can be effectively actuated under low-frequency OMF. Hence, MNPs covalently bound to hydrophilic polymer chains grafted onto the surface of polyamide membranes have been shown to lead to magnetically responsive solid surfaces capable of events rejuvenation in the vicinity of the interface [48]. Likewise, the work by Zhang et al. [49] is noteworthy as it demonstrates the importance of near-surface agitation in photocatalytic reactions. Although magnetic microparticles were used in their approach, enhanced performance of magnetic photocatalytic films was reported in comparison to conventional films (Figure A4.3c). It must be emphasized that the preparation methods proposed for magnetoresponsive surfaces are still predominantly elaborate and complex procedures.

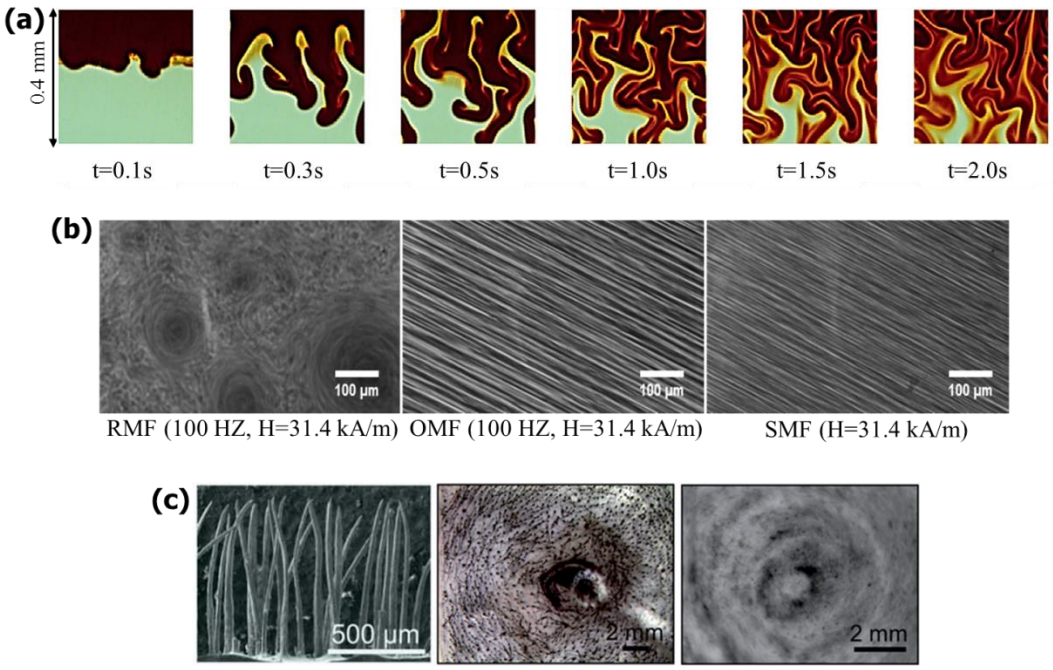

Fig A4.3 Illustration of some mixing mechanisms **(**a) Optical visualization of mixing progress between stagnant water-based ferrofluid and water under external SMF [33]; (b) Optical visualization of a ferrofluid developing vortical structures in uniform RMF unlike the frozen liner streaks under OMF and SMF [47]; (c) Left and middle pictures portray side and top views of an array of photocatalytic magnetic artificial cilia while right picture demonstrates formation of vortical flow pattern upon actuation by RMF [49].

Heat Transfer Control

Exposing MNP colloidal dispersions to an external magnetic field is a potential strategy for heat transport intensification. Hence, notable enhancement in nanofluid thermal conductivity beyond the limits of Maxwell-Garnett theory can be achieved [50]. Application of an external SMF has been shown to trigger incipience of chain-like structures in *quiescent* ferrofluids. The very existence of such assemblies in hydromagnetostatic ferrofluid conditions leads to an anisotropic enhancement in thermal conductivity in the direction of applied SMF (Figure A4.4) [50-52] in spite of the opposing Brownian agitation and steric/electrostatic repulsive forces by the surfactant [21]. The dynamics of aggregate formation is a subject of extensive investigations and good theoretical accounts are available [21,53]. Regarding sheared ferrofluids, numerous experimental studies also attempted to enhance heat transfer in uniform or gradient SMF as well as under low-frequency OMF [54-58]. These studies accordingly echoed the possibility of heat transfer coefficient enhancement *via* magnetic field actuation in laminar flows, especially with gradient fields and/or higher magnetic field intensities [58]. Nevertheless, heat transport intensification for flowing ferrofluids still lacks comprehensive mechanistic studies to give further insights regarding the precise role of MNPs in heat transfer enhancement.

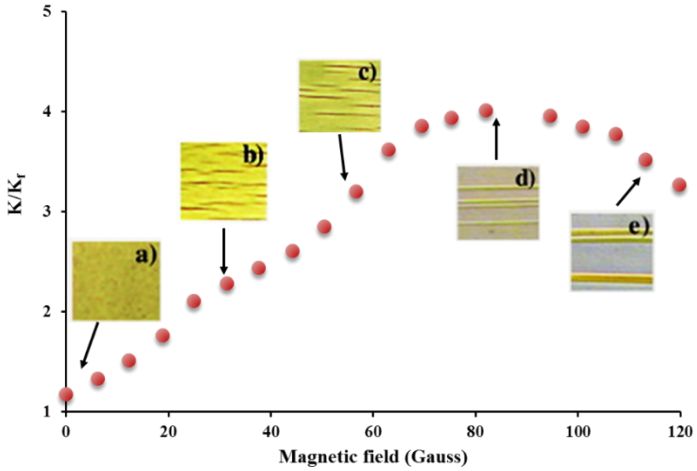

Fig A4.4 Enhancement as a function of SMF intensity of the thermal conductivity ratio normalized with respect to thermal conductivity with disabled field. Insets show optical images in zero magnetic field (a) and increasing magnetic field intensities (b-e) [59].

In addition to tuning the thermal properties of nanofluids by restructuring their nano-inclusions, MNPs are also capable of propagating heat to the surrounding media by absorbing magnetic energy from polarized fields [60]. As unfavorable heat transport in chemical reactors may cause irreparable setbacks on product formation, catalyst activity, mechanical integrity, system's safety, etc., several advantages can be expected from remote heating of MNPs to achieve uniform heat propagation and thus improved reaction selectivity or prevention of catalyst activity loss [61]. In view of these advantages, magnetic heating of chemical reactions is yet to be developed further in the future. In this regard, investigations are trending toward designing magnetic nano-catalysts with applications in macro and micro-scale reactors [62-64]. An exciting challenge for further research on this subject is to elucidate how localized magnetic heating can improve catalytic processes from both product quality and energy consumption standpoints.

Concluding remarks

A growing body of literature is highlighting the role of magnetic field actuation of magnetic nanoparticles as a potential means for process intensification and where magnetostatics and transport phenomena in ferrofluids must go hand in hand to devise genuine and practical solutions relevant to chemical engineering. Depending on the types of magnetic fields and properties of the magnetic media, a diversity of responses of MNPs and ferrofluids may be triggered by what appears to be numerous mechanisms and behaviors waiting for elucidation and better understanding. Hence, akin to any other emerging field, challenges, new opportunities and practical issues are yet to be addressed. Ferrofluids, in spite of their versatile functions in transport phenomena, are vulnerable to destabilization by changes in pH or ionic strength, in addition to restrictions to chemical reactions assisted by magnetic materials to be run below the latter's Curie temperature. Research applications of MNPs in transport phenomena in conjunction with chemical reactions are still at infancy and where veritable advances are foreseen by exposing how magnetism and reaction engineering may cooperate for the sake of more efficient chemical processes. Until now only the most basic application of MNPs in developing magnetically separable catalysts is well documented in the literature. However, there is room for formidable progress on bifunctional magnetic nanomaterials that simultaneously merge the functions of catalysis and transport phenomena.

Nomenclature

Latin letters	Description	Units
$\mathbf{B}$	Magnetic flux density	T
f_0	Larmor frequency of the magnetization vector	Hz
$\mathbf{F}$	External body force density	N/m^3
$\mathbf{F_m}$	Kelvin body force density	N/m^3
$\mathbf{H}$	Magnetic field vector	A/m
I	Moment of inertia density of magnetic nanoparticles	m^2
K	Anisotropy constant	J/m^3
k_B	Boltzmann's constant	J/K
$\mathbf{M}$	Magnetization vector	A/m
$\mathbf{M_0}$	Saturation magnetization vector	A/m
p	Pressure	Pa
V_H	Hydrodynamic volume of nanoparticles	m^3
V_p	Magnetic particle core volume	m^3
t	Time	s
T	Absolute temperature	K
$\mathbf{u}$	Velocity vector	m/s
Greek letters	**Description**	**Units**
ζ	Vortex viscosity	Pa s
η	Dynamic viscosity	Pa s
η'	Shear spin viscosity	Kg m s^{-1} rd^{-1}
λ'	Bulk spin viscosity	Kg m s^{-1} rd^{-1}
μ_0	Absolute magnetic permeability of vacuum	N/A^2
ρ	Density	Kg/m^3
τ	Effective relaxation time	s
τ_b	Brownian relaxation time	s
τ_n	Neelian relaxation time	s
χ_i	Initial magnetic susceptibility	-
$\boldsymbol{\omega}$	Spin density vector	s^{-1}

References

1. Torres-Diaz I, Rinaldi C: Recent progress in ferrofluids research: novel applications of magnetically controllable and tunable fluids. *Soft Matter* 2014,**10**,8584-8602.
2. Rosensweig RE: *Ferrohydrodynamics*. Dover Publications; 1997.
3. Batlle X, Labarta A: Finite-size effects in fine particles: magnetic and transport properties. *J Phys D: Appl Phys* 2002,**35**, 15-42.
4. Rosensweig RE: Continuum equations for magnetic and dielectric fluids with internal rotations. *J Chem Phys* 2004,**121**,1228-1242.
5. Shliomis MI: Effective viscosity of magnetic suspensions. *J Exp Theor Phys* 1972,**34**,1291-1294.
6. Odenbach S, Thurm S: Magnetoviscous effects in ferrofluids. In *Ferrofluids: Magnetically Controllable Fluids and Their Applications*. Edited by Odenbach S. Springer; 2002,185-201.
7. Larachi F, Desvigne D: Magnetoviscous control of wall channeling in packed beds using magnetic nanoparticles - Volume-average ferrohydrodynamic model and numerical simulations. *Chem Eng Sci* 2006,**61**,1627-1657.

8. Morozov K, Shliomis M, Zahn M: Magnetoviscosity in suspensions of grains with finite magnetic anisotropy. *Phys Rev E*, 2006,**73**, 066312.
9. Bacri JC, Perzynski R, Shliomis MI, Burde GI: Negative-viscosity effect in a magnetic fluid. *Phys Rev Lett* 1995,**75**,2128-2131.
10. Torres-Diaz I, Cortes A, Cedeno-Mattei Y, Perales-Perez O, Rinaldi C: Flows and torques in Brownian ferrofluids subjected to rotating uniform magnetic fields in a cylindrical and annular geometry. *Phys Fluids* 2014,**26**,012004.
11. Torres-Diaz I, Rinaldi C, Khushrushahi S, Zahn M: Observations of ferrofluid flow under a uniform rotating magnetic field in a spherical cavity. *J App Phys* 2012,**111**,07B313.
12. Zeuner A, Richter R, Rehberg I: Experiments on negative and positive magnetoviscosity in an alternating magnetic field. *Physical Review E* 1998,**58**,6287-93.
13. Schumacher KR, Sellien I, Knoke GS, Cader T, Finlayson BA: Experiment and simulation of laminar and turbulent ferrofluid pipe flow in an oscillating magnetic field. *Phys Rev E* 2003,**67**,026308.
14. Schumacher KR, Riley JJ, Finlayson BA: Effects of an oscillating magnetic field on homogeneous ferrofluid turbulence. *Phys Rev E* 2010,**81**,016317.
15. Larachi F, Desvigne D: Ferrofluid magnetoviscous control of wall flow channeling in porous media. *China Part* 2007,**5**,50-60.
16. Larachi F, Desvigne D: Ferrofluid induced-field effects in inhomogeneous porous media under linear-gradient dc magnetic fields. *Chem Eng Process*, 2007,**46**,729-735.
17. Hajiani P, Larachi F: Reducing Taylor dispersion in capillary laminar flows using magnetically excited nanoparticles: Nanomixing mechanism for micro/nanoscale applications. *Chem Eng J*, 2012,**203**,492-498.
18. Hajiani P, Larachi F: Controlling lateral nanomixing and velocity profile of dilute ferrofluid capillary flows in uniform stationary, oscillating and rotating magnetic fields. *Chem Eng J* 2013,**223**,454-466.
19.Hajiani P, Larachi F: Magnetic-field assisted mixing of liquids using magneticnanoparticles. *Chem Eng Process*, 2014,**84**,31-37.
20. Munir A, Wang J, Zhu Z, Zhou HS: Residence time distribution analysis of magnetic nanoparticle-enhanced mixing using time-dependent magnetic actuation in microfluidic system. *Microfluid Nanofluid*, 2011,**10**,735-747.
21. Faraudo J, Camacho J: Cooperative magnetophoresis of superparamagnetic colloids: theoretical aspects. *Colloid Polym Sci*, 2010,**288**,207-215.
22. Heinrich D, Goni AR, Osan TM, Cerioni LMC, Smessaert A, Klapp SHL, Faraudo J, Pusiol DJ, Thomsen C: Effects of magnetic field gradients on the aggregation dynamics of colloidal magnetic nanoparticles. *Soft Matter* 2015,**11**,7606-7616.
23. Leong SS, Ahmad Z, Lim J: Magnetophoresis of superparamagnetic nanoparticles at low field gradient: hydrodynamic effect. *Soft Matter* 2015,**11**,6968-6980.
24. Rosensweig RE: Fluidization - Hydrodynamic stabilization with a magnetic field. *Science* 1979,**204**,57-60.
25. Zong BN, Meng XK, Mu XH, Zhang XX: Magnetically stabilized bed reactors. *Chin J Catal* 2013,**34**,61-68.
26. Li J, Zhou L, Zhu QS, Li HZ: Enhanced Methanation over Aerogel $NiCo/Al_2O_3$ Catalyst in a Magnetic Fluidized Bed. *Ind Eng Chem Res*, 2013,**52**,6647-6654.
27. Cheng M, Xie WH, Zong BN, Sun B, Qiao MH: When Magnetic Catalyst Meets Magnetic Reactor: Etherification of FCC Light Gasoline as an Example. *Sci Rep*, 2013,**3**,1-5.
28. Jovanovic GN, Atwater JE, Znidarsic-Plazl P, Plazl I: Dechlorination of polychlorinated phenols on bimetallic Pd/Fe catalyst in a magnetically stabilized fluidized bed. *Chem Eng J*, 2015,**274**,50-60.

29. Zhang JL, Zhang M, Li W, Li XF, Meng XK, Zong BN: Local heat transfer properties in co- and counter-current G-L-S magnetically stabilized fluidized beds. *Particuology*, 2011,**9**,44-50.
30. Yoshida J, Nagaki A, Iwasaki T, Suga S: Enhancement of chemical selectivity by microreactors. *Chem Eng Technol*, 2005,**28**,259-266.
31. Bourne JR: Mixing and the selectivity of chemical reactions. *Org Process Res Dev* 2003,**7**,471-508.
32. Rossi LM, Costa NJS, Silva FP, Wojcieszak R: Magnetic nanomaterials in catalysis: advanced catalysts for magnetic separation and beyond. *Green Chem*, 2014,**16**,2906-2933.
33. Kitenbergs G, Erglis K, Perzynski R, Cebers A: Magnetic particle mixing with magnetic micro-convection for microfluidics. *J Magn Magn Mater* 2015,**380**,227-230.
34. Tsai T-H, Liou D-S, Kuo L-S, Chen P-H: Rapid mixing between ferro-nanofluid and water in a semi-active Y-type micromixer. *Sens Actuator A-Phys* 2009,**153**,267-273.
35. Wen C-Y, Liang K-P, Chen H, Fu L-M: Numerical analysis of a rapid magnetic microfluidic mixer. *Electrophoresis* 2011,**32**,3268-3276.
36. Zhu G-P, Nam-Trung N: Rapid magnetofluidic mixing in a uniform magnetic field. *Lab Chip* 2012,**12**,4772-4780.
37. Wang ZM, Varma VB, Xia HM, Wang ZP, Ramanujan RV: Spreading of a ferrofluid core in three-stream micromixer channels. *Phys Fluids*, 2015,**27**,052004.
38. Yang RJ, Hou HH, Wang YN, Fu LM: Micro-magnetofluidics in microfluidic systems: A review. *Sens Actuator B-Chel* 2016,**224**,1-15.
39. Wen C-Y, Yeh C-P, Tsai C-H, Fu L-M: Rapid magnetic microfluidic mixer utilizing AC electromagnetic field. *Electrophoresis* 2009,**30**,4179-4186.
40. Munir A, Zhu Z, Wang J, Zhou H: FEM analysis of magnetic agitation for tagging biomolecules with magnetic nanoparticles in a microfluidic system. *Sens Actuator B-Chem* 2014,**197**,1-12.
41. Hajiani P, Larachi F: Remotely excited magnetic nanoparticles and gas-liquid mass transfer in Taylor flow regime. *Chem Eng Sci* 2013,93:257-265.
42. Komati S, Suresh AK: CO2 absorption into amine solutions: a novel strategy for intensification based on the addition of ferrofluids. *J Chem Technol and Biotechnol* 2008,**83**,1094-1100.
43. Samadi Z, Haghshenasfard M, Moheb A: CO2 Absorption Using Nanofluids in a Wetted-Wall Column with External Magnetic Field. *Chem Eng Technol* 2014,**37**,462-470.
44. Suresh AK, Bhalerao S: Rate intensification of mass transfer process using ferrofluids. *Indian J Pure Appl Phys* 2002,**40**,172-184.
45. Saien J, Bamdadi H, Daliri S: Liquid-liquid extraction intensification with magnetite nanofluid single drops under oscillating magnetic field. *J Ind Eng Chem* 2015,**21**,1152-1159.
46. Hajiani P, Larachi F: Giant effective liquid-self diffusion in stagnant liquids by magnetic nanomixing. *Chem Eng Process* 2013,**71**,77-82.
47. Gravel O, Lauzon-Gauthier J, Duchesne C, Larachi F: Inception of vortical coherent structures from spinning magnetic nanoparticles in rotating magnetic fields - New nanofluid microscale mixing tool. *Chem Eng J* 2015,**260**,338-346.
48. Himstedt HH, Yang Q, Dasi LP, Qian XH, Wickramasinghe SR, Ulbricht M: Magnetically Activated Micromixers for Separation Membranes. *Langmuir* 2011,**27**,5574-5581.
49. Zhang D, Wang W, Peng F, Kou J, Ni Y, Lu C, Xu Z: A bio-inspired inner-motile photocatalyst film: a magnetically actuated artificial cilia photocatalyst. *Nanoscale* 2014,**6**,5516-5525.
50. Shima PD, Philip J, Raj B: Role of microconvection induced by Brownian motion of nanoparticles in the enhanced thermal conductivity of stable nanofluids. *Appl Phys Lett* 2009,**94**,223101.

51. Philip J, Shima PD, Raj B: Enhancement of thermal conductivity in magnetite based nanofluid due to chainlike structures. *Appl Phys Lett* 2007,**91**,203108.
52. Patel J, Parekh K, Upadhyay RV: Maneuvering thermal conductivity of magnetic nanofluids by tunable magnetic fields. *J Appl Phys* 2015,**117**,243906.
53 Faraudo J, Andreu JS, Camacho J: Understanding diluted dispersions of superparamagnetic particles under strong magnetic fields: a review of concepts, theory and simulations. *Soft Matter* 2013,**9**,6654-6664.
54. Goharkhah M, Ashjaee M, Shahabadi M: Experimental investigation on convective heat transfer and hydrodynamic characteristics of magnetite nanofluid under the influence of an alternating magnetic field. *Int J Therm Sci* 2016,**99**,113-124.
55. Goharkhah M, Salarian A, Ashjaee M, Shahabadi M: Convective heat transfer characteristics of magnetite nanofluid under the influence of constant and alternating magnetic field. *Powder Technol* 2015,**274**,258-267.
56. Yarahmadi M, Goudarzi HM, Shafii MB: Experimental investigation into laminar forced convective heat transfer of ferrofluids under constant and oscillating magnetic field with different magnetic field arrangements and oscillation modes. *Exp Therm Fluid Sci* 2015,**68**,601-611.
57. Nkurikiyimfura I, Wang YM, Pan ZD: Heat transfer enhancement by magnetic nanofluids-A review. *Renew Sustainable Energy Rev* 2013,**21**,548-561.
58. Azizian R, Doroodchi E, McKrell T, Buongiorno J, Hu LW, Moghtaderi B: Effect of magnetic field on laminar convective heat transfer of magnetite nanofluids. *Int J Heat Mass Tran* 2014,**68**,94-109.
59. Angayarkanni SA, Philip J: Review on thermal properties of nanofluids: Recent developments. *Adv Colloid Interface Sci* 2015,225:146-176.
60. Rosensweig RE: Heating magnetic fluid with alternating magnetic field. *J Magn Magn Mater* 2002,**252**,370-374.
61. Houlding TK, Rebrov EV: Application of alternative energy forms in catalytic reactor engineering. *Green Process Synth* 2012,**1**,19-31.
62. Houlding TK, Gao PZ, Degirmenci V, Tchabanenko K, Rebrov EV: Mechanochemical synthesis of TiO_2/$NiFe_2O_4$ magnetic catalysts for operation under RF field. *Mat Sci Eng B-solid* 2015,**193**,175-180.
63. Zadrazil A, Stepanek F: Remote control of reaction rate by radiofrequency heating of composite catalyst pellets. *Chem Eng Sci* 2015,**134**,721-726.
64. Meffre A, Mehdaoui B, Connord V, Carrey J, Fazzini PF, Lachaize S, Respaud M, Chaudret B: Complex Nano-objects Displaying Both Magnetic and Catalytic Properties: A Proof of Concept for Magnetically Induced Heterogeneous Catalysis. *Nano Lett* 2015,**15**,3241-32418.